ICFO – Institut de Ciències Fotòniques
&
Universitat Politècnica de Catalunya –
Barcelona Tech

Doctoral Thesis

Quantum-enhanced imaging with SPAD array cameras

Author:
Robin Camphausen

Supervisor:
Prof. Valerio Pruneri

A thesis submitted in fulfillment of the requirements for the degree of Doctor of Philosophy

in the

Optoelectronics Group

February 17, 2023

Declaration of Authorship

I, Robin CAMPHAUSEN, declare that this thesis titled, "Quantum-enhanced imaging with SPAD array cameras" and the work presented in it are my own. I hereby certify that:

- The thesis I am submitting is my own original work, and that the material included has not been published or submitted elsewhere for the award of any degree or diploma, except where otherwise explicitly indicated.
- Where required, permission has been sought to reproduce in this thesis original material from published works for which I am an author.
- I am aware of ICFO's policies concerning plagiarism, including disciplinary actions that may result from plagiarism.
- Any use of the works of any other author, in any form, is properly acknowledged at their point of use.

Signed: _____

Date: _____

Abstract

Entangled photon pairs can enhance optical imaging capabilities. Phase imaging allows detecting fine detail of transparent samples without potentially invasive fluorescent labelling, and here entanglement enables a higher signal-to-noise ratio (SNR) than possible with only classical light. Spatial correlations from spontaneous parametric down conversion (SPDC) photon pair sources can also be used to increase spatial resolution and robustness to noise and aberrations in imperfect optical systems. Quantum imaging therefore represents a powerful approach to push imaging science beyond its current limits.

Until recently, the principal barrier to implementing useful quantum imaging schemes based on entangled photons has been technological, as scalable image sensors capable of multi-photon imaging were unavailable. However, this situation has changed with the development of single photon avalanche diode (SPAD) array cameras, as well as efficient high brightness entangled photon pair sources based on SPDC. These advances have led to the required components now approaching relative technological maturity, opening the window towards engineering useful and scalable systems that exploit entanglement in order to improve optical imaging.

In this thesis, we show the development of a quantum imaging platform able to perform practical and fast spatially resolved multi-photon coincidence imaging with high SNR. Special focus is placed on wide-field entanglement-enhanced phase imaging capability, in order to extend experimental sensitivity beyond limits imposed by classical light. The main components of our platform are: sources of hyper-entangled photon pairs, a large field-of-view optical imaging system with phase measurement capabilities, and coincidence imaging using SPAD array cameras. More specifically, the thesis describes:

- The first realization of a wide-field entanglement-enhanced phase imager. Wide-field here refers to the ability to acquire images across the entire field-of-view simultaneously (i.e. without need for pixel-to-pixel scanning, sometimes also called full-field). Quantum-enabled super-sensitivity in phase imaging beyond the capability of equivalent classical measurement is demonstrated by careful experimental noise and resource analysis methods. Our system's capabilities were tested through several sample measurements corresponding to use cases with real-world relevance, including nanometre-scale feature step heights in transparent material, biomedical protein microarrays, as well as birefringent phase samples.

- The development of general experimental and numerical tools to calculate photon pair coincidence images and videos from SPAD array cameras, with photon-counting and time-tagging readout modalities, as well as the retrieval of phase images resulting from multi-photon entanglement interference, by adapting techniques from interferometry and holography. We performed also a detailed study and optimization of the influence of different experimental parameters resulting image quality factors.

- The evolution and optimization of our system towards real-time quantum imaging capability. Acquisition speed is a key element of usefulness, and in this thesis we integrate, first, a visible-wavelength entangled photon source, and second, a novel time-tagging SPAD array camera. The resulting entanglement enabled imager presents an improvement by at least four orders of magnitude in measurement speed compared to previous state-of-the-art demonstrations, resulting in the ability to record $\sim$Hz frame rate entangled photon pair coincidence videos. We show that this system, besides phase imaging, has additional applications in the form of real-time entangled state fidelity monitoring, and real-time point spread function characterization of optical systems which has important applicability to adaptive optical imaging.

Resumen

Los pares de fotones entrelazados pueden mejorar la capacidad de obtención de imágenes. La formación de imágenes de fase permite detectar detalles de muestras transparentes con alta precisión y sin necesitar marcas fluorescentes potencialmente invasivas. Además, el entrelazamiento permite una mayor relación señal-ruido (SNR, por sus siglas en inglés) de la que es posible utilizando luz clásica. Las correlaciones espaciales de las fuentes de pares de fotones basadas en conversión paramétrica descendente espontánea (SPDC, por sus siglas en inglés) también pueden ser empleadas para aumentar la resolución espacial, y la robustez frente al ruido y a las aberraciones. Por tanto, las técnicas de captación de imagen cuántica son una potente estrategia para impulsar el campo de la ciencia de la fotografía especializada más allá de sus límites actuales.

La mayor barrera en la implementación de esquemas de captación de imágenes cuánticas basadas en fotones entrelazados es principalmente tecnológica, al carecer de sensores de imagen escalables capaces de detectar imágenes multifotónicas. No obstante, el desarrollo de cámaras de matriz de fotodiodos de avalancha de fotón único (SPAD, por sus siglas en inglés), y de fuentes de pares de fotones entrelazados de alta eficiencia y brillo, basadas en SPDC, ha cambiado el panorama actual. Estos avances han permitido que los componentes necesarios alcancen una relativa madurez tecnológica, lo que abre una ventana de oportunidad para la ingeniería de sistemas útiles que aprovechan el entrelazamiento para mejorar la imagen óptica.

En esta tesis, mostramos el desarrollo de una plataforma de captación de imágenes cuántica práctica y rápida, capaz de generar imágenes mediante el uso de coincidencias multifotónicas. Principalmente, nos centramos en la capacidad de formar imágenes de fase de campo amplio, mejoradas por entrelazamiento. Los componentes principales de nuestra plataforma son: fuentes de pares de fotones hiperentrelazados, un sistema óptico de imagen con un gran campo de visión y capacidad de medición de fase, y formación de imagen mediante la detección en coincidencias utilizando cámaras SPAD. Específicamente, la tesis describe:

- La primera realización de un sistema de captación de imágenes de fase en configuración de campo amplio mejorado por entrelazamiento. Utilizando métodos de análisis del ruido y de los recursos, se logró demostrar la supersensibilidad en la medición de fase facilitada por iluminación con luz cuántica. Las capacidades de nuestro sistema se probaron con medidas correspondientes a ejemplos del mundo real, por ejemplo, midiendo microarreglos ultrafinos (grosor de $\sim$nm) en materiales transparentes, muestras biomédicas de microarrays de proteínas, y de fase birrefringente.

- El desarrollo de herramientas numéricas y experimentales generales para calcular imágenes y vídeos de coincidencias de pares de fotones con cámaras SPAD, con modos de lectura de conteo de fotones y etiquetado de tiempo. Además, se desarrolló la recuperación de imágenes de fase del entrelazamiento, adaptando técnicas de interferometría y holografía. Asimismo, se realizó un estudio detallado sobre la influencia de diferentes parámetros experimentales en los factores de calidad de imagen.

- La evolución y optimización de nuestro sistema hacia la formación de imágenes cuánticas en tiempo real. Se integró primero una fuente de fotones entrelazados de longitud de onda visible y, seguidamente, una nueva cámara SPAD con marcado temporal. El sistema resultante presenta una mejora de al menos cuatro órdenes de magnitud en la velocidad de medición en comparación con otras demostraciones. Esto confiere al sistema la capacidad de grabar vídeos de coincidencias de pares de fotones entrelazados con una tasa de fotogramas de $\sim$Hz. Este sistema, además de medir la fase, tiene aplicaciones para monitorizar tanto la fidelidad de estados de entrelazamiento como la caracterización de la función de dispersión de punto.

Acknowledgements

I would like to express my gratitude to several people without whom this thesis would not have been possible.

First of all, I would like to thank my supervisor Valerio Pruneri, for making this PhD in such an interesting project possible at all. Ever since joining Valerio's group I have felt only support and encouragement to learn new science and push technology forward. I am grateful for all the time and effort dedicated to me, as well as the trust and independence I was afforded such that I feel I could grow as a person and scientist.

I have to also thank all the members of the Optoelectronics group at ICFO, past and present. You all contribute to creating a really special supportive and stimulating atmosphere, which it was a pleasure to work in. In particular, I would like to thank my (unofficial) co-supervisor Álvaro for the unfailing guidance, motivation, time, and effort, and for imparting a wealth of experience in the lab, as well as serving as frequent sounding board willing to indulge every crazy idea. Special thanks must go also to my optical-table-mate Alex for the many interesting and useful discussions problem-solving together. And deepest thank you to the other members of our "(quantum) imaging team", Daniel, Adam, Evelyn, Rajdeep, Giacomo, Martin, Valeria, Birger, Deeksha, Roland, Luc, Sebastian, Javi – you all created a very nice working relationship, and I have enjoyed the collaboration with you and learnt a lot!

Furthermore, I would like to thank all the hugely knowledgeable and talented collaborators from outside of ICFO I have had the privilege to work with. Federica, Franco, Iris, Fabio, Francesca, Alessandro, Simone, Adrià, Fabian, Markus, Carlos, Daniele, Hugo – I have learnt an incredible amount, and found the experiences as stimulating and challenging as they were rewarding.

Special thanks to all ICFO staff that help to make it such a unique place, it is a great privilege to have experts in every field preoccupy themselves with all our non-research needs such that we are able to focus only on science. This thesis could not have happened without the wonderful staff working in the mechanical workshop, electronic workshops, logistics and facilities, HR and project management, purchasing, travel, and management. For all your efforts, I am very grateful.

To all friends and housemates (in Barcelona and elsewhere) I have been fortunate enough to know, who provided welcome distractions from the lab both day and night: it's been amazing, and I owe it to you.

Finally, thank you to my family, for their continued loving help and support. To my parents Mami and Papi, to Colin and Rachel, to Consuelo and Emilio, Mari Cruz, Koon Hock, Daniel and Miriam, Yolanda, Oscar, Yolanda and Bruno, thank you for everything. And lastly, our little family, Marta and Toffee, you keep me happy and sane. Marta, for your love and strength and for everything, thank you.

Contents

List of Common Abbreviations

SPAD	Single Photon Avalanche Diode
ISA	Image Sensor Array
SNR	Signal-to-Noise Ratio
CAR	Coincidences-to-Accidentals Ratio
CMOS	Complementary Metal-Oxide-Semiconductor
SPDC	Spontaneous Parametric Down Conversion
EPS	Entangled Photon Source
VEPS	Visible-wavelength Entangled Photon Source
SNL	Shot Noise Limit
SQL	Standard Quantum Limit
ppKTP	Periodially Poled Potassium Titanyl Phosphate (KTP)
BBO	Beta Barium Borate
QPM	Quasi-Phase Matching
FoV	Field Of View
LIM	Large Field-of-view Interference Microscope
SI	Sagnac Interferometer
PSDH	Phase Shifting Digital Holography
HWP	Half-wave Plate
BS	Beam-splitter

PBS Polarizing Beam-splitter

NIR Near-InfraRed

CW Continuous Wave

PDE Photon Detection Efficiency

SLM Spatial Light Modulator

Chapter 1

Introduction

Seeing is believing: optical imaging is perhaps the most important means through which we understand the world. In science and technology, devices and methods have developed that improve upon the abilities of the human eye, making visible what was "invisible", and revolutionizing understanding across many fields. For example, enhanced imaging capabilities in biology have uncovered inner processes that dictate the functioning of living organisms, while in material science they have enabled precise fabrication of ever finer structures at micro and nanoscale [1, 2]. These advances have led to applications in a wide range of sectors such as health and diagnostics, and industrial metrology.

1.1 Classical optical imaging and its limitations

There are three essential ingredients in optical imaging. First, a light source illuminates the object of interest. Second, light from the object is collected by an optical system, which forms an *image* of the object. Third, the light is then detected by a detector capable of faithfully registering the image. Significant advances in any of these three steps improve imaging capabilities, which often leads to new insights or applications [3]. The development of bright and stable light sources as well as efficient low noise cameras allows increasingly sensitive imaging, in which slight differences in samples are accurately represented in detected images [4]. Refinements in optical lenses and mirrors have resulted in powerful microscopes, providing images of small-scale sample features at high spatial resolution. Spatial resolution is further being improved by a battery of fluorescence imaging techniques [1]. Optical systems capable of interference imaging, visualizing phase shifts in the probe light, allow detecting completely transparent features against equally transparent samples and substrates [5–8]. Increasing camera acquisition speed has led to being able to record sample dynamics [9].

However nowadays, in many cases continuing these improvement steps one faces difficulties due to fundamental properties of light, rather than technical imperfections of experimental equipment. Prominently, imaging *sensitivity*, which relates to the smallest change in a sample detectable by the measurement, is now largely limited by the photon statistics of classical light (and not by specifications of light source and/or detector). To be concrete, it is well known that detecting classical light with a means number of M photons incurs an uncertainty of $\sqrt{M}$

photons due to the so-called *shot noise* [4, 10]. In other words, increasing the signal-to-noise ratio (SNR) necessarily requires increasing the number of illumination photons M. But, many samples are themselves modified or even damaged by too high illumination levels, and thus M cannot be increased arbitrarily high [11]. Further challenges include imaging samples deep inside complex media (such as cells in living tissue), where light from the object is distorted in propagation. Here, typically active adaptive optical imaging systems are required to obtain sharp images, however, optimizing such adaptive optics is an iterative procedure, and often the necessary characterization of aberrations is difficult to obtain [12, 13]. In addition, image spatial resolution is limited by diffraction of light to approximately half of the illumination wavelength [3]. While this limit can be beaten using fluorescence imaging techniques [14, 15], fluorophores themselves can interfere with samples under studied, representing therefore a potentially invasive method.

1.2 Quantum imaging

A relatively new approach that seeks to overcome the aforementioned limitations is quantum imaging. Emerging from fundamental studies in quantum optics and quantum information, a number of techniques relying on quantum resources have been identified that can help to surpass the limits of classical imaging [16, 17]. From quantum metrology it is known that multi-photon entangled states enable phase measurements with higher sensitivity than possible classically [10, 18]. This can therefore allow surpassing shot noise-limited SNR, thus reaching in critical samples a higher sensitivity without resorting to damaging illumination intensities [19, 20]. Spatial or momentum correlations between the constituent photons forming multi-photon quantum states of light can aid in complex imaging situations, for example by rejecting strong scattering [21, 22] or in optimizing adaptive optics [23]. Super-resolution quantum microscopy makes use of spatially correlated or entangled multi-photon states to surpass diffraction limited spatial resolution without requiring fluorescent labelling [24, 25]. Exploiting quantum resources has also enabled new imaging modalities which have no classical counterparts, such as imaging with undetected photons [26], and imaging based on the Hong-Ou-Mandel effect [27].

Quantum imaging using multi-photon quantum states of light places specific requirements on the essential ingredients of optical imaging described above. First, clearly the light source must emit multi-photon states, which then illuminate the object. For the case of quantum states consisting of two entangled photons (i.e. entangled photon pairs), there exists a readily available solution in the form of spontaneous parametric down conversion (SPDC) in bulk nonlinear crystals [28]. The increased prominence of quantum networks has, in recent years, led to rapid development of SPDC entangled photon sources (EPSs), which therefore now represent a platform with high technological maturity. Second, the imaging detector must likewise be capable of detecting these multi-photon states. Until recently,

this latter requirement in particular could not be satisfied in a practical and scalable manner. In order to detect multi-photon states, it is necessary to count temporal *correlations* between photon detections [29]. In intuitive terms: if a multi-photon state is generated at a particular moment in time, we would expect all the photons constituting this state to arrive at the detector at the same time. Measuring multi-photon behaviour therefore means that the imaging detector must be capable of registering with a high degree of accuracy the occurrence of such *coincidences*, that is, multiple temporally correlated detections.

Coincidence imaging is, in principle, feasible with "traditional" image sensor technologies. Using electron-multiplying charge-coupled device (EMCCD) and even ordinary charge-coupled device (CCD) cameras, it is possible to retrieve the wanted temporal correlations through statistical analysis of a large dataset of many intensity images [30, 31]. However, due to slow readout speeds and non-negligible technical noise, using EMCCD and CCD cameras for quantum imaging results in extremely low acquisition speeds of many hours or even days. Intensified CCD cameras have also been used in proof-of-principle quantum imaging demonstrations, but suffer from similar drawbacks [32]. The practicality of quantum imaging with EMCCDs and ICCDs is further detrimentally affected by the need for expensive custom components difficult to mass-produce: EMCCDs require bulky active cooling equipment to achieve sufficiently low camera technical noise, while ICCDs rely on high voltage analogue electronics in the intensifier (photocathode, microchannel plate, and phosphor screen) [33]. A more natural solution to the problem of detecting temporal coincidences is offered by so-called single-photon detectors, such as single-photon avalanche diodes (SPADs), and superconducting nanowire single-photon detectors (SNSPDs) [34, 35]. These detection technologies natively allow registering photon detections with zero readout noise and high temporal resolution (below nanosecond level) [29, 36]. SPADs and SNSPDs have been the detectors of choice in experimental quantum optics for many years. However, until recently they were only available in "single-pixel" format, that is, as stand-alone units integrating only one detector. In fact, while quantum-enhanced phase imaging was shown already using SPAD detectors in Refs. [37] and [38], these works do not represent true imaging platforms as the entangled photons probing a sample were detected with single-pixel detectors and images were constructed by scanning the sample point-by-point. This inherently limits scalability due to a range of practical drawbacks, including mechanical vibrations and long-term reliability issues caused by moving parts, the necessity of complex synchronization procedures between pixel-scanning and light detection, and prohibitively long scanning times.

The realization of two-dimensional arrays of SPADs fabricated in standard complementary metal oxide semiconductor (CMOS) processes represents the most important recent advance in quantum imaging. The *SPAD array cameras* thus fabricated are mass-producible and therefore scalable and affordable in principle [39]. SPAD array cameras allow low noise, extremely fast coincidence counting at room temperature operation [40, 41], and moreover in relevant performance parameters such as pixel number and detection efficiency are beginning to approach if not surpass competing camera technologies [42]. Therefore, the combination of SPDC-based entangled photon sources and SPAD array cameras, with both platforms

presently reaching relatively high degree of technological maturity, presents an opportunity to develop practical quantum imaging techniques that may become useful beyond laboratory proof-of-principle demonstrations.

In this thesis, we push forwards the development of quantum imaging, integrating SPDC entangled photon sources and SPAD array cameras, as a means to extend beyond the current limits of optical imaging science. Our primary focus is the realization of quantum-enhanced phase imaging. The motivation for focusing on phase imaging is two-fold: quantitative phase imaging is increasingly being adopted in biomedicine as less invasive than the more established fluorescence imaging methods [8], and it is well-known that by using entanglement the phase measurement sensitivity can be improved with respect to the classical shot noise limit described above [18]. Moreover, our work on entanglement-enhanced phase imaging complements existing active research directions seeking to enhance spatial resolution with SPDC and SPAD array cameras [43]. The secondary focus of this thesis is more exploratory: having optimized a practical and scalable quantum imaging system based on SPDC and SPAD arrays, we would like to understand whether SPDC spatial correlations can be utilized in advanced microscopic imaging techniques.

1.3 Thesis objectives

This thesis is dedicated to advancing practical and scalable quantum-enhanced imaging techniques. To this end the main objectives of this thesis are:

- Realization of a wide-field entanglement-enhanced phase imager. Wide-field here refers to the ability to acquire images across the entire field-of-view (FoV) simultaneously (sometimes also called full-field).
- Development of computational methods to recover coincidence images and videos from SPAD array cameras, as well as the retrieval of phase images resulting from multi-photon entanglement interference.
- Detailed study of the influence of different experimental parameters on coincidence image quality factors, such as sensitivity, as well as theoretical and experimental techniques to optimize target image specifications.
- Optimization of entanglement-enhanced phase imaging acquisition speed through the use of first a visible-wavelength entangled photon source, and second, a novel time-tagging SPAD array camera, up to real-time quantum imaging capability.
- Demonstration of additional applications in the form of real-time entangled state fidelity monitoring, by imaging interference fringe contrast, and exploiting SPDC spatial correlations for real-time point spread function characterization of optical systems, which is important in adaptive optical imaging.

1.4 Thesis outline

The thesis is structured as follows:

Chapter 2 introduces quantum states of light, and describes the most common way to generate two-photon quantum states, spontaneous parametric down conversion (SPDC). Some details on the experimental configurations that allow generating entanglement in polarization and space-momentum using SPDC are also provided.

Chapter 3 describes how coincidences can be measured by SPAD array cameras, which enables the detection and imaging of entangled photon states. First introducing the simplest possible coincidence counting setup consisting of two single-pixel SPADs, these techniques are then extended to photon-counting, and time-tagging SPAD array cameras.

Chapter 4 provides a mathematical description of the interference of light. The formalism for classical and entangled N-photon N00N state interference is presented, as well as two methods to retrieve an unknown sample phase: firstly, inverting the sinusoidal dependence of an interferometer output detection signal on the sample phase, and secondly, phase-shifting digital holography (PSDH). Chapter 4 also presents a quantification of the experimental uncertainty in phase measurements, allowing therefore to compare relative sensitivities between different phase measurements.

Chapter 5 presents the first experimental demonstration of an entanglement-enabled super-sensitive phase imager operating in a wide-field configuration. This is achieved by exploiting hyper-entanglement, simultaneous N00N state entanglement in polarization and correlations in a massive pixel mode state space, enabling the retrieval of phase information with a large field-of-view (FoV) using a SPAD array camera. The feasibility of this approach is demonstrated by retrieving phase images of birefringent and non-birefringent test samples, including a protein microarray sample which demonstrates the applicability for biomedical diagnostic applications. Sensitivity enhancements over equivalent classical measurements agreeing with theoretical predictions are also shown.

Chapter 6 describes how a visible-wavelength entangled photon source can enable high-speed quantum imaging. By operating at high SPAD array detection efficiency, acquisition speed is increased by more than an order of magnitude compared to Chapter 5. The accurate retrieval of nanometre scale height differences is also demonstrated. Lastly, Chapter 6 introduces a method to quantify phase sensitivity, which is independent of phase image spatial distribution.

Chapter 7 presents results combining visible-wavelength entangled photon pair illumination and a new time-tagging SPAD array camera with a near unity duty cycle. Firstly, SPDC photon pair spatial correlations are used to obtain real-time videos of an imaging system's point spread function (PSF). Secondly, Chapter 7 demonstrates real-time wide-field imaging of interference fringes resulting from classical and two-photon N00N state interference, where fringe contrast can be used to optimize interference visibility. Thirdly real-time wide-field entanglement-enhanced phase imaging (similar to Chapters 5 and 6) is shown at $\sim$Hz frame rate.

Chapter 8 summarizes the main results of this thesis, and gives a brief outlook on potential future developments.

1.5 List of Publications

This thesis contains results and discussions, which are in preparation, have been submitted, or are published in peer-reviewed journals:

1.5.1 Publications included in this thesis

- Robin Camphausen, Álvaro Cuevas, Luc Duempelmann, Roland A. Terborg, Ewelina Wajs, Simone Tisa, Alessandro Ruggeri, Iris Cusini, Fabian Steinlechner, Valerio Pruneri. **A quantum-enhanced wide-field phase imager**. Science Advances, 7(47), 2021.

- Robin Camphausen, Adrià Sansa Perna, Álvaro Cuevas, Alexander Demuth, Javier Arrés Chillón, Markus Gräfe, Fabian Steinlechner, Valerio Pruneri. **Fast quantum-enhanced imaging with visible-wavelength entangled photons**. Optics Express, 31(4), 2023.

- Robin Camphausen, Álvaro Cuevas, Alexander Demuth, Javier Arrés Chillón, Alessandro Ruggeri, Francesca Madonini, Federica Villa, Adrià Sansa Perna, Markus Gräfe, Fabian Steinlechner, Valerio Pruneri. **Real-time entanglement-enhanced imaging** (in preparation).

1.5.2 Other relevant publications and conference presentations

- Alexander Demuth, Robin Camphausen, Álvaro Cuevas, Nick F. Borrelli, Thomas P. Seward III, Lisa Lamberson, Karl W. Koch, Alessandro Ruggeri, Francesca Madonini, Federica Villa, Valerio Pruneri. **Quantum light transport in phase-separated Anderson localization fiber**. Communications Physics 5(261), 2022.

- Fabio Severini, Iris Cusini, Francesca Madonini, Davide Brescia, Robin Camphausen, Álvaro Cuevas, Simone Tisa, Federica Villa. **Spatially-resolved Event-driven 24×24-pixels SPAD Imager with 100% duty cycle for low power Quantum Entanglement detection** (accepted for publication in IEEE Journal of Solid-State Circuits).

- Álvaro Cuevas, Daniel Tiemann, Robin Camphausen, Rajdeep Mukherjee, Iris Cusini, Antonio Panzani, Federica Vila, Valerio Pruneri. **Multipass wide-field phase imager** (in preparation).

- Robin Camphausen, Adrià Sansa Perna, Álvaro Cuevas, Javier Arrés Chillón, Alexander Demuth, Markus Gräfe, Fabian Steinlechner, Valerio Pruneri. **Fast and practical quantum imaging enabled by visible-wavelength entangled photons**. QCMC 2022, Lisbon, Portugal, July 2022 (Poster).

- Robin Camphausen, Álvaro Cuevas, Valerio Pruneri. **Widefield super-sensitive phase imaging using N00N state illumination**. CLEO 2021, Virtual Conference, May 2021.

- Robin Camphausen, Álvaro Cuevas, Valerio Pruneri. **SPAD array camera as photon number-resolving imaging device**. QTech 2020 Quantum Technology International Conference, Barcelona, Spain, November 2020.
- Robin Camphausen, Rubaiya Hussain, Roland A. Terborg, Luc Duempelmann, Álvaro Cuevas, Ewelina Wajs, Sandra Diefenbach, Valerio Pruneri. **Detection of particles, micro-organisms and biomarkers using CMOS image sensors**. Nanobio&med, Barcelona, Spain, November 2019 (Key note).
- Robin Camphausen, Álvaro Cuevas, Roland A. Terborg, Luc Duempelmann, Fabian Steinlechner, Valerio Pruneri. **Super-resolution phase imaging by detecting entangled photons with a SPAD-array camera**. Single Photon Workshop 2019, Milan, Italy, October 2019 (Poster).
- Rubaiya Hussain, Robin Camphausen, Roland A. Terborg, Luc Duempelmann, Álvaro Cuevas, Valerio Pruneri. **Large field of view imaging with classical and quantum light**. EOS European Optical Society: Optical Microsystems OμS19, Anacapri, Italy, September 2019 (Invited talk).

Chapter 2

Generating Entangled Photon Pairs

One of the most important developments in modern physics was the realization that a quantum mechanical description of the world allows for profoundly different behaviour than classical physics. Effects such as probability amplitude interference and entanglement were once studied out of interest at a fundamental level, but are now essential to a huge number of promised quantum-enabled applications [44].

This chapter gives a brief introduction to quantum states of light, including entanglement. We also provide a basic description of the most common way to generate two-photon quantum states, spontaneous parametric down-conversion (SPDC). Lastly, this chapter presents some detail on the experimental configurations that allow using SPDC to generate entanglement in polarization and space-momentum degrees of freedom. Note that we focus here only on essential background for experiments presented in later chapters, and make no claim to great mathematical rigour. For a more in-depth treatment of the subject, the interested reader is referred to the standard quantum optics and quantum mechanics textbooks [29, 36, 45, 46].

2.1 Basic Concepts – Quantum states and entanglement

Quantum physics teaches us the fundamental insight that any physical theory of the world only tells us the *probability* for a system to be found in a certain state [46–48]. In contrast to classical probabilities, the quantum mechanical description of the world involves a phase term. For example, consider a weighted (classical) coin, with probability P_{Heads} of landing on Heads when flipped, where P_{Heads} is a real number between 0 and 1. Landing on Heads and Tails are mutually exclusive outcomes, so the probability of Tails is $P_{\text{Tails}} = 1 - P_{\text{Heads}}$. In the case of a quantum system, the analogous situation is represented by the quantum state vector, or "wave function", $|\Psi\rangle$:

$$|\Psi\rangle = \alpha\,|\psi_1\rangle + \beta\,|\psi_2\rangle\,, \tag{2.1}$$

where the basis vectors $|\psi_1\rangle$ and $|\psi_2\rangle$ are mutually exclusive possible states of the system. The probability amplitudes α and β are complex numbers satisfying the condition $|\alpha|^2 + |\beta|^2 = 1$. The probability of measuring the quantum system described by $|\Psi\rangle$ in the state $|\psi_1\rangle$ is given by $|\langle\psi_1|\Psi\rangle|^2 \equiv \alpha^*\alpha \langle\psi_1|\psi_1\rangle + \beta^*\beta \langle\psi_1|\psi_2\rangle = |\alpha|^2$, where if $\alpha \equiv a\exp(i\phi_\alpha)$, we have the complex conjugate $\alpha^* \equiv a\exp(-i\phi_\alpha)$. Generalizing Eq. 2.1, let us consider a set of orthogonal state vectors $\{|\psi_i\rangle\}$, satisfying $\langle\psi_i|\psi_j\rangle = \delta_{ij}$. If all $|\psi_i\rangle$ represent possible states of a quantum system, any linear combination thereof is also a valid state [46]:

$$|\Psi\rangle = \sum_i \alpha_i |\psi_i\rangle, \text{ where}$$
$$\sum_i |\alpha_i|^2 = 1. \tag{2.2}$$

Every orthogonal basis vector can be thought of as a degree of freedom of the quantum system, where a state with D non-zero weighting coefficient α_i represents a D-level quantum system (sometimes also called a D-dimensional system [49]). Formally, such a D-level system is said to be described by a state vector residing in a D-dimensional linear unitary vector space, or Hilbert Space.

Not all physical systems can be described by a single state vector. Those that can are said to be in a pure state, while those that cannot are known as mixed states. A mixed state is described as a sum of projection operators:

$$\hat{\rho} = \sum_i p_i |\psi_i\rangle \langle\psi_i|, \tag{2.3}$$

where $\sum_i p_i = 1$, and $p_i \geq 0$ can be thought of as the probability of the system being in the pure state $|\psi_i\rangle$. Equation 2.3 is known as the density matrix, and can be used to determine the purity of a quantum state:

$$\mathcal{P} = \mathrm{Tr}(\hat{\rho}^2) \begin{cases} = 1 & \text{for pure states,} \\ < 1 & \text{for mixed states.} \end{cases} \tag{2.4}$$

If two quantum systems are independent from each other, and are described by (pure) state vectors $|\psi_A\rangle$ and $|\psi_B\rangle$, respectively, the joint system is denoted by the tensor product $|\psi_A\rangle \otimes |\psi_B\rangle$. For concreteness, let us consider the example where $|\psi_A\rangle = \alpha_1 |\psi_1\rangle + \alpha_2 |\psi_2\rangle$ and $|\psi_B\rangle = \beta_1 |\psi_1\rangle + \beta_2 |\psi_2\rangle$. The tensor product is therefore

$$|\psi_A\rangle \otimes |\psi_B\rangle = \alpha_1\beta_1 |\psi_1\psi_1\rangle_{AB} + \alpha_1\beta_2 |\psi_1\psi_2\rangle_{AB} + \alpha_2\beta_1 |\psi_2\psi_1\rangle_{AB} + \alpha_2\beta_2 |\psi_2\psi_2\rangle_{AB}, \tag{2.5}$$

where $|\psi_i\psi_j\rangle_{AB} = |\psi_i\rangle_A |\psi_j\rangle_B$ denotes the state of quantum system A in $|\psi_i\rangle$ and B in $|\psi_j\rangle$. In general, a state $|\Psi\rangle$ is known as separable if it can be separated into a tensor product between two other state vectors (i.e. $\exists\, |\psi_i\rangle$, $|\psi_j\rangle$ such that $|\Psi\rangle = |\psi_i\rangle \otimes |\psi_j\rangle$).

Looking at Eq. 2.5, simply by removing some terms the following state can be constructed:

$$|\psi_3\rangle = \alpha_1\beta_1 |\psi_1\psi_1\rangle_{AB} + \alpha_2\beta_2 |\psi_2\psi_2\rangle_{AB}, \tag{2.6}$$

where α_1, β_1, α_2, and β_2 must be rescaled in Eq. 2.6 compared to Eq. 2.5 such that $|\alpha_1\beta_1|^2 + |\alpha_2\beta_2|^2 = 1$. What is peculiar about Eq. 2.6 is that $|\psi_3\rangle$ cannot, in fact, be decomposed into the tensor product of two other states. That is, $|\psi_3\rangle$ represents two quantum systems A and B, which cannot be described independently of each other. Indeed we see that measuring system A to be in state $|\psi_1\rangle$ immediately means that system B must be in state $|\psi_1\rangle$ too, as $|\psi_3\rangle$ contains no $|\psi_1\psi_2\rangle_{AB}$ term. In the language of the Copenhagen interpretation of quantum mechanics, measuring A in state $|\psi_1\rangle$ causes the wave function to collapse such that B must also be in state $|\psi_1\rangle$. This effect is known as entanglement, and two or more quantum systems described by the same non-separable wave function are said to be entangled [29, 46, 47].

In analogy to bits, classical systems with two possible states "0" and "1", two-dimensional quantum states are often named "qubits", with their two basis states denoted $|\mathbf{0}\rangle$ and $|\mathbf{1}\rangle$, respectively. While bits are used to represent information in classical information processing, qubits ("quantum bits") are used to represent *quantum information*, which serves as the "language" for quantum computation and quantum communication. An important class of entangled states between two qubits is represented by the four Bell states, defined as follows [29, 46]:

$$|\Phi^+\rangle_{AB} = \frac{1}{\sqrt{2}}\left(|\mathbf{00}\rangle_{AB} + |\mathbf{11}\rangle_{AB}\right), \tag{2.7}$$

$$|\Phi^-\rangle_{AB} = \frac{1}{\sqrt{2}}\left(|\mathbf{00}\rangle_{AB} - |\mathbf{11}\rangle_{AB}\right), \tag{2.8}$$

$$|\Psi^+\rangle_{AB} = \frac{1}{\sqrt{2}}\left(|\mathbf{01}\rangle_{AB} + |\mathbf{10}\rangle_{AB}\right), \tag{2.9}$$

$$|\Psi^-\rangle_{AB} = \frac{1}{\sqrt{2}}\left(|\mathbf{01}\rangle_{AB} - |\mathbf{10}\rangle_{AB}\right). \tag{2.10}$$

At this point, despite possessing the basic mathematical tools to describe the quantum state of a physical system, we might still ask ourselves what function is served by the probability amplitudes of a state being complex numbers. We illustrate this now through an explicit example: let us define the following states, in terms of the qubit basis vectors:

$$|+\rangle = \frac{1}{\sqrt{2}}\left(|\mathbf{0}\rangle + |\mathbf{1}\rangle\right), \tag{2.11}$$

$$|-\rangle = \frac{1}{\sqrt{2}}\left(|\mathbf{0}\rangle - |\mathbf{1}\rangle\right). \tag{2.12}$$

Measuring the qubit state $|\psi_\phi\rangle = 1/\sqrt{2}\,(|\mathbf{0}\rangle + \exp(i\phi)\,|\mathbf{1}\rangle)$ in the $|+\rangle$ basis therefore results in the following:

$$\begin{aligned} |\langle +|\psi_\phi\rangle|^2 &= \left|\langle +|\,\frac{1}{\sqrt{2}}\left(\frac{|+\rangle+|-\rangle}{\sqrt{2}} + e^{i\phi}\frac{|+\rangle-|-\rangle}{\sqrt{2}}\right)\right|^2 \\ &= \frac{1+\cos\phi}{2}. \end{aligned} \tag{2.13}$$

Similarly, projecting both A and B in $|\Phi_\phi\rangle = \frac{1}{\sqrt{2}}\,(|\mathbf{00}\rangle_{AB} + \exp(i\phi)\,|\mathbf{11}\rangle_{AB})$ onto the $|+\rangle$ basis:

$$\begin{aligned} |\langle +|_B\langle +|_A\,|\Phi_\phi\rangle_{AB}|^2 =& \left|\langle +|_B\langle +|_A\,\frac{1}{\sqrt{2}}\left(\frac{|+\rangle_A+|-\rangle_A}{\sqrt{2}}\right)\left(\frac{|+\rangle_B+|-\rangle_B}{\sqrt{2}}\right)\right. \\ &\left. + \langle +|_B\langle +|_A\,\frac{e^{i\phi}}{\sqrt{2}}\left(\frac{|+\rangle_A-|-\rangle_A}{\sqrt{2}}\right)\left(\frac{|+\rangle_B-|-\rangle_B}{\sqrt{2}}\right)\right|^2 \\ =& \frac{1+\cos\phi}{4}. \end{aligned} \tag{2.14}$$

We see that the measurement outcomes in Eq. 2.13 and Eq. 2.14 depend on the phase ϕ of the probability amplitudes in $|\psi_\phi\rangle$ and $|\Phi_\phi\rangle$, respectively. That is, complex probability amplitudes enable describing not only the relative probability of states, but also their *interference*. Interestingly, a recent landmark study has shown that quantum theory must, in fact, contain complex numbers for a complete description of the world [50, 51]. In other words, there exist physically realizable systems which cannot be accurately described using only real numbers.

2.2 Photonic quantum states of light

Section 2.1 introduced some basic concepts to represent the quantum state of a system, without making reference to any particular physical implementation. Here, we show how different quantum states can be *realized* by photons.

2.2.1 Photon number states

The concept of the "photon", that is, a single particle or wave packet of light, can be derived by the quantization of the electromagnetic field as described by Maxwell's equations, and the quantum harmonic oscillator [29, 52, 53]. The ground state of the quantum harmonic oscillator representing the quantized energy levels of the electromagnetic field is known as the vacuum $|\text{vac}\rangle$. The operators defined to raise and lower the energy level in this field are known as the creation and annihilation operators, denoted by convention as $\hat{a}^\dagger$ and $\hat{a}$, respectively. Applying the creation operator to the vacuum field results in the generation of a single electromagnetic quanta – a photon. The photon number state $|n\rangle$, or Fock state, represents the state with a definite number of n electromagnetic quanta (i.e. n photons). The creation

operator can then be defined by its operation as follows

$$\hat{a}^\dagger |n\rangle = \sqrt{(n+1)}\, |n+1\rangle\,, \tag{2.15}$$

and the annihilation operator as

$$\hat{a}\, |n\rangle = \sqrt{n}\, |n-1\rangle\,. \tag{2.16}$$

This allows expressing the Fock state $|n\rangle$ in terms of repeated applications of the creation operator on the vacuum state:

$$|n\rangle = \frac{(\hat{a}^\dagger)^n}{\sqrt{n!}} |\text{vac}\rangle\,. \tag{2.17}$$

It is also useful to define the photon number operator $\hat{n} = \hat{a}^\dagger \hat{a}$, which yields the number of photons of a state:

$$\begin{aligned} \langle n|\, \hat{n}\, |n\rangle &= \langle n|\, n^{1/2}((n-1)+1)^{1/2}\, |n\rangle \\ &= \langle n|\, n\, |n\rangle = n. \end{aligned} \tag{2.18}$$

Fock states display highly non-classical behaviour, as their variance in photon number is zero. However, coherent states, which behave like classical light fields emitted by lasers, can be represented in terms of photon number states [29]:

$$|\alpha\rangle = e^{-|\alpha|^2/2} \sum_{n=0}^{\infty} \frac{\alpha^n}{\sqrt{n!}} |n\rangle\,. \tag{2.19}$$

Using the photon number operator, the mean photon number of a coherent state $|\alpha\rangle$ is given by the expectation value

$$\langle \alpha|\, \hat{n}\, |\alpha\rangle = |\alpha|^2 = \overline{n}. \tag{2.20}$$

This matches with the classical notion of the intensity of a coherent electromagnetic field. The probability mass function of $|\alpha\rangle$, as a function of photon number, is then given by

$$\begin{aligned} \mathcal{P}(n) = |\, \langle n|\alpha\rangle\, |^2 &= e^{-|\alpha|^2} \frac{(|\alpha|^2)^n}{n!} \\ &= \frac{\overline{n}^n e^{-\overline{n}}}{n!}. \end{aligned} \tag{2.21}$$

Equation 2.21 is a Poissonian distribution with variance $\overline{n}$. That is, a coherent state of light, with mean number of photons $\overline{n}$, always has an uncertainty in photon number with standard deviation of $\sqrt{\overline{n}}$. This phenomenon is known as *shot noise* [29, 54].

2.2.2 Polarization degree of freedom

Two-dimensional quantum states (i.e. qubits) can be encoded in the polarization degree of freedom of photons. Polarization qubits have been extensively studied: as they can be generated experimentally with relative ease; many of the pioneering demonstrations of quantum information processing were first performed using polarization qubits [55–57]. Moreover, as polarization qubits have been shown to maintain their quantum state well during propagation through turbulent atmospheric free-space links, they have become the medium of choice for free-space quantum communication [58–61].

Begin by defining the $|H\rangle$ and $|V\rangle$, as the following single photon Fock states:

$$|H\rangle \equiv \hat{a}_H^\dagger |\text{vac}\rangle , \tag{2.22}$$

$$|V\rangle \equiv \hat{a}_V^\dagger |\text{vac}\rangle , \tag{2.23}$$

where the H (V) subscript on the $\hat{a}^\dagger$ operators indicates that the photon is created in the horizontal (vertical) polarization mode. In other words, $|H\rangle$ ($|V\rangle$) represents a single photon with linear horizontal (vertical) polarization. $|H\rangle$ and $|V\rangle$ make for natural qubit basis vectors, that is:

$$|\mathbf{0}\rangle \equiv |H\rangle , \tag{2.24}$$

$$|\mathbf{1}\rangle \equiv |V\rangle . \tag{2.25}$$

Note the bold font of the logical qubit state $|\mathbf{1}\rangle$ to distinguish it explicitly from the single photon Fock state $|1\rangle$. Further, it is useful to define the diagonal ($|D\rangle$) and anti-diagonal ($|A\rangle$) linear polarization states:

$$|D\rangle \equiv \frac{|H\rangle + |V\rangle}{\sqrt{2}}, \tag{2.26}$$

$$|A\rangle \equiv \frac{|H\rangle - |V\rangle}{\sqrt{2}}, \tag{2.27}$$

as well as the right-handed circular ($|R\rangle$) and left-handed circular ($|L\rangle$) polarization states:

$$|R\rangle \equiv \frac{|H\rangle + i\,|V\rangle}{\sqrt{2}}, \tag{2.28}$$

$$|L\rangle \equiv \frac{|H\rangle - i\,|V\rangle}{\sqrt{2}}. \tag{2.29}$$

In practice of course it is arbitrary which directions are designated as "horizontal" and "vertical". Typically, however, for laboratory experiments performed using setups mounted on optical tables, we designate the direction parallel to the table surface as "horizontal".

Using a polarized single photon state we can therefore replicate the single-qubit interference described by Eq. 2.13, projecting the state $|\psi_\phi\rangle = 1/\sqrt{2}\,(|H\rangle + \exp(i\phi)\,|V\rangle)$

into the diagonal polarization:

$$
\begin{aligned}
|\langle D|\psi_\phi\rangle|^2 &= \left|\langle D|\left(\frac{1}{\sqrt{2}}\left(\frac{|D\rangle+|A\rangle}{\sqrt{2}}+e^{i\phi}\frac{|D\rangle-|A\rangle}{\sqrt{2}}\right)\right)\right|^2 \\
&= \frac{1+\cos\phi}{2}.
\end{aligned} \tag{2.30}
$$

In practice, the $\langle D|$ projection is achieved simply by passing the light through a diagonally oriented linear polarizer.

Continuing with the designation $|\mathbf{0}\rangle \equiv |H\rangle$ and $|\mathbf{1}\rangle \equiv |V\rangle$, it is clear that the Bell states (Eq. 2.7-2.10) can be realized using two entangled polarized photons. For example $|\Phi^+\rangle = 1/\sqrt{2}(|HH\rangle_{AB} + |VV\rangle_{AB})$, which represents two photons A and B, entangled in their polarization degrees of freedom. Note that at this point it is important to clarify what is meant by calling one photon"A", and the other photon "B". Photons are bosons, which means that two photons do not obey the Pauli exclusion principle, and can be completely identical in every way [29]. However, a pure state consisting of a pair of photons with the same polarization H (for example), but identical in every other way, is simply a two-photon Fock state in the H polarization mode, i.e. $(\hat{a}_H^\dagger)^2/2\,|\text{vac}\rangle$ (from Eq. 2.17). It would be meaningless in this case to label one photon "A" and the other "B". On the other hand, it is necessary to use such labels to "keep track" of the two individual photons, if they are distinguishable in some degree of freedom other than polarization, for example spatial mode, frequency, time-bin, or orbital angular momentum [62, 63]. Therefore, we can now write out a two-qubit interference effect analogous to Eq. 2.14, by projecting the state $|\Psi\rangle_{AB} = (|HH\rangle_{AB} + e^{i(\phi_A+\phi_B)}\,|VV\rangle_{AB})/\sqrt{2}$ into the diagonal linear polarization basis. The subscripts A and B refer to the two photons' respective spatial modes (or, equivalently, frequency modes, or time-bins, etc).

$$
\begin{aligned}
|\langle D|_B\langle D|_A|\Psi\rangle_{AB}|^2 &= \left|\langle D|_B\langle D|_A\left(\frac{|HH\rangle_{AB}+e^{i(\phi_A+\phi_B)}|VV\rangle_{AB}}{\sqrt{2}}\right)\right|^2 \\
&= \Bigg|\langle D|_B\langle D|_A\frac{1}{\sqrt{2}}\left(\frac{|D\rangle_A+|A\rangle_A}{\sqrt{2}}\right)\left(\frac{|D\rangle_B+|A\rangle_B}{\sqrt{2}}\right) \\
&\quad + \langle D|_B\langle D|_A\frac{e^{i(\phi_A+\phi_B)}}{\sqrt{2}}\left(\frac{|D\rangle_A-|A\rangle_A}{\sqrt{2}}\right)\left(\frac{|D\rangle_B-|A\rangle_B}{\sqrt{2}}\right)\Bigg|^2 \\
&= \frac{1+\cos(\phi_A+\phi_B)}{4}.
\end{aligned} \tag{2.31}
$$

In contrast to Eq. 2.14, here the phase term between $|HH\rangle_{AB}$ and $|VV\rangle_{AB}$ is $(\phi_A + \phi_B)$, explicitly specifying the phase acquired by photon A and photon B (although, the interference in Eq. 2.31 only depends on the sum of the two single photon phases).

A special case of Eq. 2.31 is represented by the situation in which photons A and B *are* indistinguishable, that is, modes A and B are the same. In this case we

can drop the subscripts and write the state as $|\Psi\rangle = (|HH\rangle + e^{i(2\phi)}|VV\rangle)/\sqrt{2}$, so that Eq. 2.31 becomes

$$|\langle DD|\Psi\rangle|^2 = \frac{1+\cos 2\phi}{4}, \tag{2.32}$$

where ϕ still represents the single-photon phase, i.e. the phase acquired by each of the two photons constituting the entangled state. As pointed out above, $|HH\rangle$ and $|VV\rangle$ are simply the two-photon Fock states with horizontally and vertically polarized photons, respectively. Therefore $|\Psi\rangle$ can also be written as

$$|\Psi\rangle = \frac{|20\rangle_{HV} + e^{i2\phi}|02\rangle_{HV}}{\sqrt{2}}, \tag{2.33}$$

that is, the mode subscripts now refer to the H and V polarization modes. In this thesis, the notation $|HH\rangle$ ($|VV\rangle$) will be preferred in general, but is always completely equivalent to $|20\rangle_{HV}$ ($|02\rangle_{HV}$). Equation 2.33 is a two-photon entangled state, but it can be readily seen that the same form can be extended to Fock states with an arbitrary number of photons:

$$|\Psi_{\mathrm{N00N}}\rangle = \frac{|n0\rangle_{HV} + |0n\rangle_{HV}}{\sqrt{2}}, \tag{2.34}$$

where, as indicated by the state name's subscript, this class of N-photon entangled photon states is named the class of N00N states (the origin of this term should be fairly obvious from the form of the notation in the Fock state basis). Of course, while here N00N states are expressed in terms of polarization modes, it is equally possible to construct N00N states with N photons in any two modes, whether these be two spatial modes, two time-bin modes, and so on. Passing a N-photon N00N state through a single-photon phase ϕ between the two modes (that is, a single photon would acquire phase ϕ), results in

$$|\Psi_{\mathrm{N00N}}\rangle(\phi) = \frac{|n0\rangle_{HV} + e^{in\phi}|0n\rangle_{HV}}{\sqrt{2}}. \tag{2.35}$$

Therefore, we see that N00N states *amplify* a phase they acquire by a factor of N, where N is the number of entangled photons constituting $|\Psi_{\mathrm{N00N}}\rangle$.

2.3 Spontaneous parametric down-conversion (SPDC)

In order to generate quantum states of the type introduced in Sections 2.1 and 2.2, spontaneous parametric down-conversion (SPDC) represents the method with, at present, the highest level of technological maturity [28, 64, 65]. SPDC has been studied extensively, and there exists a large experimental as well as theoretical "toolbox" to optimize a setup for entanglement generation. In SPDC, a material with second-order optical nonlinearity is illuminated by a pump light source, where pump photons are converted into pairs of longer wavelength photons. This

interaction is governed by momentum and energy conservation laws, which ensure correlations between the two generated photons – this property is what leads to naturally emerging entanglement in a variety of degrees of freedom [62, 63].

2.3.1 SPDC photon-pair generation

When light passes through a dielectric material, the electromagnetic field induces the polarization of the optical medium. This can be written as

$$\mathbf{P} = \epsilon_0 \left(\chi^{(1)}\mathbf{E} + \chi^{(2)}\mathbf{EE} + \chi^{(3)}\mathbf{EEE} + ... \right), \tag{2.36}$$

where ϵ_0 is the permittivity of vacuum, and $\chi^{(n)}$ represents the n^{th} order susceptibility of the medium [66]. The first-order susceptibility $\chi^{(1)}$ describes all linear optical effects, such as refraction of light. The higher-order terms govern *nonlinear* optical interactions in the material. In particular, the $\chi^{(2)}$ describes second-order effects such as second harmonic generation, and spontaneous parametric down-conversion (SPDC).

Fig. 2.1, adapted from Ref. [67], shows the main features of SPDC photon pair generation. A pump beam, normally a laser (blue beam in Fig. 2.1(a)), passes through a material with non-negligible second-order susceptibility, normally a crystal ("χ^2 crystal" in Fig. 2.1(a)). We assume that the pump laser is monochromatic, with pump photons of frequency ω_p (i.e. wavelength $\lambda_p = \omega_p/2\pi$) and momentum $\mathbf{k}_p$. Then, due to the $\chi^{(2)}$ interaction in the crystal, with low probability one pump photon is converted into two SPDC photons named the signal and idler, with frequencies ω_s and ω_i, and momenta $\mathbf{k}_s$ and $\mathbf{k}_i$, respectively. By convention $\omega_s > \omega_i$, that is, $\lambda_s < \lambda_i$. As shown in Fig. 2.1(b) and (c), SPDC also requires the conservation of momentum and energy:

$$\mathbf{k}_p = \mathbf{k}_s + \mathbf{k}_i \tag{2.37}$$

$$\omega_p = \omega_s + \omega_i, \tag{2.38}$$

where Eq. 2.38 relies on the Planck relation for photon energy $E = \hbar\omega$. If we define the light propagation axis as the z direction, the photon wave vector $\mathbf{k}$ can be decomposed into transverse ($\mathbf{k}^\perp$) and longitudinal ($\mathbf{k}^z$) components, i.e., $\mathbf{k} \equiv \mathbf{k}^z + \mathbf{k}^\perp$. Therefore, if the pump is collimated or weakly focused, $\mathbf{k}_p^\perp \approx 0$, and thus $\mathbf{k}_s^\perp \approx \mathbf{k}_i^\perp$. This results in the axially symmetric ring-shaped emission pattern seen in Fig. 2.1(a) [67–70].

2.3.2 Phase matching

Equation 2.37 requires the p, s and i electromagnetic waves to be in phase with each other [65, 69]. Fulfilling this so-called *phase matching* condition is non-trivial, because in general any material will have different refractive indices for the three wavelengths λ_p, λ_s and λ_i. In order to nonetheless satisfy Eq. 2.37, two commonly used techniques are birefringent phase matching, and quasi-phase matching through periodic poling. Birefringent phase matching uses a birefringent $\chi^{(2)}$

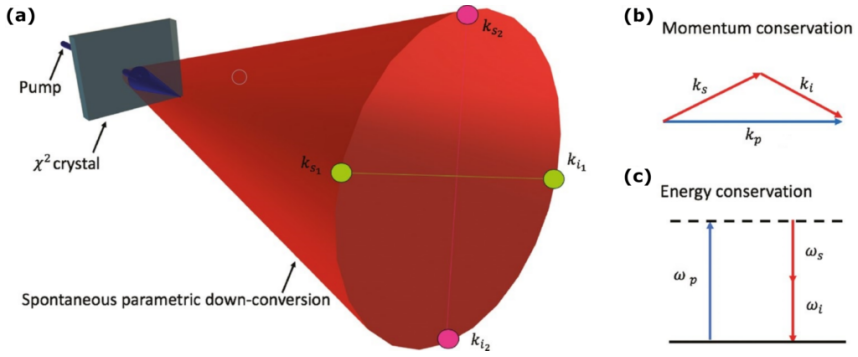

FIGURE 2.1: **SPDC overview.** **(a)** Schematic of SPDC process, showing pump laser (blue), nonlinear crystal (gray), and photon pair emission profile (red). Pairs of yellow and pink points show two example photon pairs, with signal and idler momenta symmetric around pump propagation axis. **(b)** and **(c)** show conservation of momentum and energy, respectively. Figure adapted from Ref. [67].

crystal, such that the difference between ordinary and extraordinary refractive indices compensates the chromatic dispersion for a given λ_p, λ_s and λ_i combination [28, 66]. The idea behind quasi-phase matching (QPM) through periodic poling can be appreciated by writing the following expression for the phase mismatch between the p, s and i waves:

$$\Delta\mathbf{k} = \mathbf{k}_p - \mathbf{k}_s - \mathbf{k}_i - \mathbf{k}_m, \tag{2.39}$$

where Eq. 2.37 is satisfied when $\Delta\mathbf{k} = 0$, and $\mathbf{k}_m = 0$ for uniform nonlinear crystals, in which $\chi^{(2)}$ is constant. On the other hand, the second-order susceptibility can be made to periodically vary as a function of the longitudinal position z, inverting the sign (i.e. the poling) of $\chi^{(2)}$ after every period Λ. This results in non-zero $\mathbf{k}_m$, according to $|\mathbf{k}_m| = 2\pi/\Lambda$ [71]. Moreover, $\Lambda(T)$ depends on the temperature T of the crystal. Therefore, QPM through periodic poling enables satisfying Eq. 2.37 in a wide range of conditions, by controlling the crystal temperature [72]. Note that, while $\chi^{(2)}$ is a second-rank tensor, it normally contains only a single relevant non-zero component. Depending on which nonlinear component governs the SPDC interaction, one distinguishes between three types of phase matching:

- Type-0: pump, signal, and idler photons all have the same polarization;
- Type-I: signal and idler have the same polarization, which is orthogonal to the pump;
- Type-II: signal and idler polarizations are orthogonal to each other.

In the work described in Chapter 5 of this thesis, a periodically poled potassium titanyl phosphate (ppKTP) nonlinear crystal was used, which has length

$L = 20\,\text{mm}$ and room temperature poling period $\Lambda(T = 20\,^{\circ}\text{C}) = 3.425\,\mu\text{m}$, and was pumped with a $\lambda_p = 405.6\,\text{nm}$ laser. These parameters favour SPDC under type-0 QPM. Fine-tuning the temperature of the ppKTP crystal controls $\mathbf{k}_m(T)$, which in turn determines the λ_p, λ_s and λ_i combination for which Eq. 2.39 equals 0. Therefore, we can set the SPDC generation to be *degenerate* ($\lambda_s = \lambda_i$), or *non-degenerate* ($\lambda_s \neq \lambda_i$) [72]. One example of such a temperature-spectrum tuning curve is shown in Fig. 2.2, where at $T \approx 39^{\circ}\text{C}$ the emission is degenerate, while for $T > 39^{\circ}\text{C}$ it becomes non-degenerate (with $\lambda_i - \lambda_s$ increasing as T rises). In

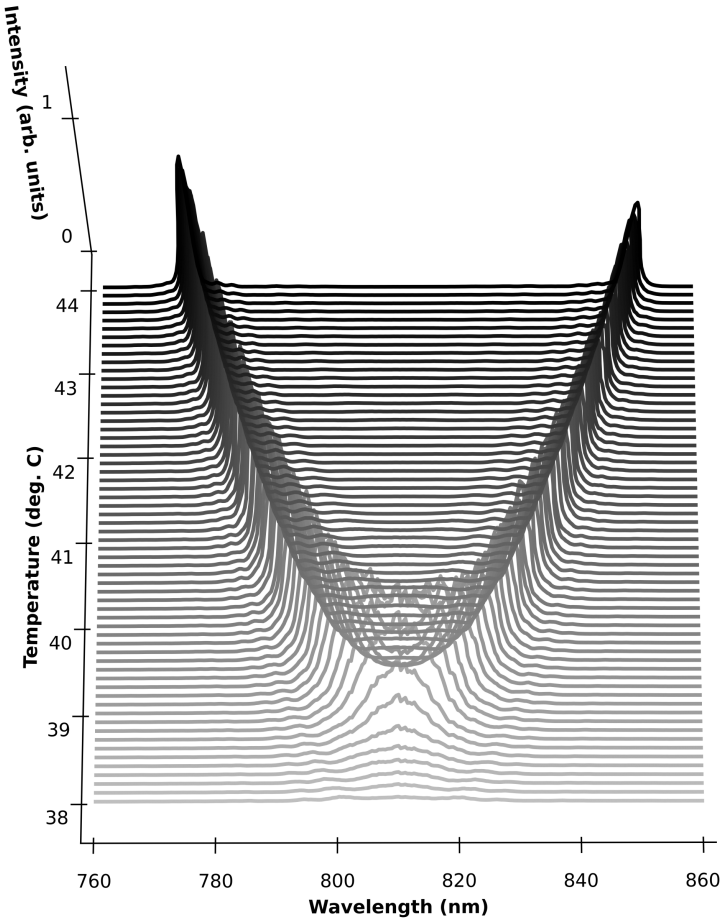

FIGURE 2.2: **Experimental SPDC spectra for ppKTP.** Pumping a 20 mm ppKTP crystal (Raicol), with a 405.6 nm laser (Toptica), the normalized spectra show tuning from degenerate to non-degenerate regimes as a function of crystal temperature. Spectra acquired using a fibre-coupled spectrometer (Ocean Insight).

the work described in Chapters 6 and 7, SPDC photon pairs were generated in uniform (i.e., not periodically poled) barium borate (BBO) nonlinear crystals, of

length 2.5 mm and pumped by a 266 nm laser. Here, degenerate emission was produced through birefringent type-I phase matching, which is fine-tuned by adjusting the BBO crystal tilt angle with respect to the pump propagation axis [73].

Lastly, we note that, while not forming part of this thesis, frequency correlations in SPDC (as can be seen in Fig. 2.2) are useful in a number of spectroscopy and sensing applications [74–76].

2.3.3 Space-momentum distribution of SPDC two-photon state

From Ref. [65, 69], the Hamiltonian describing the SPDC interaction can be written as

$$\hat{H}_I = \epsilon_0 \int dV \boldsymbol{\chi}^{(2)} \hat{\mathbf{E}}_p^+(\mathbf{r},t)\hat{\mathbf{E}}_s^-(\mathbf{r},t)\hat{\mathbf{E}}_i^-(\mathbf{r},t) + \text{H.c.}, \tag{2.40}$$

where $\hat{\mathbf{E}}^+(\mathbf{r},t) = \hat{\mathbf{E}}^-(\mathbf{r},t)^\dagger$ represents the electric field operator at position $\mathbf{r}$ and time t, V is the interaction volume, and "H.c." stands for "Hermitian conjugate". Following the derivation in Ref. [69], Eq. 2.40 can also be expressed as

$$\hat{H}_I = \chi^{(2)}_{\text{eff}} \int_V d^3r \int d^3k_p \int d^3k_s \int d^3k_i \hat{a}_p(\mathbf{k}_p)\hat{a}_s^\dagger(\mathbf{k}_s)\hat{a}_i^\dagger(\mathbf{k}_i) e^{i\Delta\mathbf{k}\cdot\mathbf{r}} + e^{-i(\omega_s+\omega_i-\omega_p)t} + \text{H.c.}, \tag{2.41}$$

where $\chi^{(2)}_{\text{eff}}$ now contains the interaction strength, and $\Delta\mathbf{k}$ is given by Eq. 2.39. Explicitly, Eq. 2.41 describes the removal of a pump photon with momentum $\mathbf{k}_p$ and frequency ω_p through the annihilation operator $\hat{a}_p(\mathbf{k}_p)$, and the creation of the signal (idler) photon, with momentum $\mathbf{k}_s$ ($\mathbf{k}_i$), and frequency ω_s (ω_i), through the creation operator $\hat{a}_s^\dagger(\mathbf{k}_s)$ ($\hat{a}_i^\dagger(\mathbf{k}_i)$). This conversion is maximized when $\Delta\mathbf{k} = 0$.

Equation 2.41 can be simplified to the following two-photon mode function, representing the two-photon amplitude of signal (idler) photon with transverse wave vector $\mathbf{k}_s^\perp$ ($\mathbf{k}_i^\perp$) [70]:

$$\gamma(\mathbf{k}_s^\perp, \mathbf{k}_i^\perp, \omega_s, \omega_i) \propto E_p(\mathbf{k}_s^\perp + \mathbf{k}_i^\perp)\,\text{sinc}\left(\frac{L}{4\mathbf{k}_p}|\mathbf{k}_s^\perp - \mathbf{k}_i^\perp|^2 + \varphi(T,\lambda_p,\lambda_s,\lambda_i)\right). \tag{2.42}$$

Here, L is the length of the crystal, while the phase mismatch parameter φ is proportional to Eq. 2.39, and depends on the crystal temperature and refractive indices at λ_p, λ_s and λ_i, as calculated from the Sellmeier equation [77, 78].

Assuming that the signal and idler photons are quasi-monochromatic, and that the pump beam in the crystal has a Gaussian spatial profile, Eq. 2.42 can be simplified to [79]

$$\gamma(\mathbf{k}_s^\perp, \mathbf{k}_i^\perp) = \frac{\sigma_+\sigma_-}{\pi}\exp\left[-\frac{\sigma_+^2}{4}|\mathbf{k}_s^\perp + \mathbf{k}_i^\perp|^2 - \frac{\sigma_-^2}{4}|\mathbf{k}_s^\perp - \mathbf{k}_i^\perp|^2\right], \tag{2.43}$$

where σ_- and σ_+^{-1} are the standard deviations of Gaussian functions describing photon pair position and (transverse) momentum correlations respectively, while σ_+ is the Gaussian waist of the pump laser spot [80]. A lens can convert a momentum distribution into a position distribution, allowing therefore to image Eq. 2.43 in the SPDC far-field (i.e., the Fourier plane of the SPDC photon pair "birth zone").

This is shown in Chapter 3 (e.g. Fig. 3.4, Fig. 3.5), as well as in Ref. [40, 80, 81]. The Fourier transform of Eq. 2.43 yields the spatial correlation function:

$$\gamma(\mathbf{r}_s, \mathbf{r}_i) \equiv \frac{1}{\pi\sigma_+\sigma_-} \exp\left[-\frac{|\mathbf{r}_s + \mathbf{r}_i|^2}{4\sigma_+^2} - \frac{|\mathbf{r}_s - \mathbf{r}_i|^2}{4\sigma_-^2}\right], \tag{2.44}$$

where $\mathbf{r}_s$ and $\mathbf{r}_i$ are the spatial coordinates of the photons. We are able to measure Eq. 2.44 by replicating the SPDC near-field (the photon pair "birth zone" inside the $\chi^{(2)}$ crystal) onto a detector. This can be achieved through a 4f imaging system, that is, a telescope with two lenses relaying an object plane to an image plane four focal distances away [40, 80, 81]. The irradiance (the intensity profile) is obtained by tracing out one of the two photons in Eq. 2.44. SPDC processes generated by a large pump spot in a bulk crystal satisfy the condition $\sigma_-/\sigma_+ \ll 1$ [82].

Equations 2.43 and 2.44 cannot be separated into the tensor product of individual functions in terms of the signal or idler photon. Therefore, SPDC photon pairs are entangled in momentum and space. Note that Eq. 2.43 and 2.44 are approximations that are only valid at exactly the SPDC near-field or far-field planes. For the general form of the SPDC space-momentum state, the interested reader is referred to Ref. [83].

Lastly, note that it is not strictly valid to think of SPDC photon pairs as two-photon Fock states; rather, this approximation is only valid when neglecting higher order emission terms [29]. The pump laser is a coherent state, which is converted with extremely low efficiency into SPDC, which thus inherits the Poissonian statistics of the pump. Therefore, SPDC photon pair statistics follow the Poissonian distribution that characterizes coherent states (Eq. 2.21). In other words, a SPDC process emitting at a rate of $\overline{n}$ photon pairs per unit time, will have a standard deviation in number of photon pairs of $\sqrt{\overline{n}}$.

2.3.4 Polarization entanglement from SPDC

SPDC generates entanglement "for free" in a number of degrees of freedom, such as space-momentum (as described in Sect. 2.3.3), as well as frequency, time-bin, and orbital angular momentum [62, 63, 84–87]. However, a single SPDC process generally does not suffice to produce polarization entanglement. Rather, this requires coherently combining two separate SPDC processes, which have different polarizations but are otherwise indistinguishable [28]. In practice, coherence between two separate SPDC processes is straightforward to achieve by using the same laser beam as the pump for both (for example by splitting it into two beams), and then recombining the two SPDC emissions with perfect temporal and spatial overlap. Many designs for polarization entangled photon sources (EPSs) are based on this principle [28, 88–94].

For a comprehensive recent review of generating polarization entanglement with SPDC, the interested reader is referred to Ref. [28]. Here, we briefly introduce the EPS schemes used in this thesis. Figure 2.3 shows the EPS design used for experiments presented in Chapter 5, which is based on a Sagnac interferometer (SI) and was originally developed in Ref. [92]. Here polarization entanglement

is generated by combining the clockwise and counter-clockwise type-0 photon pair generations at the polarizing beam-splitter (PBS), resulting in a two-photon N00N state (red beam exiting towards the right). On the other hand, the crossed-crystal scheme used in Chapters 6 and 7 is shown in Fig. 2.4. This EPS combines two type-I SPDC processes, generated sequentially in two BBO crystals with orthogonal orientation to each other. Spatial and temporal overlap between the two generations is optimized by two additional BBO crystals, and an yttrium orthovanadate (YVO4) crystal , respectively.

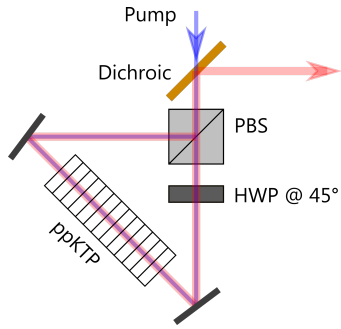

FIGURE 2.3: **Sagnac interferometer polarization-EPS.** A diagonally polarized pump (i.e. $|D\rangle = (|H\rangle + |V\rangle)/\sqrt{2}$, blue arrow) enters the triangular "loop". The pump's $|V\rangle$ component propagates counter-clockwise, generating $|VV\rangle$ photon pairs in the pp-KTP crystal, which are rotated to by the half-wave plate (HWP) to $|HH\rangle$. The pump's $|H\rangle$ component propagates clockwise and is rotated to $|V\rangle$ by the HWP before generating $|VV\rangle$ photon pairs in the crystal. The $|HH\rangle$ and $|VV\rangle$ generations are combined at the PBS and separated from the pump with a dichroic mirror.

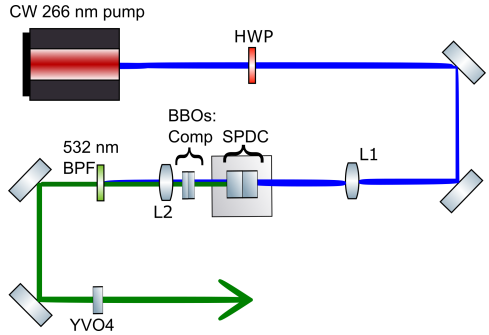

FIGURE 2.4: **Crossed-crystal polarization-EPS.** The $|D\rangle$ polarized pump (blue) generates $|HH\rangle$ and $|VV\rangle$ SPDC photon pairs (green) in the first and second BBO crystal. The two SPDC processes are overlapped spatially and temporally using two further BBO crystals and a YVO4 crystal, respectively. Figure adapted from Ref. [73].

Imaging the near-field of the EPS outputs (for both the EPSs shown in Fig. 2.3 as well as 2.4), the state detected at the image plane can be described by the tensor product between Eq. 2.44 and the two-photon polarization N00N state Eq. 2.35. We can write this as

$$|\psi\rangle = \int d^2r_s \int d^2r_i \gamma(\mathbf{r}_s, \mathbf{r}_i) \left(\hat{a}_H^\dagger(\mathbf{r}_s)\hat{a}_H^\dagger(\mathbf{r}_i) + \hat{a}_V^\dagger(\mathbf{r}_s)\hat{a}_V^\dagger(\mathbf{r}_i)) \right) |\text{vac}\rangle \,, \tag{2.45}$$

which relies on the simplification that the two-photon spatial distribution γ is the same for HH and VV (i.e. $\gamma = \gamma_{HH} = \gamma_{VV}$). Fulfilling this condition with the SI EPS requires some careful alignment, as described in Sect. 5.3.3.

Lastly, note that in the SPDC near-field, γ (Eq. 2.44) rapidly approaches zero for $|\mathbf{r}_s - \mathbf{r}_i| > \sigma_-$. That is, the two photons are most likely to be detected close to each other within a radius given by the position correlation width. Therefore Eq. 2.45 can be approximated by the hyper-entangled state:

$$|\psi\rangle \approx \sum_{\mathbf{r}} (|H\rangle_{\mathbf{r}} |H\rangle_{\mathbf{r}} + |V\rangle_{\mathbf{r}} |V\rangle_{\mathbf{r}}) \tag{2.46}$$

where for clarity we neglect the spatially dependent amplitude, which follows the shape of the normalized irradiance. The integral was transformed into a sum due to discretization of modes in a pixelated detection system. In other words, we can think of Eq. 2.46 as describing many parallel two-photon polarization N00N states, with two spatially correlated photons always likely to be detected in the same spatial "mode" $\mathbf{r}$ of width σ_-.

Chapter 3

Imaging Photon Coincidences with Cameras

Chapter 2 introduced multi-photon quantum states of light, such as entangled photon pairs from SPDC. If we have a setup that produces such states, naturally the question now arises how to detect them: if our measurement apparatus detects two (or more) photons, how do we know that they "belong together"? That is, how do we know that the individual photon detections came together from a single multi-photon state, rather than originating from separate, uncorrelated states? The answer is, by counting *coincidences* – simultaneous detections of multiple photons within a given time window. As long as this *coincidence window* is short enough, we can be reasonably certain that a coincidence event corresponds to a measurement of the multi-photon state that interests us. Nevertheless, as uncorrelated photons may be accidentally detected together in a coincidence window, these so-called *accidentals* must also be accurately characterized.

Counting coincidences and accidentals therefore represents an essential technique in the experimental quantum optics toolbox, having been used in a huge number of works, including pioneering experiments at the foundations of the field [29, 95–97]. Coincidence counting is also required in almost all applications of optics to quantum technology use cases, such as photonic quantum computing [55, 98], quantum communication [58, 61, 99–103], and quantum metrology [37, 104, 105].

This chapter outlines how coincidences can be measured by single-photon avalanche diodes (SPADs) as well as SPAD array cameras, which is the key experimental capability that enables the detection and imaging of entangled photon states. In particular, we first describe the simplest possible coincidence counting setup consisting of two single-pixel SPADs, followed by an extension of these techniques to photon-counting, and time-tagging SPAD array cameras. This chapter is presented in the context of SPDC two-photon states, focusing therefore on two-photon coincidence counting. However, we note that methods presented here can be extended to detect coincidences between more than two photons.

3.1 Coincidences and Accidentals in a Two-Channel System

Coincidence counting in two-channel detection systems is a well-established technique in experimental quantum optics. Figure 3.1 shows a schematic of an idealized coincidence counting experiment; here we assume that a SPDC source pumped by a continuous wave (CW) laser generates pairs of photons which can be perfectly separated such that one of the photons is directed to optical Channel 0, and the other to Channel 1. The two photons are then detected by two single-photon avalanche diode (SPAD) detectors, which emit an electrical pulse upon registering a detection event. Here photons are depicted as red dots, entering the setup from the left, where the separation between consecutive photon pair generations follows the Poissonian statistics of the SPDC pump laser. Furthermore, Fig. 3.1 shows how in the ideal coincidence detection scheme all photons are detected with perfect efficiency by the two SPADs, converting each detection into an electrical pulse (depicted by red square pulse). Finally, a coincidence counter, as depicted by the "&" symbol, registers coincidence events whenever two pulses arrive within the time window τ_c (light blue shaded area). In practice, in such experimental systems, the coincidence logic is usually implemented through the use of an AND gate, or by time-tagging detections (i.e. recording the pulses' time of arrival) [29, 54]. As seen in Fig. 3.1, a coincidence detection therefore provides evidence of a SPDC photon pair emission.

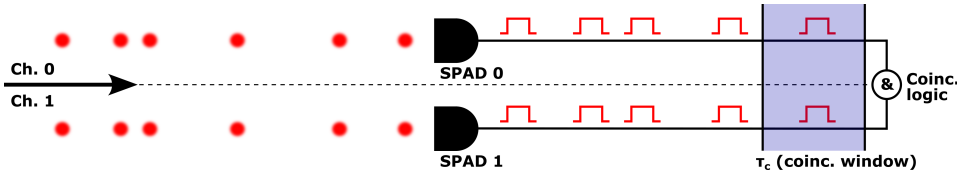

FIGURE 3.1: Idealized coincidence counting scheme in a two-channel setup, detecting cw-SPDC photon pairs.

In contrast to the the idealized picture presented by Fig. 3.1, any real experimental setup will inevitably suffer from imperfections, which are schematically represented in Fig. 3.2. As depicted by the beamsplitter elements, any real optical channel will have a non-ideal optical efficiency $\eta_{\text{opt}} < 1$, representing the probability of a photon being transmitted all the way to the detector. Additionally, photon detectors such as SPADs will in reality possess a non-ideal detection efficiency $\eta_{\text{det}} < 1$. While nowadays highly optimized setups exist with both η_{opt} and η_{det} close to unity [100, 106], for a highly precise quantum measurement the remaining non-ideal behaviour nonetheless has to be taken into account [107]. Moreover, real detectors manifest non-zero temporal jitter t_{jit}, that is, uncertainty in the photon detection time [108]. In practice, temporal jitter can usually be neglected by ensuring that the coincidence window τ_c is set to be significantly wider than t_{jit}. Especially for fibre-coupled SPDC sources, it is also important to take into account the heralding efficiency $\eta_{\text{h}} \leq 1$, the joint probability for *both* photons to be emitted

correctly to their respective channel [92, 109, 110]. On the other hand, in the free-space configuration (i.e. directing SPDC photon pairs towards detectors using only free-space bulk optics) it is relatively straightforward to achieve η_h close to unity. The outcome of the experimental imperfections can be observed in Fig. 3.2 – while in the idealized scheme of Fig. 3.1 every pair of photons converts deterministically to a pair of electrical pulses, in a realistic scenario optical and detection losses will cause some photons to lose their corresponding "partner" photon (or indeed, maybe both photons are lost). Therefore it can happen that two photodetections originating from uncorrelated single photons are registered within the same time window τ_c and are therefore counted as a coincidence, despite not corresponding to a SPDC photon pair. The ability to characterize and subtract these *accidental* coincidences is thus crucial, and can be performed through the use of a simple mathematical model.

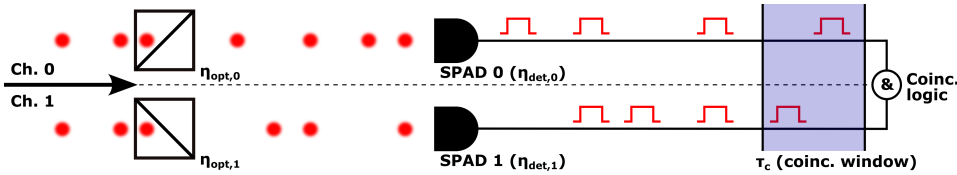

FIGURE 3.2: Coincidence counting in a two-channel setup, taking into account non-ideal optical and detection efficiencies (detecting cw-SPDC photon pairs). The effect of loss is to cause some photon pairs to lose their "partner", leading to the potential detection of accidental coincidences from uncorrelated photons.

Let us assume that the SPDC source produces photon pair at a rate R_0 (pairs/s), and Channels 0 and 1 have optical and detection efficiencies of $\eta_{\text{opt},0}$ and $\eta_{\text{opt},1}$, and $\eta_{\text{det},0}$ and $\eta_{\text{det},1}$, respectively. In the linear counting regime, i.e. at sufficiently low rates to avoid saturation effects, the coincidence detection rate can then be expressed as

$$R_{\text{cc,det}} = D\eta_h\eta_{\text{opt0}}\eta_{\text{opt1}}\eta_{\text{det0}}\eta_{\text{det1}}R_0 + R_{\text{acc}}. \tag{3.1}$$

Here, R_{acc} is the accidental coincidence rate, and $D \leq 1$ is the duty cycle, which represents the ratio between the total active time of the detection apparatus and the total acquisition time t_{acq}. As illustrated in Fig. 3.3, the effect of a non-ideal duty cycle $D < 1$ is simply to reduce the effective experimental acquisition time. Note that all experiments described in this thesis used a free-space source configuration, and we can thus neglect the η_h term in Eq. 3.1.

We can also write out expressions for the singles rates (i.e. corresponding simply to the single photon counts on each channel) as follows:

$$R_{\text{sc},0} = D\left(\eta_{\text{opt},0}\eta_{\text{det},0}R_0 + R_{\text{D},0}\right), \tag{3.2}$$

$$R_{\text{sc},1} = D\left(\eta_{\text{opt},1}\eta_{\text{det},1}R_0 + R_{\text{D},1}\right), \tag{3.3}$$

where $R_{\text{D},0}$ and $R_{\text{D},1}$ are the dark count rates of SPAD 0 and SPAD 1, that is, the noise counts generated by the detectors independently of real photon detections. Dark counts are mostly generated by free electrons in a SPAD due to thermally

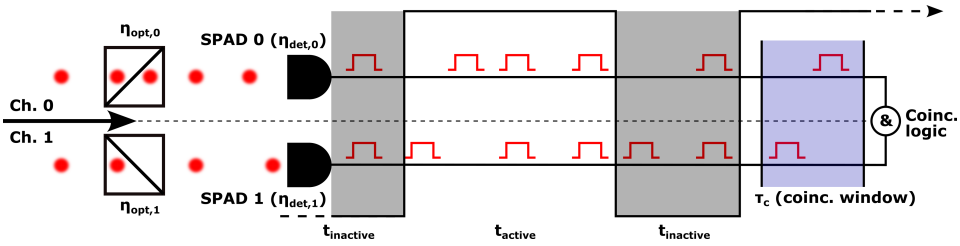

FIGURE 3.3: Coincidence counting in a two-channel setup, illustrating the effect of duty cycle $D < 1$. Grey-shaded regions correspond to times where the detection system is inactive, i.e. photons arriving during these times will not contribute to single photon detections nor to coincidences. Note that as in Fig. 3.2, $\eta_{\text{opt}} < 1$, and $\eta_{\text{det}} < 1$.

induced instabilities, and can usually be reduced by cooling down the detector [111–113]. In addition, the black-body radiation spectrum from objects at room temperature, while centred at mid-infrared wavelength, has a small but non-zero tail in the near-infrared and visible wavelengths. For extremely low levels of light, black-body radiation must therefore also be taken into account in $R_{\text{D},0}$ and $R_{\text{D},1}$ [114]. It is convenient to define the *active* single count rates $R'_{\text{sc},0}$ and $R'_{\text{sc},1}$, corresponding to the detected count rates only during the active times t_{active}:

$$R'_{\text{sc},0} \equiv \frac{R_{\text{sc},0}}{D}, \tag{3.4}$$

$$R'_{\text{sc},1} \equiv \frac{R_{\text{sc},1}}{D}. \tag{3.5}$$

In other words, we can think of $R'_{\text{sc},0}$ and $R'_{\text{sc},1}$ as the singles rates we would detect if the duty cycle was 100%. Now, given $R'_{\text{sc},0} > 0$ and $R'_{\text{sc},1} > 0$, we can see intuitively from Fig. 3.2 and 3.3 that even in the absence of any real correlations between the two channels, there is a non-zero probability for two detections to fall within the coincidence window τ_c. This accidental coincidence rate can be expressed as

$$R_{\text{acc}} = D R'_{\text{sc},0} R'_{\text{sc},1} \tau_c. \tag{3.6}$$

As $R_{\text{sc},0}$ and $R_{\text{sc},1}$ are directly measured quantities (the count rates registered by the two detectors), we can thus use Eq. 3.4, 3.5, and 3.6 to accurately estimate how many of the detected coincidences (Eq. 3.1) were due to accidentals. The real coincidence rate R_{cc} is therefore simply

$$R_{\text{cc}} = R_{\text{cc,det}} - R_{\text{acc}}. \tag{3.7}$$

We will see that the idea behind Eq. 3.7 suffices to extend coincidence counting ability to SPAD arrays with many pixels.

3.2 Coincidences and Accidentals in a Camera

The most obvious difference between a SPAD array camera and the simple system presented in Section 3.1 is the number of detectors. A SPAD array camera is a detector array containing many SPAD pixels, each of which can be considered equivalent to the optical and detection channels in the previous section's setup. Therefore, in a SPAD array we count two-photon coincidences between all possible combinations of pixel pairs, that is, every given pixel can register coincidences with all other pixels. Note that for some specialized SPAD array designs, depending on the sensor architecture, one cannot retrieve coincidences between all pixel-pair combinations [39, 42]. However, such limitations did not apply to the SPAD array cameras used in this thesis. Therefore, for a SPAD array camera with N pixels, the coincidence counts are represented by an array with $N \times N$ elements. Eq. 3.7 can then simply be extended to the SPAD array camera scenario, to represent coincidence rates between pixel pairs:

$$R_{\mathrm{cc}}(i,j) = R_{\mathrm{cc,det}}(i,j) - R_{\mathrm{acc}}(i,j), \tag{3.8}$$

where i and j are the indices of the two pixels (i.e., $1 \leq i \leq N$, $1 \leq j \leq N$). Note also that it is often more convenient to work with the total number of detected coincidences over an experimental acquisition time t_{acq}. We can therefore define the total detected coincidences for a given pixel pair $[i,j]$ as

$$\mathrm{cc}(i,j) = t_{\mathrm{acq}} R_{\mathrm{cc}}(i,j), \tag{3.9}$$

$$\mathrm{cc}_{\mathrm{det}}(i,j) = t_{\mathrm{acq}} R_{\mathrm{cc,det}}(i,j), \tag{3.10}$$

$$\mathrm{acc}(i,j) = t_{\mathrm{acq}} R_{\mathrm{acc}}(i,j). \tag{3.11}$$

Similarly, it is useful to define the total detected single photons for a given pixel:

$$\mathrm{sc}(i) = t_{\mathrm{acq}} R_{\mathrm{sc}}(i), \tag{3.12}$$

where $R_{\mathrm{sc}}(i)$ is, equivalent to Eq. 3.2 and 3.3, the rate of single photon detections on pixel i.

When calculating coincidences between pairs of pixels on a single SPAD array camera, two additional caveats normally apply when interpreting $R_{\mathrm{cc}}(i,j)$ or $\mathrm{cc}(i,j)$: first, the terms $\mathrm{cc}(i,j)$ and $\mathrm{cc}(j,i)$ refer to the same pair of pixels and are thus equal. Second, as individual SPAD pixels are threshold detectors, only able to distinguish between zero and one or more photons, we are unable to count coincidences between a pixel and itself, that is $\mathrm{cc}(i,i) = 0$. These points do not apply, on the other hand, in the case of calculating coincidences between two separate SPAD arrays (i.e. pixels i and j on separate SPAD array detectors). In mass-producible complementary metal-oxide-semiconductor (CMOS) fabricated SPAD arrays we can also make the simplifying assumption that all pixels have the same detection efficiency η_{det}.

The following sub-sections describe details of the specific implementation of Eq. 3.8 for photon-counting and photon-timetagging SPAD array cameras.

3.2.1 Photon-counting SPAD arrays

In this thesis, photon-counting refers to cameras which provide image frames as output, where the information contained in every frame is the number of photons detected on each pixel over the frame exposure time. The commercially available Micro Photon Devices SPC3, which is based on the sensor described by Ref. [115] and was used for the work described in Chapter 5, represents an example of a photon-counting SPAD sensor. In the following, we restrict ourselves to the condition where every pixel receives either zero or one photon; as we will see in Sect. 3.5 satisfying this condition is required to obtain high SNR. Note however that the method described here was already extended to include acquisitions with > 1 photons per pixel in Ref. [30].

Let us assume that SPDC photon pairs are directed to a photon-counting SPAD array camera, which records a total of M image frames, with an exposure time t_{exp} per frame. The total experimental exposure time is therefore simply $M \times t_{\text{exp}}$. However, the experimental acquisition time t_{acq} (i.e. the actual duration of the experiment) is normally longer than the total exposure time, as the minimum frame time is determined by the camera sensor's readout speed. For example, the Micro Photon Devices SPC3 is a general purpose SPAD camera, which reads out and transfers information for every pixel in every frame regardless of whether a detection occurred or not. Its shortest possible frame time t_{frame} is 10.4 µs, which is obtained simply by multiplying the pixel readout time (~ 5 ns) by the number of pixels [115]. On the other hand, the frame exposure time t_{exp} can be as short as 10 ns giving therefore, in the most extreme case, a duty cycle of $D = t_{\text{exp}}/t_{\text{frame}} \approx 0.1\%$, while $t_{\text{acq}} = M \times t_{\text{frame}}$.

If pixels register either zero or one photon in a frame, having detections on both pixels i and j in one frame can be considered a coincidence, with a coincidence window given by the frame exposure time, i.e. $\tau_c = t_{\text{exp}}$. We can therefore express the total detected coincidence counts (i.e. equivalent to Eq. 3.10) over all M frames, for pixel pair $[i, j]$, as

$$\text{cc}_{\text{PC,det}}(i,j) = \sum_{l=1}^{M} I_{l,i} I_{l,j}, \tag{3.13}$$

where $I_{l,i} \in \{0,1\}$ represents the value returned by the i^{th} pixel in the l^{th} frame, and the "PC" subscript stands for photon-counting. In order to use Eq. 3.8 to remove the accidentals, we need the active single photon detection rates (i.e. equivalent to Eq. 3.4 and 3.5):

$$\begin{aligned} R'_{\text{sc,PC}}(i) &= \frac{\text{sc}(i)}{t_{\text{acq}} D} \\ &= \frac{1}{t_{\text{acq}} D} \sum_{l=1}^{M} I_{l,i}. \end{aligned} \tag{3.14}$$

We can substitute $R'_{\mathrm{sc,PC}}(i)$ into Eq. 3.6:

$$\begin{aligned} R_{\mathrm{acc,PC}}(i,j) =& D\left(\frac{1}{t_{\mathrm{acq}}D}\sum_{m=1}^{M} I_{m,i}\right)\left(\frac{1}{t_{\mathrm{acq}}D}\sum_{n=1}^{M} I_{n,j}\right) t_{\mathrm{exp}} \\ =& \frac{t_{\mathrm{exp}}}{t_{\mathrm{acq}}^2 D}\sum_{m,n=1}^{M} I_{m,i}I_{n,j} \\ =& \frac{1}{Mt_{\mathrm{acq}}}\sum_{m,n=1}^{M} I_{m,i}I_{n,j}. \end{aligned} \tag{3.15}$$

Therefore, using Eq. 3.8, we arrive at the following expression for the coincidence counts $\mathrm{cc}_{\mathrm{PC}}$ between any two arbitrary pixels i and j:

$$\begin{aligned} \mathrm{cc}_{\mathrm{PC}}(i,j) =& \mathrm{cc}_{\mathrm{PC,det}}(i,j) - t_{\mathrm{acq}}R_{\mathrm{acc,PC}}(i,j) \\ =& \sum_{l=1}^{M} I_{l,i}I_{l,j} - \frac{1}{M}\sum_{m,n=1}^{N} I_{m,i}I_{n,j}, \end{aligned} \tag{3.16}$$

which has similar form to the coincidence counting equations in Ref. [40, 116]. Note that Eq. 3.16 does not depend on the frame exposure time t_{exp}, nor the frame time t_{frame}. That is, Eq. 3.16 allows us to accurately calculate coincidences between all camera pixels simply by acquiring M binary (pixel values 0 or 1) intensity image frames. As pointed out in Ref. [40], in general a large number of frames ($M \gtrsim 10^7$) is needed for the experimental quantity $\mathrm{cc}_{\mathrm{PC}}(i,j)$ to provide an accurate estimate of the actual photon pair probability. Therefore SPAD array cameras, capable of extremely high frame rates ($\sim 10^6$Hz demonstrated [41]), represent the only practical option to evaluate Eq. 3.16 without resorting to acquisition times of many hours or even days [39].

An example of a single counts image (Eq. 3.14) and coincidence counts calculated from Eq. 3.16 can be seen in Fig. 3.4, which shows images calculated from $M = 1.2 \times 10^7$ binary intensity frames acquired by our Micro Photon Devices SPC3 camera over an acquisition time of $t_{\mathrm{acq}} = 120\,\mathrm{s}$. Here spatially anti-correlated photon pairs were generated by imaging the far-field of an SPDC source (810 nm wavelength, from ppKTP nonlinear crystal – see Sect. 2.3), corresponding to the joint probability distribution Eq. 2.43. In Fig. 3.4(a) we see the total single-photon counts $\mathrm{sc}_{\mathrm{PC}}$ for all pixels, that is, the intensity image which shows the characteristic ring shaped profile of SPDC far-field emission [93]. On the other hand, Fig. 3.4(b) and (c) show the coincidences $\mathrm{cc}_{\mathrm{PC}}$ with two example single pixels (indicated by white "X"), that is, the conditional coincidence counts $\mathrm{cc}_{\mathrm{PC}}(x,y|x_i,y_i)$ (conditional upon a detection at pixel i, with the pixel index expressed in terms of its x and y coordinates for clarity). Here we clearly see that Eq. 3.16 accurately captured the anti-correlated nature of the SPDC far-field photon pairs, as in Fig. 3.4(b) and (c) we see strong coincidence peaks on the opposite side of the SPDC ring profile from the single fixed pixel.

Sometimes it is of use to subdivide a M-frame acquisition into Q sub-acquisitions, calculating the coincidences for each sub-acquisition separately. This can be achieved

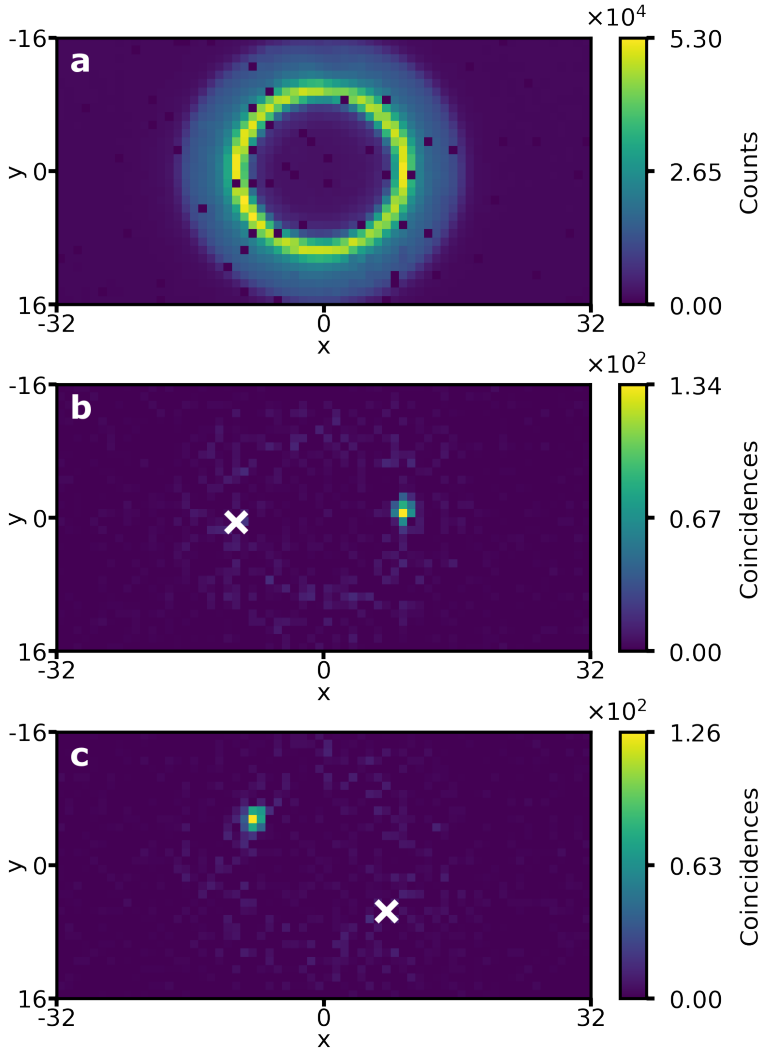

FIGURE 3.4: **SPDC singles and coincidences from photon-counting SPAD array. (a)** Single-photon counts sc_{PC} of SPDC far-field. **(b)** and **(c)** Two-photon coincidences cc_{PC} of anti-correlated photon pairs in SPDC far-field, with single fixed pixels as indicated by white "X". Images calculated from $M = 1.2 \times 10^7$ binary intensity frames.

by modifying Eq. 3.16 as follows:

$$\mathrm{cc}_{\mathrm{PC}}(i,j,p,q) = \sum_{l=p}^{q} I_{l,i} I_{l,j} - \frac{1}{q-p+1} \sum_{m,n=p}^{q} I_{m,i} I_{n,j}, \tag{3.17}$$

which calculates the coincidences from the sub-acquisition starting at the p^{th}, and ending at the q^{th} recorded frame. That is, a total M-frame acquisition can be subdivided into Q sub-acquisitions, with $(p,q) = [(1, M/Q), (M/Q+1, 2M/Q), ..., ((Q-1)M/Q+1, M)]$. By setting $p = 1$ and $q = M$, Eq. 3.17 reverts to Eq. 3.16. In other words, we can think of Eq. 3.17 as dividing a single coincidence acquisition into a "movie" consisting of Q individual coincidence arrays, where we emphasize that Eq. 3.17 calculates the accidentals individually for every (p,q) sub-group.

Note that a photon-counting SPAD array camera is not fundamentally different to any other low-noise camera, capable of reliably counting the exact number of photons detected in a pixel in one frame. In the binary intensity regime (i.e. pixels detect 0 or 1 photon per frame) intensified CCD (ICCD), or electron-multiplying CCD (EMCCD) cameras are capable of coincidence counting using similar techniques to the method described here, albeit at much lower frame rates and correspondingly longer experiment times [80, 117, 118]. Moreover, currently a new generation of low-noise CMOS image sensors, marketed under the terms "quantitative CMOS (qCMOS)" or "Quanta Image Sensor (QIS)", is being developed and released [119–121]. Under some conditions, these cameras may also be considered "photon-counting", and could therefore in the future be used in quantum imaging including the experiments described in this thesis [122].

3.2.2 Photon-timetagging SPAD arrays

In contrast to photon-counting cameras described in Sect. 3.2.1, photon time-tagging SPAD array cameras represent a fundamentally different implementation paradigm. Rather than every camera pixel having an electronic counting element that records only the number of detections within a frame exposure, time-tagging SPAD array pixels possess a time-to-digital converter (TDC) which is capable of recording the time at which a photon was detected [39, 42]. Coincidences can therefore be calculated by counting all pairs of detections that occurred within coincidence time window τ_c. Moreover, as the timing information of all photon detections is known, using time-tagging SPAD array cameras we can also measure coincidences with a non-zero inter-photon offset time [81]. This capability is crucial for example in calculating the full second-order coherence function $g^{(2)}$ [29].

Let us assume that light (e.g. SPDC photon pairs) is directed to a photon time-tagging SPAD array camera, which records timestamps $\mathrm{ts}(i)$ of all photon detections. Here $\mathrm{ts}(i)$ represents the time of detection with respect to the start of the experimental acquisition, at pixel i. That is, for acquisition time t_{acq}, we have $0 \leq \mathrm{ts}(i) \leq t_{\mathrm{acq}}$. Rather than a series of intensity image frames (as with photon-counting SPAD arrays), the time-tagging SPAD array camera therefore provides a list of T total timestamps as an output. As each timestamp $\mathrm{ts}(i)$ is associated to a given i^{th} pixel, T can be subdivided into T_i components, that is, the total number

of timestamped photon detections recorded by the i^{th} pixel. This yields simple expressions for the singles counts and count rates:

$$\text{sc}_{\text{TT}}(i) = T_i, \tag{3.18}$$

$$R_{\text{sc,TT}}(i) = \frac{T_i}{t_{\text{acq}}}, \tag{3.19}$$

where the "TT" subscript stands for "time-tagging". Note that pixel data readout in time-tagging SPAD arrays typically occurs in frames, where each pixel is often limited to registering one time-stamped photon detection per frame [39]. Thus, in order to avoid saturation effects with time-tagging SPAD arrays, care must be taken to ensure the probability of > 1 photons arriving to a single pixel within a frame exposure time remains negligible. Moreover, at the SPAD sensor level, each pixel's time-tagging element is typically only capable of recording a photon's time of arrival with respect to the start of the frame, or a synchronising trigger signal [39, 123–125]. Depending on the specific time-tagging camera implementation it is therefore necessary to add a frame-number dependent offset to each frame's timestamp, in order to obtain the global timestamp $\text{ts}(i)$. As with photon-counting cameras, the duty cycle D is generally also determined by the time required to read out detections in each frame. However, in time-tagging cameras τ_c is not determined by the frame exposure time, therefore enabling coincidence counting with simultaneously high duty cycle and short coincidence window.

Timestamps $\text{ts}(i)$ are expressed in timebins with temporal length t_b, as determined by the electronic time-tagger's temporal resolution. Choosing therefore a coincidence window τ_c larger than the detection system's jitter t_{jit} allows us to count coincidences between pixels i and j according to

$$\text{cc}_{\text{TT,det}}(i,j,\tau_c,\tau_o) = \sum_{l=1}^{T_i}\sum_{m=1}^{T_j} \text{Th}\left(|\text{ts}_l(i) - \tau_o - \text{ts}_m(j)| - \tau_c\right), \tag{3.20}$$

where $\text{ts}_l(i)$ represents the l^{th} timestamp recorded for pixel i, τ_o is the the inter-photon delay offset time, and $\text{Th}(x)$ is a threshold function defined as follows

$$\text{Th}(x) = \begin{cases} 1 & \text{if } x \leq 0, \\ 0 & \text{if } x > 0. \end{cases} \tag{3.21}$$

In order to calculate the accidentals (to subtract them from Eq. 3.20) we can again make use of Eq. 3.6, substituting the singles rate obtained from Eq. 3.19:

$$\begin{aligned} R_{\text{acc,TT}}(i,j,\tau_c,\tau_o) &= D(\tau_o)\left(\frac{1}{t_{\text{acq}}D(\tau_o)}T_i\right)\left(\frac{1}{t_{\text{acq}}D(\tau_o)}T_j\right)\tau_c \\ &= \frac{\tau_c}{t_{\text{acq}}^2 D(\tau_o)}T_iT_j. \end{aligned} \tag{3.22}$$

Note that in general, depending on the specific time-tagging camera implementation details, the duty cycle depends on the coincidence inter-photon time offset

τ_o, as reflected by the dependency shown in Eq. 3.22. This is explored in Ref. [126] and [81], however, as in this thesis all coincidence measurements were performed with $\tau_o = 0$ we can neglect this dependence here. Therefore, again using Eq. 3.8 to combine Eq. 3.20 and 3.22, we arrive at the following expression for the coincidence counts $\mathrm{cc}_{\mathrm{TT}}$ between any two arbitrary pixels i and j:

$$\mathrm{cc}_{\mathrm{TT}}(i,j,\tau_c,\tau_o) = \left(\sum_{l=1}^{T_i} \sum_{m=1}^{T_j} \mathrm{Th}\left(|\mathrm{ts}_l(i) - \tau_o - \mathrm{ts}_m(j)| - \tau_c \right) \right) - \frac{\tau_c}{t_{\mathrm{acq}} D(\tau_o)} T_i T_j. \tag{3.23}$$

Eq. 3.23 involves a double sum over T_i and T_j, which means that calculating the full coincidence matrix $\mathrm{cc}_{\mathrm{TT}}$ for all $[i,j]$ pixel pairs from an acquisition with T total recorded timestamps requires T^2 operations. This is computationally inefficient and rapidly becomes impractical for large T. However, for $\tau_o = 0$ (as was the case for all results shown in this thesis) we can make use of the fact that it is extremely unlikely for the condition $|\mathrm{ts}_l(i) - \mathrm{ts}_m(j)| - \tau_c \leq 0$ to be satisfied if $\mathrm{ts}_l(i)$ and $\mathrm{ts}_m(j)$ are separated by many elements in the global list containing T timestamps. Therefore Eq. 3.23 becomes

$$\mathrm{cc}_{\mathrm{TT}}(i,j,\tau_c,\tau_o = 0,\mathcal{K}) = \left(\sum_{l=1}^{T_i} \sum_{m=\mathcal{P}l-\mathcal{K}}^{\mathcal{P}l+\mathcal{K}} \mathrm{Th}\left(|\mathrm{ts}_l(i) - \mathrm{ts}_m(j)| - \tau_c \right) \right) - \frac{\tau_c}{t_{\mathrm{acq}} D(0)} T_i T_j, \tag{3.24}$$

where $\mathcal{P} = \mathrm{nint}(T_j/T_i)$, i.e. T_j/T_i rounded to the nearest integer, is a proportionality term to account for different singles count rates on pixels i and j, and $\mathcal{K}$ is an empirical variable chosen such that $\mathrm{cc}_{\mathrm{TT}}(i,j,\tau_c,\tau_o = 0,\mathcal{K}) = \mathrm{cc}_{\mathrm{TT}}(i,j,\tau_c,\tau_o = 0,\mathcal{K}+1)$ is satisfied. Eq. 3.24 therefore reduces the computational steps required to $\sim 2\mathcal{K}T$, where $\mathcal{K} \ll T$ (in acquisitions for this thesis, typically $\mathcal{K} \approx 10$, while $T > 10^6$). In the remainder of this thesis, for conciseness in notation $\mathrm{cc}_{\mathrm{TT}}(i,j,\tau_c)$ denotes $\mathrm{cc}_{\mathrm{TT}}(i,j,\tau_c,\tau_o = 0,\mathcal{K})$, with $\mathcal{K}$ determined empirically as described above, and D denotes $D(\tau_o = 0)$ unless otherwise explicitly stated.

Note that in defining the proportionality term $\mathcal{P}$, the implicit assumption was made that the count rates on pixels i and j stay constant throughout the experimental acquisition. However, in general, the coincidence distribution may change over time, such as when using quantum imaging to record dynamic scenes as described in Chapter 7. In such a scenario Eq. 3.24 is no longer valid, and can therefore only be used to record coincidences from static scenes, while for counting coincidences that are expected to change over time, the formula becomes:

$$\mathrm{cc}_{\mathrm{TT}}(i,j,\tau_c) = \left(\sum_{l=1}^{T} \sum_{m=l-\mathcal{K}}^{l+\mathcal{K}} \mathrm{Th}\left(|\delta_{i'i}\mathrm{ts}_l(i') - \delta_{j'j}\mathrm{ts}_m(j')| - \tau_c \right) \right) - \frac{\tau_c}{t_{\mathrm{acq}} D} T_i T_j, \tag{3.25}$$

where $\mathrm{ts}_l(i')$ represents the l^{th} timestamp, out of the global timestamp list with T elements, and i' and j' are dummy variables (i.e. that change on every iteration of l or m, respectively) which represent the pixel index of the l^{th} or m^{th} timestamp, respectively. $\delta_{i'i}$ is the Kronecker delta function.

Lastly, analogously to Eq. 3.17, it can be useful to divide a time-tagging acquisition with T elements into separate sub-acquisitions, calculating coincidences for each sub-acquisition. This can be achieved by modifying Eq. 3.25 as follows:

$$\mathrm{cc}_{\mathrm{TT}}(i,j,\tau_c,p,q) = \left(\sum_{l=T(p)}^{T(q)} \sum_{m=l-\mathcal{K}}^{l+\mathcal{K}} \mathrm{Th}\left(|\delta_{i'i}\mathrm{ts}_l(i') - \delta_{j'j}\mathrm{ts}_m(j')| - \tau_c \right) \right) - \frac{\tau_c \left(T_i(q) - T_i(p)\right)\left(T_j(q) - T_j(p)\right)}{(q-p)D}. \tag{3.26}$$

Here p and q represent the start and end respectively of the sub-acquisition, that is, Eq.3.26 calculates coincidences using timestamps that satisfy the condition $p < \mathrm{ts}(i) \leq q$. $T(p)$ represents the number of timestamps (over all pixels) with value $< p$, while $T_i(p)$ represents the number of timestamps for pixel i with value $< p$. That is, a total T-timestamps acquisition can be subdivided into Q sub-acquisitions, with $(p,q) = [(0, t_{\mathrm{acq}}/Q), (t_{\mathrm{acq}}/Q+1, t_{\mathrm{acq}}M/Q), ..., ((Q-1)t_{\mathrm{acq}}/Q+1, t_{\mathrm{acq}})]$. By setting $p = 0$ and $q = t_{\mathrm{acq}}$, Eq. 3.26 reverts to Eq. 3.25.

In this thesis, a recently developed time-tagging SPAD array camera prototype was used for the work described in Chapter 7 [123], calculating coincidences according to Eq. 3.24, 3.25, or 3.26. This camera was developed by POLIMI (Politecnico di Milano) and Micro Photon Devices as part of the European project "Q-MIC", and will for conciseness in notation henceforth be referred to in this thesis as the QMIC24x24tdc camera. The QMIC24x24tdc camera has 24×24 pixels and implements a readout design optimized for photon pair imaging, which enables it to count coincidences with a coincidence window τ_c of 2 ns, and a duty cycle of close to 100%.

An example of a single counts image (Eq. 3.19) and coincidence counts calculated from Eq. 3.24 can be seen in Fig. 3.5, which shows images calculated from $T = 2.0 \times 10^6$ total timestamps acquired by the QMIC24x24tdc camera. As in Fig. 3.4, here spatially anti-correlated photon pairs were generated by imaging the far-field of an SPDC source (810 nm wavelength, from ppKTP nonlinear crystal – see Sect. 2.3), corresponding to the joint probability distribution Eq. 2.43. In Fig. 3.5(a) we see the total single-photon counts $\mathrm{sc}_{\mathrm{TT}}$ for all pixels, showing the SPDC emission's characterisitic ring profile, as in Fig. 3.4(a). Fig. 3.5(b) and (c) show the coincidences $\mathrm{cc}_{\mathrm{TT}}$ with two example single pixels (indicated by white "X"), analogous to Fig. 3.4(b) and (c). We clearly see that Eq. 3.24 accurately represented the SPDC far-field anti-correlations, as in Fig. 3.5(b) and (c) we see strong coincidence peaks on the opposite side of the SPDC ring profile from the single fixed pixel. Note also, that the acquisition time to produce Fig. 3.4 was 120 s, while the data for Fig. 3.5 was collected in only 0.07 s. This gives us a first indication of the remarkable improvement in imaging speed enabled by the QMIC24x24tdc camera, which is explored in detail in Chapter 7.

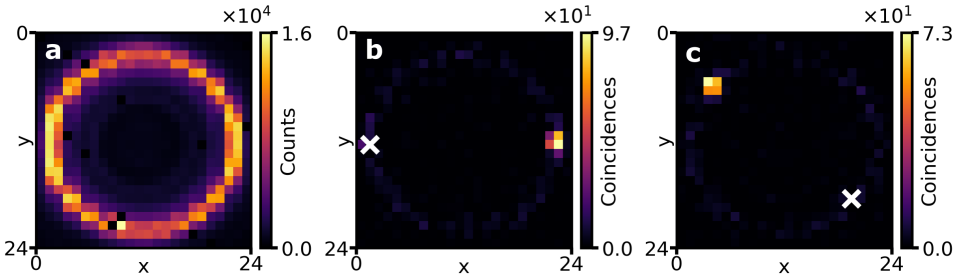

FIGURE 3.5: **SPDC singles and coincidences from time-tagging SPAD array. (a)** Single-photon counts sc_{TT} of SPDC far-field. **(b)** and **(c)** Two-photon coincidences cc_{TT} of anti-correlated photon pairs in SPDC far-field, with single fixed pixels as indicated by white "X". Images calculated from $M = 2.0 \times 10^6$ timestamped photon detections.

3.3 Noise in SPAD Array Camera Coincidence Counts

While Eq. 3.2 and 3.3 include terms due to the SPAD's dark count rates, in the subsequent derivations of Eq. 3.16, 3.24, and 3.25 these were not explicitly further taken into account. Indeed, due to typical dark count rates of $<10^2$ counts/pixel/s for the SPAD array cameras used in this thesis, dark counts did not normally represent a significant source of noise (with the exception of very noisy outlier "hot pixels", which can be electronically deactivated). Moreover, SPAD detectors, unlike other camera technologies, do not manifest any readout noise, which therefore also does not have to be taken into account in coincidence calculations [34]. Nevertheless, we will see that imaging with entangled photons based on counting coincidences benefits greatly from two noise removal steps, applied to the coincidence matrix $cc(i, j)$ in post-processing: first, subtracting cross-talk coincidences, and second, removing spatially uncorrelated noise.

3.3.1 Crosstalk in SPAD Array Cameras

Cross-talk in SPAD array cameras is caused by the breakdown flashing of individual SPAD pixels. When a single SPAD pixel detects a photon, it can re-emit secondary ones due to hot carrier relaxation [113, 127, 128]. As these secondary photons are emitted in all directions, it is possible for them to trigger detections in other nearby SPAD pixels, leading to noise coincidences that did not results from real photon pairs, nor can be attributed to accidentals.

Single-pixel SPAD detector modules also display the same breakdown flashing behaviour. However, in multi-channel coincidence setups that use separate single-pixel SPADs for each channel (e.g. as shown in Sect. 3.1), it is typically straightforward to implement optical isolation such that no spurious coincidences result from breakdown flashes [129]. On the other hand, in SPAD array cameras containing many SPAD pixels, which are CMOS-fabricated in a single monolithic array, it is highly non-trivial to block all possible photon emission paths between pixels

[127]. While fabricating opaque isolation trenches in the silicon between adjacent SPAD pixels is a promising approach to lower cross-talk [130, 131], in currently available SPAD arrays remaining cross-talk coincidences nonetheless represent a significant source of noise.

As cross-talk events are caused by real initial detections, the number of cross-talk (ct) coincidences $\mathrm{cc}_{\mathrm{xt}}$ between pixels i and j can be modelled as the spurious detections at pixel i caused by a secondary emission from a real photon detection at pixel j, and vice-versa [81]:

$$\begin{aligned}\mathrm{cc}_{\mathrm{xt}}(i,j) =& \mathrm{cc}_{\mathrm{xt}}(i|j) + \mathrm{cc}_{\mathrm{xt}}(j|i) \\ =& P_{\mathrm{xt}}(i|j)\mathrm{sc}(j) + P_{\mathrm{xt}}(j|i)\mathrm{sc}(i),\end{aligned} \tag{3.27}$$

where $P_{\mathrm{xt}}(i|j)$ represents the probability of detecting a cross-talk event at pixel i, conditional on an initial photon detection at pixel j, and $\mathrm{sc}(i)$ is the number of detections accumulated at a pixel i during the integration time (i.e. see Eq. 3.14 or 3.14). Therefore, Eq. 3.27 can in principle be used to remove cross-talk coincidences, as long as the probabilities $P_{\mathrm{xt}}(i|j)$ are known. However, note that for a SPAD array with N pixels, $P_{\mathrm{xt}}(i|j)$ contains N^2 elements (for every possible pixel-pair). That is, characterizing the full $P_{\mathrm{xt}}(i|j)$ array represents an extremely difficult experimental task, requiring the individual illumination of every single pixel [132]. Fortunately, due to excellent repeatability and uniformity in modern CMOS fabrication, normally the simplifying approximation can be made that relative cross-talk probabilities do not vary across the SPAD array and only depend on the distance between two pixels [81, 133]:

$$\mathrm{cc}_{\mathrm{xt}}(i,j) \approx P_{\mathrm{xt}}(\Delta x, \Delta y)(\mathrm{sc}(j) + \mathrm{sc}(i)), \tag{3.28}$$

where $\Delta x = |x_i - x_j|$ and $\Delta y = |y_i - y_j|$ (with i and j explicitly expressed in terms of their x and y coordinates). In this thesis, the simplified cross-talk probability matrix $P_{\mathrm{xt}}(\Delta x, \Delta y)$ was measured, for both the photon-counting and the time-tagging SPAD arrays, by acquiring coincidences with the sensor covered. In this situation that detections were only generated by dark counts, and as dark counts between different pixels are uncorrelated, detected coincidences are thus due to cross-talk [134].

The map of crosstalk coincidence probabilities P_{xt}, as a function of Δx and Δy, for our photon-counting Micro Photon Devices SPC3 SPAD array camera is shown in Fig. 3.6. The figure shows only the central region of $P_{\mathrm{xt}}(\Delta x, \Delta y)$, with pixel displacement close to zero, as the crosstalk probability is negligible for larger pixel-pair displacements. The total cross-talk probability (summing over all P_{xt} terms) was found to be 0.16%. Similarly, $P_{\mathrm{xt}}(\Delta x, \Delta y)$ with pixel displacement close to zero, for our time-tagging QMIC24x24tdc camera is shown in Fig. 3.7. In this case the total cross-talk probability (summing over all P_{xt} terms) was found to be 0.043%.

Note that P_{xt} depends in fact only on $\Delta x = |x_i - x_j|$ and $\Delta y = |y_i - y_j|$, that is, the absolute distances between the pixels. Therefore the probability map is symmetric about zero, i.e. $P_{\mathrm{xt}}(x_i - x_j, y_i - y_j) = P_{\mathrm{xt}}(x_j - x_i, y_i - y_j) = P_{\mathrm{xt}}(x_i - x_j, y_j - y_i) = P_{\mathrm{xt}}(x_j - x_i, y_j - y_i)$.

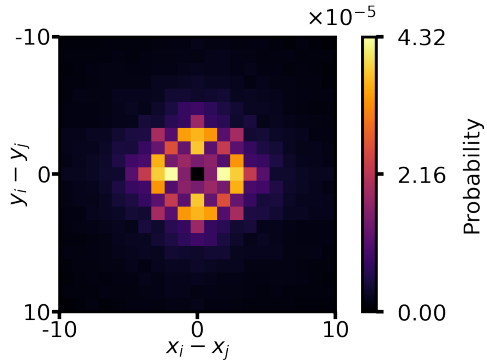

FIGURE 3.6: **Probability of crosstalk coincidences for Micro Photon Devices SPC3.** Total cross-talk probability 0.16%. Cross-talk map calculated from $M = 2.8 \times 10^9$ binary intensity frames with camera sensor covered, acquired over $t_{\text{acq}} = 2.9 \times 10^4$s.

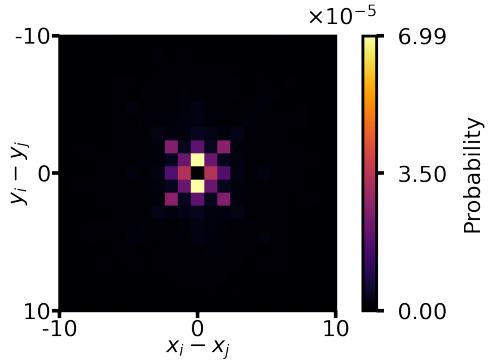

FIGURE 3.7: **Probability of crosstalk coincidences for QMIC24x24tdc.** Total cross-talk probability 0.043%. Cross-talk map calculated from $T = 2.0 \times 10^7$ timestamps with camera sensor covered, acquired over $t_{\text{acq}} = 9.2 \times 10^2$s.

Cross-talk coincidences calculated according to Eq. 3.28 were therefore always subtracted from measured coincidences for work presented in this thesis. The effect of this post-processing step is illustrated in Fig. 3.8 and 3.9. Fig. 3.8 shows a QMIC24x24tdc acquisition of SPDC far-field photons (Eq. 2.43), similar to Fig. 3.5. However, here the colour map range is intentionally limited in order to visualize cross-talk coincidences. In particular, Fig. 3.8(a) plots the coincidences $\text{cc}_{\text{TT}}(x, y|10, 2)$, that is, the coincidences with the single pixel $[x_i, y_i] = [10, 2]$ (white "X", analogous to Fig. 3.5(b) and (c)). The bright spot at the bottom of Fig. 3.8(a) clearly shows the expected coincidences corresponding to the anti-correlated SPDC far-field photon pairs (over-saturated, due to the limited colour map scale). However, close to the single fixed pixel indicated by the white "X" we can also observe a bright clustering with higher coincidence counts than the background level, as seen magnified in the image inset which shows the 25 image pixels around $[10, 2]$. Here

there should not be any real photon pair coincidences from the anti-correlated SPDC emission, and therefore we attribute these coincidences to cross-talk. Summing over this 25-pixel region-of-interest (ROI) gives 12.0 coincidence counts. Fig. 3.8(b) shows the expected cross-talk coincidences $\mathrm{cc}_{\mathrm{xt}}(x, y|10, 2)$, calculated using Eq. 3.28, where $P_{\mathrm{xt}}(\Delta x, \Delta y)$ is the distribution shown in Fig. 3.7 – note the similarity between Fig. 3.7 and the inset of Fig. 3.8(b). Fig. 3.8(c) shows the coincidence map $\mathrm{cc}_{\mathrm{TT}}(x, y|10, 2) - \mathrm{cc}_{\mathrm{xt}}(x, y|10, 2)$, that is, subtracting Fig. 3.8(b) from Fig. 3.8(a). As seen especially in the inset of Fig. 3.8(c), the cluster of coincidence counts around image pixel $[10, 2]$ has decreased in brightness, with the 25-pixel ROI now summing to -0.3 coincidences. Note that of course the detection of negative coincidences is unphysical; this is a reflection of the probabilistic nature of Eq. 3.28, which subtracts only an estimate of the cross-talk, with some non-zero noise about the true coincidence counts remaining.

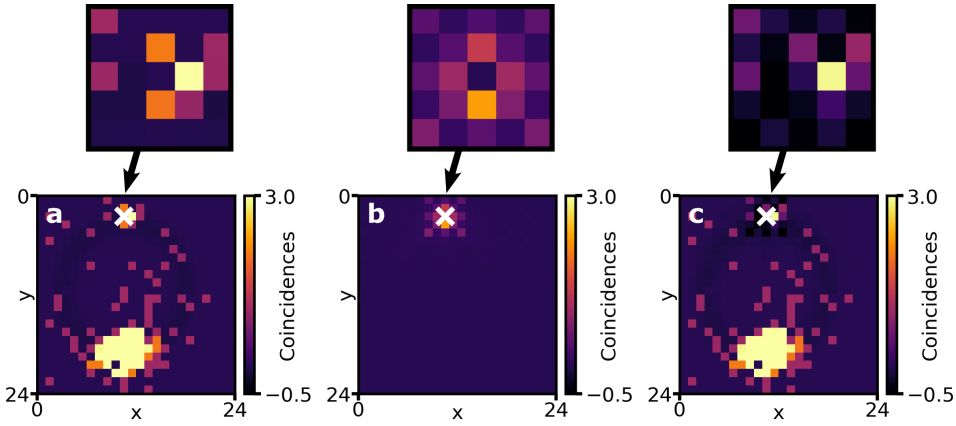

FIGURE 3.8: **Effect of cross-talk subtraction in SPDC far-field coincidences (single pixel) (a)** $\mathrm{cc}_{\mathrm{TT}}(x, y|10, 2)$ without cross-talk subtraction. **(b)** $\mathrm{cc}_{\mathrm{xt}}(x, y|10, 2)$ expected cross-talk coincidences for pixel $[10, 2]$. **(c)** Coincidences with pixel $[10, 2]$, with cross-talk removed (i.e. **(b)** - **(a)**). Insets show the 5×5 image pixel region-of-interest around $[10, 2]$.

Fig. 3.9 on the other hand shows the same QMIC24x24tdc acquisition of SPDC far-field photons as Fig. 3.8 (Eq. 2.43), however plotting only the y coordinates of the i and j pixel indices of the coincident detections. Fig. 3.9(a) displays the coincidence counts without cross-talk subtraction, where again, as in Fig. 3.8, the colour map range is intentionally limited such that cross-talk coincidences can be visualized. We clearly see the expected SPDC far-field anti-correlation ($y_i \propto -y_j$) diagonal, over-saturated due to the limited colour scale. The cross-talk manifests itself here as a correlated diagonal ($y_i \propto y_j$), as shown also in Ref. [80, 81]. In Fig. 3.9(b) we can observe the coincidence counts with cross-talk calculated according to Eq. 3.28 subtracted, again plotting only the y coordinates of detections and with the same colour map limits as Fig. 3.9(a). Clearly the spatially correlated diagonal, corresponding to cross-talk coincidences, is greatly reduced in Fig. 3.9(b) compared to Fig. 3.9(a), though we can see that the subtraction is not perfect –

again a reflection of the probabilistic nature of Eq. 3.28. Fig. 3.9(c) plots the same (cross-talk-subtracted) coincidences as Fig. 3.9(b), however with the full colour map range, indicating that the probability of real SPDC photon pair coincidences far outweighs the residual cross-talk counts remaining after the probabilistic post-processing step.

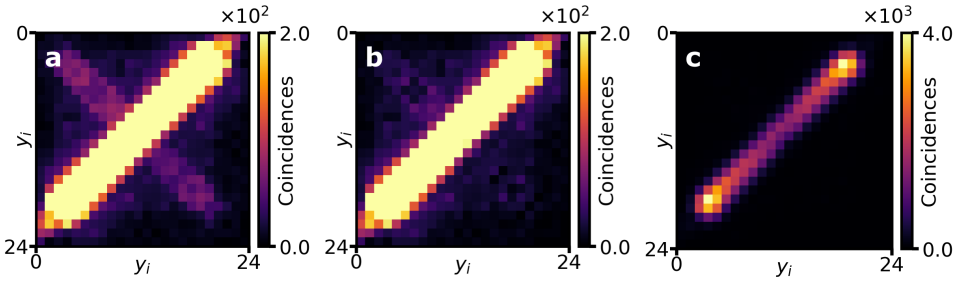

FIGURE 3.9: **Effect of cross-talk subtraction in SPDC far-field coincidences (y coordinates). (a)** $\mathrm{cc_{TT}}$ without cross-talk subtraction. **(b)** and **(c)** $\mathrm{cc_{TT}} - \mathrm{cc_{xt}}$. Colour map range reduced in **(a)** and **(b)**.

3.3.2 Uncorrelated noise removal

All coincidence maps shown in this Chapter thus far have been acquisitions of SPDC far-field, spatially anti-correlated photons described by Eq. 2.43, which lend themselves well to an intuitive visual explanation of cross-talk coincidences. However, as explored in Chapter 4, in order to use the enhanced phase-sensing capabilities of entangled N00N states when imaging samples, it is necessary for both photons of an entangled pair to pass through the same point of the sample. This requires acquiring SPDC photon pairs imaged at the near-field plane, with a joint probability density governed by Eq. 2.44. Fortunately, counting coincidences in the SPDC near-field allows a second noise removal post-processing step, in addition to the cross-talk subtraction described in Sect. 3.3.1: in the near-field we expect all detected coincidences originating from real photon pairs to be strongly correlated in space, that is, to be registered at (almost) the same spatial location [69, 82]. Therefore, after characterizing the expected possible separation between real photon pair events, any coincidence with greater spatial separation between detections can be assumed to constitute spatially uncorrelated noise. See also Ref. [21] for a similar idea.

Spatially uncorrelated noise coincidences are attributed to, for example, spurious reflections in the setup, stray light, and imperfections in the nonlinear crystal generating some SPDC photon pairs with low, or even lacking spatial correlation. The following describes the fitting procedure used to filter out such spatially uncorrelated noise. We begin by noting that, as was shown already in Fig. 3.4 and Fig. 3.5, for a fixed given pixel i with coordinates $[x_i, y_i]$, the set of coincidences with all other pixels forms a two-dimensional image $\mathrm{cc}(x, y|x_i, y_i)$, that is, the coincidences conditional on a detection at pixel i. For every i^{th} pixel, $\mathrm{cc}(x, y|x_i, y_i)$ is

fit with a two-dimensional Gaussian model of the form

$$G_i(x,y) = A_i \exp\left[\frac{-((x-x_{0,i})^2+(y-y_{0,i})^2)}{2\sigma^2_{\text{fit},i}}\right] \tag{3.29}$$

where A_i is an amplitude fitting parameter, $[x_{0,i}, y_{0,i}]$ is the peak location, and $\sigma_{\text{fit},i}$ is the fitted waist. Note that, when both photons are detected on the same SPAD array, we have $[x_{0,i}, y_{0,i}] = [x_i, y_i]$. On the other hand, this is not the case when the two photons are detected on different SPAD arrays (or equivalently, on separate sections of one SPAD array sensor which act as two separate cameras). This is the reason why the $x_{0,i}$ and $y_{0,i}$ fitting parameters are necessary in Eq. 3.29. The width of the averaged Gaussian fitting function σ_{fit} used for filtering out spatially uncorrelated noise is then obtained by taking the mean of all fitted $\sigma_{\text{fit},i}$ values. Moreover, for coincidences between two separate SPAD arrays, we can calculate the offsets between the Gaussian peak $[x_{0,i}, y_{0,i}]$ and the pixel $[x_i, y_i]$, i.e. $d_{x,i} = x_{0,i} - x_i$ and $d_{y,i} = y_{0,i} - y_i$. The offset values d_x and d_y used in the Gaussian fitting for filtering are again obtained by taking the mean of all $d_{x,i}$ and $d_{y,i}$ values (averaged over all pixels i). Note that this method assumes that photon pair correlations are uniform across the camera sensor, and that differences in $\sigma_{\text{fit},i}$, and $d_{x,i}$ and $d_{y,i}$, between different i^{th} pixels are simply due to local variations in photon counting statistics. Therefore, the following averaged Gaussian model is used for fitting and filtering:

$$G(i,j) = \exp\left[\frac{-((x_j-x_{0,i})^2+(y_j-y_{0,i})^2)}{2\sigma^2_{\text{fit}}}\right], \tag{3.30}$$

with $[x_{0,i}, y_{0,i}] = [x_i, y_i]$ when detecting both photons on the same SPAD array, and $[x_{0,i}, y_{0,i}] = [x_i + d_x, y_i + d_y]$, when detecting photons on separate arrays.

Figures 3.10 and 3.11 show examples of SPDC near-field photon pair detections and the corresponding fittings with Eq. 3.30. Here coincidences were acquired using the Micro Photon Devices SPC3 camera (Eq. 3.16), with cross-talk (Eq. 3.28) already subtracted. In Fig. 3.10(a) and (b) we can see the coincidences with the single fixed pixel $i = [15, 11]$ (white "X" in Fig. 3.10(a)), with both photons detected on the same SPAD array. As pointed out earlier, in Sect. 3.2, in this configuration we cannot detect coincidences of a pixel with itself. That is, $\text{cc}(i,i) = \text{cc}(15,11|15,11) = 0$, which can be clearly observed in Fig. 3.10(b), where the coincidence value drops to zero at $x = 15$. Figure 3.10(c) and Fig. 3.10(d) show the averaged Gaussian fitting $G(x,y|15,11)$ (Eq. 3.30) for pixel $[15,11]$. On the other hand, Fig. 3.11 shows near-field SPDC coincidences acquired with the two photons detected on separate halves of the Micro Photon Devices SPC3 camera, that is, equivalent to having been detected on two separate SPAD arrays. Figures 3.11(a) and (b) show again the coincidences with single fixed pixel $i = [15, 11]$ (white "X" in Fig. 3.11(a)). However, in contrast to Fig. 3.10(a) and (b) we can see that $d_x \neq 0$, as the centre of the photon correlation peak clearly does not coincidence with the single pixel $[15, 11]$. Moreover, we can see clearly in Fig. 3.11(b) that $\text{cc}(i,i) = \text{cc}(15,11|15,11) \neq 0$, as the coincidences of an image pixel with itself

in this case still involves two separate physical SPADs. Analogous to Fig. 3.10(c) and Fig. 3.10(d), Fig. 3.11(c) and Fig. 3.11(d) show the averaged Gaussian fitting $G(x, y|15, 11)$ (Eq. 3.30) for pixel $[15, 11]$.

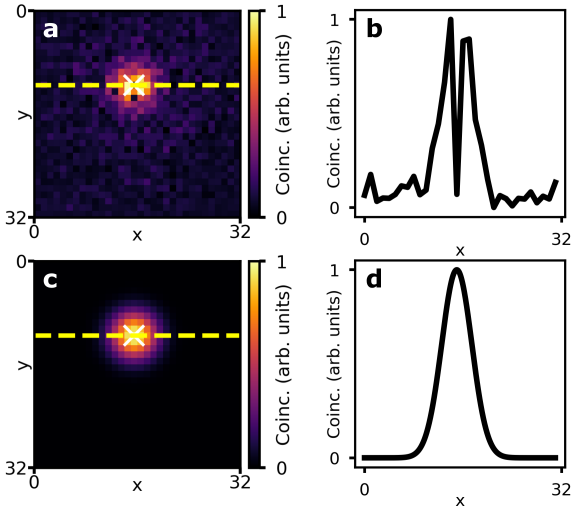

FIGURE 3.10: **SPDC near-field coincidences and fitting, both photons on same SPAD array. (a)** Coincidences with single fixed pixel $[15, 11]$ (white "X"). **(c)** Gaussian fitting $G(x, y|15, 11)$. **(b)** and **(d)** Cross-sections along yellow dashed lines in **(a)** and **(c)**, respectively.

Once the averaged fitting function $G(i, j)$ (Eq. 3.30) has been characterized, the filtered coincidence counts $\mathrm{cc_F}$, with spatially uncorrelated noise coincidences to be removed, are then calculated according to

$$\mathrm{cc_F}(i,j) = \begin{cases} \mathrm{cc}(i,j) - \mathrm{cc_{xt}}(i,j), & \text{if} \quad G(i,j) > t, \\ 0, & \text{otherwise}, \end{cases} \tag{3.31}$$

where $\mathrm{cc}(i, j)$ is calculated using Eq. 3.16 or 3.23 (or Eq. 3.17 or 3.26 in the case of considering sub-acquisitions), and $\mathrm{cc_{xt}}(i, j)$ is calculated using Eq. 3.28. t is a threshold parameter ranging from 0 (no filtering) and 1 (filtering out all coincidences). The effect of Eq. 3.31 is shown in Fig. 3.12 and 3.13. Fig. 3.12(a) and (b) show the coincidences plotted in Fig. 3.10(a) and (b), filtered with a threshold parameter of $t = 0.1$. In particular, in Fig. 3.12(b) we can see that the coincidence terms for which $G(x, y|15, 11) \leq 0.1$ (grey shading) have been set to zero, removing the background noise visible in Fig. 3.10(a). Fig. 3.12(c) shows the binary mask effected by Eq. 3.31, that is, white image pixels here represent those coincidence terms for which $G(x, y|15, 11) > 0.1$, and which are therefore not set to zero. Fig. 3.12(d) displays again a cross-section of the fitting function $G(x, y|15, 11)$ (as in Fig. 3.10(d)), with the horizontal red line indicating the threshold $t = 0.1$, and grey shading corresponding to the $G(x, y|15, 11) \leq 0.1$ condition as in Fig. 3.12(b). Similarly, Fig. 3.13(a) and (b) show the coincidences plotted in Fig. 3.11(a) and

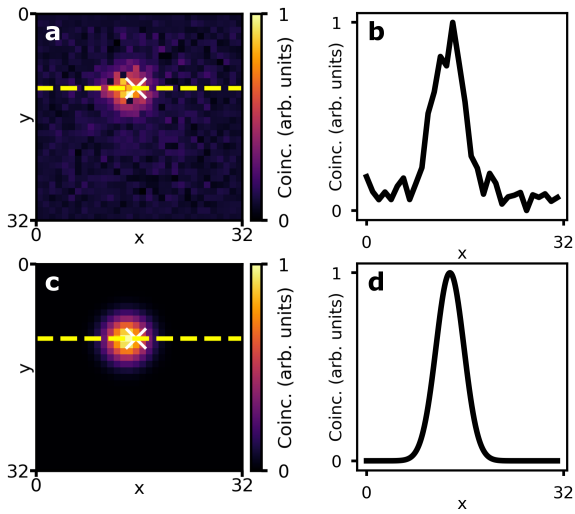

FIGURE 3.11: **SPDC near-field coincidences and fitting, each photon on separate SPAD array.** **(a)** Coincidences with single fixed pixel $[15, 11]$ (white "X"). **(b)** and **(d)** Cross-sections along yellow dashed lines in **(a)** and **(c)**, respectively.

(b), but much more strongly filtered now with a threshold parameter of $t = 0.6$. As in Fig. 3.10(a) and (b), Eq. 3.31 sets to zero those coincidence terms for photon pairs well-separated compared to the near-field correlation width, removing the background noise visible in Fig. 3.11(a) and (b), but with a much narrower, strongly correlated coincidence peak remaining as compared to Fig. 3.12. As for Fig. 3.12(c) and (d), Fig. 3.13(c) and (d) display the binary mask and fitting function $G(x, y|15, 11)$ respectively, for $t = 0.6$, which is indicated by the horizonal red line in Fig. 3.13(d).

In general, increasing the filtering threshold t results in a higher SNR, but in a lower overall number of recorded coincidence counts. Therefore, for acquisitions in this thesis, values of t between 0.1 and 0.5 were chosen in order to optimize the balance between SNR and total coincidence counts.

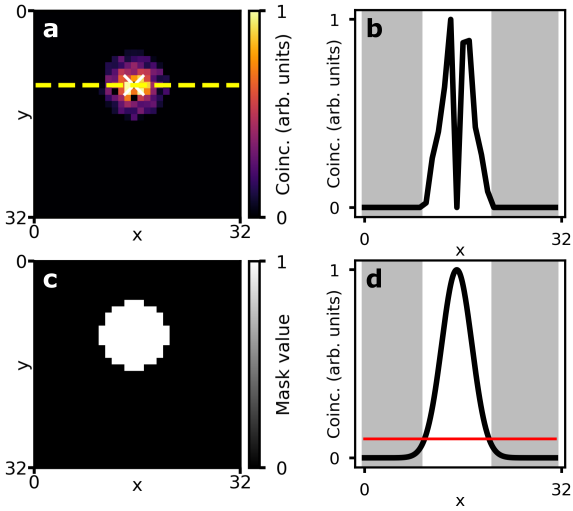

FIGURE 3.12: **Filtered SPDC near-field coincidences (t=0.1), both photons on same SPAD array.** **(a)** $\mathrm{cc_F}(x, y|15, 11)$, i.e. Fig. 3.10(a) filtered according to Eq. 3.31. **(b)** Cross-section along yellow dashed line in **(a)**. **(c)** Binary filtering mask. White, $\mathrm{cc_F}(i, j) = \mathrm{cc}(i, j) - \mathrm{cc_{xt}}(i, j)$; black $\mathrm{cc_F}(i, j) = 0$. **(d)** As Fig. 3.10. Red line, $t = 0.1$.

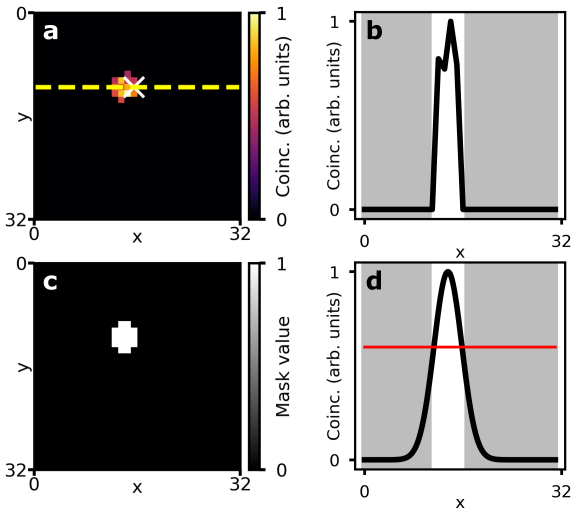

FIGURE 3.13: **Filtered SPDC near-field coincidences (t=0.6), each photon on separate SPAD array.** **(a)** $\mathrm{cc_F}(x, y|15, 11)$, i.e. Fig. 3.11(a) filtered according to Eq. 3.31. **(b)** Cross-section along yellow dashed line in **(a)**. **(c)** Binary filtering mask. White, $\mathrm{cc_F}(i, j) = \mathrm{cc}(i, j) - \mathrm{cc_{xt}}(i, j)$; black $\mathrm{cc_F}(i, j) = 0$. **(d)** As Fig. 3.11. Red line, $t = 0.6$.

3.4 Mapping coincidence counts onto images

The filtered coincidence array $\mathrm{cc_F}(i,j)$ obtained from Eq. 3.31, when pixel indices i and j are represented in terms of their x and y coordinates, is a four-dimensional quantity with array size $W \times Z \times W \times Z$. Here W and Z are the image width and height, respectively, that is the number of pixels in the x and y dimension of the camera sensor. However, in imaging applications, we are normally interested in obtaining information about a two-dimensional sample. This necessitates therefore the reduction of the four-dimensional $\mathrm{cc_F}([x_i,y_i],[x_j,y_j])$ array to a two-dimensional coincidence image $\mathrm{ci}(x,y)$, using the following:

$$\mathrm{ci}(x,y) = \sum_{x'=1}^{W}\sum_{y'=1}^{Z} \mathrm{cc_F}(x,y,x',y'), \tag{3.32}$$

where $\mathrm{cc_F}(x,y,x',y')$ is calculated using Eq. 3.31. Eq. 3.32 relies on photon pairs being spatially correlated at the point of detection, which is the case when imaging the SPDC near-field. In this regime, the conditional coincidence map for a given fixed pixel $\mathrm{cc_F}(x,y|x_i,y_i)$, describes a point-like image with the width of the spot described by the photon pair correlation width (σ_{fit} from Eq. 3.30), or determined by the threshold parameter t in Eq. 3.31. Given a narrow width for $\mathrm{cc_F}(x,y|x_i,y_i)$, we can trace out one of the photon detection locations, integrating as indicated by Eq. 3.32 to obtain the two-photon counts at $[x_i,y_i]$. In other words, we can think of the coincidence image as a two-photon"intensity" image, where each image pixel was broadened by a point-spread function given by the (possibly filtered) two-photon spatial correlation width.

Example coincidence images are shown in Fig. 3.14, displaying data acquired using the QMIC24x24tdc SPAD array camera. Here a test sample (square "blocks" across the field-of-view) was generated with a spatial light modulator, using the experimental setup described in detail in Chapter 7. Illuminating this test sample with the entangled photon pair state described by Eq. 2.46, and projecting into the diagonal polarization basis (as detailed in Sect. 2.2.2) results in a detected two-photon intensity that depends on the test sample phase. For Fig. 3.14(a) and (b), the coincidence images were calculated with filtering thresholds (in Eq. 3.31) of $t = 0$ (i.e. no filtering) and $t = 0.6$ (strong filtering), respectively. Fig. 3.14(c) and (d) show the unfiltered, and strongly filtered coincidences with the single pixel $[3,8]$, while Fig. 3.14(e) and (f) similarly shows the unfiltered, or strongly filtered, coincidences with pixel $[8,15]$. The image pixels $[3,8]$ and $[8,15]$ in the coincidence images Fig. 3.14(a) and (b), therefore correspond to the sum of all coincidence counts plotted in Fig. 3.14(c) and (d) ($[3,8]$), and Fig. 3.14(c) and (d) ($[8,15]$), respectively. Comparing Fig. 3.14(a) and (b) also illustrates the effect of filtering (Eq.3.31): Fig. 3.14(b) shows stronger edge contrast but lower total counts in comparison to Fig. 3.14(a).

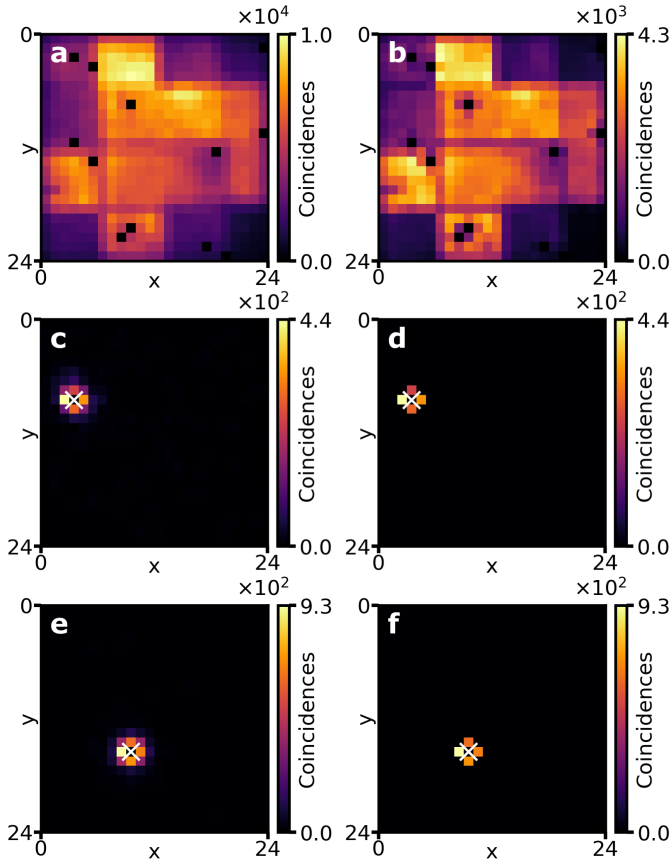

FIGURE 3.14: **Coincidence imaging, unfiltered and strongly filtered. (a)** and **(b)** Coincidence image (Eq. 3.32). **(c)** and **(d)** Coincidences with single pixel $[3, 8]$. **(e)** and **(f)** Coincidences with single pixel $[8, 15]$. **(a)**, **(c)**, **(e)**, unfiltered ($t = 0$) coincidences. **(b)**, **(d)**, **(f)**, strongly filtered ($t = 0.6$) coincidences.

3.5 Signal-to-noise Ratio of Coincidence Counting

In an ideal SPDC imaging experiment, without detector noise, with perfect efficiency, and no accidental coincidences, the coincidence image noise is only limited by the Poissonian statistics of the SPDC emission, i.e. $\mathrm{sd}(\mathrm{ci})_{\mathrm{ideal}} = \sqrt{\mathrm{ci}}$ [29, 54]. In other words, the ideal, shot noise-limited, signal-to-noise ratio (SNR) is $\mathrm{SNR}_{\mathrm{ci,ideal}} = \mathrm{ci}/\mathrm{sd}(\mathrm{ci})_{\mathrm{ideal}} = \sqrt{\mathrm{ci}}$ [135]. However, we expect this SNR to decrease due to real experimental considerations. This section presents an empirical method for characterizing the decrease in coincidence counting SNR, with respect to the shot noise-limited ideal case.

We can find detailed theoretical treatments of the SNR of SPDC photon pair

imaging under various experimental conditions in Ref. [136] and [116]. In particular, a thorough "recipe" for maximizing SNR is provided by Ref. [116] in combination with Ref. [30]. However, that article's definition of the SNR is not convenient for optimizing the sensitivity of phase measurements, as is one aim of this thesis. Instead, we define here a single noise parameter κ, which characterizes how close an experimental measurement comes to the shot noise limit:

$$\kappa^{(N)} \equiv \mathrm{SNR}^{(N)}_{\mathrm{ideal}} / \mathrm{SNR}^{(N)}_{\mathrm{exp}} \tag{3.33}$$

$$= \left(\frac{\langle m^{(N)} \rangle}{\sqrt{\langle m^{(N)} \rangle}} \right) / \left(\frac{\langle m^{(N)} \rangle}{\mathrm{sd}(m^{(N)})_{\mathrm{exp}}} \right)$$

$$= \frac{\mathrm{sd}(m^{(N)})_{\mathrm{exp}}}{\sqrt{\langle m^{(N)} \rangle}}. \tag{3.34}$$

The superscript (N) refers to the number of photons constituting a coincidence, that is, $m^{(N)}$ denotes a measurement of m N-fold coincidence events. In particular, for $(N) = (1)$, $m^{(1)}$ represents simply a classical intensity measurement of single photon counts. $(N) = (2)$ represents two-fold coincidences resulting, for example, from SPDC photon pairs with $m^{(2)}$ calculated according to Eq. 3.32. The angled brackets in $\langle m^{(N)} \rangle$ denote this term as the expected value of $m^{(N)}$, that is, the "true" value one would obtain by averaging infinitely many ideal measurements of $m^{(N)}$. Lastly, $\mathrm{sd}(m^{(N)})_{\mathrm{exp}} \leq \mathrm{sd}(m^{(N)})_{\mathrm{ideal}}$ represents the standard deviation of an experimental measurement of $m^{(N)}$. Note that the substitution $\mathrm{sd}(m^{(N)})_{\mathrm{ideal}} = \sqrt{\langle m^{(N)} \rangle}$ is only correct when the N-fold multiphoton emission is governed by Poissonian statistics, as is the case for SPDC, but not for deterministic single photon emitters [29, 137–139]. As described in Sect. 4.3, knowledge of $\kappa^{(N)}$ combined with the interference visibility suffices to determine the sensitivity of a phase imaging experiment. For conciseness, in the remainder of this thesis "κ" will be assumed to denote "$\kappa^{(2)}$", while for the classical case "$\kappa^{(1)}$" will explicitly retain its superscript.

Here, we calculate κ (Eq. 3.34) from a series of experimental coincidence counting sets, in order to illustrate how SNR depends on different acquisition parameters. The SPDC near-field from our ∼811 nm EPS (see Sect. 2.3.4 and Chapter 5) was imaged using the Micro Photon Devices SPC3 camera, with pump laser power 0.62 mW. Acquiring a total number of $M \approx 4.9 \times 10^7$ binary intensity frames, using Eq. 3.17 we calculated the coincidence counts for $Q = 101$ sub-acquisitions (containing $M/Q \approx 4.8 \times 10^5$ frames each). These coincidence sub-acquisitions are post-processed using Eq. 3.31, and integrated across the whole camera sensor (i.e. $\mathrm{cc}_{\mathrm{F,sum}} \equiv \sum_{i,j} \mathrm{cc}_{\mathrm{F}}(i,j)$), yielding a one-dimensional array of 101 summed coincidence values. We evaluate Eq. 3.34 by estimating $\langle m^{(2)} \rangle$ and $\mathrm{sd}(m^{(N)})_{\mathrm{exp}}$ from the empirical $\mathrm{mean}(\mathrm{cc}_{\mathrm{F,sum}})$ and $\mathrm{sd}(\mathrm{cc}_{\mathrm{F,sum}})$, respectively (where $\mathrm{mean}(\mathrm{cc}_{\mathrm{F,sum}})$ and $\mathrm{sd}(\mathrm{cc}_{\mathrm{F,sum}})$ are calculated from the 101 sub-acquisitions).

In Fig. 3.15 and 3.16, solid dots of the same colour represent individual sub-acquisitions of the same measurement, with $\mathrm{mean}(\mathrm{cc}_{\mathrm{F,sum}})$ indicated by the dashed line. The corresponding experimental parameter and calculated κ value can be read in the label to the right of each sub-acquisition set. On the left, the blue "bell curves" depict the empirical coincidence count distributions, while the red curves show the theoretical distributions of ideal shot noise limited counts, given by a Gaussian around mean $\mathrm{mean}(\mathrm{cc}_{\mathrm{F,sum}})$ with standard deviation $\sqrt{\mathrm{mean}(\mathrm{cc}_{\mathrm{F,sum}})}$. Note, as always $\mathrm{mean}(\mathrm{cc}_{\mathrm{F,sum}}) \gg 0$, it is valid to approximate the shot noise (i.e. Poisson distribution) with a Gaussian. Moreover, note that the (horizontal) amplitude of each distribution is arbitrary, and was chosen simply to maximize readability. A high degree of overlap between the red and blue distributions therefore indicates close to ideal experimental noise, i.e. $\kappa \approx 1$, while the case where the blue curve is wider than the red one corresponds to $\kappa > 1$.

Figure 3.15 compares different filtering thresholds t (as used in Eq. 3.31), with the coincidence window $\tau_c = 10\,\mathrm{ns}$ in all cases. As expected intuitively, increasing the filtering threshold decreases the counts. However, κ does not significantly differ between coincidences that are very weakly ($t = 0.01$) and strongly ($t = 0.5$) filtered. That is, weak spatial filtering based on SPDC near-field correlations suffices to achieve near-optimal coincidence counting SNR, while strong spatial filtering serves only to improve spatial resolution (as seen in Fig. 3.14). Figure 3.16 compares different coincidence windows τ_c (with constant filtering threshold $t = 0.5$). We see that for larger τ_c, the experimental noise value becomes worse. This follows from Eq. 3.6, as for larger τ_c the relative probability of accidental coincidences (compared to real coincidences) increases, which adds noise [116].

Significantly, Fig. 3.15 and 3.16 also show that, by choosing the right acquisition parameters, it is possible to operate in the near-ideal regime ($\kappa \approx 1$). Therefore, in experiments of this thesis κ was always empirically optimized to yield close to optimal coincidence counting SNR.

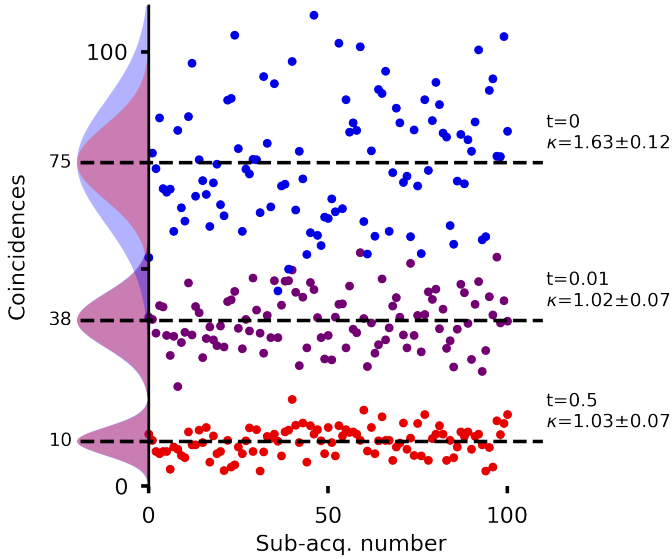

FIGURE 3.15: **Sub-acq. coincidences and κ, for different filtering thresholds.** t = 0, 0.01, 0.5 (top to bottom). $\tau_c = 10$ ns.

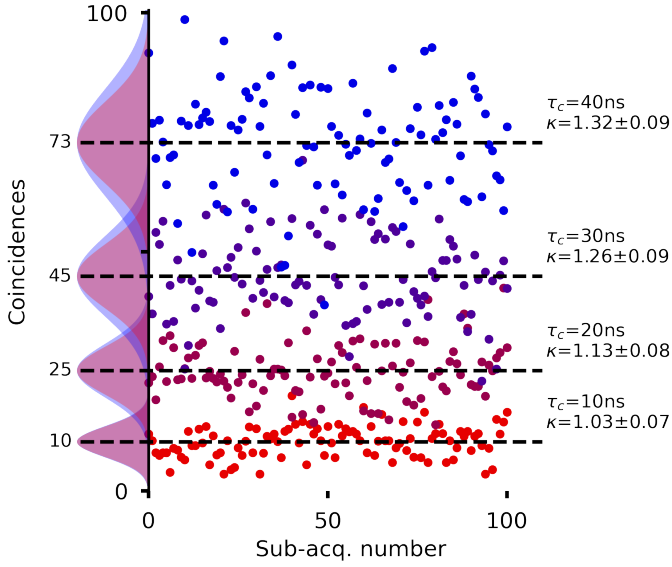

FIGURE 3.16: **Sub-acq. coincidences (filtered, $t = 0.5$) and κ, for different τ_c.** τ_c = 40 ns, 30 ns, 20 ns, 10 ns (top to bottom).

Chapter 4

Interferometry and Phase Measurements

The ability to measure the phase of light is hugely useful in many areas of science, ranging from fundamental experiments such as the detection of gravitational waves [140], to existing real-world applications such as label-free biomedical imaging [8]. In Chapter 2 we saw how a quantum mechanical description of the world allows for single and multi-photon interference, including with entangled states. This chapter will outline how such interference (detected using methods from Chapter 3 for example) can be used to *infer* the unknown phase of a sample.

This chapter introduces the requisite mathematical ingredients to describe the interference of light, in an abstracted *interferometer* setup, in the presence of a sample phase and a controllable offset phase. The formalism for classical and entangled N-photon N00N state interference is presented, as well as two methods to retrieve an unknown sample phase. Firstly, single-measurement phase retrieval simply inverts the sinusoidal dependence of an interferometer output detection signal on the sample phase. Secondly, phase-shifting digital holography (PSDH) uses several controlled offset-shifted detections to retrieve a sample phase, requiring less prior knowledge of the experimental system than in the single-measurement case. Lastly, this chapter presents a quantification of the experimental uncertainty in phase measurements, allowing therefore to compare relative sensitivities between different phase measurements. For a more extensive treatment of the topics introduced in this chapter, the interested reader is referred to Ref. [7] and [53].

4.1 Interferometry with classical light

The canonical phase measurement using classical light can be represented by the interferometer shown in Fig. 4.1. Here light enters into two arms: the "Probe", where it passes through a sample phase ϕ, and an offset phase α, and the "Ref", which is controlled such that the light in the two arms is perfectly in phase if ϕ and α are 0. Let the input electric fields in each arm be $\mathbf{E}_{\text{Probe}} = \mathbf{E}_{\text{Ref}} = (E_{\text{IN}}/\sqrt{2}) \exp\left(i(\omega t - \mathbf{k}\cdot\mathbf{r})\right)$, and the total intensity of the two input fields $I_{\text{IN}} =$

$2|E_{\text{IN}}/\sqrt{2}\exp\left(i(\omega t - \mathbf{k}\cdot\mathbf{r})\right)|^2$. Note that $\mathbf{E}_{\text{Probe}}, \mathbf{E}_{\text{Ref}} \in \mathbb{C}$, while $(E_{\text{IN}}/\sqrt{2}) \in \mathbb{R}$ is the electric field amplitude. In the phase factor, ω is the photon frequency and t the time, while $\mathbf{k}$ and $\mathbf{r}$ represent the wave vector and spatial coordinate, respectively [141].

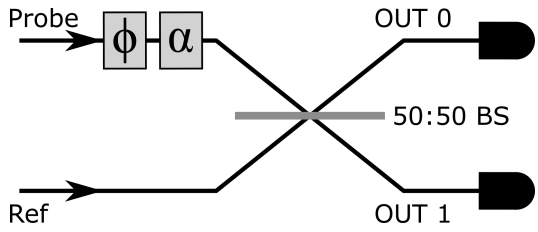

FIGURE 4.1: **Classical phase measurement.** Interfering a probe beam, which passes through sample phase ϕ and controlled offset phase α, with a reference beam at a 50:50 beam splitter (BS) allows detecting output intensities that depend on $\phi + \alpha$.

In Fig. 4.1, the two interfering arms have single spatial modes; therefore the dependence on spatial coordinate $\mathbf{r}$ reduces to only the propagation (longitudinal) direction z, and $\mathbf{k}$ can be simplified to the scalar quantity $k_z = 2\pi/\lambda$, where λ is the photon wavelength. After propagating a distance z' from the inputs to the beam splitter, the two electric fields evolve to $\mathbf{E}_{\text{Probe}} = (E_{\text{IN}}/\sqrt{2})\exp\left(i(\omega t - k_z z' + \phi + \alpha)\right)$ and $\mathbf{E}_{\text{Ref}} = (E_{\text{IN}}/\sqrt{2})\exp\left(i(\omega t - k_z z')\right)$. They then combine at the beam splitter to give output fields (at "OUT 0" and "OUT 1" as indicated in Fig. 4.1):

$$\mathbf{E}_{\text{OUT0}} = \frac{E_{\text{IN}}}{\sqrt{2}}\left(\frac{e^{i(\omega t - k_z z'')}(1 + e^{i(\phi+\alpha)})}{\sqrt{2}}\right), \tag{4.1}$$

$$\mathbf{E}_{\text{OUT1}} = \frac{E_{\text{IN}}}{\sqrt{2}}\left(\frac{e^{i(\omega t - k_z z'')}(1 - e^{i(\phi+\alpha)})}{\sqrt{2}}\right), \tag{4.2}$$

where z'' takes into account the additional propagation distance to the detectors. Therefore the detected intensity is found by taking the modulus-squared of $\mathbf{E}_{\text{OUT0}}$ and $\mathbf{E}_{\text{OUT1}}$:

$$I^{(1)}_{\text{OUT0}} = \left|\left(\frac{E_{\text{IN}}e^{i(\omega t - k_z z'')}}{2}\right)\left(1 + e^{i(\phi+\alpha)}\right)\right|^2 = I^{(1)}_{\text{IN}}\left(\frac{1 + \cos(\phi+\alpha)}{2}\right), \tag{4.3}$$

$$I^{(1)}_{\text{OUT1}} = \left|\left(\frac{E_{\text{IN}}e^{i(\omega t - k_z z'')}}{2}\right)\left(1 - e^{i(\phi+\alpha)}\right)\right|^2 = I^{(1)}_{\text{IN}}\left(\frac{1 - \cos(\phi+\alpha)}{2}\right). \tag{4.4}$$

That is, the measured intensity at the output only depends on the input intensity and the phase difference $(\phi + \alpha)$, while the common phase term $(\omega t - k_z z'')$ can be neglected. Here, the "(1)" superscript indicates explicitly that these intensities results from single-photon (i.e. classical) interference, as opposed to multi-photon effects that will be treated in Sect. 4.2.

Any real measurement will involve imperfections. Detector noise or stray light will result in a background intensity offset $I^{(1)}_{\text{Bkg}}$, and a non-50/50 beam splitter will lead to lower classical interference visibility $\mathcal{V}^{(1)} \leq 1$. Moreover, optical and detection efficiencies are usually below unity. Therefore, taking these factors into account, we can write a slightly more general version of Eq. 4.3 and 4.4:

$$I^{(1)}_{\text{OUT0}}(\phi,\alpha) = I^{(1)}_{\text{Bkg}} + \eta^{(1)}_0 I^{(1)}_{\text{IN}} \left(\frac{1 + \mathcal{V}^{(1)} \cos(\phi + \alpha)}{2} \right), \tag{4.5}$$

$$I^{(1)}_{\text{OUT1}}(\phi,\alpha) = I^{(1)}_{\text{Bkg}} + \eta^{(1)}_1 I^{(1)}_{\text{IN}} \left(\frac{1 - \mathcal{V}^{(1)} \cos(\phi + \alpha)}{2} \right). \tag{4.6}$$

Here the dependence of the measured intensities on phase factors ϕ and α is written explicitly on the left-hand side. The total efficiency for output mode 0 (1) is denoted by $\eta^{(1)}_0$ ($\eta^{(1)}_1$), which includes both optical and detection efficiency as described in Sect. 3.1. The intensities $I^{(1)}$ can be interpreted as quantifying the number of single photons.

In order to realize light fields in the "Probe" and "Ref" arms with equal amplitudes and in phase with each other, in practice it is often easiest to use the Mach-Zehnder Interferometer (MZI) setup shown in Fig. 4.2, where a single input is split by a beam splitter to the two interferometer arms [7].

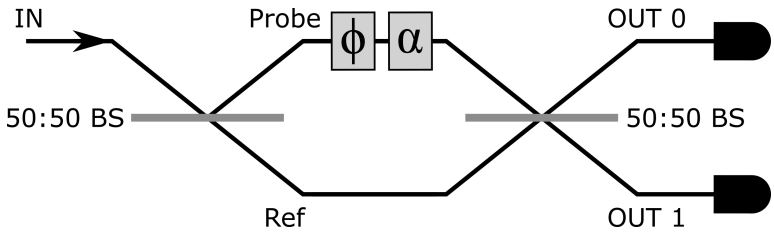

FIGURE 4.2: **Mach-Zehnder Interferometer.** Generating Probe and Ref beams that are in phase and have equal amplitude is straightforward when splitting a single input with a 50:50 beam splitter (BS).

4.1.1 Phase retrieval using classical light

The expressions Eq. 4.5 and 4.6 are interesting because they allow inferring the sample phase ϕ, which in turn yields information about the physical characteristics of a sample that give rise to a phase difference. Clearly, from looking at Eq. 4.5 and 4.6, if $I^{(1)}_{\mathrm{Bkg}}$, $I^{(1)}_{\mathrm{IN}}$, $\mathcal{V}^{(1)}$, $\eta^{(1)}_0$, and α are all known to high precision, it is possible to calculate ϕ simply by inverting the expression for $I^{(1)}_{\mathrm{OUT0}}(\phi,\alpha)$ (Eq. 4.5):

$$\hat{\phi}^{(1)}_0 = \arccos\left[\frac{1}{\mathcal{V}^{(1)}}\left(\frac{2(I^{(1)}_{\mathrm{OUT0}}(\phi,\alpha) - I^{(1)}_{\mathrm{Bkg}})}{\eta^{(1)}_0 I^{(1)}_{\mathrm{IN}}} - 1\right)\right] - \alpha, \tag{4.7}$$

with the circumflex, "0" subscript and "(1)" superscript on $\hat{\phi}^{(1)}_0$ indicating that this is an experimental *estimate* of ϕ, from a classical (single-photon) intensity measurement at output 0. This circumflex notation serves to explicitly distinguish an experimentally retrieved value $\hat{\phi}$ from the "true" sample phase ϕ. That is, it is impossible for an experimenter to obtain perfectly precise knowledge of the actual value of ϕ itself. On the other hand, a good measurement is able to provide an estimate of ϕ, that approaches the true value for increasing experimental precision. The estimate $\hat{\phi}$ always has an experimental *error* $\mathrm{sd}(\hat{\phi}) > 0$, whose magnitude is inversely proportional to the *sensitivity* of our phase measurement. Refer to Sect. 4.3 for further detail.

While Eq. 4.7 allows inferring sample phase ϕ using a single experimental measurement, often it is unfeasible or experimentally difficult to accurate know $I^{(1)}_{\mathrm{Bkg}}$, $I^{(1)}_{\mathrm{IN}}$, and $\mathcal{V}^{(1)}$. In such cases, ϕ can nonetheless be retrieved accurately using a technique known as phase-shifting digital holography (PSDH), which only requires the ability to control the offset phase α [6, 7, 142]. The most commonly used variant of PSDH requires setting the offset phase to four different values $\alpha = \{0, \pi/2, \pi, 3\pi/2\}$, acquiring therefore four separate intensity measurements $I^{(1)}_{\mathrm{OUT}}(\phi,\alpha)$. This four-step PSDH method will be used in this thesis, and is thus described in the following. However, note that if an experimental setup does not permit setting α precisely to the required integer multiples of $\pi/2$, an alternative variant of PSDH works by scanning α semi-continuously over many steps [143].

Returning to the interferometer of Fig. 4.1 and 4.2, we can explicitly write out the four measurement terms at the "0" output, with $\alpha = \{0, \pi/2, \pi, 3\pi/2\}$:

$$I^{(1)}_{\text{OUT0}}(\phi, 0) = I^{(1)}_{\text{Bkg}} + \eta^{(1)}_0 I^{(1)}_{\text{IN}} \left(\frac{1 + \mathcal{V}^{(1)} \cos(\phi)}{2} \right), \tag{4.8}$$

$$\begin{aligned} I^{(1)}_{\text{OUT0}}(\phi, \frac{\pi}{2}) &= I^{(1)}_{\text{Bkg}} + \eta^{(1)}_0 I^{(1)}_{\text{IN}} \left(\frac{1 + \mathcal{V}^{(1)} \cos(\phi + \pi/2)}{2} \right) \\ &= I^{(1)}_{\text{Bkg}} + \eta^{(1)}_0 I^{(1)}_{\text{IN}} \left(\frac{1 - \mathcal{V}^{(1)} \sin(\phi)}{2} \right), \end{aligned} \tag{4.9}$$

$$\begin{aligned} I^{(1)}_{\text{OUT0}}(\phi, \pi) &= I^{(1)}_{\text{Bkg}} + \eta^{(1)}_0 I^{(1)}_{\text{IN}} \left(\frac{1 + \mathcal{V}^{(1)} \cos(\phi + \pi)}{2} \right) \\ &= I^{(1)}_{\text{Bkg}} + \eta^{(1)}_0 I^{(1)}_{\text{IN}} \left(\frac{1 - \mathcal{V}^{(1)} \cos(\phi)}{2} \right), \end{aligned} \tag{4.10}$$

$$\begin{aligned} I^{(1)}_{\text{OUT0}}(\phi, \frac{3\pi}{2}) &= I^{(1)}_{\text{Bkg}} + \eta^{(1)}_0 I^{(1)}_{\text{IN}} \left(\frac{1 + \mathcal{V}^{(1)} \cos(\phi + 3\pi/2)}{2} \right) \\ &= I^{(1)}_{\text{Bkg}} + \eta^{(1)}_0 I^{(1)}_{\text{IN}} \left(\frac{1 + \mathcal{V}^{(1)} \sin(\phi)}{2} \right). \end{aligned} \tag{4.11}$$

Using the trigonometric identity $\tan x = \sin x / \cos x$, we see that Eq. 4.8-4.11 can be combined in order to calculate the sample phase [7]:

$$\hat{\phi}^{(1)}_0 = \tan^{-1} \left[\frac{I^{(1)}_{\text{OUT0}}(\phi, \frac{\pi}{2}) - I^{(1)}_{\text{OUT0}}(\phi, \frac{3\pi}{2})}{I^{(1)}_{\text{OUT0}}(\phi, \pi) - I^{(1)}_{\text{OUT0}}(\phi, 0)} \right]. \tag{4.12}$$

Here we have, therefore, an expression estimating the sample phase ϕ that does not rely on any accurate knowledge of $I^{(1)}_{\text{Bkg}}$, $I^{(1)}_{\text{IN}}$, $\eta^{(1)}$, or $\mathcal{V}^{(1)}$. The only prerequisite for Eq. 4.12 is that $I^{(1)}_{\text{Bkg}}$, $I^{(1)}_{\text{IN}}$, and $\mathcal{V}^{(1)}$ remain constant across all four constituent PSDH measurements, which is an experimentally straightforward requirement.

Eq. 4.7 and 4.12 provide two different means to estimate of ϕ, using the measurements at output 0. Similarly, the estimation of ϕ from intensity measurement at output 1 is written as $\hat{\phi}^{(1)}_1$, and is found by inverting Eq. 4.6 (analogous to Eq. 4.7) or through PSDH (analogous to Eq. 4.12). The final experimental estimate of the sample phase ϕ is found by combining all measurements according to

$$\hat{\phi}^{(1)} = \frac{\hat{\phi}^{(1)}_0 + \hat{\phi}^{(1)}_1}{2}. \tag{4.13}$$

4.2 Interferometry with N00N states

An extensive body of work in the scientific literature studies the interesting fact that using multi-photon entangled N00N states enables so-called super-sensitive phase measurements, that is, phase measurements with higher sensitivity than possible using classical light [18, 19, 37, 38, 55, 144]. This section will present a brief overview of quantum-enabled phase measurements using N00N states, analogously to the classical light case introduced in Sect. 4.1. Sect. 4.3 then discusses the sensitivity of classical and quantum phase measurements, and describes quantitatively what is meant by "super-sensitivity".

Fig. 4.3 shows the "quantum" analogue of the canonical phase measurement setup Fig. 4.1. Instead of describing the light in the system in terms of classical electromagnetic fields, we now use the formalism introduced in Chapter 2, in particular, Sect. 2.1 and 2.2.2. For a N-photon N00N state, the input is therefore $(|N,0\rangle_{\text{Ref,Probe}} + |0,N\rangle_{\text{Ref,Probe}})/\sqrt{2}$, that is, the coherent superposition of N photons all in the Ref mode or the Probe mode. The yellow "∞" in Fig. 4.3 represents the entanglement between the two modes. After the Probe light passes through ϕ and α, the state immediately before the beam splitter (BS) can be written as

$$|\Psi\rangle = \frac{|N,0\rangle_{\text{Ref,Probe}} + e^{iN(\phi+\alpha)}\,|0,N\rangle_{\text{Ref,Probe}}}{\sqrt{2}}. \tag{4.14}$$

Note the similarity between Eq. 4.14 and Eq. 2.34, with horizontal (vertical) po-

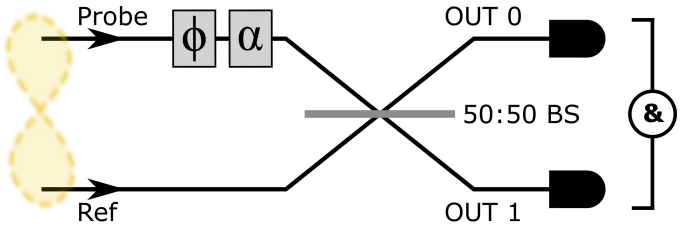

FIGURE 4.3: **Quantum phase measurement.** Interfering N entangled photons, with all N photons either acquiring sample phase ϕ and controlled offset phase α, or passing through reference arm.

larization modes in the latter corresponding to Ref (Probe) modes in the former expression. After passing through the beam splitter, the Probe and Ref modes are projected into output 0 and 1 modes according to

$$|1\rangle_{\text{OUT0}} = \frac{|1\rangle_{\text{Ref}} + |1\rangle_{\text{Probe}}}{\sqrt{2}}, \tag{4.15}$$

$$|1\rangle_{\text{OUT1}} = \frac{|1\rangle_{\text{Ref}} - |1\rangle_{\text{Probe}}}{\sqrt{2}}, \tag{4.16}$$

With $|1\rangle_i$ representing a single-photon Fock state in mode i (following the notation convention of Sect. 2.2). Again, note the similarity to Eq. 2.26 and 2.27. Expressing

$|\Psi\rangle$ (Eq. 4.14) in terms of the two output modes results in the following:

$$|\Psi\rangle \rightarrow \frac{1}{\sqrt{2}}\left[\left(\frac{|1\rangle_{\text{OUT0}}+|1\rangle_{\text{OUT1}}}{\sqrt{2}}\right)^N + e^{iN(\phi+\alpha)}\left(\frac{|1\rangle_{\text{OUT0}}-|1\rangle_{\text{OUT1}}}{\sqrt{2}}\right)^N\right]$$
$$\rightarrow \frac{1}{2^{(N+1)/2}}\left[\sum_{K=0}^{N}\sqrt{\binom{N}{k}}\,|N-k,k\rangle_{\text{OUT0,OUT1}}\left(1+(-1)^k e^{iN(\phi+\alpha)}\right)\right], \quad (4.17)$$

where $\binom{N}{k}$ represents the k^{th} binomial coefficient for power N.

Unlike for the classical case, where there are only two available output intensity measurements ($I^{(1)}_{\text{OUT0}}$ and $I^{(1)}_{\text{OUT1}}$, i.e. Eq. 4.5 and 4.6), for two-mode interference with an N-photon N00N state we have to take into account $N+1$ possible measurement outcomes. These correspond to the projections into the $|N-k,k\rangle_{\text{OUT0,OUT1}}$ bases, for k going from 0 to N. To be explicit, we can measure the outcome of N photons in output 0 and 0 photons in output 1, $N-1$ photons in 0 and 1 photon in 1, $N-1$ photons in 0 and 2 photon in 1, and so on, up to 0 photons in output 0 and all N photons in output 1. Experimentally, this requires the ability to measure coincidences between photon-number-resolving detectors, that is, the ability to simultaneously count $N-k$ photons at the output 0 detector, and k photons at the output 1 detector. This is represented by the "&" symbol in Fig. 4.3. The probability to measure $|\Psi\rangle$ (Eq. 4.14) with a $|N-k,k\rangle_{\text{OUT0,OUT1}}$ output is given by:

$$|\,\langle N-k,k|_{\text{OUT1,OUT0}}\,|\Psi(\phi,\alpha)\rangle\,|^2 = \frac{1}{2^N}\binom{N}{k}\left(1+(-1)^k\cos\left(N(\phi+\alpha)\right)\right). \quad (4.18)$$

In order to relate the probability Eq. 4.18 to the number of detected coincidences, analogously to the classical input intensity $I^{(1)}_{\text{IN}}$, we can define the multi-photon input "intensity" $I^{(N)}_{\text{IN}}$. This quantity $I^{(N)}_{\text{IN}}$ can be interpreted to mean the number of identical copies of the N-photon N00N state (Eq. 4.14) that are sent through the interferometer setup (Fig. 4.3). That is, the total number of single photons used in a measurement with $I^{(N)}_{\text{IN}}$ entangled states is simply $NI^{(N)}_{\text{IN}}$, as each N00N state consists of N single photons. This then allows writing the N-fold coincidence measurement version of Eq. 4.5 and 4.6:

$$I^{(N)}_{(N-k),k}(\phi,\alpha) = I^{(N)}_{\text{Bkg}} + \eta^{(N)}_{(N-k),k} I^{(N)}_{\text{IN}}\left[\frac{1}{2^N}\binom{N}{k}\left(1+(-1)^k\mathcal{V}^{(N)}\cos\left(N(\phi+\alpha)\right)\right)\right]$$
$$\equiv I^{(N)}_{\text{Bkg}} + W_{N,k}\left(1+(-1)^k\mathcal{V}^{(N)}\cos\left(N(\phi+\alpha)\right)\right), \quad (4.19)$$

where $I^{(N)}_{(N-k),k}$ denotes the number of recorded coincidence events with $N-k$ photons detected at output 0, and k photons detected at output 1. Analogous to Eq. 4.5 and 4.6, Eq. 4.19 takes into account some experimental imperfections, with $I^{(N)}_{\text{Bkg}}$ representing the background (N-fold) coincidence detections, and $\mathcal{V}^{(N)} \leq 1$

representing the (N-fold) interference visibility. The N-fold efficiency is represented by $\eta^{(N)}_{(N-k),k}$, that is, the combined optical and detection efficiency to measure an N-fold coincidence with $N-k$ and k photon detections in output mode 0 and 1, respectively. In the second line, we define $W_{N,k} \equiv \eta^{(N)}_{(N-k),k} I^{(N)}_{\mathrm{IN}} \binom{N}{k} / 2^N$ for conciseness in notation. Note that for $N = 1$, Eq. 4.19 reduces to the classical case (Eq. 4.5 and 4.6).

There are two major difficulties in the experimental realization of Eq. 4.19 for arbitrarily high N. The first is the generation of the N-photon N00N state (Eq. 2.34 or 4.14). As outlined in Chapter 2, producing the $N = 2$ N00N state is feasible. However, thus far the only experiments generating so-called high-N00N states with with $N > 2$, have produced mixtures of N00N states with a range of relatively small $N \lesssim 10$, rather than a pure state [10, 145, 146]. The second difficulty lies in detecting N-fold coincidences: as in Chapter 3, the N-fold efficiency $\eta^{(N)}$ can usually just be expressed as the N^{th} power of the single photon efficiency $\eta^{(1)}$, that is, $\eta^{(N)} = (\eta^{(1)})^N$ [147]. Therefore, for $\eta^{(1)} < 1$, $\eta^{(N)}$ rapidly shrinks to zero as N increases, unless great care is taken to optimize the efficiency (i.e. ensuring $\eta^{(1)} \approx 1$).

4.2.1 Phase retrieval using N00N states

Analogous to Eq. 4.7, we can invert Eq. 4.19 to find the following expression for the sample phase ϕ:

$$\hat{\phi}^{(N)}_{(N-k),k} = \frac{1}{N} \arccos \left[\frac{(-1)^k}{\mathcal{V}^{(N)}} \left(\frac{1}{W_{N,k}} \left(I^{(N)}_{(N-k),k}(\phi, \alpha) - I^{(N)}_{\mathrm{Bkg}} \right) - 1 \right) \right] - \alpha, \quad (4.20)$$

where $\hat{\phi}^{(N)}_{(N-k),k}$ represents the experimental estimate of the sample phase ϕ, retrieved from measurements of N-fold coincidences with $N-k$ photons detected at output 0, and k photons detected at output 1. Similar to Eq. 4.7, evaluating Eq. 4.20 requires accurate knowledge of $I^{(N)}_{\mathrm{Bkg}}$, $I^{(N)}_{\mathrm{IN}}$, $\mathcal{V}^{(N)}$, $\eta^{(N)}_{(N-k),k}$, and α. When this accurate knowledge is experimentally unfeasible or difficult to obtain, we can again use PSDH, acquiring four separate $I^{(N)}_{(N-k),k}(\phi, \alpha)$ coincidence measurements with controlled offsets $\alpha = \{0, \pi/(2N), \pi/N, 3\pi/(2N)\}$. Analogous to the argument from Eq. 4.8-4.12, we can therefore write an expression for the sample phase in terms of the four $I^{(N)}_{(N-k),k}(\phi, \alpha)$ measurements:

$$\hat{\phi}^{(N)}_{(N-k),k} = \frac{1}{N} \tan^{-1} \left[\frac{I^{(N)}_{(N-k),k}(\phi, \frac{\pi}{2N}) - I^{(N)}_{(N-k),k}(\phi, \frac{3\pi}{2N})}{I^{(N)}_{(N-k),k}(\phi, \frac{\pi}{N}) - I^{(N)}_{(N-k),k}(\phi, 0)} \right]. \quad (4.21)$$

That is, Eq. 4.21 allows retrieving the sample phase ϕ, with the only prerequisites that α can be experimentally controlled to high precision, and that $I^{(N)}_{\mathrm{Bkg}}$, $I^{(N)}_{\mathrm{IN}}$, $\eta^{(N)}_{(N-k),k}$, and $\mathcal{V}^{(N)}$ remain constant during all four acquisitions.

Therefore, using Eq. 4.20 or 4.21, we are able to obtain $N+1$ different experimental estimates of the sample phase ϕ, corresponding to the measurements in all the $|N-k,k\rangle_{\mathrm{OUT0,OUT1}}$ bases (i.e. $N-k$ and k detections at output 0 and 1, respectively). Notice that, from Eq. 4.19, as long as the background is negligible ($I^{(N)} \ll W_{N,k}$) each $I^{(N)}_{(N-k),k}$ term is scaled by $W_{N,k}$. That is, of $I^{(N)}_{\mathrm{IN}}$ input states, $\eta^{(N)}_{(N-k),k} I^{(N)}_{\mathrm{IN}} \binom{N}{k}/2^N$ of these contribute to the $I^{(N)}_{(N-k),k}$ measurement. Each $\hat{\phi}^{(N)}_{(N-k),k}$ phase estimate therefore used a $\binom{N}{k}/2^N$ proportion of the total number of input states, and should thus receive the corresponding weighting in the final phase estimate using all detections:

$$\hat{\phi}^{(N)} = \sum_{k=0}^{N} \frac{1}{2^N} \binom{N}{k} \hat{\phi}^{(N)}_{(N-k),k}. \tag{4.22}$$

Note that by substituting $N=1$ we obtain the classical case Eq. 4.13.

4.3 Sensitivity of phase measurement

As mentioned already in Sect. 4.1, the circumflex on $\hat{\phi}^{(1)}$ and $\hat{\phi}^{(N)}$ indicate that these are experimental *estimates* of the true sample phase ϕ. These estimates have non-zero *uncertainties* $\mathrm{sd}(\hat{\phi}^{(1)})$ and $\mathrm{sd}(\hat{\phi}^{(N)})$, that is, the standard deviation of any experimental measurement of ϕ will approach (but never reach) 0 for ever more precise measurements. The *sensitivity* of a phase measurement is inversely proportional to this uncertainty.

It is well known that $\mathrm{sd}(\hat{\phi}^{(1)}) \propto 1/\sqrt{I^{(1)}_{\mathrm{IN}}}$. Indeed, for the best possible classical phase measurement, at the so-called standard quantum limit (SQL), this relation becomes an equality $\mathrm{sd}(\hat{\phi}^{(1)}_{\mathrm{SQL}}) = 1/\sqrt{I^{(1)}_{\mathrm{IN}}}$ [53]. Therefore, using only classical resources, a phase measurement can be performed with arbitrarily small uncertainty simply by increasing the illumination intensity $I^{(1)}_{\mathrm{IN}}$. However, as discussed in Chapter 1, in many cases there is an upper limit on the number of photons that can be used. The reason for this is that illuminating with too many photons can optically modify or even damage a sample, as well as saturate detectors [18, 20, 144, 148–152]. This motivates using quantum resources (such as N-photon N00N states) for phase measurements, due to the well known fact that it is possible to satisfy the condition $\mathrm{sd}(\hat{\phi}^{(N)}) < \mathrm{sd}(\hat{\phi}^{(1)})$ for the *same* number of photons used [53]. This effect is known as super-sensitivity.

In this section we will follow the derivation of $\mathrm{sd}(\hat{\phi}^{(N)})$, similarly to Ref. [153] and [38], based also on our publication Ref. [144]. We will see here the theory of some quantum metrology results using N-photon N00N states, in the presence of experimental imperfections that are relevant to the experiments described in later chapters of this thesis. For a more general treatment of measurement sensitivity using quantum resources, the interested reader is referred to Ref. [53].

This section makes extensive use of the error propagation formula, [154]:

$$\mathrm{sd}(f) = \sqrt{\sum_j \left[\left(\frac{\partial f}{\partial x_j} \right)^2 \mathrm{sd}(x_j)^2 \right]} \tag{4.23}$$

where in general f is a function that depends on variables x_j. In the case of finding an expression for $\mathrm{sd}(\hat{\phi}^{(N)})$, the error propagation formula must be applied twice. In the first instance, f corresponds to $\hat{\phi}^{(N)}$, which is a function of variables $\hat{\phi}^{(N)}_{(N-k),k}$, according to Eq. 4.22. This requires knowing $\mathrm{sd}(\hat{\phi}^{(N)}_{(N-k),k})$, and therefore in the second instance f corresponds to $\hat{\phi}^{(N)}_{(N-k),k}$, and x_j are the $I^{(N)}_{(N-k),k}$ measurements. Therefore, to find $\mathrm{sd}(\hat{\phi}^{(N)})$, explicitly Eq. 4.23 becomes:

$$\mathrm{sd}(\hat{\phi}^{(N)}) = \sqrt{\sum_{k=0}^{N} \left[\left(\frac{\partial \hat{\phi}^{(N)}}{\partial \hat{\phi}^{(N)}_{(N-k),k}} \right)^2 \left(\mathrm{sd}(\hat{\phi}^{(N)}_{(N-k),k}) \right)^2 \right]} \tag{4.24}$$

$$= \sqrt{\sum_{k=0}^{N} \left[\left(\frac{\partial \hat{\phi}^{(N)}}{\partial \hat{\phi}^{(N)}_{(N-k),k}} \right)^2 \left(\sum_j \left(\frac{\partial \hat{\phi}^{(N)}_{(N-k),k}}{\partial I^{(N)}_{(N-k),k}(\phi, \alpha_j)} \right)^2 \mathrm{sd}\left(I^{(N)}_{(N-k),k}(\phi, \alpha_j) \right)^2 \right) \right]}, \tag{4.25}$$

where the partial derivative term on the right of Eq. 4.25 is calculated from Eq. 4.20 or Eq. 4.21, depending on the type of phase retrieval. In case $\hat{\phi}^{(N)}_{(N-k),k}$ is retrieved using PSDH (Eq. 4.21), the α_j terms correspond to $\{0, \pi/(2N), \pi/N, 3\pi/(2N)\}$ (see Sect. 4.2.1).

Evaluating Eq. 4.25 requires $\mathrm{sd}(I^{(N)}_{(N-k),k}(\phi, \alpha))$, which is quantified by the measurement noise parameter $\kappa^{(N)} \geq 1$ introduced in Sect. 3.5:

$$\mathrm{sd}\left(I^{(N)}_{(N-k),k}(\phi, \alpha) \right) = \kappa^{(N)} \sqrt{I^{(N)}_{(N-k),k}(\phi, \alpha)} \tag{4.26}$$

$$\approx \kappa^{(N)} \sqrt{W_{N,k} \left(1 + (-1)^k \mathcal{V}^{(N)} \cos\left(N(\phi + \alpha) \right) \right)}. \tag{4.27}$$

Here the approximation in the second line is valid if $I^{(N)}_{\mathrm{Bkg}} \ll W_{N,k}$, that is, if the background in Eq. 4.19 is negligible compared to the detections originating from the interfering Ref and Probe beams. In the experiments presented in this thesis, this approximation was usually valid, as stray light could be reduced through optical isolation and filtering, while detector noise was far lower than the entangled photon detection rate.

4.3.1 Sensitivity of single-measurement phase retrieval

In order to find $\mathrm{sd}(\hat{\phi}^{(N)}_{(N-k),k})$, where $\hat{\phi}^{(N)}_{(N-k),k}$ is calculated according to Eq. 4.20, we have to apply the error propagation formula Eq. 4.23. In this case there is only one partial derivative term ($\partial f/\partial x_j$), which corresponds to $\partial\hat{\phi}^{(N)}_{(N-k),k}/\partial I^{(N)}_{(N-k),k}$. However, in order to simplify the calculation, we can make use of a mathematical trick from Ref. [38, 153], inverting the partial derivative to obtain the following:

$$\mathrm{sd}(\hat{\phi}^{(N)}_{(N-k),k}) = \sqrt{\left[\frac{1}{\partial I^{(N)}_{(N-k),k}/\partial\phi}\right]^2 \left[\mathrm{sd}\left(I^{(N)}_{(N-k),k}(\phi,\alpha)\right)\right]^2}. \tag{4.28}$$

That is, rather than having to calculate $\partial\hat{\phi}^{(N)}_{(N-k),k}/\partial I^{(N)}_{(N-k),k}$, we use the explicit dependence of $I^{(N)}_{(N-k),k}$ on ϕ (Eq. 4.19) to find the much simpler partial derivative $\partial I^{(N)}_{(N-k),k}/\partial\phi$, which equals

$$\frac{\partial I^{(N)}_{(N-k),k}}{\partial\phi} = W_{N,k}(-1)^{k+1}\mathcal{V}^{(N)}N\sin\left(N(\phi+\alpha)\right). \tag{4.29}$$

Then, substituting Eq. 4.27 and 4.29 into Eq. 4.28 yields

$$\mathrm{sd}(\hat{\phi}^{(N)}_{(N-k),k}) = \frac{\kappa^{(N)}}{|\mathcal{V}^{(N)}N\sin\left(N(\phi+\alpha)\right)|}\sqrt{\frac{1+(-1)^k\mathcal{V}^{(N)}\cos\left(N(\phi+\alpha)\right)}{W_{N,k}}} \tag{4.30}$$

Lastly, $\mathrm{sd}(\hat{\phi}^{(N)})$ can be found by substituting Eq. 4.22 and 4.30 into Eq. 4.24:

$$\mathrm{sd}(\hat{\phi}^{(N)}) = \frac{\kappa^{(N)}}{|\mathcal{V}^{(N)}N\sin\left(N(\phi+\alpha)\right)|}\sqrt{\sum_{k=0}^{N}\frac{\binom{N}{k}}{2^N}\left(\frac{1+(-1)^k\mathcal{V}^{(N)}\cos\left(N(\phi+\alpha)\right)}{\eta^{(N)}_{(N-k),k}I^{(N)}_{\mathrm{IN}}}\right)}. \tag{4.31}$$

The term inside the square root reduces to the following:

$$\begin{aligned}\sum_{k=0}^{N}\frac{\binom{N}{k}}{2^N}\left(\frac{1+(-1)^k\mathcal{V}^{(N)}\cos\Theta}{\eta^{(N)}_{(N-k),k}I^{(N)}_{\mathrm{IN}}}\right) &= \frac{1+\mathcal{V}^{(N)}\cos\Theta+1-\mathcal{V}^{(N)}\cos\Theta}{2\eta^{(N)}I^{(N)}_{\mathrm{IN}}}\\ &= \frac{1}{\eta^{(N)}I^{(N)}_{\mathrm{IN}}},\end{aligned} \tag{4.32}$$

where $\Theta \equiv N(\phi+\alpha)$, and we make use of the fact that $\sum_{k=0,k\text{ even}}^{N}\binom{N}{k} = \sum_{k=1,k\text{ odd}}^{N}\binom{N}{k} = 2^{N-1}$, as well as the simplifying assumption that $\eta^{(N)}_{(N-k),k} = \eta^{(N)}$ is the same for

all $|N-k,k\rangle_{\text{OUT0,OUT1}}$ measurement bases. Therefore Eq. 4.31 is equal to

$$\text{sd}(\hat{\phi}^{(N)}) = \frac{\kappa^{(N)}}{\mathcal{V}^{(N)} N \sqrt{\eta^{(N)} I_{\text{IN}}^{(N)}} |\sin(N(\phi+\alpha))|}. \tag{4.33}$$

If we want to compare the uncertainty of the N-photon N00N state-retrieved phase estimate $\text{sd}(\hat{\phi}^{(N)})$ to a classical measurement with an equal number of photons, recall that each of the $I_{\text{IN}}^{(N)}$ input states consists of N single photons. Therefore, if we let M be the total number of single photons used (i.e. in the classical case $M = I_{\text{IN}}^{(1)}$), we make the substitution $I_{\text{IN}}^{(N)} = M/N$ and Eq. 4.33 becomes:

$$\text{sd}(\hat{\phi}^{(N)}) = \frac{\kappa^{(N)}}{\mathcal{V}^{(N)} \sqrt{\eta^{(N)} N M} |\sin(N(\phi+\alpha))|}. \tag{4.34}$$

Note that Eq. 4.34 depends on $\phi+\alpha$, and is minimized whenever $|\sin(N(\phi+\alpha))| = 1$, that is, whenever $N(\phi+\alpha) = (m-1/2)\pi$, with $m \in \mathbb{Z}$. We can define the phase sensitivity enhancement $\mathcal{S}^{(N)}$ provided by a N-photon N00N state:

$$\mathcal{S}^{(N)} = \frac{1/\text{sd}(\hat{\phi}^{(N)})}{1/\min(\text{sd}(\hat{\phi}^{(1)}))}. \tag{4.35}$$

That is, a N-photon N00N state phase measurement improves sensitivity compared to an ideal classical phase measurement if $\mathcal{S}^{(N)} > 1$. From Eq. 4.34 we see that, in the case of non-ideal experimental parameters ($\kappa^{(N)} > 1$, $\mathcal{V}^{(N)} < 1$, $\eta^{(N)} = (\eta^{(1)})^N < 1$), we obtain $\mathcal{S}^{(N)} > 1$ by picking α to minimize $\text{sd}(\hat{\phi}^{(N)})$, and as long as the condition $(\eta^{(1)})^N N (\mathcal{V}^{(N)}/\kappa^{(N)})^2 > 1$ is satisfied. This is illustrated in Fig. 4.4, which plots $\mathcal{S}^{(N)}$ over a 2π phase range (i.e. $\phi+\alpha$), varying $\kappa^{(N)}$, $\mathcal{V}^{(N)}$and $\eta^{(1)}$, for N00N states with $N = 1,2,3$. Note that $N = 1$ of course corresponds to the classical case (with non-ideal $\kappa^{(1)}$, $\mathcal{V}^{(1)}$and $\eta^{(1)}$ parameters as specified in the figure).

The regime where $\mathcal{S}^{(N)} > 1$ is referred to as phase *super-sensitivity* [53, 105]. With ideal experimental parameters $\kappa^{(N)} = 1$, $\mathcal{V}^{(N)} = 1$, $\eta^{(N)} = 1$ (and setting α to minimize $\text{sd}(\hat{\phi}^{(N)})$), we retrieve the well known result of the maximum phase sensitivity enhancement $\mathcal{S}_{\text{max}}^{(N)}$ provided by a N-photon N00N state compared to classical light [18, 53, 105]:

$$\begin{aligned} \mathcal{S}_{\text{max}}^{(N)} &= \frac{1/\min(\text{sd}(\hat{\phi}^{(N)}))}{1/\min(\text{sd}(\hat{\phi}^{(1)}))} \\ &= \sqrt{N}. \end{aligned} \tag{4.36}$$

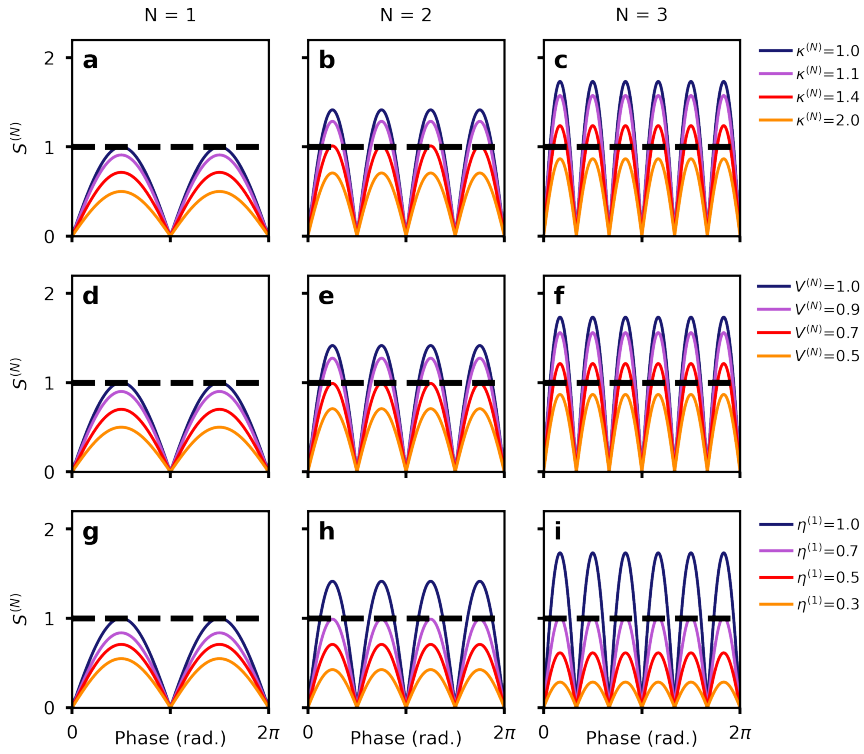

FIGURE 4.4: **Sensitivity enhancement $\mathcal{S}^{(N)}$ for single-measurement phase retrieval. (a), (b), (c)** Varying $\kappa^{(N)}$, with $\mathcal{V}^{(N)} = 1$, $\eta^{(1)} = 1$. **(d), (e), (f)** Varying $\mathcal{V}^{(N)}$, with $\kappa^{(N)} = 1$, $\eta^{(1)} = 1$. **(g), (h), (i)** Varying $\eta^{(1)}$, with $\kappa^{(N)} = 1$, $\mathcal{V}^{(N)} = 1$. First column, N=1. Second column, N=2. Third column, N=3. Dashed line in all cases indicates sensitivity of an ideal classical phase measurement.

4.3.2 Sensitivity of PSDH phase retrieval

On the other hand, when the sample phase ϕ is estimated according to PSDH, the expression for $\mathrm{sd}(\hat{\phi}^{(N)}_{(N-k),k})$ differs from Eq. 4.30. In this case the function f in the error propagation formula Eq. 4.23 corresponds to Eq. 4.21, while there are four x_j variables corresponding to $I^{(N)}_{(N-k),k}(\phi, \alpha_j)$, with $\alpha_j = \{0, \pi/(2N), \pi/N, 3\pi/(2N)\}$

(from Sect. 4.2.1). The four partial derivatives $\partial f/\partial x_j$ are therefore

$$\frac{\partial\hat{\phi}^{(N)}_{(N-k),k}}{\partial I^{(N)}_{(N-k),k}(\phi,0)} = \frac{-\partial\hat{\phi}^{(N)}_{(N-k),k}}{\partial I^{(N)}_{(N-k),k}(\phi,\frac{\pi}{N})}$$
$$= \frac{I^{(N)}_{(N-k),k}(\phi,\frac{\pi}{2N}) - I^{(N)}_{(N-k),k}(\phi,\frac{3\pi}{2N})}{N\left(\left(I^{(N)}_{(N-k),k}(\phi,0) - I^{(N)}_{(N-k),k}(\phi,\frac{\pi}{N})\right)^2 + \left(I^{(N)}_{(N-k),k}(\phi,\frac{\pi}{2N}) - I^{(N)}_{(N-k),k}(\phi,\frac{3\pi}{2N})\right)^2\right)} \tag{4.37}$$

and

$$\frac{\partial\hat{\phi}^{(N)}_{(N-k),k}}{\partial I^{(N)}_{(N-k),k}(\phi,\frac{\pi}{2N})} = \frac{-\partial\hat{\phi}^{(N)}_{(N-k),k}}{\partial I^{(N)}_{(N-k),k}(\phi,\frac{3\pi}{2N})}$$
$$= \frac{I^{(N)}_{(N-k),k}(\phi,\frac{\pi}{N}) - I^{(N)}_{(N-k),k}(\phi,0)}{N\left(\left(I^{(N)}_{(N-k),k}(\phi,0) - I^{(N)}_{(N-k),k}(\phi,\frac{\pi}{N})\right)^2 + \left(I^{(N)}_{(N-k),k}(\phi,\frac{\pi}{2N}) - I^{(N)}_{(N-k),k}(\phi,\frac{3\pi}{2N})\right)^2\right)}. \tag{4.38}$$

Before substituting Eq. 4.37-4.38 into Eq. 4.23, some simplifications can be made. Firstly we have:

$$I^{(N)}_{(N-k),k}(\phi,0) + I^{(N)}_{(N-k),k}(\phi,\frac{\pi}{N}) = I^{(N)}_{(N-k),k}(\phi,\frac{\pi}{2N}) + I^{(N)}_{(N-k),k}(\phi,\frac{3\pi}{2N}) = 2W_{N,k}, \tag{4.39}$$

relying on the identities $\cos(x+\pi) = -\cos(x)$ and $\cos(x+\pi/2) = -\sin(x)$. Also, as before, we assume that $I^{(N)}_{\text{Bkg}} \ll W_{N,k}$, neglecting therefore the $I^{(N)}_{\text{Bkg}}$ term from Eq. 4.19. Secondly:

$$I^{(N)}_{(N-k),k}(\phi,0) - I^{(N)}_{(N-k),k}(\phi,\frac{\pi}{N}) = 2W_{N,k}(-1)^k\mathcal{V}^{(N)}\cos(N\phi) \tag{4.40}$$

$$I^{(N)}_{(N-k),k}(\phi,\frac{\pi}{2N}) - I^{(N)}_{(N-k),k}(\phi,\frac{3\pi}{2N}) = -2W_{N,k}(-1)^k\mathcal{V}^{(N)}\sin(N\phi). \tag{4.41}$$

The denominator of all the partial derivate expressions Eq. 4.37-4.38 is thus simply $N(2W_{N,k}\mathcal{V}^{(N)})^2$ (using the identity $\sin^2 x + \cos^2 x = 1$). Therefore, we can substitute Eq. 4.40 and 4.41 into Eq. 4.37 and 4.38, which in turn are substituted, together

with Eq. 4.27, into Eq. 4.23. This yields the following expression for $\mathrm{sd}(\hat{\phi}^{(N)}_{(N-k),k})$:

$$\mathrm{sd}(\hat{\phi}^{(N)}_{(N-k),k}) = \kappa^{(N)} \left[\left(\frac{\cos(N\phi)}{2N\mathcal{V}^{(N)} W_{N,k}} \right)^2 \left(I^{(N)}_{(N-k),k}(\phi, 0) + I^{(N)}_{(N-k),k}(\phi, \frac{\pi}{N}) \right) + \left(\frac{\sin(N\phi)}{2N\mathcal{V}^{(N)} W_{N,k}} \right)^2 \left(I^{(N)}_{(N-k),k}(\phi, \frac{\pi}{2N}) + I^{(N)}_{(N-k),k}(\phi, \frac{3\pi}{2N}) \right) \right]^{1/2} \tag{4.42}$$

$$= \frac{\kappa^{(N)}}{N\mathcal{V}^{(N)}\sqrt{2W_{N,k}}}. \tag{4.43}$$

Note that, contrast to Eq. 4.30, Eq. 4.43 is independent of both ϕ and α. Finally, analogous to Eq. 4.31, we can find $\mathrm{sd}(\hat{\phi}^{(N)})$, this time by substituting Eq. 4.22 and 4.43 into Eq. 4.24:

$$\mathrm{sd}(\hat{\phi}^{(N)}) = \frac{\kappa^{(N)}}{N\mathcal{V}^{(N)}} \sqrt{\sum_{k=0}^{N} \frac{\binom{N}{k}}{2^N} \frac{1}{2\eta^{(N)}_{(N-k),k} I^{(N)}_{\mathrm{IN}}}} = \frac{\kappa^{(N)}}{N\mathcal{V}^{(N)}\sqrt{2\eta^{(N)} I^{(N)}_{\mathrm{IN}}}}, \tag{4.44}$$

where, as for Eq. 4.33 the simplifying assumption was made that the efficiency $\eta^{(N)}_{(N-k),k} = \eta^{(N)}$ is the same for all $|N-k,k\rangle_{\mathrm{OUT0,OUT1}}$ measurement bases. Similarly to Eq. 4.34, we are again interested in knowing $\mathrm{sd}(\hat{\phi}^{(N)})$ as a function of total number of single photons used in the phase estimation. Note that phase retrieval using PSDH (Eq. 4.21) requires four separate measurements, *each* with $I^{(N)}_{\mathrm{IN}}$ input states, where states consist of N single photons. Therefore, again denoting the total number of single photons used as M, we now have to make the substitution $I^{(N)}_{\mathrm{IN}} = M/4N$, in order to obtain

$$\mathrm{sd}(\hat{\phi}^{(N)}) = \frac{\kappa^{(N)}\sqrt{2}}{\mathcal{V}^{(N)}\sqrt{\eta^{(N)} NM}}. \tag{4.45}$$

As in Sect. 4.3.1, we can calculate the phase sensitivity enhancement $\mathcal{S}^{(N)}$, which has the same form as Eq. 4.35:

$$\mathcal{S}^{(N)} = \frac{1/\mathrm{sd}(\hat{\phi}^{(N)})}{1/\min(\mathrm{sd}(\hat{\phi}^{(1)}))}. \tag{4.46}$$

Analogous to Fig. 4.4, in Fig. 4.5, we see how $\mathcal{S}^{(N)}$ varies as a function of $\kappa^{(N)}$, $\mathcal{V}^{(N)}$and $\eta^{(1)}$, for N00N states with $N = 1, 2, 3$ (where again $N = 1$ corresponds to the classical case). We see that, for PSDH-retrieved phase estimates, $\mathcal{S}^{(N)}$ is

independent of the phase $\phi + \alpha$. Similar to results from Ref. [107, 147], again $\mathcal{S}^{(N)} > 1$ if the condition $(\eta^{(1)})^N N(\mathcal{V}^{(N)}/\kappa^{(N)})^2 > 1$ is satisfied.

In the ideal case of $\kappa^{(N)} = 1$, $\mathcal{V}^{(N)} = 1$, and $\eta^{(N)} = 1$, as in Sect. 4.3.1, the maximum phase sensitivity enhancement provided by a N-photon N00N state $\mathcal{S}^{(N)}_{\max}$ has the following well known form [18, 53, 105]:

$$\begin{aligned} \mathcal{S}^{(N)}_{\max} &= \frac{1/\mathrm{sd}(\hat{\phi}^{(N)})}{1/\mathrm{sd}(\hat{\phi}^{(1)})} \\ &= \sqrt{N}. \end{aligned} \tag{4.47}$$

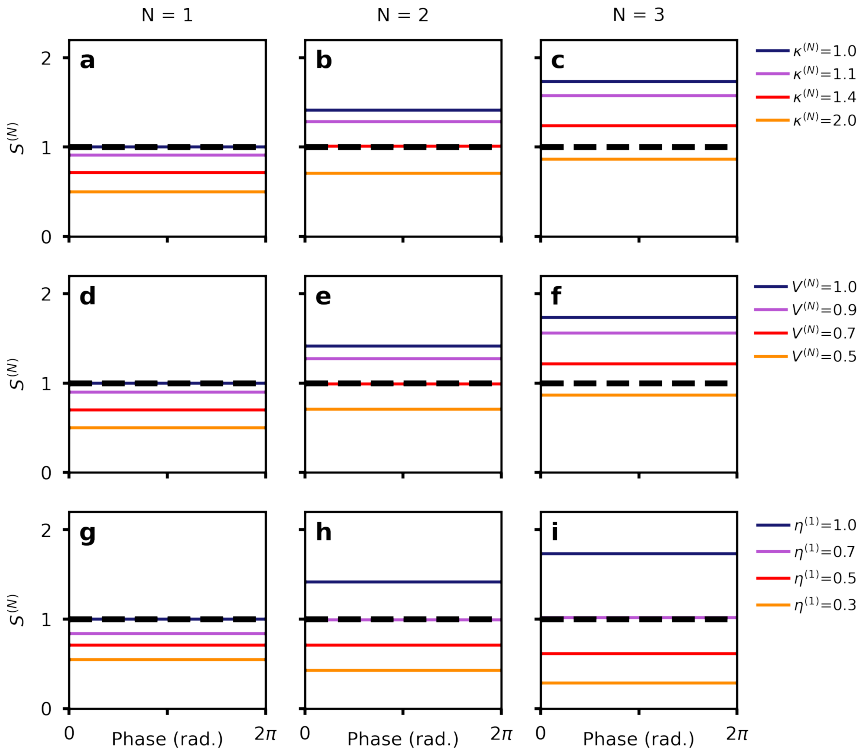

FIGURE 4.5: **Sensitivity enhancement $\mathcal{S}^{(N)}$ for PSDH phase retrieval. (a), (b), (c)** Varying $\kappa^{(N)}$, with $\mathcal{V}^{(N)} = 1$, $\eta^{(1)} = 1$. **(d), (e), (f)** Varying $\mathcal{V}^{(N)}$, with $\kappa^{(N)} = 1$, $\eta^{(1)} = 1$. **(g), (h), (i)** Varying $\eta^{(1)}$, with $\kappa^{(N)} = 1$, $\mathcal{V}^{(N)} = 1$. First column, N=1. Second column, N=2. Third column, N=3. Dashed line in all cases indicates sensitivity of an ideal classical phase measurement.

Comparing Eq. 4.45, the measurement uncertainty of a PSDH-retrieved phase estimate, to the single-measurement phase retrieval case (Eq. 4.34), we can make

two observations. Firstly, Eq. 4.45 is independent of ϕ and α. That is, a PSDH-retrieved phase estimate will always have the lowest possible measurement uncertainty regardless of the value of ϕ, without requiring careful optimization of α in order to minimize $\mathrm{sd}(\hat{\phi}^{(N)})$. This represents a significant advantage of PSDH, in addition to its other well known benefits of not requiring accurate knowledge of illumination intensity, background noise and interference visibility. However, the second observation is that the minimum $\mathrm{sd}(\hat{\phi}^{(N)})$ enabled by Eq. 4.34 (i.e. the SQL in the case of $N = 1$, $\kappa^{(N)} = 1$, $\mathcal{V}^{(N)} = 1$, and $\eta^{(N)} = 1$) is lower by a factor of $\sqrt{2}$ than Eq. 4.45. In other words, the "price" to pay for the advantages of PSDH, is a $\sqrt{2}$ times larger measurement noise compared to the optimal single-measurement phase retrieval.

4.3.3 Sensitivity with post-selected coincidence counting

The astute reader will notice that the condition $(\eta^{(1)})^N N(\mathcal{V}^{(N)}/\kappa^{(N)})^2 > 1$ requires $\eta^{(1)}$ to be higher than $N^{\frac{-1}{N}}$ to beat an ideal classical phase measurement (see Fig. 4.4(h), (i) and 4.5(h), (i)). Therefore, in the following chapters, using the two-photon N00N states produced by our SPDC setups (see Sect. 2.3), we would need an exceedingly high total efficiency $> 70.7\%$ to achieve phase super-sensitivity ($\mathcal{S}^{(2)} > 1$). Unfortunately, using SPAD array cameras this is at present technologically infeasible.

For this reason it is standard practice in the literature to *post-select* for coincidence counting, that is, only considering those photons which were detected as part of a coincidence, while ignoring those that were not detected [17, 37, 38, 144]. The effect of post-selecting coincidences is to artificially set the detection efficiency to unity, and only taking into account the $\mathcal{V}^{(N)}$ and $\kappa^{(N)}$ imperfections. Post-selected proof-of-principle demonstrations represent important advances because they almost "complete the puzzle" of super-sensitivity, with high detection efficiency representing the remaining piece that is likely to be achieved through near-term technological advances (e.g., Ref. [155] demonstrates a SPAD array with efficiency close to the critical 70.7% value, while Ref. [156] demonstrates a SPAD pixel compatible with large scale array fabrication with peak efficiency 82.5%).

Chapter 5

Widefield Super-sensitive Phase Imaging

5.1 Abstract

Quantum techniques can be used to enhance the signal-to-noise ratio in optical imaging. Leveraging the latest advances in single photon avalanche diode array cameras and multi-photon detection techniques, here we introduce a super-sensitive phase imager, which uses space-polarization hyper-entanglement to operate over a large field-of-view without the need of scanning operation. We show quantum-enhanced imaging of birefringent and non-birefringent phase samples over large areas, with sensitivity improvements over equivalent classical measurements carried out with equal number of photons. The potential applicability is demonstrated by imaging a biomedical protein microarray sample. Our technology is inherently scalable to high resolution images, and represents an essential step towards practical quantum-enhanced imaging.

5.2 Introduction

Entanglement can enhance precision measurements beyond the possibilities of classical optics [18, 157]. This is of particular importance to applications that necessarily involve low photon flux, where shot noise becomes a limiting factor. Such a situation may be encountered when imaging organic or living samples that can suffer from photo-sensitive effects [158], including chemical changes at molecular level or disruption of cell functions [148, 149]. In the biomedical field, label-free analysis involving classical illumination is usually considered a non-invasive approach. However, recent evidence shows that for some applications even relatively low classical light levels suffice to induce changes in the sample, ranging

from permanent photodamage [151], to more subtle alterations that nonetheless impact measurement accuracy [152]. Photosensitivity must also be taken into account when probing fragile quantum gas states [159] or atomic ensembles [20]. In all the above cases it therefore becomes attractive to perform phase imaging using non-classical states of light, such as N00N states consisting of N entangled photons between two optical modes, which are well known to yield a signal-to-noise ratio (SNR) enhancement of $\sqrt{N}$ over equivalent classical measurements [10, 18, 19, 105, 157, 160]. This effect is known as super-sensitivity.

Entanglement-enhanced phase imaging was demonstrated already for both birefringent [38] and non-birefringent [37] phase samples. However, neither of these works represent true imaging platforms as the entangled photons probing a sample were detected with single-pixel detectors and images were constructed by scanning the sample point-by-point. This inherently limits scalability due to a range of practical drawbacks, which can include mechanical vibrations and long-term reliability issues caused by moving parts, synchronization between pixel-scanning and light detection necessitating complex calibration procedures, and prohibitively long scanning times.

Here we show, for the first time, an entanglement-enabled super-sensitive phase imager operating in a *wide-field* configuration. This is achieved by bringing together techniques introduced in Chapters 2, 3 and 4. We exploit hyper-entanglement, that is, simultaneous N00N state entanglement in polarization and correlations in a massive pixel mode state space (Sect. 2.3.4). This lets our system operate scan-free, and enables the retrieval of phase information with a large field-of-view (FoV), using a SPAD array camera (Sect. 3.2) and digital holography computational methods (Sect. 4.1.1 and 4.2.1). Entangled photons are imaged using our photon-counting Micro Photon Devices SPC3 camera [115], allowing us to acquire spatially resolved multi-photon images with very high SNR (Sect. 3.2.1 and 3.5). We demonstrate the experimental feasibility of our approach by retrieving precise phase images of birefringent and non-birefringent test samples, including a protein microarray sample which demonstrates the applicability for biomedical diagnostic applications. The ability to measure birefringent phase samples has also important applications in material science and crystallography [161]. We show a sensitivity enhancement over equivalent classical measurements of 1.39 ± 0.11 and 1.25 ± 0.06, for the birefringent and non-birefringent samples respectively. Our method is inherently scalable to larger images with more pixels and represents an essential step towards a practically useful quantum-enhanced biological and material inspection imaging platform.

5.3 Experimental setup and methods

In our entanglement-enhanced phase imaging system, a large FoV interferometric microscope (LIM) enables classical and N00N state interferometry. Space-polarization hyper-entangled N00N states are generated by a Sagnac interferometer scheme SPDC entangled photon source (EPS) [92], and projected into diagonal two-photon polarization bases before being detected by our SPAD array camera [144].

5.3.1 Large field-of-view interferometric microscope (LIM)

The large FoV interferometric microscope (LIM) is a versatile phase imaging platform developed in the Optoelectronics group at ICFO [143, 162], and was used in experiments of this chapter, as well as Chapters 6 and 7. The LIM measures phase differences by interfering laterally displaced polarization states, and can be used for a number of applications, including the detection of microorganisms [163], detection of disease biomarkers [164, 165], inspection of three-dimensional embedded material features [166], and live-cell imaging [167].

As shown in Fig. 5.1, the crucial components of the LIM are two Savart plates (SPs; SP_1 and SP_2). For an input beam, SP_1 laterally displaces horizontally (H) polarized photons in one direction and the vertically (V) polarized photons in the orthogonal direction, thereby introducing a shear (S) between the two polarization components. Later, SP_2 is placed with an opposite orientation to SP_1 in order to revert this shear, which effectively forms a Mach-Zehnder interferometer (MZI) at each (lateral) spatial location, with the MZI modes separated from each other by the shear distance. The Savart plates (United Crystals) in our LIM induce a shear of 450 µm. Motorized tuning of the pitch angle of SP_1 with respect to the light propagation axis induces a controlled bias phase α between the two sheared spatial modes and associated polarization components after SP_2 [143, 168], over a large scanning range $0 < \alpha < 50\pi$, with no measurable beam deviation.

For each lateral spatial location $\mathbf{r}$ the LIM induces a phase difference $\Theta(\mathbf{r})$ between H and V that depends on the sample, as well as the bias phase α. The LIM can be operated in two configurations, for birefringent and non-birefringent phase samples. In the birefringent phase imaging configuration, the total phase $\Theta(\mathbf{r})$ after SP_2 equals $\Theta_b(\mathbf{r}) = \phi_b(\mathbf{r}) + \alpha$, where $\phi_b(\mathbf{r})$ is a spatially dependent birefringent sample phase. This is illustrated in Fig. 5.1(a), where the shown phase profile is always between H and V polarized light. On the other hand, for measuring a non-birefringent phase sample, the sample is placed between SP_1 and SP_2 of the LIM. In this configuration the LIM imprints a non-birefringent sample phase $\phi_{nb}(\mathbf{r})$ between the SPs onto a birefringent phase between H and V after SP_2. This results in the total phase $\Theta_{nb}(\mathbf{r}) = \phi_{nb}(\mathbf{r} + S/2) - \phi_{nb}(\mathbf{r} - S/2) + \alpha$, where S is the shear distance between H and V induced by the SPs, as shown in Fig. 5.1(b).

Now, let us suppose that we have the ability to project the LIM output into the diagonal ($D = (H + V)/\sqrt{2}$, see Eq. 2.26) and anti-diagonal ($A = (H - V)/\sqrt{2}$, see Eq. 2.27) polarization modes. In this case, the interferometer formed by the LIM at each lateral spatial location $\mathbf{r}$ is exactly analogous to the prototypical interferometer presented in Sect. 4.1 and 4.2. Explicitly, H and V in the LIM correspond, respectively, to the "Ref" and "Probe" modes from Chapter 4. Likewise, D and A here correspond, respectively, to the "OUT 0" and "OUT 1" modes from Chapter 4. Indeed, as can be seen in Fig. 5.2, this ability is in fact provided, by a half-wave plate (HWP) at 22.5° after the LIM's SP_2, and a lateral displacement polarizing beam splitter (dPBS), which directs $D(A)$ photons to the left(right).

We note that the LIM differs from the well-known Nomarski differential interference contrast (DIC) microscope, in that the light passing through the sample in the LIM is (almost) collimated, rather than strongly focused as in DIC microscopy [143, 169]. The effect of this is to greatly increase the FoV, while sacrificing some

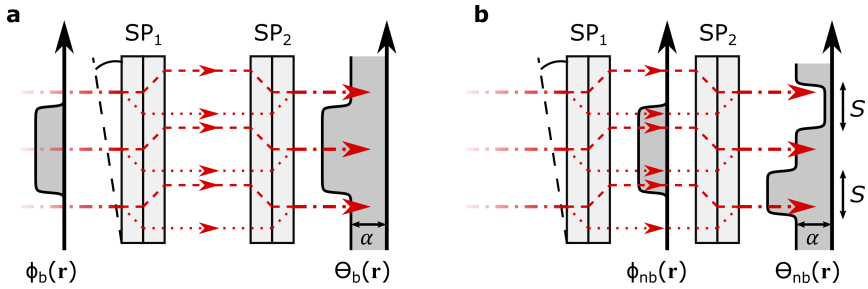

FIGURE 5.1: **LIM details. (a)** Detecting birefringent phase samples with the LIM. **(b)** Detecting non-birefringent phase samples with the LIM. In both **(a)** and **(b)**, three example trajectories are shown through the LIM, dashed lines correspond to H, and dotted lines to V polarized light. SP_1 is tilted using the pitch angle with respect to the optical axis.

lateral spacial resolution. Moreover, the depth of field in a DIC microscope is typically small, limited by the Rayleigh length of a strongly focused illumination spot. On the other hand, in the LIM the depth of field is large, with Fourier back-propagation algorithms allowing the accurate numerical retrieval of multiple image planes, spread across a longitudinal range of several millimetres, from a single acquisition [166]. We also note that using the LIM to image non-birefringent phase samples (Fig. 5.1(b)) causes the formation of a double-image, corresponding to the positive and negative sample phase (as we will be see for example in Fig. 5.10 and 6.2). While the double-image contains already all information of the sample phase, it can nonetheless be convenient to remove one of the two images using a computational technique known as "ghost average", in order to obtain a direct faithful representation of the sample spatial features [166].

5.3.2 Combined optical setup

Figure 5.2 shows the full setup used to implement our wide-field entanglement-enhanced phase imager. Hyper-entangled photon pairs are generated by SPDC within a Sagnac interferometer (SI). Here, a CW single-mode laser (Toptica TopMode) at 405.6 nm wavelength is used to pump a type-0 periodically poled Potassium Titanyl Phosphate (ppKTP) crystal inside the SI. Entanglement in the polarization degree of freedom is then generated by combining the clockwise and counter-clockwise photon pair generations in the SI (see Sect. 2.3.4 and 5.3.3). That is, through the superposition of these two SPDC processes, the source generates the two-photon N00N state $(|2_H 0_V\rangle + |0_H 2_V\rangle)/\sqrt{2}$ [92]. The entangled photon pairs are centred at 811.2 nm wavelength, and the ppKTP crystal is temperature controlled using a Peltier oven in order to satisfy the degenerate phase matching condition. The laser power, measured before the SI, was fixed to 3 mW for background measurements and fixed to 0.6 mW for sample measurements.

As described in Sect. 2.3.3, the correlated nature of SPDC photon pair generation yields space-momentum entanglement [82]. In the near-field of the entangled

state (i.e., at the generation plane) both photons are spatially correlated (approximately in the same spatial position) [170]. As shown in Fig. 5.2, this near-field plane is imaged onto a spatial light modulator (SLM, Holoeye Pluto-2), using two lenses of focal lengths $L_1 = 300\,\text{mm}$ and $L_2 = 2500\,\text{mm}$ in a 4f configuration. A second 4f telescope re-images the nearfield into our LIM and onto the Micro Photon Devices SPC3 photon-counting SPAD array camera, using two further lenses. In this case, for measuring the first (birefringent) test sample these lenses had focal lengths $L_3 = 250\,\text{mm}$ and $L_4 = 500\,\text{mm}$, while for the second (non-birefringent) sample these lenses had focal lengths $L_3 = 500\,\text{mm}$ and $L_4 = 500\,\text{mm}$. Note that a $810 \pm 5\,\text{nm}$ band-pass filter (BPF) is placed before the camera to remove environment noise and spurious pump light. Our SPC3 SPAD camera has a pixel pitch of $150\,\mu\text{m}$, and is fitted with a microlens array, giving an effective pixel fill factor (FF) of $\approx 75\%$. Therefore, the overall photon detection efficiency at 811.2 nm (taking into account FF) is approximately 3% [115]. The LIM and camera are separated by less than the Rayleigh range of the imaging system. Therefore the SLM, the LIM and the SPAD camera are at conjugate planes of the SPDC plane, where photon pairs are spatially correlated [170]. The quantum state after propagating through the entire setup, can thus be expressed as

$$|\Psi\rangle \approx \sum_{\mathbf{r},\mathbf{r}'} \left[|H\rangle_{\mathbf{r}} |H\rangle_{\mathbf{r}'} + e^{i2\Theta(\mathbf{r})} |V\rangle_{\mathbf{r}} |V\rangle_{\mathbf{r}'} \right] \tag{5.1}$$

where we neglect normalisation coefficients for clarity. Here, $\mathbf{r}$ and $\mathbf{r}'$ are the transverse coordinates of the two spatially correlated photons, which are close in space and thus acquire approximately the same phase ($\Theta(\mathbf{r}) \approx \Theta(\mathbf{r}')$). The sample and setup therefore cause the two-photon entangled state to acquire a total phase difference between H and V of $2\Theta(\mathbf{r}) \approx \Theta(\mathbf{r}) + \Theta(\mathbf{r}')$. We note the similarity of Eq. 5.1 to Eq. 2.46. Recall from Sect. 2.3.4 that Eq. 2.46 and Eq. 2.45 require identical photon pair space-momentum distributions for the two SI SPDC processes (i.e. the clockwise and counter-clockwise ones). Section 5.3.3 describes the alignment process through which this condition is satisfied, thereby ensuring that Eq. 5.1 is a valid description of the quantum state in our system.

5.3.3 Alignment of HH and VV photon pairs

We aligned the HH and VV photon pair generations of our entangled photon source such that they are indistinguishable in position and momentum correlations, which is the crucial requirement that justifies the use of Eq. 5.1. During the alignment, we used our SPC3 SPAD array camera to capture coincidences from the SI SPDC generations, using Eq. 3.16 as described in Sect. 3.2.1 (and subtracting cross-talk, Eq. 3.28).

Position correlations are measured in a discretized space determined by the SPAD camera resolution, where we consider $\mathbf{r} \longrightarrow \mathbf{r}_i$ and $\mathbf{r}' \longrightarrow \mathbf{r}_j$. By projecting the coincidences measured in the near-field into the difference coordinates $\mathbf{r}_i - \mathbf{r}_j$, in the presence of SPDC position correlations one obtains a Gaussian peak with waist σ_-, as can be seen from Eq. 2.44. Through iterative alignment we ensure that the correlation widths for the HH (clockwise) and VV (counter-clockwise)

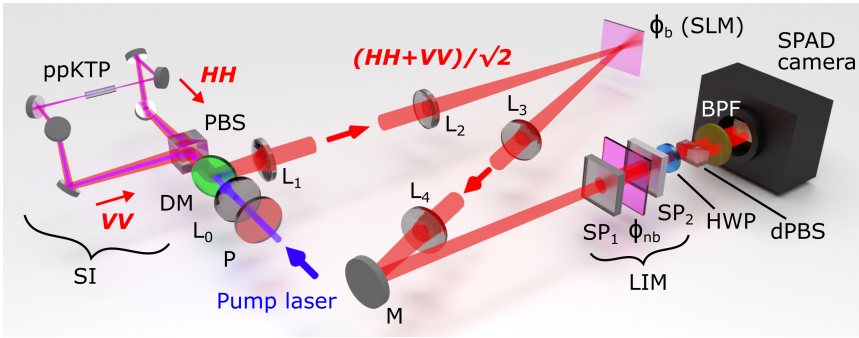

FIGURE 5.2: **Full entanglement-enhanced wide-field phase imaging setup.** SI - Sagnac Interferometer, PBS - polarizing beam splitter, HWP - half-wave plate, L - lenses, DM - dichroic mirror, M - mirror, ϕ_b - birefringent sample (SLM), ϕ_{nb} - non-birefringent sample, SP - Savart plate, dPBS - lateral displacement polarizing beam splitter, BPF - band-pass filter.

SI generations are equal, as can be seen in Fig. 5.3. We confirmed that the correlations widths are matching by fitting a two-dimensional Gaussian function to the difference coordinates projected coincidences, obtaining $\sigma_{-,HH} = 264 \pm 1\mu m$ for the HH photon pairs, and $\sigma_{-,VV} = 275 \pm 2\mu m$ for the VV photon pairs (uncertainties are fitting errors). Note that the theoretically expected SPDC spatial correlation width at the near-field generation plane can be calculated according to $\sigma_{-,\text{theo}} = \sqrt{0.455 L_{\text{xtal}} \lambda_p/(2\pi)}$ [80], where $L_{\text{xtal}} = 20\,\text{mm}$ is the ppKTP crystal length, and $\lambda_p = 405.6\,\text{nm}$ is the pump laser wavelength. Taking into account the 8.3-fold magnification factor from the crystal to camera planes, we obtain $\sigma_{-,\text{theo}} \approx 200\,\mu\text{m}$, which is slightly smaller than the experimentally measured values. This discrepancy is attributed to an imperfect longitudinal alignment of the camera plane with the true image plane. We also note that in Fig. 5.3 it can be seen that the amplitudes of the HH and VV generations are different, which we attribute to polarization-dependent losses in optical components of our system. We compensated for this effect however, by increasing the laser pump power for one generation with respect to the other.

We likewise characterized the momentum correlations of the HH and VV generations, by letting $\mathbf{k}_i^\perp$ and $\mathbf{k}_j^\perp$ represent the respective transverse momenta of the two detected photons. We image the SPDC far-field after lens L_1 (see Fig. 5.2), where the detected lateral position coordinates can be mapped to the transverse momenta, which in turn are projected into sum coordinates $(\mathbf{k}_i^\perp + \mathbf{k}_j^\perp)$. Accordingly, as seen in Eq. 2.43, one obtains a Gaussian peak with waist σ_+^{-1}, the momentum correlation width. We again aligned the HH and VV generations such that their momentum correlations were equal, which is shown in Fig. 5.4. Through an iterative alignment procedure, we moreover ensured that the HH and VV generations had equal correlation widths for *both* position and momentum

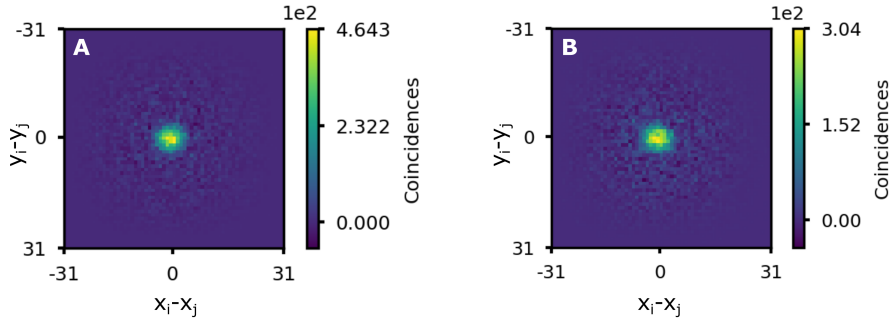

FIGURE 5.3: **Alignment of position correlations for photon pairs from HH and VV generations. (A)** HH generation photon coincidences projected into the difference coordinates $\mathbf{r}_i - \mathbf{r}_j$. Fitted correlation width $\sigma_{-,HH} = 264 \pm 1\mu m$. **(B)** VV generation photon coincidences projected into the difference coordinates $\mathbf{r}_i - \mathbf{r}_j$. Fitted correlation width $\sigma_{-,VV} = 275 \pm 2\mu m$.

correlations. We confirmed that the momentum correlation widths are matching again by fitting a two-dimensional Gaussian function, where we obtained $\sigma^{-1}_{+,HH} = 311 \pm 1\mu m$ for the HH photon pairs, and $\sigma^{-1}_{+,VV} = 326 \pm 2\mu m$ for the VV photon pairs (uncertainties are fitting errors). The Gaussian width of the laser spot in the ppKTP crystal was estimated to be $\sigma_+ \approx 250\,\mu$m, which lets us calculate the expected theoretical SPDC momentum correlation in the far-field $\sigma^{-1}_{+,\text{theo}}$, scaling by the factor $(\lambda_{\text{SPDC}} f_{\text{FF}})/(2\pi)$, where $\lambda_{\text{SPDC}} = 811.2\,$nm is the SPDC wavelength, and $f_{\text{FF}} = 300\,$mm is the focal length of L_1 (i.e. the lens used to image the far-field) [80]. This yields therefore $\sigma^{-1}_{+,\text{theo}} \approx 150\,\mu$m, which is significantly smaller than the experimentally measured correlations. Similar to the near-field case, this discrepancy is explained by imperfect longitudinal alignment of the camera, which in the far-field case was especially difficult due to space constraints in the optical setup. Nevertheless, this satisfied the requirement of equal correlation widths in position and momentum, after which we finally ensured excellent spatial overlap of the intensity profiles of the two generations, completing the alignment.

5.3.4 Coincidence imaging

Using our SPC3 SPAD array camera, we measure spatially resolved photon coincidences using the method described in Sect. 3.2.1. Recall that the coincidences, with accidentals subtracted, can be calculated from a large number of binary intensity frames according to Eq. 3.16 [30]. Coincidences are counted in the three possible polarization bases, corresponding to $\langle DD|\Psi\rangle$, $\langle AA|\Psi\rangle$, and $\langle DA|\Psi\rangle$ measurements. These three projections correspond to the following photon pair detection scenarios:

1. $cc_{DD}(i,j)$ – Pixels i and j both on the left half of the camera, i.e. a $\langle DD|$ polarization projection,

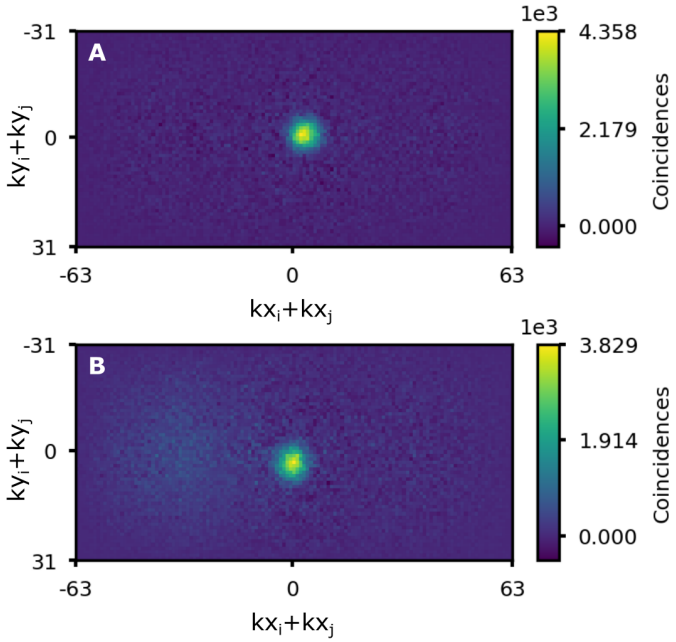

FIGURE 5.4: **Alignment of momentum correlations for photon pairs from HH and VV generations. (A)** HH generation photon coincidences projected into the transverse momentum sum coordinates $\mathbf{k}_i^{\perp} + \mathbf{k}_j^{\perp}$. Fitted correlation width $\sigma^{-1}_{+,HH} = 311 \pm 1 \mu m$. **(B)** VV generation photon coincidences projected into the transverse momentum sum coordinates $\mathbf{k}_i^{\perp} + \mathbf{k}_j^{\perp}$. Fitted correlation width $\sigma^{-1}_{+,VV} = 326 \pm 2 \mu m$. These images were acquired during the alignment process, ensuring equal momentum correlation widths but prior to ensuring spatial overlap of the HH and VV emissions. This accounts for the relative displacement between the peaks.

2. $cc_{AA}(i,j)$ – Pixels i and j both on the right half of the camera, i.e. a $\langle AA|$ polarization projection,

3. $cc_{DA}(i,j)$ – Pixels i and j on different halves of the camera, i.e. a $\langle DA|$ polarization projection.

The SPC3 SPAD camera was operated at a frame rate of 96 kHz, with a deadtime of 120 ns. For sample and background measurements we used an exposure time of 10 ns and 70 ns per frame. During acquisitions, frames are first read into the camera's internal memory, which is then emptied via USB3 link into an external PC random access memory. In parallel, the PC executes a control and analysis script, which calculates the coincidences from the incoming frames, and saves the coincidence data to disk.

The calculated coincidence counts were then post-processed in order to remove the two sources of noise described in Sect. 3.3.1 and 3.3.2: cross-talk and

spatially uncorrelated noise. Only the coincidence counts cc_{DD} and cc_{AA} include significant crosstalk. As described in detail in Sect. 3.3.1, crosstalk coincidences occur in SPAD cameras, because after a real photon detection in pixel i, photons can be emitted from that location and detected by a nearby pixel j with probability $P_{\text{ct}}(j|i)$ [127], or vice versa [81]. For cc_{DD} and cc_{AA}, both photons are detected on the same half of the camera sensor. Therefore, cross-talk can overlap with real coincidences and must be removed. The crosstalk probability can be approximated to depend only on the displacement between pixels $\Delta x = |x_i - x_j|$, $\Delta y = |y_i - y_j|$ (i and j expressed in terms of their x and y coordinates) [133]. As described in Sect. 3.3.1, we characterized the crosstalk probability $P_{\text{ct}}(\Delta x, \Delta y)$ by counting coincidences with the camera sensor covered, such that detections were only generated by dark counts. The map of $P_{\text{ct}}(\Delta x, \Delta y)$ for our SPC3 SPAD array can be seen in Fig. 3.6. Using $P_{\text{ct}}(\Delta x, \Delta y)$, we then calculate the crosstalk coincidences with Eq. 3.28, in order to subtract them from the cc_{DD} and cc_{AA} values obtained from Eq. 3.16. cc_{DA} on the other hand, is not affected by crosstalk because in this case the monitored pixels are physically far apart on separate halves of the camera, and as seen in Fig. 3.6, $P_{\text{ct}}(\Delta x, \Delta y)$ becomes negligible for large $(\Delta x, \Delta y)$. We also removed spatially uncorrelated noise from all three polarization projection coincidence counts, using the method described in Sect. 3.3.2. This involved fitting the Gaussian model Eq. 3.29 to the measured coincidence counts, and filtering out spatially uncorrelated coincidences with the thresholding function defined by Eq. 3.31 (with $t = 0.5$).

Finally, the filtered coincidence counts for each polarization projection were transformed into a two-dimensional coincidence image (ci) using Eq. 3.32. That is, the $\text{ci}_{DD}(\mathbf{r})$, $\text{ci}_{DA}(\mathbf{r})$, and $\text{ci}_{AA}(\mathbf{r})$ coincidence images correspond to the two-photon "intensities" $I^{(2)}_{2,0}$, $I^{(2)}_{1,1}$, and $I^{(2)}_{0,2}$ (from Sect. 4.2), respectively. The SNR of these coincidence images was experimentally characterized, following the method detailed in Sect. 3.5, where SNR is quantified by the dimensionless parameter $\kappa \equiv \kappa^{(2)}$. By tuning the laser pump power, frame exposure time, and filtering threshold parameter, we were able to optimize the SNR, obtaining a value of $\kappa = 1.05$.

5.3.5 Classical and N00N state interference

Our setup has the capability to probe one-photon (classical) and 2-photon N00N state interference. The total phase factor $2\Theta(\mathbf{r})$ in Eq. 5.1 acquired by the two-photon state $|\Psi\rangle$ modulates the two-photon probability after projecting into D and A polarizations, as is achieved by the half-wave plate (HWP) at 22.5° and lateral displacement polarizing beam splitter (dPBS) after the LIM. We obtain the possible two-photon measurement outcomes simply by writing out Eq. 4.18 explicitly

for the polarization modes (with $N = 2$):

$$|\langle DD|\Psi(\mathbf{r})\rangle|^2 = \frac{1+\cos 2\Theta(\mathbf{r})}{4} \tag{5.2}$$

$$|\langle DA|\Psi(\mathbf{r})\rangle|^2 = \frac{1-\cos 2\Theta(\mathbf{r})}{2} \tag{5.3}$$

$$|\langle AA|\Psi(\mathbf{r})\rangle|^2 = \frac{1+\cos 2\Theta(\mathbf{r})}{4}. \tag{5.4}$$

For the classical case ($N = 1$) we simply replace the entangled photon pair illumination in our setup with classical, diagonally polarized light. Again, from Eq. 4.18, we obtain the possible measurement outcomes:

$$\left|\langle D|\left(\frac{|H\rangle + e^{i\Theta(\mathbf{r})}}{\sqrt{2}}\right)\right|^2 = \frac{1+\cos\Theta(\mathbf{r})}{2} \tag{5.5}$$

$$\left|\langle A|\left(\frac{|H\rangle + e^{i\Theta(\mathbf{r})}}{\sqrt{2}}\right)\right|^2 = \frac{1-\cos\Theta(\mathbf{r})}{2}. \tag{5.6}$$

5.3.6 Phase-shifting interferometry

As outlines in Sect. 4.2.1, by acquiring a series of coincidence images at controlled offsets α, an unknown sample phase can be retrieved using phase-shifting digital holography (PSDH) [7]. Here, we took advantage of the tunable LIM bias phase, controlled through the motorized pitch tilting angle of SP_1 of the LIM, to set $\alpha = \{0, \pi/4, \pi/2, 3\pi/4\}$. This then allows retrieving the sample phase image for each polarization projection's coincidence image series. For example, for $\mathrm{ci}_{DD}(\mathbf{r})$:

$$\hat{\phi}^{(2)}_{DD}(\mathbf{r}) = \frac{1}{2}\tan^{-1}\left[\frac{ci_{DD}(\mathbf{r},\pi/4) - ci_{DD}(\mathbf{r},3\pi/4)}{ci_{DD}(\mathbf{r},\pi/2) - ci_{DD}(\mathbf{r},0)}\right], \tag{5.7}$$

which is equivalent to Eq. 4.21, with $N = 2$, $k = 0$. Following the convention introduced in Chapter 4, the circumflex on $\hat{\phi}^{(2)}_{DD}(\mathbf{r})$ indicates that it is an estimator of the sample phase, while the "DD" subscript and "(2)" superscript indicate, respectively, that the estimator is calculated from the experimental DD measurement of 2-photon N00N state interference. Analogous to Eq. 5.7, $\hat{\phi}^{(2)}_{DA}(\mathbf{r})$ and $\hat{\phi}^{(2)}_{AA}(\mathbf{r})$ are calculated using the corresponding coincidence images. The N00N state-retrieved phase estimate combining all three projections is therefore (using Eq. 4.22):

$$\hat{\phi}_{\mathrm{N00N}}(\mathbf{r}) = \left(\hat{\phi}^{(2)}_{DD}(\mathbf{r}) + 2\hat{\phi}^{(2)}_{DA}(\mathbf{r}) + \hat{\phi}^{(2)}_{AA}(\mathbf{r})\right)/4. \tag{5.8}$$

Similarly, a phase estimate can be obtained using only classical (single-photon) intensity measurements $I^{(1)}_D$ and $I^{(1)}_A$, proportional to the probabilities Eq. 5.5 and

5.6, respectively. In this case, we obtain

$$\hat{\phi}_D^{(1)} = \tan^{-1}\left[\frac{I_D^{(1)}(\mathbf{r},\pi/2) - I_D^{(1)}(\mathbf{r},3\pi/2)}{I_D^{(1)}(\mathbf{r},\pi) - I_D^{(1)}(\mathbf{r},0)}\right], \tag{5.9}$$

which is equivalent to Eq. 4.12. Equation 5.9 calculates the phase estimated from intensity measurements in the D projection. Analogously, $\hat{\phi}_A^{(1)}$ is calculated by substituting in $I_A^{(1)}$ intensities. The phase estimate retrieved from classical interference, combining D and A, is thus

$$\hat{\phi}_{\text{Classical}}(\mathbf{r}) = \left(\hat{\phi}_D^{(1)}(\mathbf{r}) + \hat{\phi}_A^{(1)}(\mathbf{r})\right)/2. \tag{5.10}$$

To correctly set the four required offset phases, we first scanned through the interference curves by tilting SP_2 (shown in Fig. 5.5), which produces a continuous scan on α. We then fitted a cosine to the data, to extract the right SP_2 tilts for the required offset phases.

5.4 Results

5.4.1 Entangled state characterization

We characterized the quality of the entangled state by acquiring a series of coincidence count measurements (ci_{DD}, ci_{DA}, ci_{AA}) while scanning through the LIM offset phase α, with no sample present. In Fig. 5.5 we see that quantum two-photon interference manifests twice the periodicity of the single-photon interference, which is the expected signature of phase super-resolution for N00N state interference [10, 160]. That is, for an offset phase α which is applied by a given tilt of SP_1 in the LIM, the classical state acquires the phase α, while the N00N state acquires the phase 2α. When integrating coincidences across the whole SPAD array camera (Fig. 5.5B), a relatively low fitted visibility of $\mathcal{V}_{overall} = 0.670 \pm 0.022$ is obtained. However, as shown in Fig. 5.5C, when analysing the coincidences of one fixed pixel (i.e. a single pixel in the ci_{DD}, ci_{DA}, ci_{AA} coincidence images), the fitted visibility is $\mathcal{V}_{local} = 0.94 \pm 0.06$. This result indicates high local fidelity with respect to the theoretical state $|\Psi\rangle$, validating the super-sensitive capabilities of our quantum resource [38, 107]. The discrepancy in visibility between Fig. 5.5B and C indicates a spatially-dependent phase background across the N00N state wave-front, which we characterize and remove when imaging samples.

5.4.2 Theoretical sensitivity enhancement

To model the expected sensitivity enhancement from our entanglement-enhanced phase imager, we compare the noise (standard deviation) of the two phase estimates $\hat{\phi}_{\text{Classical}}$ and $\hat{\phi}_{\text{N00N}}$, calculated using Eq. 5.10 and 5.8, respectively. From

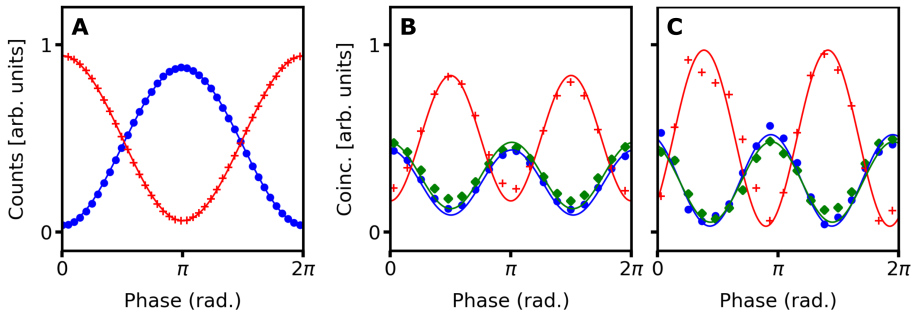

FIGURE 5.5: **Classical vs N00N state interference. (A)** Classical interference integrating across whole camera. Red crosses and blue circles correspond to $\langle D|$ and $\langle A|$ projections, respectively. **(B)** N00N state interference integrating across whole camera. **(C)** N00N state interference with a single fixed pixel. For **(B)** and **(C)**, red crosses, blue circles and green diamonds correspond to $\langle DA|$, $\langle DD|$ and $\langle AA|$ projections, respectively. Solid lines are fitting curves. The doubled periodicity in **(B)** and **(C)** as compared to **(A)**, is obtained by the tilting of SP_1 in the LIM, which induces a phase α in the classical state, and 2α in the N00N state.

Sect. 4.3, we recall that Eq. 4.45 quantifies the standard deviation of an experimental phase estimate, using M photons under experimental conditions described by parameters $\kappa^{(N)}$, $\mathcal{V}^{(N)}$ and $\eta^{(N)}$.

The single-photon (classical) efficiency of the SPC3 SPAD camera used in this work was $\eta^{(1)} \approx 0.03$ (see Sect. 5.3.2), which is far lower than the $1/\sqrt{2} \approx 0.707$ value required for a $N = 2$ N00N state to beat an ideal classical phase measurement. Therefore, in this work, coincidences are counted in post-selection (see Sect. 4.3.3). The effect of this is to artificially set $\eta^{(1)} = 1$, and thus only κ and $\mathcal{V}^{(2)}$ have an effect on the expected sensitivity enhancement. See also Sect. 5.5 for further discussion of this point.

For the two-photon N00N state measurement, we obtained $\kappa^{(2)} = \kappa = 1.05$ (Sect. 5.3.4) and $\mathcal{V}^{(2)} = \mathcal{V}_{local} = 0.94 \pm 0.06$ (Sect. 5.4.1). We would like to compare the uncertainty of our entanglement-enabled phase measurements with an ideal classical phase retrieval, with phase retrieval in both cases through PSDH. Therefore, for the classical case, also using M photons, we set $\kappa^{(1)} = 1$ and $\mathcal{V}^{(1)} = 1$. Then we can numerically evaluate the relative reduction in uncertainty enabled by the N00N-state phase retrieval: $sd(\hat{\phi}_{\text{N00N}})/sd(\hat{\phi}_{\text{Classical}}) = 0.79 \pm 0.05$. Note that as pointed out in Sect. 4.3, when using PSDH phase retrieval, the measurement uncertainty (i.e. also the reduction in uncertainty) is independent of the sample phase.

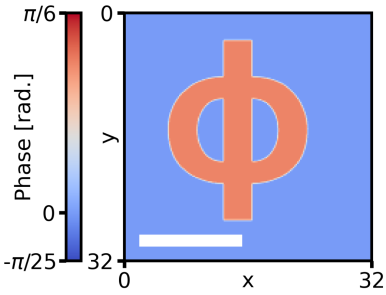

FIGURE 5.6: Birefringent phase profile applied to SLM. Scale bar, 1 mm at sample plane.

5.4.3 Super-sensitive imaging of birefringent sample

We first investigated the entanglement-enhanced phase imaging capabilities of our system by measuring a birefringent test sample generated by the SLM (pattern shown in Fig. 5.6). An equal number of photodetections was used to retrieve a phase image using classical (single-photon) intensity interference, and entanglement-enhanced (two-photon) N00N state interference. Over all four phase-shifted images a total of $I_{tot} = 8.18 \times 10^5$ single-photon detection events, and $ci_{tot} = 4.06 \times 10^5$ two-photon coincidences were recorded (i.e. $I_{tot} \approx 2ci_{tot}$). The total acquisition time for the entanglement-enhanced sample measurement was 24 hours, recording 2.07×10^9 binary intensity frames (6 hours at 96 kHz frame rate) at each PSDH step. We also calculated the spatially dependent background phase (i.e. with no sample present), using PSDH with four acquisition steps of 2.76×10^9 binary intensity frames (8 hours at 96 kHz frame rate) each. For the classical case, on the other hand, the total acquisition time was 2.9 s.

Figure 5.7 shows the experimental N00N state phase images, retrieved using PSDH and coincidence images ci_{DD}, ci_{DA}, and ci_{AA}. In particular, the experimental phase estimate $\hat{\phi}^{(2)}_{DD}(\mathbf{r})$ was calculated by subtracting the phase profile shown in 5.7A from the one shown in 5.7B. Similarly, $\hat{\phi}^{(2)}_{DA}(\mathbf{r})$ and $\hat{\phi}^{(2)}_{AA}(\mathbf{r})$ were obtained from the phase images shown in 5.7C and D, and 5.7E and F, respectively. The non-zero background phase profile (5.7A, C, E) is caused by several factors. Imperfect collimation of the beam through the LIM results in a distortion of the wavefront difference between the H and V polarized photons [171]. We have also observed that various components in the optical path going from the entangled photon source to the LIM, most of all the dichroic mirror, induce small birefringent effects which again cause spatially dependent phase differences between the H and V polarized photons. Imperfect alignment of the Sagnac interferometer and inhomogeneities in the ppKTP crystal also result in non-zero phase distortion. We note that for the N00N state generation it is experimentally much more difficult to eliminate or reduce this background phase than in the classical case. The reason for this is that the hyper-entangled N00N state we have used is generated by indistinguishability between two separate SPDC processes, where the aforementioned sources of phase distortion apply individually to each of the two generations. That

is, the spatially dependent background phase profile in our system is due to the difference in phase between two separate SPDC processes. Eliminating the background then involves aligning both SPDC processes such that they *simultaneously* have flat wave-fronts with zero phase difference between them across the entire FoV. In practice, this was experimentally extremely challenging to achieve, and we were therefore unable to fully remove the background phase profile. Integrating over all pixels then leads to the reduction in N00N-state interference visibility for the summed pixel case (Fig. 5.5B). On the other hand, for the classical case, the D polarized classical probe beam consisted of a single SPDC generation rotated by 45 degrees. Experimentally it was far easier to align well the single SPDC generation, such that the background was virtually eliminated, resulting in a high classical interference visibility close to unity (Fig. 5.5A).

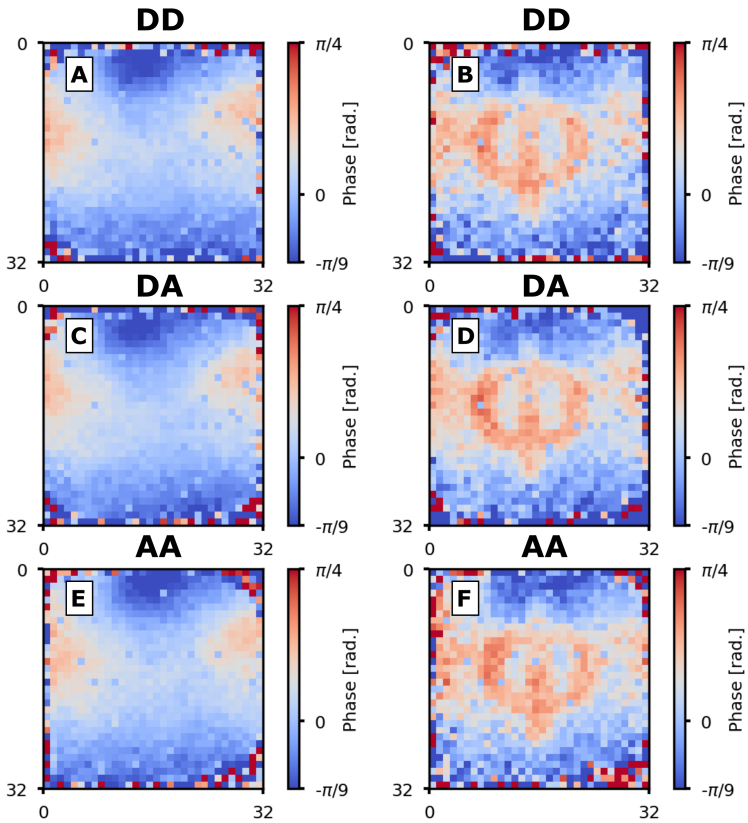

FIGURE 5.7: **Retrieved phase images for birefringent test sample measurement. (A)** and **(B)** Background and sample retrieved phase for $\langle DD|$ polarization projection. **(C)** and **(D)** Background and sample retrieved phase for $\langle DA|$ polarization projection. **(E)** and **(F)** Background and sample retrieved phase for $\langle AA|$ polarization projection.

Fig. 5.8A shows the classical phase estimate image $\hat{\phi}_{\text{Classical}}$ (Eq. 5.10). Fig. 5.8C

on the other hand, shows the entanglement-enhanced phase estimate $\hat{\phi}_{\mathrm{N00N}}$, (Eq. 5.8). Fig. 5.8B and D show cross-sections of the background noise in the classical and entanglement-enhanced phase estimate images, respectively. Comparing to Fig. 5.6, we see that Fig. 5.8A and C both show the recovered sample phase well, whose accuracy is further confirmed with the zero-normalized cross-correlation image matching metric (details in Appendix A). In order to quantify the sensitivity enhancement that our protocol provides, we compute the local uncertainty (LU) of the images, that is the root-mean-squared differences between all pairs of neighbouring pixels [38]. The regions indicated by the black rectangles in Fig. 5.8A and C respectively were used to calculate the LU, yielding $LU_{\mathrm{Classical}} = 0.091 \pm 0.005$ and $LU_{\mathrm{N00N}} = 0.065 \pm 0.004$, where the errors in LU represent the statistical standard error. We therefore obtained a reduction in noise from $\hat{\phi}_{\mathrm{Classical}}$ to $\hat{\phi}_{\mathrm{N00N}}$, which can be seen qualitatively by comparing the roughness of Fig. 5.8B and D, and numerically as $LU_{\mathrm{N00N}}/LU_{\mathrm{Classical}} = 0.72 \pm 0.06$. The above result is consistent with the expected phase super-sensitivity for our system $sd(\hat{\phi}_{\mathrm{N00N}})/sd(\hat{\phi}_{\mathrm{Classical}}) = 0.79 \pm 0.05$ (Sect. 5.4.2), and close to the theoretical bound of $1/\sqrt{2} \approx 0.707$.

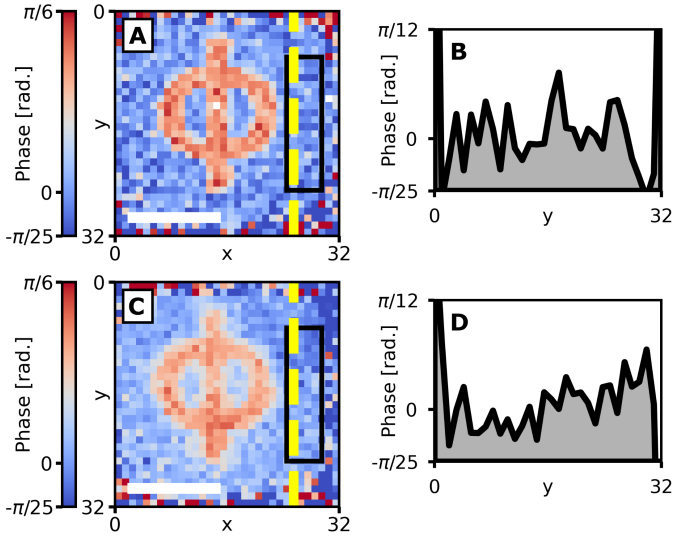

FIGURE 5.8: **Retrieved phase images of a birefringent sample. (A)** Classical phase image $\hat{\phi}_{\mathrm{Classical}}$. **(B)** Cross-section of phase profile along yellow dashed line in **(A)**. **(C)** Entanglement-enhanced phase image $\hat{\phi}_{\mathrm{N00N}}$. **(D)** Cross-section of phase profile along yellow dashed line in **(C)**. Black rectangles in **(A)** and **(C)** indicate area used for LU calculations. Clearly the pixel-to-pixel noise is reduced in **(C)** and **(D)** compared to **(A)** and **(B)**. The reduced edge contrast in **(C)** is due to the relatively large photon spatial correlation width, but can be addressed by engineering an entangled photon source with tighter spatial correlation. Scale bars, 1 mm at sample plane.

5.4.4 Super-sensitive imaging of protein microarray sample

In the second test of our entanglement-enhanced phase imager we imaged a non-birefringent phase sample, which was implemented by fabricating a microarray of protein spots on a glass slide. This is similar to clinical microarray assays, where a range of capture antibodies are spotted onto a glass slide, each binding with a specific biomarker (e.g. an indicator of a disease). Measuring a change in signal for a given spot therefore confirms the presence or absence of a certain condition, aiding in rapid diagnosis [172]. Here, the microarray test sample was fabricated using commercially available Pierce Recombinant Protein A/G (Thermo Scientific 21186). First the stock solution at 5 mg/mL was diluted using milli-Q water to a final concentration of 500 µg/mL. This was then spotted (using a SCIENION sci-FLEARRAYER S3 spotter) onto a borosilicate glass slide (NEXTERION Slide E, SCHOTT), coated with a multi-purpose epoxysilane layer that covalently binds most types of bio-molecules including amino- and non-modified DNA, RNA, and proteins. Spots of diameter 500 µm were made with 1000 µm centre-to-centre spacing, and the sample was left to dry overnight (24 hours) before measuring. Accurately imaging the phase jumps due to the presence or absence of proteins in the biological sample, and showing a quantum enhancement in this measurement confirms the direct applicability of our entanglement-enhanced imaging system to diagnostics applications.

Using the LIM in the configuration shown in Fig. 5.1b, the microarray test sample (ϕ_{nb}) was inserted into the imager for measuring. As with the birefringent sample, an equal number of photodetections was used to reconstruct the phase image estimates $\hat{\phi}_{\text{Classical}}$ and $\hat{\phi}_{\text{N00N}}$ ($I_{tot} = 3.16 \times 10^6$ single-photon detection events, and $ci_{tot} = 1.55 \times 10^6$ two-photon coincidences, i.e. $I_{tot} \approx 2ci_{tot}$), permitting a fair comparison of phase sensitivity for the two methods. The sample acquisition time for the N00N state phase was 7 hours per PSDH step (2.42×10^9 binary intensity frames), that is, 28 hours in total across all four steps. In addition, as for the birefringent test sample (Sect. 5.4.3), the background phase was retrieved using PSDH, with a 4 hour (1.38×10^9 frames) acquisition time per step (i.e. 16 hours in total). For the classical case, on the other hand, the total acquisition time was 3.2 s.

Equivalent to Fig. 5.7, in Fig. 5.9 we see the experimental N00N state phase images, retrieved using PSDH and coincidence images ci_{DD}, ci_{DA}, and ci_{AA}. Again, the experimental phase estimate $\hat{\phi}^{(2)}_{DD}(\mathbf{r})$ was calculated subtracting the 5.9A phase image from the 5.9B one. Similarly, $\hat{\phi}^{(2)}_{DA}(\mathbf{r})$ and $\hat{\phi}^{(2)}_{AA}(\mathbf{r})$ were obtained from the 5.7C and D, and 5.7E and F phases, respectively. Fig. 5.10A shows a reference phase image retrieved under high intensity illumination, whereas in Fig. 5.10B and Fig. 5.10C are shown the low intensity illumination (single-photon) and entanglement enhanced phase estimates $\hat{\phi}_{\text{Classical}}$ (Eq. 5.10) and $\hat{\phi}_{\text{N00N}}$ (Eq. 5.8), respectively.

Horizontal cross-sections of the phase images (Fig. 5.10D-F) confirm the accuracy of the entanglement-enhanced measurement compared to both classical ones. The contrast between spots and surrounding background, indicating the presence and absence of proteins respectively, is clear in all measurements, which confirms the suitability of the technique for probing diagnostic microarrays. We

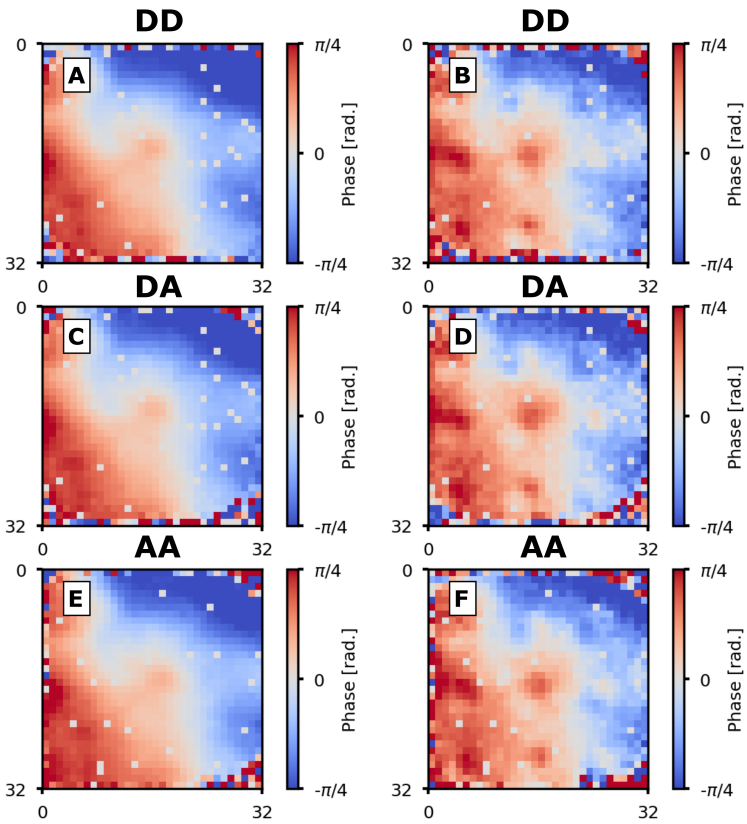

FIGURE 5.9: **Retrieved phase images for non-birefringent test sample measurement. (A)** and **(B)** Background and sample retrieved phase for $\langle DD|$ polarization projection. **(C)** and **(D)** Background and sample retrieved phase for $\langle DA|$ polarization projection. **(E)** and **(F)** Background and sample retrieved phase for $\langle AA|$ polarization projection.

again compare the LU, using the areas defined by the black rectangles. The extracted values are $LU_{\text{Classical}} = 0.059 \pm 0.002$ and $LU_{\text{N00N}} = 0.047 \pm 0.001$, which provides an enhancement of $LU_{\text{N00N}}/LU_{\text{Classical}} = 0.80 \pm 0.04$, again consistent with the predicted phase super-sensitivity of 0.79 ± 0.05 (Sect. 5.4.2) and close to the theoretical bound of $1/\sqrt{2} \approx 0.707$.

5.5 Discussion

Our proof-of-principle demonstration of quantum-enhanced imaging represents a first step towards a real-world advantage for specific bio-imaging use cases that require imaging sample phases with a lower photon number than classically possible. As pointed out in Ref. [173] and [11], besides photodamage, which is readily

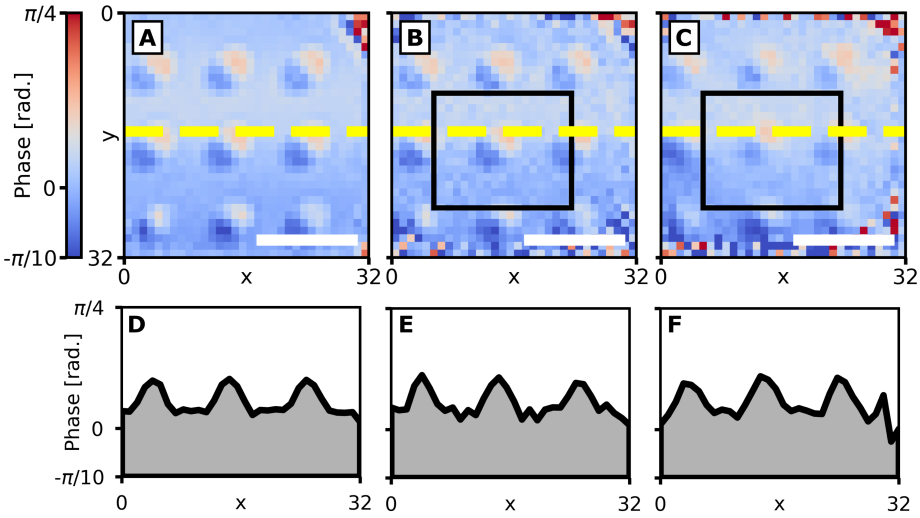

FIGURE 5.10: **Retrieved phase images of a non-birefringent protein microarray sample.** **(A)** Reference phase image from high intensity classical illumination. **(B)** Low intensity (single-photon level) classical illumination phase image $\hat{\phi}_{\text{Classical}}$. **(C)** Entanglement-enhanced phase image $\hat{\phi}_{\text{N00N}}$. **(D)-(F)** Cross-sections of phase profiles along yellow dashed lines in **(A)-(C)**. Black rectangles in **(B)** and **(C)** indicate area used for *LU* calculations. All three experimental conditions show clear contrast between regions of high protein binding (circular spots) to regions with no binding (background). The entanglement-enhanced method **(C)** manifests less pixel-to-pixel noise than its classical counterpart **(B)**, for an equal number of photons detected. Scale bars, 2 mm at sample plane.

observed upon sample inspection, also experimentally significant are photosensitive effects caused by illumination levels orders of magnitude below the damage threshold. Such effects may not be obvious to the user but still adversely affect measurement reliability, and include altering of gene expression [149], enzyme activity [152], and acceleration of oxidation and reduction reactions in cells [148]. Comprehensive quantitative data on these phenomena is scant [173], especially for phase imaging, which has only recently begun to supplant fluorescence microscopy in biomedical applications [8]. However, for instance, for Ref. [152] rough calculations indicate that light-induced changes become noticeable starting from only $\sim 10^9 - 10^{11}$ photons at the cell level – a light budget comparable to illumination levels enabled by state-of-the-art entangled photon sources. A promising application for quantum-enabled super-sensitive imaging may then be the long-term inspection of photosensitive bio-samples, such as the monitoring of biomarkers from a patient subjected to an evolving disease [163], or the characterization of slow changes in neural cells [174]. In such a case a small photon budget must be stretched across a period of hours or days, and therefore even the $\sqrt{2}$

sensitivity enhancement enabled by 2-photon N00N states would lead to a useful improvement in measurement capacity.

Moreover, it is straightforward to extend our protocol to larger N00N states or other non-classical light states with $N > 2$ photons. Analogously to what is shown here, if all N photons of the state are spatially correlated, a SPAD array camera can measure the $N > 2$ multi-photon coincidence images, so the phase can be retrieved using PSDH with a theoretical sensitivity enhancement of $\sqrt{N}$, rather than the $\sqrt{2}$ factor currently afforded by entangled photon pairs. However, using SPDC to generate N00N states with many photons is experimentally very challenging, with past demonstrations showing only probabilistic generation of N00N states with relatively small N [145, 160]. On the other hand, recent progress in quantum dot, and cavity based entangled photon sources has been promising [175–177], and we are therefore hopeful that N00N state sources with high N may become available in the future, which will enable greater sensitivity enhancements in our system.

In our experiment, the image resolution of 32×32 pixels was only limited by the sensor of our SPAD array camera. Based on recent developments of megapixel resolution SPAD arrays [155, 178], we expect that our protocol can be fully exploited for highly detailed quantum-enhanced phase imaging. We note that our protocol becomes susceptible to errors when the correlation width between photons is comparable to the sample feature size, as in this case it is likely that the two photons acquire different phases. This implies a breakdown in the approximations that lead to Eq. 5.1 (i.e. the condition $\Theta(\mathbf{r}) \approx \Theta(\mathbf{r}')$ is no longer satisfied), and leads to reduced edge contrast, as can be seen in the blurred edges of the "ϕ" pattern in Fig. 5.8D. Entangled photon sources with a tighter photon pair correlation width will therefore improve spatial resolution.

Sensitivity comparisons between the classical and quantum-enhanced measurements were made here for an equal number of photons counted, with post-selection used for coincidence counting (see Sect. 4.3.3). Photon losses due to imperfect optical efficiencies were not taken into account, which is standard practice in almost all works on quantum-enhanced phase measurements to date [19, 37, 38, 160]. However, as N00N state phase measurements are highly sensitive to loss, a real sensitivity advantage can only be shown by comparing an equal number of photons at the sample [107], which necessitates very high optical efficiencies [147]. To this end, future work will focus on developing entangled photon sources at shorter wavelengths in combination with enhanced efficiency SPAD array cameras [179], in order to dramatically improve system optical efficiency. Another promising approach would be to use superconducting nanowire single-photon detectors (SNSPD), which routinely achieve detection efficiencies of close to unity [106]. In particular, SNSPD image sensors have recently been demonstrated [180, 181] which, while currently possessing some limitations, could in future be used for the required high efficiency coincidence image detection. Lastly, future work will also focus on modifying our method to achieve enhanced phase imaging using other quantum states that have less demanding optical efficiency requirements than N00N states [146, 182–185]. We are therefore optimistic that the technological requirements for our method to yield a true quantum advantage over classical phase measurements will soon be met.

In this work the coincidence acquisition speed was limited by the SPAD camera readout scheme and photon detection efficiency (PDE), which resulted in much longer quantum imaging acquisition times than for the classical case. Firstly, we employed a SPAD camera intended for general use, that thus reads out and transfers information for all pixels regardless of whether they detected a photon or not, in every frame. Thus, the shortest achievable frame time is simply the readout time per pixel multiplied by the number of pixels, in our case 10.4 µs. This is $\sim 10^3$ times longer than the exposure time per frame, leading to a very low duty cycle and correspondingly slow acquisitions. Moreover, as we image with low photon numbers, a large overhead of useless data (pixels with no detections) is generated. To solve this issue, future work will make use of emerging SPAD arrays specialized for sparse event detection, with optimized asynchronous or event-driven readout schemes that only read out and transfer useful coincidence information [39]. Secondly, for a given PDE η, the coincidence detection efficiency is η^2 – in our case yielding an available coincidence detection rate $\sim$30 times lower than single-photon detection. We anticipate further improvements in detection technology that will allow this problem to be addressed in the foreseeable future. See Appendix B for a more detailed exploration of these details and a comparison with single-pixel detector scanning based imaging.

Note that despite also using holographic phase retrieval, the phase imager presented in this work is quite different from the quantum-enabled holography technique from Ref. [31]. In that work two photons are spatially separated and non-local photon correlations are needed for holographic reconstruction. In our system on the other hand, both entangled photons pass through the sample together, which is the crucial aspect that enables our system to achieve super-sensitive phase imaging.

We also note that the optical centroid measurement (OCM) coincidence image mapping, as introduced by Ref. [24] and used for example in Ref. [25], is not suitable for a direct phase sensitivity comparison with classical images (as is the main aim of this chapter). The OCM maps a four-dimensional two-photon coincidence vector (e.g. Eq. 3.31) onto the two-dimensional coordinate $(\mathbf{r}_i + \mathbf{r}_j)/2$ with four times the number of (virtual) pixels compared to the physical SPAD array (a factor of two on each axis) [186]. Therefore, for an equal number of total photons across the field-of-view (FoV), an OCM-mapped coincidence image will have only one quarter of the photons per pixel as a classical image, with correspondingly higher noise, thereby negating any possible photon-number advantage. The unsuitability of the OCM for super-sensitive phase imaging is not surprising when considering its aim of spatial super-resolution [24, 25], as it is true in general that a larger total light budget is required for imaging smaller spatial features without decreasing sensitivity.

In conclusion, we have successfully implemented a practical large FoV, scan-free quantum-enhanced phase imaging protocol, capable of retrieving phase images with decreased noise compared to equivalent classical measurements. Our system uses space-polarization hyper-entanglement, generated by an integrated source of quantum light, and combines a lens-free interferometric microscope

with robust phase-scanning mechanism and novel data processing of images produced by a SPAD array camera. Polarization entanglement is exploited as a resource for phase super-sensitivity, while photon pair spatial correlations ensure that coincidence detections are confined to nearby pixels, thereby enabling scan-free simultaneous multi-photon imaging on many spatial modes across the whole FoV. For birefringent and non-birefringent phase samples we measured reductions in noise of the retrieved phase images, by factors of 0.72 ± 0.06 and 0.80 ± 0.04, whose inverse values yield the sensitivity enhancements of 1.39 ± 0.11 and 1.25 ± 0.06, respectively. Precise measurement of a protein microarray demonstrate that biomarkers can be well identified. We expect systematic calibrations of the phase-response of specific samples to allow identifying biomarker concentration. This advance shows compatibility of our quantum-enhanced method with medical diagnostic applications, with further use cases extending to a range of material and biological inspection tasks such as monitoring photoresist-based microfabrication, inspection of semiconductor and crystal materials, and observation of living organisms without inducing cellular damage or photosensitive effects. We believe that with realistic future developments our technique will be highly competitive with respect to classical alternatives in which delicate samples cannot be analysed without risks of being significantly altered or even damaged, and that this work is thus an important step towards practically useful quantum imaging.

Chapter 6

Fast Quantum Imaging with Visible-Wavelength Entanglement

6.1 Abstract

Quantum resources can provide supersensitive performance in optical imaging and sensing. Detecting entangled photon pairs from spontaneous parametric down conversion (SPDC) with single-photon avalanche diode (SPAD) image sensor arrays (ISAs) enables practical wide-field quantum-enhanced imaging. However, matching SPDC wavelength to the peak detection efficiency range of complementary metal oxide semiconductor (CMOS) compatible mass-producible SPAD-ISAs has remained technologically elusive, resulting in low imaging speeds to date. Here, we show that a recently developed visible-wavelength entangled photon source enables high-speed quantum imaging. By operating at high detection efficiency of a SPAD-ISA, we increase acquisition speed by more than an order of magnitude compared to previous similar quantum imaging demonstrations. Besides being fast, the quantum-enhanced phase imager operating at short wavelengths retrieves nanometre scale height differences, tested by imaging evaporated silica and protein microarray spots on glass samples, with sensitivity improved by a factor of 1.351 ± 0.004 over equivalent ideal classical imaging. This work represents an important stepping stone towards scalable real-world quantum imaging advantage, and may find use in biomedical and industrial applications as well as fundamental research.

6.2 Introduction

Chapter 5 describes our realization of the first wide-field super-sensitive phase imaging system, enabled through hyper-entangled photon pairs and SPAD array camera coincidence imaging. This proof-of-principle demonstration provides a scalable path towards improving measurement capability in some applications, such as imaging sensitive biological samples, including live cells and organisms, which can be altered or even damaged if the illumination brightness is too high [148, 149, 151, 152]. Quantum-enhanced techniques, as in Chapter 5, are expected to be of particular use in specialized cases when photon budget is limited and acquisition times are long [174].

Notwithstanding promising results, the system presented in Chapter 5 does not yet provide any "real-world" usefulness. To this end, two key aims are speed and practicality. For practicality, the most important recent advance is represented by SPAD image sensor array (ISA) cameras fabricated in standard complementary metal oxide semiconductor (CMOS) processes, due to their scalability (and therefore potential cost-effectiveness), and low-noise coincidence imaging capability (as discussed extensively in Sect. 3.2.1 and 3.2.2) without requiring active cooling [39]. However, the speed of quantum imaging with SPDC photon pairs is at present far lower than in classical counterparts, limiting quantum-enabled improvements to academic interest. In Chapter 5 (Ref. [144]) we identified two main factors as the cause of current low imaging speeds: low photon detection efficiency (PDE) in SPAD-ISAs for photon pairs at the common near-infrared (NIR) SPDC emission wavelength (typically $\sim$800 nm), and low detector duty cycle.

Here, we address the first of the two aforementioned issues, and show that short-wavelength SPDC is an enabling technology for fast and practical quantum imaging. Fabrication of mass-scalable SPAD-ISAs must adhere to standard CMOS processes, resulting in very few customizable design parameters. In particular, a limited thickness of SPAD photon absorption regions presents a fundamental barrier to achieving high PDE at NIR wavelengths [42]. On the other hand, CMOS SPAD-ISA efficiencies peak in the green visible wavelength range, and can be even further optimized to approach the values of other image sensor technologies [115, 155]. In this work, we take advantage of this, and demonstrate a quantum imaging system using a recently developed green visible-wavelength (532 nm) entangled photon pair source (EPS), generating hyperentanglement in polarization and space [73]. This visible-wavelength EPS (VEPS) is combined with a compact and stable, large field-of-view ($\sim 4 \times 4\text{mm}^2$) phase imager to perform supersensitive phase imaging [144]. We show that our VEPS-enabled quantum imaging scheme is able to accurately retrieve the features of two test samples – an electron-beam evaporated silica pattern on glass, and a protein microarray. These measurements illustrate our technique's potential applicability to real-world uses, as imaging nanometre-scale height steps has important applications in semiconductor metrology [187], while protein microarrays represent a widely used biomedical diagnostic tool [172]. Introducing a phase sensitivity calculation independent of sample spatial features, we show the supersensitivity of our quantum imaging scheme which yields an increase in SNR by a factor of 1.351 ± 0.004. This is

close to the theoretically predicted $\sqrt{2} \approx 1.414$ enhancement. Compared to imaging with the widely used $\sim$800 nm EPS, for our two samples, our VEPS enabled speedups by a factor of 39, and 60, respectively. This is consistent with our SPAD-ISA's $\sim$5.3$-$9.5-fold PDE increase from the NIR to 532 nm, that is, corresponding to a $\sim$28$-$90 times higher coincidence efficiency [115].

6.3 Experimental setup and methods

Our wide-field quantum imaging platform is optimized for the measurement of large area transparent samples. Here, we improve upon the setup from Chapter 5 [144], probing again a sample held in a large field-of-view (FoV) interferometric microscope (LIM, see Sect. 5.3.1), this time using visible wavelength space-polarization hyper-entangled photon pairs. As in Chapter 5, we use the photon-counting Micro Photon Devices SPC3 SPAD camera (pixel pitch 150 µm, pixel fill factor 78%), which has PDE of $\sim$35$\pm$3% at 532 nm, compared to $\sim$5$\pm$1% at 810 nm [115].

6.3.1 Optical setup with visible-wavelength EPS

As can be seen in Fig. 6.1a, hyper-entangled photon pairs are generated in our setup by SPDC, using a crossed-crystal geometry VEPS (see Sect. 2.3.4) [73]. The collimated pump laser at 266 nm (Toptica TopWave, continuous wave, linewidth $<$1 MHz) is prepared in the diagonal polarization $|D\rangle$, (following notation established in Sect. 2.2.2). The pump then passes through four barium borate (BBO) crystals sequentially. In the first (second) BBO crystal, 532 nm wavelength photon pairs are generated by SPDC with H (V) polarization. The third and fourth BBO crystals compensate spatial walk-off between the two SPDC processes, a band-pass filter (BPF) then removes the pump, and an yttrium vanadate (YVO4) crystal is used for temporal compensation. This leaves the polarization-entangled two-photon N00N state.

The SPDC near-field is imaged onto the sample in the LIM, and then re-imaged onto the SPAD camera sensor, using two pairs of lenses in 4f configuration (see Fig. 6.1a). Therefore, as in Chapter 5, we obtain at the sample and detection planes the hyper-entangled state $|\Psi\rangle(\mathbf{r}) \approx \sum_{\mathbf{r},\mathbf{r}'}(|HH\rangle_{\mathbf{r},\mathbf{r}'} + \exp(i2\Theta(\mathbf{r}))|VV\rangle_{\mathbf{r},\mathbf{r}'})$ [82, 170]. This is equivalent to Eq. 5.1 and Eq. 2.46, where again we neglect normalisation coefficients for clarity, The term Θ represents the spatially dependent phase difference between H and V induced by the LIM and sample in each photon, and $\mathbf{r}$ and $\mathbf{r}'$ are the transverse coordinates of the two spatially correlated photons. As in Sect. 5.3.2, we have $\mathbf{r} \approx \mathbf{r}'$ is true, which implies $\Theta(\mathbf{r}) \approx \Theta(\mathbf{r}')$. That is, $|\Psi\rangle$ acquires a total phase factor of $2\Theta(\mathbf{r}) \approx \Theta(\mathbf{r}) + \Theta(\mathbf{r}')$. Lastly, a half-wave plate (HWP) and a lateral displacement polarizing beam-splitter (dPBS) project the state $|\Psi\rangle$ into the diagonal polarization measurement bases $|DD\rangle$, $|AA\rangle$, and $|DA\rangle$ before the SPAD camera.

We note that the crossed-crystal scheme here is considerably more simple to align, and that therefore the alignment procedure described for a Sagnac interferometer geometry (Sect. 5.3.3) is unnecessary. On the other hand, we note that

light must be spatially filtered in the far-field after the VEPS with a 2.5 mm aperture. This reduces the photon pairs' momentum distribution in order to minimize k-vector-dependent phase distortion inherent in crossed-crystal EPS designs [188].

6.3.2 Measuring height steps with the LIM

Section 5.3.1 introduced in some detail the large field-of-view (FoV) interferometric microscope (LIM). Here we briefly elaborate on this, in order to show explicitly how the LIM can be used to infer nanometric height steps of the features of transparent samples with known refractive index.

As illustrated in Fig. 6.1b, a non-birefringent target sample is placed between the two LIM Savart plates (SPs; SP_1 and SP_2), i.e. corresponding to the configuration shown also in Fig. 5.1b. At every lateral spatial location the LIM can be considered to form a Mach-Zehnder interferometer (MZI) for each lateral spatial location, with displacement $\mathbf{S}$ between the MZI modes. The effect of the LIM on every photon is to introduce a phase between H and V, which can be expressed in terms of the sample feature height (see Fig. 6.1b):

$$\begin{aligned}\Theta(\mathbf{r}) &= \frac{(h(\mathbf{r}+\mathbf{S}/2)-h(\mathbf{r}-\mathbf{S}/2))(n_{\text{Sample}}-n_{\text{Air}})}{\lambda/2\pi}+\alpha \\ &= \frac{\text{OPD}(\mathbf{r})}{\lambda/2\pi}+\alpha \end{aligned} \tag{6.1}$$

Here we assume a sample with uniform refractive index n_{Sample} and spatially dependent height $h(\mathbf{r})$, n_{Air} is the air refractive index, and λ is the photon wavelength. For convenience we also denote $\phi \equiv \text{OPD}/(\lambda/2\pi)$ as the phase factor induced by only the sample, which is positive or negative depending on whether the H or V trajectory is longer in the LIM.

6.3.3 Entanglement imaging method

As described in detail in Sect. 3.2.1, we can extract spatially resolved two-photon coincidences, cc between any two arbitrary pixels i and j, using a large number ($M \gtrsim 10^7$) of intensity image frames acquired by a photon-counting SPAD-ISA [30, 40]. Recall that Eq. 3.17 calculates the coincidences for a sub-acquisition (involving a sub-set of the M total binary frames) which we write here again for convenience:

$$\text{cc}(i,j,p,q) = \sum_{l=p}^{q} I_{l,i} I_{l,j} - \frac{1}{q-p+1} \sum_{m,n=p}^{q} I_{m,i} I_{n,j}. \tag{6.2}$$

This the coincidences from the p^{th} to the q^{th} intensity frame of an acquisition. The whole acquisition is recovered by setting $p = 1$ and $q = M$. As seen in Fig. 6.1a, the HWP and dPBS before the SPAD-ISA direct D (A)-polarized light to the left (right) half of the camera sensor. Therefore we can use Eq. 6.2 to directly measure

- $\langle DD|\Psi(\mathbf{r})\rangle$, $\langle AA|\Psi(\mathbf{r})\rangle$ – camera pixels i,j both on left or right half of sensor, respectively, and
- $\langle DA|\Psi(\mathbf{r})\rangle$ – pixels i,j on different halves of sensor.

Equation 6.2 cannot calculate coincidence counts for the case of both photons falling onto the same physical SPAD pixel [30]. This situation can occur in the DD and AA measurement bases, resulting in a slight loss of coincidence counts as compared to the DA measurement.

Analogous to Chapter 5, we follow the post-processing workflow for coincidence imaging established in Chapter 3. Cross-talk is removed using Eq. 6.2 (see Sect. 3.3.1), and coincidences are filtered using their position correlation (Sect. 3.3.2, Eq. 3.31). We then trace out the detection coordinates of one of the two photons to convert the filtered 4D coincidence count quantity into a 2D coincidence image $\mathrm{ci}_{pq}(x,y)$ (Sect. 3.4, Eq. 3.32). Note also that we optimized the EPS pump power ($\sim$80 mW) to obtain high coincidence counting SNR, which, following Sect. 3.5, is expressed by the dimensionless parameter $\kappa = 1.07 \pm 0.05$ (where $\kappa = 1$ for ideal SNR) [144].

Section 5.3.1 describes how motorized tilting of one of the SPs in the LIM induces a controlled bias phase α between H and V. Here we measured the coincidence interference visibility by monitoring $\mathrm{ci}(x,y)$ for different phase offsets α. Figure 6.1c shows the coincidences integrated across the whole camera, that is, $\sum_{x,y} \mathrm{ci}_{pq}(x,y)$ for each α, while Fig. 6.1d plots $\mathrm{ci}_{pq}(x_i,y_i)$ for a single fixed pixel $i \equiv [x_i,y_i]$. Both results show two interference periods as α goes from 0 to 2π, rather than a single period as in classical optics, manifesting therefore the signature of N00N states [10, 160]. However, while the fitted visibility of the single pixel coincidence curve (Fig. 6.1d) is $\mathcal{V}^{(\in)}_{\mathrm{local}} = 0.96 \pm 0.03$, the integrated coincidence curve (Fig. 6.1c) shows a lower visibility of $\mathcal{V}^{(\in)}_{\mathrm{overall}} = 0.75 \pm 0.02$. Similarly to Chapter 5, this discrepancy in visibilities is evidence of a spatially dependent phase background across the N00N state wavefront, which we measure and remove when imaging samples.

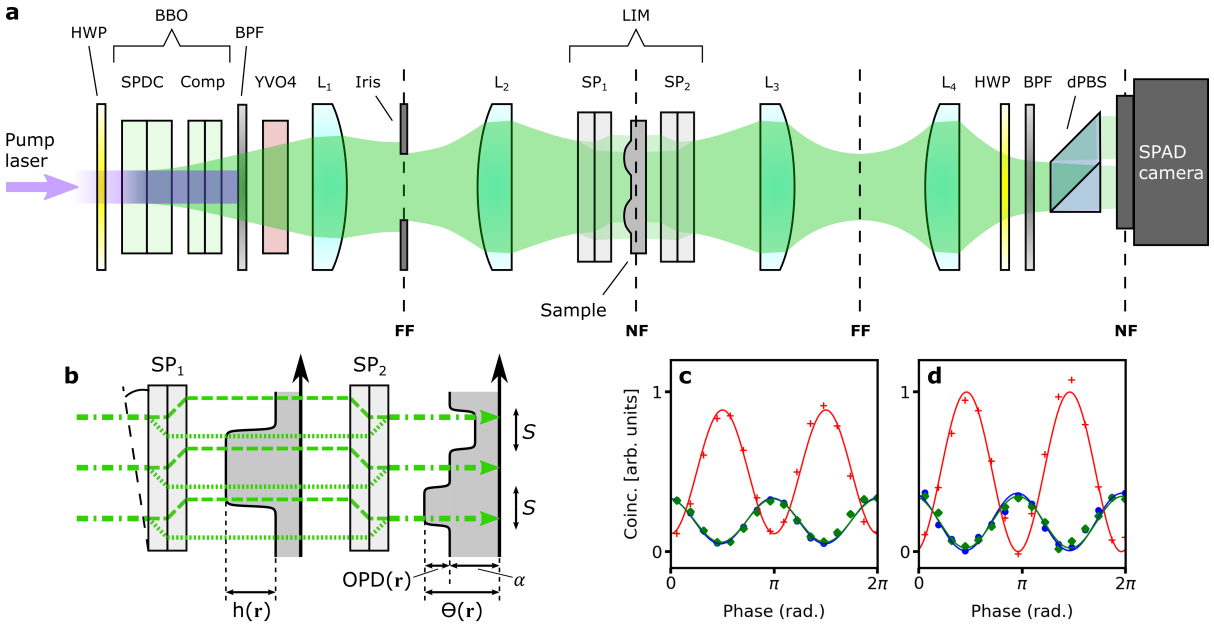

FIGURE 6.1: **(a)** Entanglement-enhanced imaging setup, 266 nm pump in violet, and entangled photon pair emission centered at 532 nm in green shading. HWP, half-wave plate; BBO, barium borate crystal (first pair for SPDC, second pair for compensation); BPF, band-pass filter; YVO4, yttrium vanadate crystal; L, lenses with focal lengths $f_1 = 100$ mm for L_1, $f_2 = 1000$ mm for L_2, $f_3 = f_4 = 200$ mm for L_3, L_4; SP, Savart plate; dPBS, lateral displacement polarizing beam splitter. **(b)** Detecting nonbirefringent sample height steps with the LIM. Example trajectories through the LIM: dashed lines, H; dotted lines, V. **(c)** N00N state interference integrating across whole camera. **(d)** N00N state interference with a single fixed pixel. For **(c)** and **(d)**: red crosses, $\langle DA|$; blue circles, $\langle DD|$; green diamonds, $\langle AA|$ projections. Solid lines are fitting curves.

6.4 Accurate phase imaging of test samples

To demonstrate the fast and accurate quantum-enhanced imaging capability of our system, we measured two test samples representative of possible use cases. First, we acquired a phase image of a silica test sample, and confirmed the accuracy of our quantum-enhanced step height estimation using an atomic force microscope (AFM) scan. Second, we demonstrated the potential applicability of our platform in the biomedical field, by imaging a protein microarray sample. Samples were illuminated with our VEPS, and coincidence images detected with the SPAD camera. Phase-shifting digital holography (PSDH) was then used to retrieve the phase induced by the sample (Sect. 4.2.1), acording to Eq. 4.21. The offset phases $\alpha = \{0, \pi/(2N), \pi/N, 3\pi/(2N)\}$ required by four-step PSDH (with $N = 1$ for classical, $N = 2$ for quantum) are set by tilting the LIM's first Savart plate (see Sect. 5.3.1).

6.4.1 Silica test sample

A silica test sample was fabricated in-house, by electron-beam evaporating silica steps of controlled height onto a borosilicate glass substrate, in the shape of the word “ICFO" as shown in Fig. 6.2c. The phase image of this silica test sample, retrieved from N00N state interference, can be seen in Fig. 6.2a, where the letters “ICFO" can readily be made out. As illustrated in Fig. 6.1b, when using the LIM to measure a non-birefringent sample, the retrieved phase contains a positive and negative double-image, which is clearly visible in Fig. 6.2a. In Fig. 6.2b we plot the x cross-sections along all rows in the area defined by the black rectangle in Fig. 6.2a, where again the positive and negative steps in phase measured are clearly visible.

Fig. 6.2a shows the phase induced by the sample $\hat{\phi}^{(2)} = \mathrm{OPD}_{\mathrm{exp}}/(\lambda/2\pi)$, expressed in radians. Recall that the "(2)" superscript indicates explicitly that this $\hat{\phi}^{(2)}$ refers to a phase estimate retrieved from a two-photon N00N state interferometric measurement (see Chapter 4). For Fig. 6.2b, we used Eq. 6.1 to convert $\hat{\phi}^{(2)}$ to the height difference $\Delta\mathrm{Height} = h(\mathbf{r} + \mathbf{S}/2) - h(\mathbf{r} - \mathbf{S}/2)$, in terms of nanometres. This required the refractive indices of silica and air at 532 nm, $n_{\mathrm{Sample}} = 1.46$ and $n_{\mathrm{Air}} = 1.00$ [189]. Taking the difference between, respectively, the mean of the ΔHeight values in the upper blue and orange shaded regions with the average of the ΔHeight values in the lower blue and orange shaded regions in Fig. 6.2b, gives an experimental estimate the sample feature step height of $h_{\mathrm{exp}} = 44 \pm 8\,\mathrm{nm}$. We confirmed the sample step height with a reference AFM measurement, as shown in Fig. 6.2c and d, where Fig. 6.2c illustrates the region on our sample scanned by the AFM as well as the AFM, and Fig. 6.2d the cross-section showing clearly the jump in sample height at the feature step. Taking the difference between the mean heights of the two grey shaded regions in Fig. 6.2d, we obtain the reference AFM measurement of the silica sample step height $h_{\mathrm{ref}} = 44.7 \pm 0.4\,\mathrm{nm}$. Our quantum-enhanced imaging system was therefore able to retrieve the sample feature height with a high degree of accuracy, thereby confirming its suitability for material science inspection tasks of transparent samples involving nanometre-scale variations in structure height.

The acquisition time for obtaining the image in Fig. 6.2a was 1200 s, and with a total number of detected coincidences of 7.2×10^5 this corresponds to a coincidence detection rate of 6.0×10^2 s^{-1}. In contrast, the fastest acquisition in Chapter 5 (Ref. [144]) counted 1.55×10^6 coincidences over a total measurement time of 28 hours, corresponding to a coincidence detection rate of 1.5×10^1 s^{-1}. Therefore, here our VEPS enabled a 39-fold increase in quantum-enhanced imaging speed compared to 5.

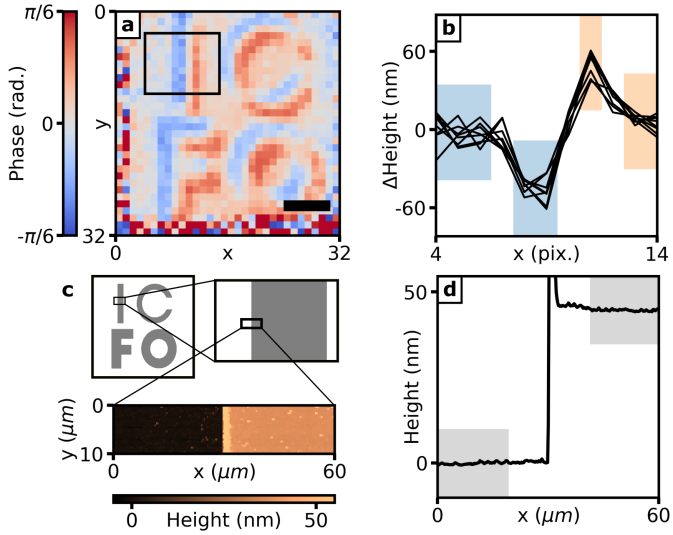

FIGURE 6.2: **Quantum-enhanced phase imaging using VEPS of silica test sample.** **(a)** Entanglement-enhanced phase image of silica sample. **(b)** cross-sections in x direction of the area defined by black rectangle in **(a)**. For the blue and orange shaded regions respectively, subtracting the mean of the right from the left regions, yields the experimental estimate of the phase induced by the sample. **(c)** AFM image of sub-section of test sample, showing jump in height from substrate to step. **(d)** Average cross-section of AFM image in (c). Scale bar in **(a)**, 1 mm both at sample and camera sensor plane.

6.4.2 Protein microarray test sample

For the second sample, as in Chapter 5, we measured a microarray of protein spots. Accurate quantum-enhanced imaging in this case demonstrates our system's potential applicability to biomedical use cases, as protein microarrays are used as clinical diagnostic tools (See Sect. 5.4.4 for details).

The microarray test sample was fabricated in-house, following the procedure described in Sect. 5.4.4 (diluting the protein solution here to 250 µg/mL). A phase image of this sample, retrieved from N00N state interference, can be seen in Fig. 6.3a, where several protein spots can readily be made out. Cross-sections of the phase image along dashed lines in Fig. 6.3a, shown in Fig. 6.3b and c, also confirm the

detection of individual protein spots. Unlike for the silica test sample (Sect. 6.4.1), it was not possible to confirm phase measurements of the mechanically fragile microarray using an AFM. We therefore acquired a reference image with bright classical illumination (i.e. using many more photons than for Fig. 6.3a), which is shown in Fig. 6.3d. Comparing Fig. 6.3d, and cross-sections in Fig. 6.3e and f, with the corresponding entanglement-enabled images Fig. 6.3a-c clearly confirms the accuracy of our quantum-enhanced imaging system.

The image in Fig. 6.3a was obtained over a total acquisition time of 3600 s, and is made up of 3.3×10^6 detected coincidences, corresponding to a coincidence detection rate of 9.2×10^2 s^{-1}. Therefore, compared to the coincidence detection rate of 1.5×10^1 s^{-1} in Chapter 5 (Ref. [144]), our VEPS-illuminated imager again enabled a huge improvement in quantum-enhanced imaging speed, by a factor of 60.

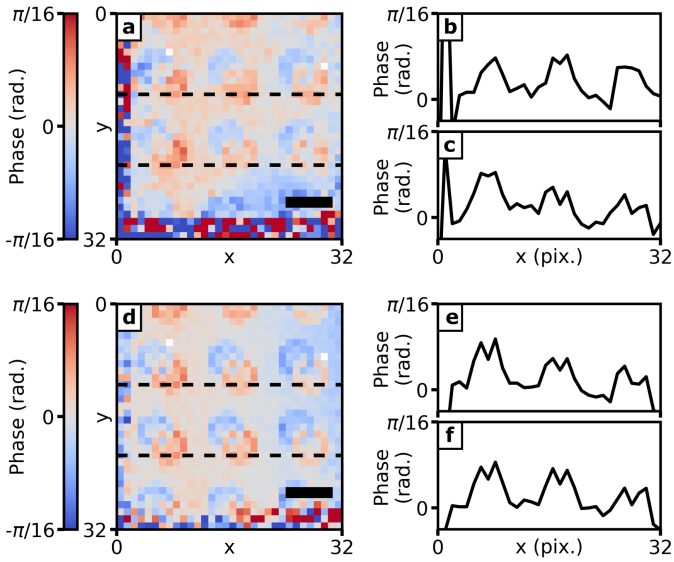

FIGURE 6.3: **Quantum-enhanced phase imaging using VEPS of protein microarray . (a)** Entanglement-enhanced phase image of protein microarray sample. **(b)** and **(c)** x cross-sections along upper and lower dashed black lines in **(a)**, respectively. **(d)** Bright classical illumination reference phase image of protein microarray sample. Colour scale the same as in **(a)**. **(e)** and **(f)** x cross-sections along upper and lower dashed black lines in **(d)**, respectively. Scale bars in **(a)**, **(d)**, 1 mm both at sample and camera sensor plane.

6.5 Supersensitivity of phase imaging

In order to prove super-sensitivity of our entanglement-enhanced phase imaging results, in Chapter 5 we compared quantum-enhanced and classical phase images

using the local uncertainty (LU), which quantifies pixel-to-pixel noise [38, 144]. However, the LU requires that images being compared have identical distribution of (lateral) spatial features. This is because we want to quantify the pixel-to-pixel differences that arise solely from noise in the phase measurements, and not from any differences in the actual spatial pattern. Therefore, there is an inherent difficulty in choosing the region of interest (ROI) for comparing LUs – for example, in Fig.5.8 it was necessary to compare ROIs well-separated from the "ϕ" feature in order not to "contaminate" the sensitivity calculation with the difference in lateral spatial resolution between Fig.5.8a and c.

It would be more rigorous to quantify a sensitivity enhancement without assuming identical lateral spatial features. Moreover, some quantum imaging modalities provide higher lateral spatial resolution than possible with classical illumination [24, 25, 186], in which case the assumption of identical spatial features will necessarily be broken. Therefore, here we extend the method from Ref. [107] to the imaging domain. This yields an empirical measure of phase uncertainty for every pixel *individually*, without reference to variations with neighbouring pixels. This phase uncertainty estimation can then compared to the theoretically expected noise of an ideal classical measurement with an equal number of photons.

We begin by recalling that the PSDH formula Eq. 4.21 retrieves the phase for N00N state interference coincidences. We can write this in terms of the coincidence images calculated from a sub-set of the full acquisition. Explicitly, for the sub-acquisition calculated using the p^{th} to the q^{th} binary intensity frames, the retrieved phase estimation is

$$\hat{\phi}^{(2)}_{pq}(\mathbf{r}) = \frac{1}{N}\tan^{-1}\left[\frac{\text{ci}_{pq}(\mathbf{r},\pi/(2N)) - \text{ci}_{pq}(\mathbf{r},3\pi/(2N))}{\text{ci}_{pq}(\mathbf{r},\pi/N) - \text{ci}_{pq}(\mathbf{r},0)}\right], \tag{6.3}$$

with $N = 2$ in our case, and $\text{ci}_{pq}(\mathbf{r},\alpha)$ being calculated for the DD, AA and DA projections (the three $\hat{\phi}^{(2)}_{pq}(\mathbf{r})$ estimates are then combined using Eq. 4.22). Recall again that the "(2)" superscript in $\hat{\phi}^{(2)}_{pq}(\mathbf{r})$ tells us that this phase estimate is retrieved from a two-photon N00N state interferometric measurement (see Chapter 4). Therefore, as detailed in Sect. 3.2.1, the full acquisition with M total frames is subdivided into Q sub-acquisitions (setting $(p,q) = [(1,M/Q),(M/Q+1,2M/Q),...,((Q-1)M/Q+1,M)]$). This yields Q different $\hat{\phi}^{(2)}_{pq}$ phase estimates, each calculated from M/Q camera frames. Some example sub-acquisition phase estimates $\hat{\phi}^{(2)}_{pq}$ are shown in Fig. 6.4, for the protein microarray test sample, and for four different numbers of sub-acquisitions $Q = 4, 8, 32, 64$. This corresponds to the full measurement over 3600 s being divided into shorter equally sized sub-acquisitions of respective durations 900 s, 450 s, 112.5 s, and 56.25 s. Figure shows all Q sub-acquisition phase values for the single pixel indicated by the black "X" in Fig. 6.4.

Now, as can be seen clearly in Fig. 6.4, for each pixel there is a variation over the retrieved sub-acquisition phase estimates. Therefore, for every pixel we can compute the standard deviation over these sub-acquisition retrieved phase values. That is, we obtain $\text{sd}(\hat{\phi}^{(2)}(\mathbf{r},Q))_{\text{emp}}$ which is an empirical measure of the

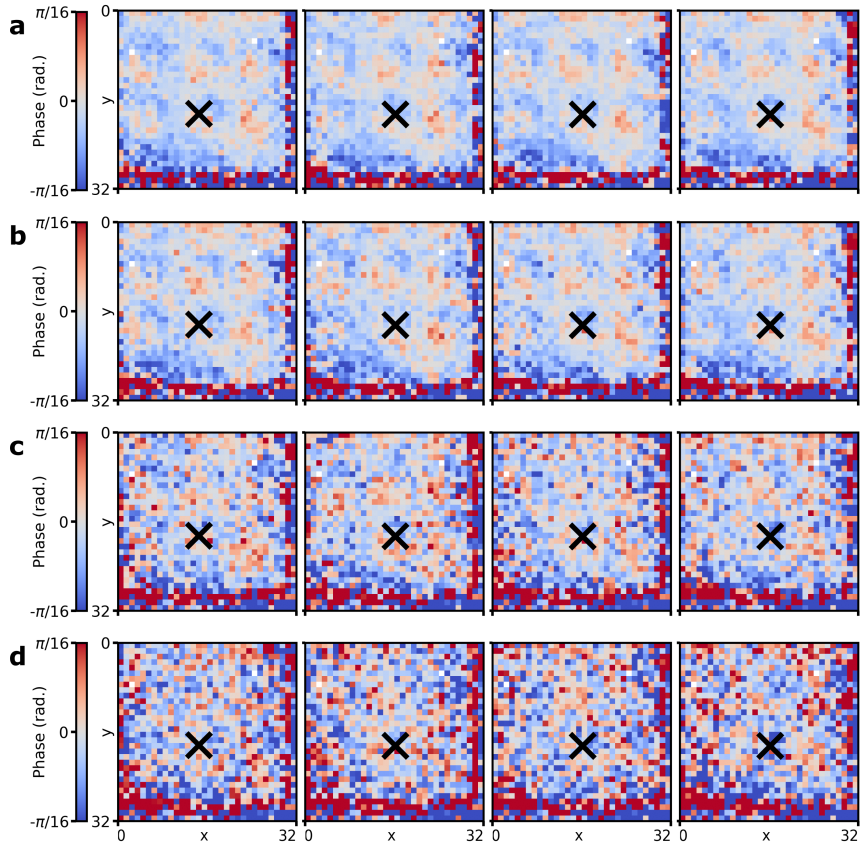

FIGURE 6.4: **Phase images retrieved from coincidence sub-acquisitions.** Each row shows first four of Q equal sub-acquisitions, where in **(a)** $Q = 4$, **(b)** $Q = 8$, **(c)** $Q = 32$, **(d)** $Q = 64$.

uncertainty in retrieved phase for each pixel, without requiring comparison to neighbouring pixels that relies on assumptions about the spatial features of the image. In order to prove super-sensitivity, we now simply have to demonstrate that $\mathrm{sd}(\hat{\phi}^{(2)}(\mathbf{r}, Q))$ is lower than $\mathrm{sd}(\hat{\phi}^{(1)})$, the theoretical phase uncertainty of an ideal classical measurement using the same number of photons. For a given Q, the mean number of photons used per sub-acquisition on a given pixel is $M(\mathbf{r}, Q) = (2/Q)\sum_{j=0}^{3} \mathrm{ci}_{pq}(\mathbf{r}, \alpha = j\pi/4)$, that is, summing over all four offset-phase settings, and multiplying by two as as each coincidence consists of two single photons. The theoretical phase uncertainty of an ideal classical PSDH-retrieved phase measurement is given by Eq. 4.44, which we reiterate here for convenience:

$$\mathrm{sd}(\hat{\phi}^{(N)}) = \frac{\kappa^{(N)}}{N\mathcal{V}^{(N)}\sqrt{2\eta^{(N)} I_{\mathrm{IN}}^{(N)}}}, \tag{6.4}$$

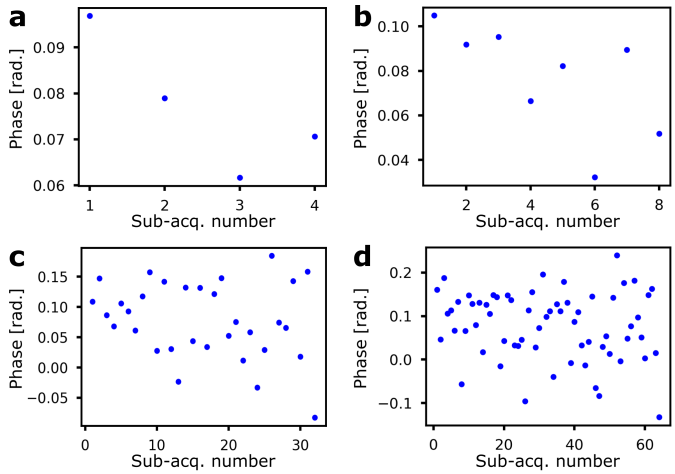

FIGURE 6.5: **Variation in phase values over coincidence sub-acquisitions.** Retrieved phase values from all Q sub-acquisitions for the single pixel marked by black "X" in Fig. 6.4. **(a)** $Q = 4$, **(b)** $Q = 8$, **(c)** $Q = 32$, **(d)** $Q = 64$.

where we set $N = 1$, $\kappa^{(1)} = 1$, $\mathcal{V}^{(1)} = 1$, and $M = M(\mathbf{r}, Q)$. Note that, as in Chapter 5, we count coincidences in post-selection here, which has the effect of artificially setting $\eta^{(2)} = (\eta^{(1)})^2 = 1$ and $\eta^{(1)} = 1$ (see Sect. 4.3.3).

We performed this analysis, dividing into $Q = \{16, 32, 64, 128\}$ equally sized sub-acquisitions. Fig. 6.6a shows $\mathrm{sd}(\hat{\phi}^{(2)}(\mathbf{r}, Q))$ for three example pixels, where the x-axis value for each data point is $M(\mathbf{r}, Q)$, the number of photons used. The dashed line represents the phase uncertainty from an ideal classical measurement ($\mathrm{sd}(\hat{\phi}^{(1)})$), while the solid line represents the theoretical uncertainty from a perfect 2-photon N00N state PSDH measurement, both as a function of the number of photons used. Clearly the empirically derived uncertainties, as shown in Fig. 6.6a, are lower than the classical bound, therefore indicating supersensitivity of the phase measurement. Error bars in Fig. 6.6a represent the statistical standard error, due to calculating standard deviation from a finite sample size. In Fig. 6.6b we show the spatially resolved enhancement in phase imaging afforded by our entanglement-enabled method. That is, using $Q = 64$ sub-acquisitions, for every single pixel, Fig. 6.6b plots the experimental phase uncertainty $\mathrm{sd}(\hat{\phi}(\mathbf{r}, Q))$ divided by the theoretical noise of an equivalent perfect classical measurement. A value below 1 in this noise reduction is therefore evidence of phase supersensitivity, which in Fig. 6.6b is represented by a blue pixel colour, showing that our system achieved supersensitivity over practically the entire FoV. We attribute the region of higher experimental noise in the bottom right corner to the presence of stray light hitting the sensor there. Fig. 6.6c shows a cross-section along the yellow dashed line in Fig. 6.6b, where the shaded area represents the statistical standard error, again due to calculating standard deviation from a finite sample size.

Fig. 6.6c clearly shows again the reduction in phase measurement noise of our system with respect to an ideal classical measurement, with a reduction close to the theoretically expected value of $1/\sqrt{2}$. By taking the mean over the area defined by the rectangle in Fig. 6.6b, we calculated the average noise reduction afforded by our method to be 0.740 ± 0.002. Taking the inverse therefore yields an average increase in sensitivity over the entire FoV of $\mathcal{S}^{(2)} = 1.351 \pm 0.004$, which is close to the theoretically expected ideal sensitivity enhancement of $\mathcal{S}^{(2)}_{\max} = \sqrt{2} \approx 1.414$.

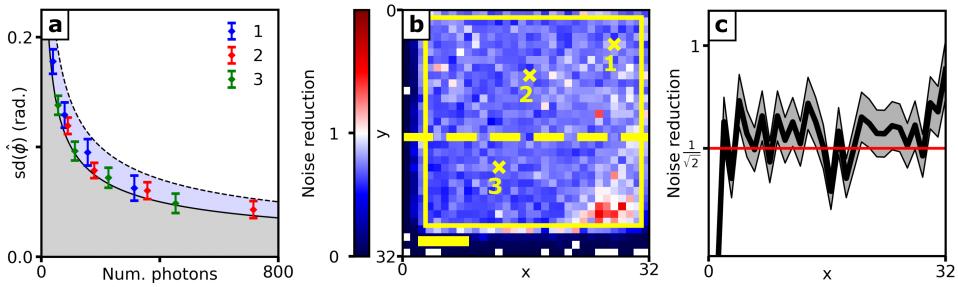

FIGURE 6.6: **(a)** Number of detected photons vs empirically measured phase uncertainty, for three example pixels. Blue shaded region, phase uncertainty lower than for ideal classical measurement. Grey shaded region, phase uncertainty lower than for ideal 2-photon N00N state measurement. **(b)** Reduction in noise enabled by quantum-enhanced method for all individual pixels. "X" show the location of pixels used for **(a)**. Rectangle, FoV used for calculating average sensitivity enhancement. Scale bar, 1 mm both at sample and camera sensor plane. **(c)** cross-section along dashed line in **(b)**.

6.6 Discussion

In this work we showed how the use of visible-wavelength entangled photon pairs results in dramatically higher detection efficiency, thereby addressing one of the two prominent issues that thus far prevented fast quantum imaging [144]. Indeed, for mass-producible CMOS SPAD array cameras, our method using VEPS illumination likely represents the only path towards high PDE quantum imaging, as standard CMOS fabrication processes place constraints on the thickness of a silicon SPAD pixel's photon absorption region, which fundamentally limits PDE at longer wavelengths [42]. The other issue discussed in Ref. [144] is camera duty cycle, which in the present work remains a limiting factor. This is due to the use of a general purpose SPAD camera, which reads out and transfers information for every pixel in every frame regardless of whether a detection occurred or not. The shortest possible frame readout time with the camera used here is 10.4 µs, which is obtained simply by multiplying the pixel readout by the number of pixels [115]. As the frame exposure time is 10 ns, we operate at a duty cycle

of ∼0.1%. However, this problem will be addressed in the near future through the use of a new generation of SPAD cameras, optimized for sparse coincidence imaging [39]. For example, the camera described in Ref. [123] can image coincidences at a rate of hundreds of kilohertz, with a duty cycle close to 100%, and has a modular design that can easily be scaled to large numbers of pixels. We anticipate therefore that, while using visible-wavelength entanglement here reduced measurement times from hours to minutes, the addition of sparse detection optimized SPAD array cameras will result in further speed improvements, to achieve real-time entanglement-enhanced quantum imaging at high spatial resolution.

We emphasize that with the present general purpose frame-based SPAD camera it would not be possible to simply use a longer frame exposure time in order to obtain a higher duty cycle, and thereby increase coincidence imaging speed. This is because the SPAD camera used here does not provide any timing information about photon detections within a frame [115]. Therefore, a longer exposure time results in lower SNR due to greater uncertainty about whether coincident photodetections originated from real SPDC photon pairs [116]. Increasing duty cycle without negatively affecting SNR therefore requires faster frame readout times and/or photodetection timing information (for example detection time-stamping), both of which are provided by the next-generation SPAD array described by Ref. [123]. When using a SPDC EPS with SPAD detectors it is generally also not possible to increase the generation rate (e.g. by increasing pump power) without incurring a penalty in SNR [116, 190]. Our technique is therefore not limited by currently achievable entangled photon emission rates.

In this work the supersensitivity of our quantum-enhanced imaging method was calculated using postselection for coincidence counting, without considering photon losses in detection. This is standard practice in almost all entanglement-enabled phase measurement experiments to date (with the notable exception of Ref. [107]), and does not affect the validity of quantum imaging proof-of-principle demonstrations [17, 37, 38, 144]. However, to achieve an actual quantum-enabled sensitivity advantage in real-world applications, detector efficiencies higher than $1/\sqrt{2} \approx 0.707$ are required when using 2-photon N00N states [107]. State-of-the art CMOS SPAD arrays are approaching this efficiency for the visible wavelength range; for example, Ref. [191] showed a PDE of 70% at 490 nm, while Ref. [155] demonstrated a PDE of 69.4% at 510 nm. Moreover, custom SPAD technologies are close to reaching these efficiencies in the red visible wavelength range, and may eventually become viable options for cameras [192]. Nevertheless, in the NIR, the critical threshold PDE $1/\sqrt{2}$ remains far out of reach for SPAD arrays [39], further emphasizing the need for visible-wavelength EPSs in useful quantum imaging. We note that recent research has identified entangled states that are more tolerant to loss in phase measurements than the N00N states used here, which may in future lower the required detection efficiency [183].

Sensitivity enhancements beyond the theoretical $\sqrt{2}$ factor in this work are enabled by states with $N > 2$ entangled photons [10, 18]. However, these are extremely challenging to experimentally realize with passive SPDC setups, in which photon generation is probabilistic and thus scales poorly for large N [10]. On the other hand, while currently lacking the required technological maturity to be used

in practical quantum imaging, alternative platforms capable of generating entanglement between many photons have shown promising developments. These include semiconductor quantum dots, high harmonic generation, trapped atoms, and SPDC combined with active feed-forward [177, 193–195]. Lastly, multipass methods represent a different approach that may yield practical supersensitive imaging, without requiring the generation of exotic large entangled states [182, 196].

An important feature of our imaging platform is its large FoV. We note that the AFM image in Fig. 6.2c only covers a very small area out of the entire test sample, which has dimensions 5 mm $\times$ 5 mm. The reason for this is that AFMs are not able to image the height of areas larger than a few $(100\,\mu\text{m})^2$, without complicated and labour-intensive scanning and image-stitching operations. Our quantum-enhanced phase imager on the other hand is able to image nanometre-height material samples of large areas in a single shot, representing an important advantage with respect to AFMs.

In conclusion, in this work we have demonstrated a fast and practical quantum-enabled supersensitive imaging platform. Through the use of a visible-wavelength (532 nm) EPS we optimized photon detection efficiency on our SPAD array camera. When imaging a silica and protein microarray test sample, this allowed us to increase imaging speed by factors of 39 and 60, respectively, compared to equivalent measurements with the commonly used NIR ($\sim$800 nm) EPS, as used in Chapter 5 [144]. We showed accurate imaging of sample phase features, with a sensitivity enhancement of 1.351 ± 0.004 over an equivalent ideal classical measurement. Our technique represents an important stepping stone towards the real-world application of quantum-enhanced imaging.

Chapter 7

Real-time Entanglement-enabled Imaging

This chapter presents a further improvement of our quantum-enhanced imaging system introduced in Chapters 5 and 6. Here, our setup now integrates the visible-wavelength entangled photon source (VEPS) used already in Chapter 6 [73], and the single photon avalanche diode (SPAD) array camera designed by Politecnico di Milano (POLIMI) and Micro Photon Devices (MPD) for the "Q-MIC" research project, (named the "QMIC24x24tdc" camera in this thesis for brevity). In contrast to the MPD SPC3 camera used in the previous chapters, the QMIC24x24tdc camera acquires photon detection timestamps, requiring the methods from Sect. 3.2.2 to count coincidences. Moreover, the QMIC24x24tdc features a close to 100% duty cycle [123]. Therefore, the combination of high detection efficiency at the VEPS's 532 nm emission and ∼100% detection duty cycle largely resolves the issues identified in Sect. 5.5 which limited quantum imaging speed. Indeed, we show here the first demonstration of real-time entanglement-enabled imaging with N00N states.

This chapter presents the results from three experiments. Firstly, we show how our setup is able to use SPDC photon pair spatial correlations to obtain real-time videos of an imaging system's point spread function (PSF), which we use to optimize the image plane focus. Secondly, we demonstrate real-time wide-field imaging of interference fringes resulting from classical and two-photon N00N state interference, where here we show how the observed fringe contrast can be used to optimize interference visibility. Lastly, we perform real-time wide-field entanglement-enhanced phase imaging of birefringent and non-birefringent test samples (based on the same principle as Chapters 5 and 6), with ∼Hz frame rate.

7.1 Experimental setup

Figure 7.1 shows the experimental setup, consisting of two main sub-systems: the visible-wavelength entangled photon source (VEPS), and the imaging system. As

in Chapter 6, the VEPS generates hyper-entangled photons by spontaneous parametric down conversion (SPDC), using a crossed-crystal geometry (see Sect. 2.3.4) [73]. Here, in Fig. 7.1 it can be seen that the 266 nm pump laser (Toptica TopWave, continuous wave, linewidth <1 MHz) power is adjusted using a half-wave plate (HWP) and polarizing beam-splitter (PBS) in series. The pump spatial mode is cleaned using two lenses ($Lf, 1$ and $Lf, 2$, with focal lengths 40 mm and 100 mm, respectively) and a 25 µm pinhole. The pump is then rotated to the diagonal (D) polarization, and passes through two pairs of barium borate (BBO) crystals and an yttrium vanadate (YVO4) crystal. As described in Sect. 6.3.1, this generates hyper-entangled photon pairs, correlated (anti-correlated) in space (momentum), and forming a N00N ($N = 2$) state in the polarization degree of freedom. The entanglement emission is collected by two lenses (L_1 and L_2, focal lengths 100 mm and 500 mm, respectively), with a 2.5 mm iris in the far-field performing k-vector filtering as in Sect. 6.3.1.

Similar to in Chapters 5 and 6, the SPDC near-field is imaged onto the LIM, re-imaged onto the spatial light modulator (SLM), and finally re-imaged again onto the sensor of our QMIC24x24tdc camera. This is achieved using two pairs of lenses in 4f configuration (see Fig. 7.1 – L_3, L_4, L_5, and L_6, focal lengths 200 mm, 200 mm, 300 mm and 100 mm, respectively). Therefore, the hyper-entangled state at the near-field (NF) planes can be written as [82, 170]

$$|\Psi(\mathbf{r})\rangle \approx \sum_{\mathbf{r},\mathbf{r}'} (|HH\rangle_{\mathbf{r},\mathbf{r}'} + \exp(i2\Theta(\mathbf{r}))\,|VV\rangle_{\mathbf{r},\mathbf{r}'}). \tag{7.1}$$

This is equivalent to Eq. 5.1 and Eq. 2.46, where we neglect normalisation coefficients for clarity. Θ represents the spatially dependent phase difference between H and V induced by the LIM, SLM and sample in each photon. The spatial coordinates $\mathbf{r}$ and $\mathbf{r}'$ are the respective transverse locations of the two spatially correlated photons, where we have $\mathbf{r} \approx \mathbf{r}'$, i.e. $\Theta(\mathbf{r}) \approx \Theta(\mathbf{r}')$, and thus $2\Theta(\mathbf{r}) \approx \Theta(\mathbf{r}) + \Theta(\mathbf{r}')$. The HWP and PBS before the camera project $|\Psi\rangle$ into the diagonal polarization measurement basis $|DD\rangle$, while the band-pass filter (BPF) removes stray light.

As described in Sect. 3.2.2, the QMIC24x24tdc camera records the time-tags of all photon detections. Therefore, following the method from Sect. 3.2.2, we can calculate coincidence images and "videos" using Eq. 3.23 and 3.26. All coincidence videos in this chapter are calculated by first recording a long full acquisition, and then, in post-processing, sub-dividing this into shorter sub-acquisitions (Eq. 3.26) each of which form one of the coincidence "video frames". However, future work will focus on calculating coincidence images at runtime, which will enable live and real-time coincidences imaging.

7.2 Point-spread function imaging in real-time

This thesis has thus far mainly focused on phase imaging schemes, without explicit discussion of (lateral) spatial resolution. However, spatial resolution is of course a critical parameter in optical microscopy, as this is what ultimately limits the size of sample features that can be imaged. In classical microscopy, when

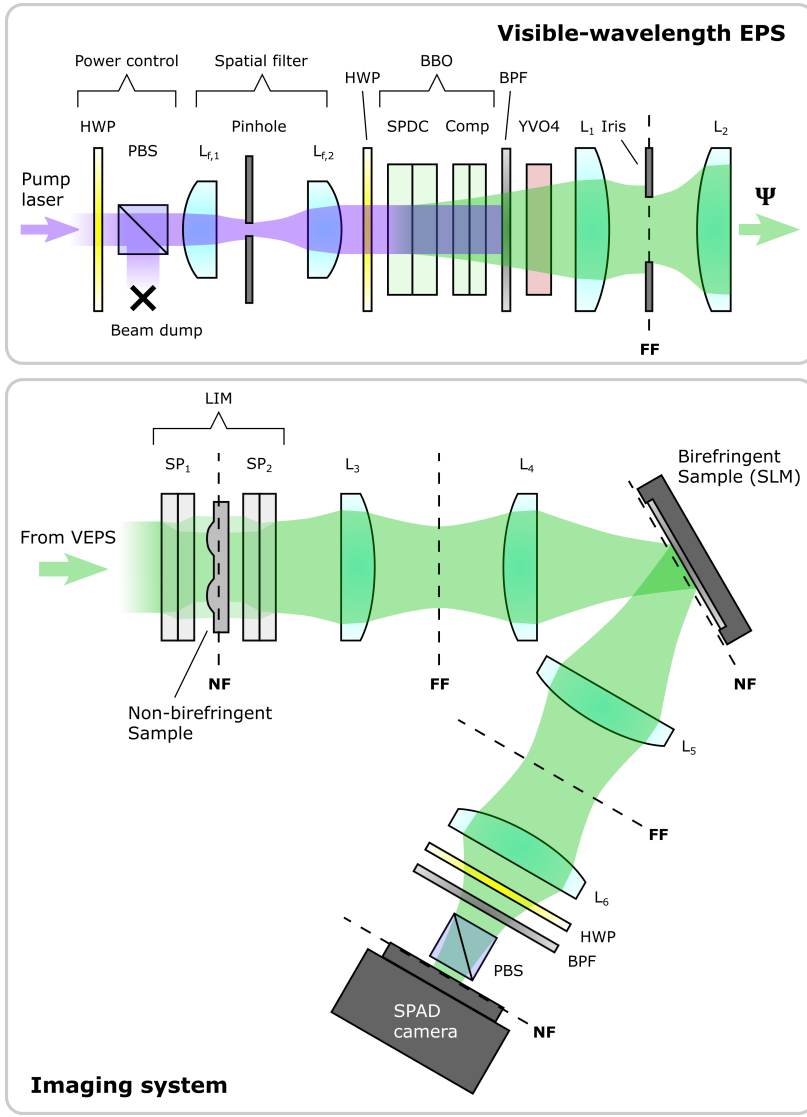

FIGURE 7.1: **Imaging system with entanglement illumination.** Top: visible-wavelength entangled photon source (VEPS). 266 nm pump in violet, and entangled photon pair emission centered at 532 nm in green shading. HWP, half-wave plate; PBS, polarizing beam-splitter; BBO, barium borate crystal (first pair for SPDC, second pair for compensation); BPF, band-pass filter; YVO4, yttrium vanadate crystal; L, lenses; NF, SPDC near-field plane; FF, SPDC far-field plane. Bottom: imaging system. LIM, large field-of-view interference microscope; SP, Savart plate; SLM, spatial light modulator.

imaging light that was simply scattered or absorbed by a sample, spatial resolution is limited by diffraction: this is the well-known Rayleigh limit and corresponds to approximately half of the wavelength of the illumination light source [1]. Nowadays, a large range of fluorescence-based imaging methods exist that can improve upon the Rayleigh limit [197–199], however, these require fluorescent labelling and are therefore considered invasive techniques. Moreover, for samples which lie inside a thick optically complex medium, even reaching the Rayleigh limit represents a highly non-trivial task, because light travelling from sample to detector can be strongly scattered and distorted. This situation applies when imaging through layers of organic tissue, which has motivated the development of adaptive optics techniques in an attempt to see biological structures and processes deep inside live organisms [13].

Spatial resolution can be quantified by the point spread function (PSF), which represents an imaging system's response to an ideal point source. In other words, when imaging an infinitesimally small light-emitting object, the intensity distribution recorded at the image plane is the PSF, and characterizes the amount of blurring added by an optical system over the imaging process [200], where here we think of the optical system as including both the optical medium containing the sample as well as external optical elements (lenses, mirrors, etc). Indeed, the image measured by an optical setup can be mathematically expressed as exactly the convolution between the object and the PSF. Experimentally characterizing the PSF constitutes therefore a critical task in most imaging applications: as the PSF quantifies optical resolution, minimizing PSF width results in maximizing resolving power. This applies to autofocus systems (the PSF is narrowest when an image is exactly in focus), as well as adaptive optics which actively correct aberrations caused by complex optical media [13].

Unfortunately, in many cases it is not straightforward to directly measure the PSF, because one normally does not have access to a point source object. This is especially true when imaging in vivo through organic tissue, where sometimes fluorescent beads are used as reference point sources, but which is not always possible due to the difficulty of insertion and potential toxicity of fluorescent markers [201, 202]. On the other hand, spatially entangled photon pairs, such as are produced by SPDC, allow directly accessing the PSF without the need for a point source [203]. This is made possible by measuring the spatial correlations between SPDC photon pairs – indeed, when projecting two-photon coincidence detections into the difference coordinates (as shown in Sect. 5.3.3, when aligning the SPDC near-field, see Fig. 5.3), the resulting distribution corresponds to the convolution of the EPS spatial correlation with the PSF [25]. That is, we can think of a bulk crystal SPDC EPS's inherent spatial correlation as a "point source", if they are much narrower than the imaging system PSF [70]. Therefore, fast coincidence imaging represents a major potential advance in imaging science, by enabling real-time characterization of PSFs. In general it is not always the case that the SPDC spatial correlations are much narrower than the PSF, and in order to ensure that this condition is satisfied it is necessary to use a very short nonlinear crystal, as the correlation width is proportional to the square root of the crystal length [80]. Moreover, as discovered by Ref. [170], SPDC spatial correlations also display three-dimensional spatial structure dependent on phase matching conditions, as

could be tuned for example by custom poling of nonlinear crystals [204]. Lastly, we note that quantum-enabled plenoptic imaging has attracted considerable interest in recent years, which can also be facilitated by the real-time characterization of SPDC two-photon spatial correlations [205, 206].

Here, we show our system's capability of real-time PSF monitoring, which we demonstrate by scanning longitudinally through the image plane focus and observing the PSF width as a function of defocus. Figure 7.2 shows the essential elements of the experimental scheme: we use the full setup shown in Fig. 7.1, however, without any birefringent or non-birefringent sample, and without making use of interference here (i.e., we do not vary the offset phase α). As indicated by Fig. 7.2, we record an acquisition using our QMIC24x24tdc camera while simultaneously moving the camera by hand along the longitudinal (optical propagation) axis, from a negative to positive defocus ($\sim -25\,\mu$m to $\sim 25\,\mu$m). The acquisition was processed following the method in Sect. 3.2.2, with sub-acquisitions of duration 0.3 s, corresponding therefore to a coincidence "video" with frame rate ~ 3 Hz.

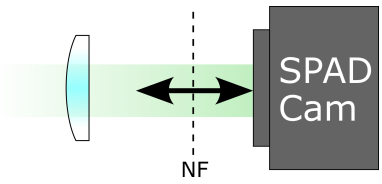

FIGURE 7.2: **Setup to observe changing PSF as function of defocus.** Full setup as in Fig. 7.1 (elements before camera not shown for clarity). SPAD array camera is manually moved along the optical propagation axis, from negative to positive defocus. NF, near-field.

Figure 7.3 shows seven selected frames (we show here every third frame for the selected acquisition time period $\sim$1.2 s to $\sim$6.7 s), where on the left is shown the difference-coordinate projection of the two-photon coincidences, while the right shows the corresponding (single-photon) intensity image for every step. We clearly observe the difference-coordinate coincidence images showing the PSF narrowing to a minimum and then broadening again as the camera is moved through the near-field plane. This is reflected also in the intensity image frames on the right of Fig. 7.3, where we see a sharp in-focus image of a speck of dust on the LIM sample holder when the difference-coordinate coincidence distribution has minimum width.

Figure 7.4 shows how real-time imaging of SPDC spatial correlations can be utilized in an autofocus system. Here, we fit a two-dimensional Gaussian model (of the form Eq. 3.29) to every difference-coordinate coincidence frame, plotting the extracted Gaussian width against the acquisition time. We clearly see that the fitted width reaches a minimum at around 4 s, before rising again. Therefore, it is straightforward to use this information to optimize the focus of an image system. Note that the SPDC-generating BBO crystals in our VEPS have a thickness of 1.5 mm [73], which yields a theoretical near-field spatial correlation width of

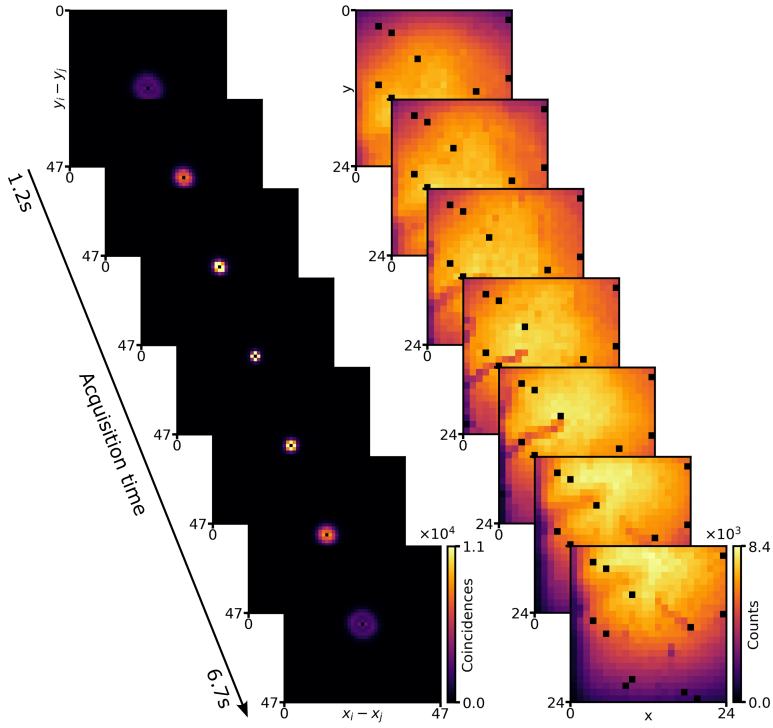

FIGURE 7.3: **Real-time PSF measurement with SPDC photon pairs.** Left: SPDC near-field coincidences projected into difference coordinates, showing the PSF which narrows to a minimum width when the imaging system is in focus. Right: intensity images, at minimum coincidence width we see in-focus image of dust speck. Note: intensity image drifts laterally due to imperfect axial alignment, while difference-coordinate coincidence image stays intrinsically centered.

5.4 µm [80]. Taking into account the magnification factor of 1.67 from the SPDC generation plane to the SPAD array camera, we see in Fig. 7.4 that the minimum observed fitted Gaussian width is considerably larger than this theoretical value (i.e. we should expect to see a minimum of $1.67 \times 5.4\,\mu\text{m} = 9.0\,\mu\text{m}$). However, the experimental spatial correlation measurement was limited by the QMIC24x24tdc camera's pixel pitch of 50 µm, and therefore obtaining a more accurate experimental estimation of the image plane would require a larger magnification factor. Figures 7.3 and 7.4 therefore clearly show that, using our setup integrating the VEPS and QMIC24x24tdc camera, we are able to perform live monitoring of an optical system's PSF. This can find uses in autofocus, as well as adaptive optics systems in general.

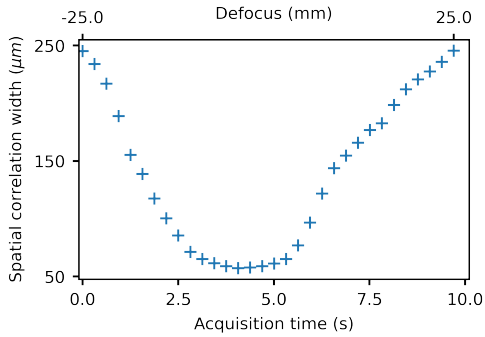

FIGURE 7.4: **Fitted Gaussian width of difference-coordinate coincidence distribution, over acquisition time**. Note: camera was moved by hand, which accounts for the varying rate of Gaussian width increase over positive defocus.

7.3 Interference visibility monitoring in real-time

A common task in experimental quantum optics is optimizing the visibility of an interference measurement. As described in Sect. 4.3.1 and 4.3.2, when estimating an unknown phase the visibility is directly linked to the sensitivity of the measurement [18, 53, 207]. More generally, experimentally observing a high interference visibility indicates high fidelity with the ideal theoretical quantum state and operation one is attempting to reproduce. This has important implications in use cases such as quantum computing, which is only scalable if fidelities surpass certain thresholds [46], and entanglement-based quantum key distribution, where the transmitted secret key rate depends on the entangled state fidelity [208, 209].

For the concrete case of classical and two-photon N00N states encoded in the polarization degree of freedom H and V, interference is maximized when the measurement corresponds to Eq. 5.5 or 5.6, and Eq. 5.2, 5.3 or 5.4, respectively – i.e. when photons are projected into exactly the D or A polarizations. This projection can be optimized by passing through a half-wave plate (HWP), followed by a polarizing beam-splitter (PBS), rotating the HWP until interference visibility is maximized. For a detection system consisting of single-pixel photon detectors, a given measurement yields only a single intensity (for classical light) or two-photon coincidence ($N = 2$ N00N state) value. This detection reading depends on the HWP rotation as well as the phase factor between the H and V polarized components of the state: ϕ in the case of the classical state $(|H\rangle + e^{i\phi}|V\rangle)/\sqrt{2}$, and 2ϕ for the N00N state $(|HH\rangle + e^{i2\phi}|VV\rangle)/\sqrt{2}$. Maximizing visibility is therefore an iterative procedure, consisting of two repeated steps. First, one scans through ϕ or 2ϕ, calculating the normalized difference between the maximum and minimum intensity or coincidence reading. Second, the HWP is rotated slightly and step 1 repeated, until the HWP orientation is found which maximizes this normalized difference. On the other hand, by using an image sensor array of single photon detectors (e.g. a SPAD array camera), we can apply a spatially dependent phase, thereby simultaneously observing all ϕ-dependent projections in the form

of an image of intensity or coincidence interference fringes. Maximizing visibility in this case only involves fine-tuning the HWP rotation while monitoring fringe contrast which can be performed both manually or by an automatized system (e.g. for active interference stabilization).

In classical interferometry, maximizing fringe contrast in intensity interference images represents a well-established optimization technique. For N00N state interference, however, coincidence imaging speeds have thus far been prohibitively slow for any practical use of the coincidence image fringes. Here, we show for the first time the real-time imaging of N00N state interference fringes on a two-dimensional image sensor, achieving a frame rate of ∼0.6 Hz. In effect, this work represents the two-dimensional imaging version of Ref. [210, 211]. The experimental setup can be seen in Fig. 7.5. This corresponds to the overall setup shown in (Fig. 7.1), without any sample in the LIM, and a spatially dependent linear phase gradient $\phi(\mathbf{r})$ applied to the SLM (SLM shown here in transmission for clarity). The classical state or two-photon N00N state in polarization is generated by the visible-wavelength source, entering the setup as shown by the arrow on the left of Fig. 7.5. The HWP is rotated to an angle θ, where we define θ of the HWP

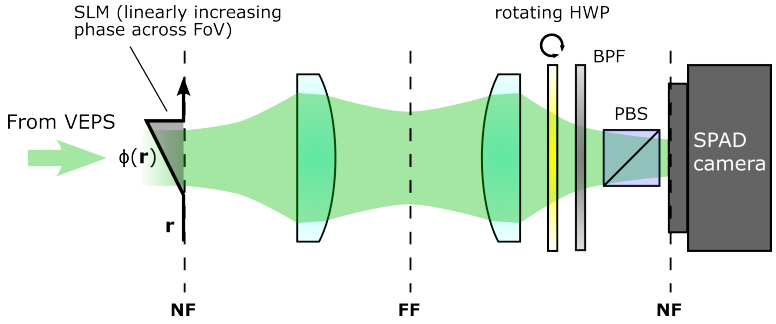

FIGURE 7.5: **Setup for measuring classical and two-photon interference fringes.** Phase on spatial light modulator (SLM) linearly increasing as a function of **r**. HWP rotated by hand, with rotation angle θ defined with respect to the H polarization axis. VEPS, visible-wavelength entangled photon source; FoV, field of view; BPF, band-pass filter; PBS, polarizing beam-splitter; NF, SPDC near-field plane; FF, SPDC far-field plane.

as the angle formed between the H polarization axis (parallel to the optical table surface) and the HWP fast axis. Passing through the HWP (rotated to angle θ), followed by the PBS has the effect of projecting into the following polarization basis, defined in terms of $|H\rangle$ and $|V\rangle$:

$$|P_\theta\rangle = \cos(2\theta)\,|H\rangle + \sin(2\theta)\,|V\rangle\,, \tag{7.2}$$

$$|P_\theta^\perp\rangle = \sin(2\theta)\,|H\rangle - \cos(2\theta)\,|V\rangle\,. \tag{7.3}$$

Note, if $\theta = 22.5°$, $|P_\theta\rangle = |D\rangle$ and $|P_\theta^\perp\rangle = |A\rangle$, the diagonal and anti-diagonal polarization, respectively (as defined in Sect. 2.2.2). In our setup (see Fig. 7.1 and 7.5) we only measure the photons in the $|P_\theta\rangle$ polarization mode, while $|P_\theta^\perp\rangle$ exits

the side port of the PBS without being detected. We can also express $|H\rangle$ and $|V\rangle$ in terms of $|P_\theta\rangle$ and $|P_\theta^\perp\rangle$:

$$|H\rangle = \cos(2\theta)\,|P_\theta\rangle + \sin(2\theta)\,|P_\theta^\perp\rangle\,, \tag{7.4}$$

$$|V\rangle = \sin(2\theta)\,|P_\theta\rangle - \cos(2\theta)\,|P_\theta^\perp\rangle\,. \tag{7.5}$$

Therefore, we can now calculate the detection probability when projecting the classical state $(|H\rangle + e^{i\phi(\mathbf{r})}\,|V\rangle)/\sqrt{2}$ into the $|P_\theta\rangle$ basis:

$$\begin{aligned}\left|\langle P_\theta|\left(\frac{|H\rangle + e^{i\phi(\mathbf{r})}\,|V\rangle}{\sqrt{2}}\right)\right|^2 &= \left(\frac{\cos(2\theta) + e^{i\phi(\mathbf{r})}\sin(2\theta)}{\sqrt{2}}\right)\left(\frac{\cos(2\theta) + e^{-i\phi(\mathbf{r})}\sin(2\theta)}{\sqrt{2}}\right)\\ &= \frac{1 + 2\cos(2\theta)\sin(2\theta)\cos(\phi(\mathbf{r}))}{2}.\end{aligned} \tag{7.6}$$

We observe that for $\theta = 22.5°$, Eq. 7.6 equals $(1+\cos(\phi(\mathbf{r})))/2$, i.e. corresponding to Eq. 5.5 (projecting into the D polarization). In this case the interference visibility with respect to $\phi(\mathbf{r})$ is maximized, with maxima at $\phi(\mathbf{r}) = 2k\pi$ (where $k \in \mathbb{Z}$) and minima at $\phi(\mathbf{r}) = (2k+1)\pi$. Similarly, for $\theta = 67.5°$, Eq. 7.6 equals $(1-\cos(\phi(\mathbf{r})))/2$, i.e. corresponding to Eq. 5.6 (projecting into the A polarization). Again the $\phi(\mathbf{r})$ interference visibility is maximized, in this case with maxima at $\phi(\mathbf{r}) = (2k+1)\pi$ and minima at $\phi(\mathbf{r}) = 2k\pi$. On the other hand, if $\theta = 0°, 45°$ or $90°$, Eq. 7.6 simply evaluates to $1/2$, with the dependence on $\phi(\mathbf{r})$ completely removed, while for other values of θ the $\phi(\mathbf{r})$ interference has lower visibility.

Similarly, we can calculate the detection probability when projecting the two-photon N00N state $|\Psi(\mathbf{r})\rangle = (|HH\rangle + e^{i2\phi(\mathbf{r})}\,|VV\rangle)/\sqrt{2}$ into the $|P_\theta P_\theta\rangle$ basis (i.e. both photons projected into the P_θ polarization):

$$\begin{aligned}|\langle P_\theta P_\theta|\Psi(\mathbf{r})\rangle|^2 &= \left|\langle P_\theta P_\theta|\left(\frac{|HH\rangle + e^{i2\phi(\mathbf{r})}\,|VV\rangle}{\sqrt{2}}\right)\right|^2\\ &= \left(\frac{\cos^2(2\theta) + e^{i2\phi(\mathbf{r})}\sin^2(2\theta)}{\sqrt{2}}\right)\left(\frac{\cos^2(2\theta) + e^{-i2\phi(\mathbf{r})}\sin^2(2\theta)}{\sqrt{2}}\right)\\ &= \frac{\cos^4(2\theta) + \sin^4(2\theta) + 2\cos^2(2\theta)\sin^2(2\theta)\cos(2\phi(\mathbf{r}))}{2}.\end{aligned} \tag{7.7}$$

Here, we see that for $\theta = 22.5°$ and $\theta = 67.5°$, Eq. 7.7 corresponds to Eq. 5.2 and 5.4, respectively, evaluating to $(1+\cos(2\phi(\mathbf{r})))/4$ in both cases. Therefore, as for Eq. 7.6, the interference as a function of $\phi(\mathbf{r})$ has maximum visibility when $\theta = 22.5°, 67.5°$, however, with double the periodicity compared to the classical case (Eq. 7.7 has maxima at $\phi(\mathbf{r}) = k\pi$, where $k \in \mathbb{Z}$; minima at $\phi(\mathbf{r}) = (k+1/2)\pi$). Again, if $\theta = 0°, 45°$ or $90°$, Eq. 7.7 yields $1/2$ (no dependence on $\phi(\mathbf{r})$), while for other values of θ the $\phi(\mathbf{r})$ interference has lower visibility.

Experimentally, we probed Eq. 7.6 and 7.7, scanning over θ by manually rotating the HWP while acquiring data with the QMIC24x24tdc camera (using Eq. 3.26

and Eq. 3.32 to calculate coincidence imaging "video frames"). At a frame rate of $\sim$0.6 Hz, both intensity and coincidence fringe images showed sufficiently high counts to be useful for accurate HWP alignment procedure. Selected frames from the "video" of classical and coincidence interference fringes can be seen in Fig. 7.6, where we note that for a given frame the maximum intensity or coincidence value was arbitrarily assigned the value of 1. Figure 7.6a shows Eq. 7.6 (with $\phi(\mathbf{r})$ increasing linearly as a function of x), with θ increasing as the acquisition proceeds. In particular, for the left-most frame of 7.6a we observe closed to maximized fringe contrast corresponding to a projection into approximately the D polarization, while the right-most frame shows the expected inversion of fringe maxima and minima, corresponding to a projection into approximately the A polarization. Middle frames show decreased visibility for $22.5^\circ < \theta < 67.5^\circ$. Similarly, Fig. 7.6b shows Eq. 7.7, where compared to Fig. 7.6a the interference fringe periodicity is doubled, reflecting the expected fact that that N00N states experience an N-fold phase factor multiplication. The left-most frame of Fig. 7.6b shows close to maximized visibility, corresponding to a projection into approximately the $|DD\rangle$ basis, while other frames show reduced visibility as the HWP is rotated to angles $22.5^\circ < \theta < 67.5^\circ$. Unlike in Fig. 7.6a, for the coincidence fringes in Fig. 7.6b there is no inversion of maxima to minima as θ increases, which reflects the fact that $|\langle DD|\Psi\rangle|^2 = |\langle AA|\Psi\rangle|^2$ (Eq. 5.2 and 5.4). Figure 7.6 therefore clearly shows that, using our setup integrating the VEPS and QMIC24x24tdc camera, we are able to perform live optimization of the classical and entanglement interference visibility, representing a major simplification of one of the most common task in experimental quantum optics.

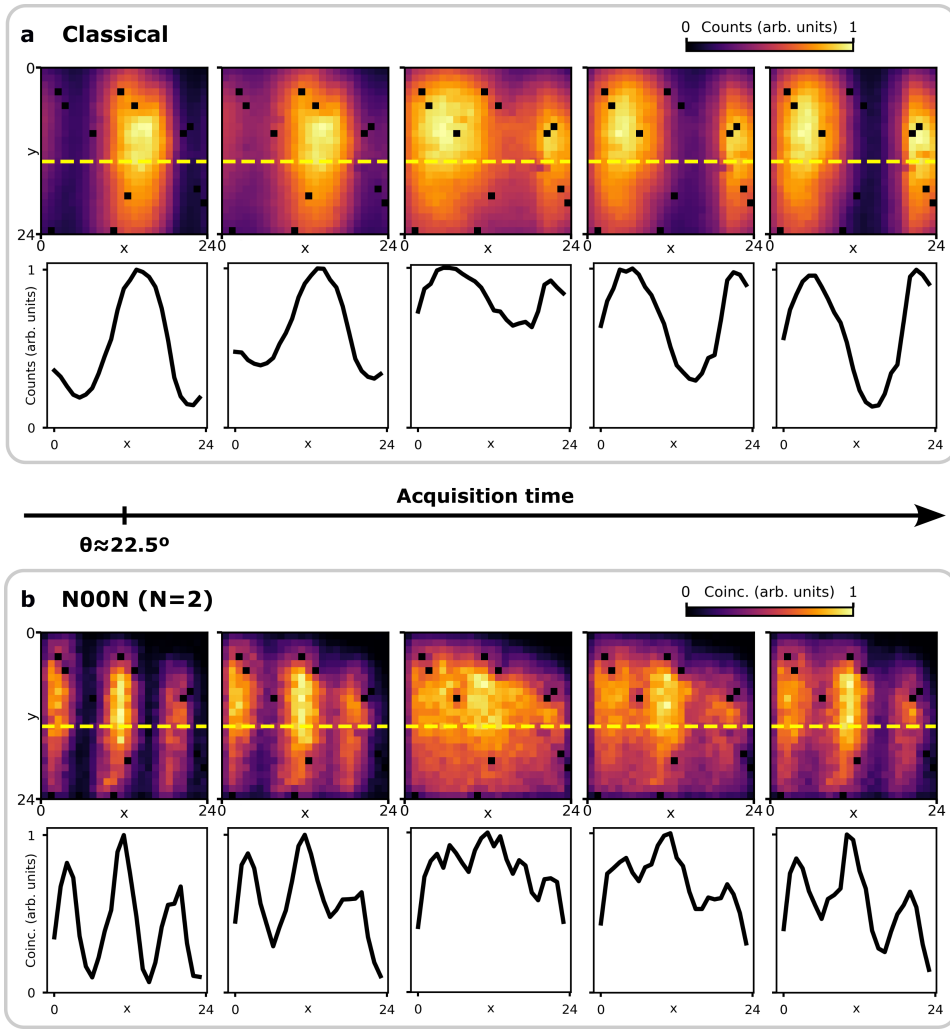

FIGURE 7.6: **Optimizing classical and N00N-state interference fringe visibility.** Selected frames from acquisition of **(a)** intensity interference fringes (Eq. 7.6), and **(b)** coincidence interference fringes (Eq. 7.7. Half-wave plate was rotated manually during acquisition, with θ increasing over acquisition time (left to right). Cross-sections along dashed yellow lines in both **(a)** and **(b)**. Leftmost frame in both (a) and (b) corresponds to $\theta \approx 22.5°$.

7.4 Real-time entanglement-enhanced phase imaging

Chapters 5 and 6 presented our realizations of wide-field entanglement-enhanced phase imagers. As described in Chapters 1 and 5, super-sensitive imaging enabled by quantum resources is expected to improve experimental capabilities whenever the total photon budget must remain low [18, 53, 105]. Applications may include imaging photosensitive biological samples which may be altered or damaged by bright light [148, 149, 151, 152, 174], as well as quantum gas states [159] or atomic ensembles [20].

Chapter 5 showed the first demonstration of a wide-field entanglement-enhanced phase imaging scheme, while Chapter 6 demonstrated how visible wavelength entangled photon pair emission provides a realistic path towards fast and efficient quantum imaging. Here, we combine these previously presented advances with the QMIC24x24tdc camera and methods developed in Sect. 3.2.2 to acquire entanglement-enhanced phase map "videos" ($\sim$Hz frame rate). Therefore, this enables for the fist time the use of quantum-enhanced phase imaging to capture dynamic scenes.

Similar to Chapter 5, we imaged birefringent and non-birefringent phase samples, where birefringent test samples were generated by a spatial light modulator (SLM), and the LIM (Sect. 5.3.1) used to image non-birefringent samples, showing the retrieval of coincidence image and phase image "video" frames. Rather than phase-shifting digital holography (PSDH), phases are retrieved here according to the single-measurement method described in Sect. 4.2.1 and 4.3.1. Finally, we calculate phase imaging sensitivity, and compare to sensitivity results from the other chapters, identifying improvements that are required for future optimization.

7.4.1 Phase retrieval without PSDH

Our previous demonstrations of quantum-enhanced phase imaging retrieved sample phase information through phase-shifting digital holography (PSDH), which has the significant advantage of not requiring a priori knowledge of the illumination brightness and spatial distribution, interference visibility and phase offset (see Sect. 4.1.1 and 4.2.1). The downside of PSDH is that recovering an unknown phase always requires multiple separate measurements (over four offset phase steps in this thesis) of the same scene. In Chapters 5 and 6, these separate measurements were acquired sequentially in time; however, this is clearly not feasible when imaging a dynamic scene as the sample phase is not constant over all PSDH steps. Another option would be to acquire all four steps simultaneously by dividing the image sensor into four sections, but this comes of course with a corresponding loss in image resolution (i.e. image pixel number). Therefore, the most feasible solution is to use the single-measurement phase retrieval as described by Eq. 4.20, which requires additional prior characterization compared to the PSDH method.

We recall from Eq. 4.19 that the two-fold coincidence measurement $I^{(2)}$ resulting from interference of a polarization-entangled two-photon N00N state can be

expressed as

$$I^{(2)}_{DD}(\Theta(\mathbf{r})) = I^{(2)}_{\text{Bkg}}(\mathbf{r}) + (\eta^{(1)})^2 I^{(2)}_{\text{IN}}(\mathbf{r}) \left[\frac{1}{4}\left(1 + \mathcal{V}^{(2)}\cos\left(2\Theta(\mathbf{r})\right)\right)\right]. \tag{7.8}$$

We now write the phase factor as $\Theta(\mathbf{r}) \equiv \phi_{\text{Sample}}(\mathbf{r}) + \phi_{\text{Bkg}}(\mathbf{r}) + \alpha$, where α is the bias phase controlled by tilting one of the LIM SPs (see Sect. 5.3.1), and $\phi_{\text{Sample}}(\mathbf{r})$ and $\phi_{\text{Bkg}}(\mathbf{r})$ are the spatially depend sample and background phases, respectively. That is, $\phi_{\text{Bkg}}(\mathbf{r})$ represents the phase induced by the setup in the absence of any sample. As described in Sect. 5.3.1, the sample phase $\phi_{\text{Sample}}(\mathbf{r})$ can be expressed in terms of a birefringent or non-birefringent phase, corresponding to the two cases shown in Fig. 5.1 a and b. In the case of a birefringent sample $\phi_b(\mathbf{r})$ (i.e. in Fig. 7.1 a test sample defined by the SLM) we have simply $\phi_{\text{Sample}}(\mathbf{r}) = \phi_b(\mathbf{r})$. On the other hand, in the case of a non-birefringent sample $\phi_{nb}(\mathbf{r})$ placed between the LIM SPs, we have $\phi_{\text{Sample}}(\mathbf{r}) = \phi_{nb}(\mathbf{r} + S/2) - \phi_{nb}(\mathbf{r} - S/2)$ (where S is the SP shear). We now write the background and input two-photon intensities ($I^{(2)}_{\text{Bkg}}(\mathbf{r})$ and $I^{(2)}_{\text{IN}}(\mathbf{r})$, respectively) as explicitly dependent on the spatial coordinate $\mathbf{r}$, to take into account spatial inhomogeneity. Note that our setup here only measures the DD polarization projection (as seen in Fig. 7.1), however, accessing the DA and AA terms is straightforward, as shown in Chapters 5 and 6.

In this experiment, we always ensure that the condition $I^{(2)}_{\text{Bkg}}(\mathbf{r}) \ll I^{(2)}_{\text{IN}}(\mathbf{r})$ is satisfied, which lets us neglect the $I^{(2)}_{\text{Bkg}}(\mathbf{r})$ term. Moreover, as in previous chapters, we count coincidences in post-processing, which artificially sets $\eta^{(1)} = 1$ (see Sect. 4.3.3). The two-photon interference visibility $\mathcal{V}^{(2)}$ was characterized as described in Sect. 5.4.1, obtaining a value of $\mathcal{V}^{(2)} = 0.90 \pm 0.08$. Therefore, analogous to Eq. 4.20, we can rearrange Eq. 7.8 to estimate the sample phase:

$$\hat{\phi}^{(2)}_{\text{Sample},DD}(\mathbf{r}) = \frac{1}{2}\arccos\left[\frac{1}{\mathcal{V}^{(2)}}\left(\frac{4I^{(2)}_{DD}(\Theta(\mathbf{r}))}{I^{(2)}_{\text{IN}}(\mathbf{r})} - 1\right)\right] - \phi_{\text{Bkg}}(\mathbf{r}) - \alpha, \tag{7.9}$$

where, following the convention from previous chapters, the circumflex, "(2)" superscript and "DD" subscript in $\hat{\phi}^{(2)}_{\text{Sample},DD}(\mathbf{r})$ indicate explicitly that this is an empirical *estimate* of the unknown sample phase ϕ_{Sample}, obtained by projecting the two-photon N00N state into the $|DD\rangle$ basis. The two-photon "intensity" $I^{(2)}_{DD}$ in our case (as in previous chapters) corresponds to the coincidence image $\text{ci}_{DD}(\mathbf{r})$, calculated according to the procedure described in Sect. 3.2.2, 3.3.1, 3.3.2, and 3.4.

From Eq. 7.9 we see that extracting the sample phase from a single ci_{DD} measurement requires characterizing $\phi_{\text{Bkg}}(\mathbf{r})$ and $I^{(2)}_{\text{IN}}(\mathbf{r})$. This characterization is performed using PSDH, where we then make the physically reasonable assumption that $\phi_{\text{Bkg}}(\mathbf{r})$ and $I^{(2)}_{\text{IN}}(\mathbf{r})$ stay constant over the duration of sample measurements. We acquire four $\text{ci}_{DD}(\Theta(\mathbf{r}))$ measurements (acquisition time $t_{\text{acq}} = 16\,\text{s}$ per step) without sample, with phase factors $\Theta_j(\mathbf{r}) = 0 + \phi_{\text{Bkg}}(\mathbf{r}) + j\pi/4$, where

$j = 0, 1, 2, 3$. Therefore, from Eq. 4.21, the background phase is:

$$\phi_{\text{Bkg}}(\mathbf{r}) = \frac{1}{2}\tan^{-1}\left[\frac{\text{ci}_{DD}(\Theta_1(\mathbf{r})) - \text{ci}_{DD}(\Theta_3(\mathbf{r}))}{\text{ci}_{DD}(\Theta_2(\mathbf{r})) - \text{ci}_{DD}(\Theta_0(\mathbf{r}))}\right]. \tag{7.10}$$

We can also define the two-photon input rate $R^{(2)}_{\text{IN}}(\mathbf{r}))$, i.e. the illumination flux of photon pairs per unit time. From Eq. 7.8 (neglecting $I^{(2)}_{\text{Bkg}}(\mathbf{r})$ and $\eta^{(1)}$), we see that we can obtain $R^{(2)}_{\text{IN}}$ from the four $\text{ci}_{DD}(\Theta_j(\mathbf{r}))$ measurements [7]:

$$R^{(2)}_{\text{IN}}(\mathbf{r})) = \frac{1}{t_{\text{acq}}}\sum_j \text{ci}_{DD}(\Theta_j(\mathbf{r})). \tag{7.11}$$

For every sample acquisition we can then simply multiply $R^{(2)}_{\text{IN}}(\mathbf{r}))$ by the sample acquisition time to obtain $I^{(2)}_{\text{IN}}(\mathbf{r})$. Thus, knowing now $\phi_{\text{Bkg}}(\mathbf{r})$ and $I^{(2)}_{\text{IN}}(\mathbf{r})$, we are able to use Eq. 7.9 to retrieve an unknown sample phase. Note that Eq. 7.10 and 7.11 of course also represent empirical parameter estimates with non-zero uncertainty. However, as we calculate $\phi_{\text{Bkg}}(\mathbf{r})$ and $I^{(2)}_{\text{IN}}(\mathbf{r})$ using an acquisition time far longer than sample measurements, their uncertainty is negliible compared to the sample measurement error.

7.4.2 Phase imaging of dynamic phase samples

We first investigated our system's entanglement-enhanced phase imaging capabilities of a dynamic scene, by measuring a birefringent test sample (generated by the SLM) of a rotating "yin and yang" symbol which varies over time. Using our QMIC24x24tdc camera (as part of the setup shown in Fig. 7.1), we recorded a full acquisition with duration 23 s. Using Eq. 3.26, this was divided into 32 equal sub-acquisitions of length 0.7 s each. These were processed to obtain coincidence image frames (method from Sect. 3.4, frame rate $\sim$1.4 Hz), which in turn were used to obtain the sample phase according to Eq. 7.9. Note that spatially uncorrelated noise was filtered out with a threshold of $t = 0.5$ (see Sect. 3.3.2, Eq. 3.31). In Fig. 7.7 we see five selected frames of the acquisition, with the left column showing coincidence images and the right column showing retrieved phase estimates (real experimental acquisition times also shown on left). We clearly see the rotating "yin and yang" pattern, both in the coincidence images as well as the phase information. This confirms our system's capability to measure dynamic birefringent samples.

Similarly, we demonstrated entanglement-enhanced imaging of a time-varying non-birefringent phase. Here we measured a silica test sample (fabricated in-house as described in Sect. 6.4.1), consisting of four parallel bars with step height 50 nm. This sample was placed into the LIM (between the Savart Plates, see Fig. 7.1 or Fig. 5.1b), and moved by hand in order to vary the sample phase distribution over time. While moving the sample, we recorded a full acquisition with duration 19 s, which was again divided into 32 equal sub-acquisitions (sub-acquisition time 0.6 s) using Eq. 3.26. As for the birefringent sample, these were

processed to obtain coincidence image frames (Sect. 3.4, frame rate $\sim$1.7 Hz), and sample phase frames (Eq. 7.9). Spatially uncorrelated noise was again filtered out with a threshold of $t = 0.5$ (Eq. 3.31). In Fig. 7.8 we see five selected frames of the acquisition, with the left column showing coincidence images and the right column showing retrieved phase estimates (real experimental acquisition times also shown on left). Note that Fig. 7.8 shows every second sub-acquisition frame, in order to make the sample movement more visible. We clearly see the pattern of the four bars, both in the coincidence images as well as the phase information. This confirms our system's capability to also measure dynamic non-birefringent samples.

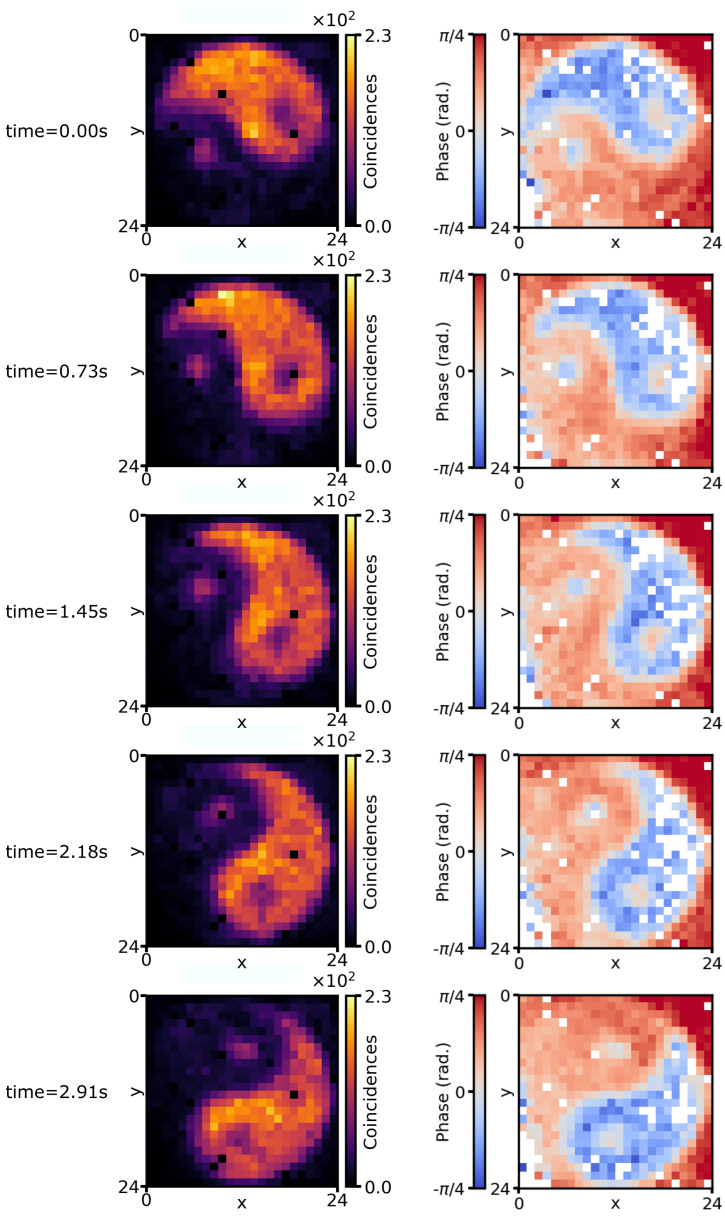

FIGURE 7.7: **Coincidence image frames and retrieved phase image frames for dynamic birefringent test sample** Left column: coincidence images $\mathrm{ci}(\mathbf{r})$ after projecting $|\Psi\rangle$ into $|DD\rangle$ basis. Right column: Retrieved phase image frames, obtained by substituting corresponding $\mathrm{ci}(\mathbf{r})$ frame into Eq. 7.9.

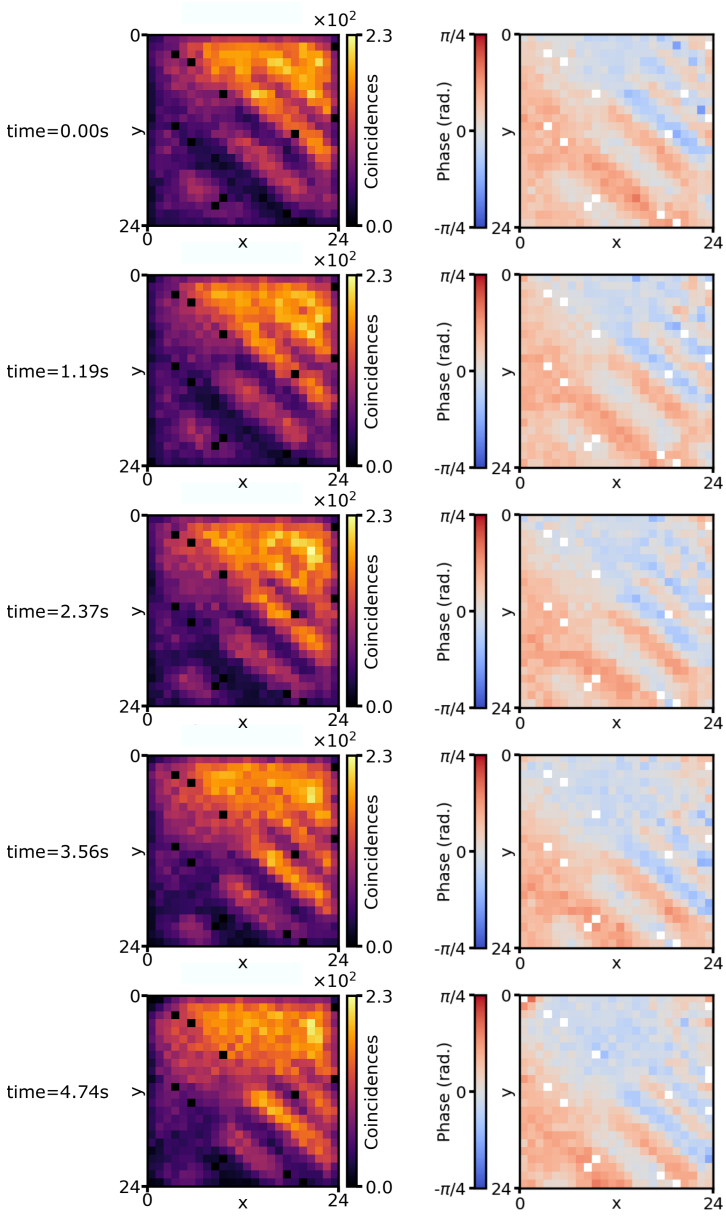

FIGURE 7.8: **Coincidence image frames and retrieved phase image frames for dynamic non-birefringent test sample** Left column: coincidence images ci($\mathbf{r}$) after projecting $|\Psi\rangle$ into $|DD\rangle$ basis. Right column: Retrieved phase image frames, obtained by substituting corresponding ci($\mathbf{r}$) frame into Eq. 7.9. Note, every second frame shown.

7.4.3 Sensitivity of phase imaging

As detailed in Sect. 4.3.1, in general when measuring an unknown phase with a N-photon N00N state, there are $N+1$ possible coincidence measurements. Obtaining the maximum phase sensitivity requires combining the phase estimates from *all* of these $N+1$ measurements (Eq. 4.22) [20]. In the case of our two-photon N00N state this corresponds to measuring the DD, DA, and AA projections, as was done in Chapters 5 and 6. However, here we only acquired coincidence images for the DD projection, which prevents us from obtaining a direct experimental quantification of entanglement-enabled phase supersensitivity. However, we can use Eq. 4.34 to estimate the reduction in phase uncertainty enabled by our setup if we were detecting th DD, DA, and AA terms, taking into account the experimental parameters κ and $\mathcal{V}^{(2)}$. Recall that κ represents the excess experimental noise of a coincidence measurement above the shot noise limit. We characterized κ following the method described in Sect. 3.5, obtaining a value of $\kappa = 1.02 \pm 0.09$. The two-photon interference visibility for this experiment was characterized in Sect. 7.4.1, with a value of $\mathcal{V}^{(2)} = 0.90 \pm 0.08$.

Figure 7.9 shows the reduction in experimental phase uncertainty compared to an ideal classical measurement with equal number of photons, as provided by measuring our two-photon N00N state. We obtain this noise reduction estimate by substituting our experiment parameters $\kappa = 1.02 \pm 0.09$ and $\mathcal{V}^{(2)} = 0.90 \pm 0.08$ into Eq. 4.34. Analogous to Fig. 6.6b, a blue pixel colour indicates lower phase measurement uncertainty than would be obtained by an ideal classical measurement, i.e. super-sensitivity. Red pixel colour on the other hand indicates an uncertainty that could still be surpassed by a measurement using only classical resources. Figure 7.9a and b show the noise reduction for the corresponding frames shown in Fig. 7.7 (i.e. the birefringent test sample) and Fig. 7.8 (i.e. the birefringent test sample), respectively. We observe a noise reduction factor below 1 in large parts of all Fig. 7.9 frames. However, Fig. 7.9a and b clearly both contain significant regions which do not achieve super-sensitivity, and moreover show dependence on the retrieved sample phases (right columns of Fig. 7.7 and 7.8). This is in contrast to Fig. 6.6b, and reflects the fact that Eq. 4.34 (unlike Eq. 4.45) depends non-trivially on the phase being measured (e.g. compare Fig. 4.4 to Fig. 4.5). Therefore these results indicate that, using our imaging system integrating VEPS and the QMIC24x24tdc camera, it is possible to perform super-sensitive phase imaging enabled by entanglement. However, one must also take care in choosing not only the correct controlled bias phase, but also the sample phase itself, which must be known to remain within a small range.

7.5 Discussion

In this chapter, we showed how the combination of our visible-wavelength entangled photon pairs and the QMIC24x24tdc camera enable real-time quantum imaging with entangled photon pairs. We therefore address both of the significant experimental issues as identified in Chapter 5 and Ref. [144]: using an entanglement source at 532 nm wavelength provides high photon detection efficiency (PDE)

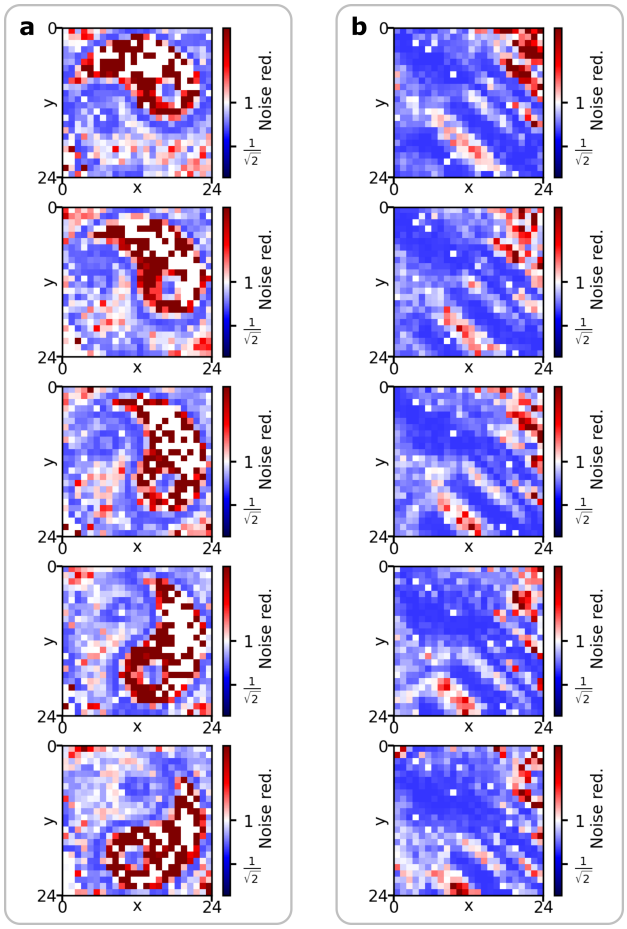

FIGURE 7.9: **Reduction in noise enabled by quantum-enhanced method.** **(a)** Frames corresponding to Fig. 7.7. **(b)** Frames corresponding to Fig. 7.8.

with mass-producible CMOS SPAD array cameras[42], and the QMIC24x24tdc camera enables ∼100% duty cycle. Therefore, from the experimental physicist's point of view, the challenge of wide-field quantum imaging with entangled photon pairs can be considered, in principle, "solved". We follow this with the immediate caveat that phase super-sensitivity without making use of post-selection coincidence counting (see Sect. 4.3.3) still requires higher PDE (at least ∼70.7%), though we note that the latest SPAD array camera demonstrated in the literature are now approaching this threshold [155]. Moreover, recent progress on the development of imaging arrays of superconducting nanowire single photon detectors (SNSPDs) has been promising, with novel architectures now capable of coincidence measurements [212, 213]. Given that SNSPDs routinely reach PDEs above 90% [106], in the future such arrays may become the technology of choice for quantum imaging with multi-photon states.

All coincidence "videos" in this chapter were calculated in post-processing, i.e. by saving acquisitions consisting of photon timestamps to disk, and then extracting individual frames afterwards (using Eq. 3.26). For some applications, such as monitoring of entanglement interference it would be beneficial to obtain a live video of coincidence image frames. Future work will focus on implementing an efficient coincidence processing algorithm at runtime, or the use of a graphics processing unit (GPU) for accelerating the calculations required to obtain a coincidence image. This will enable true live quantum imaging of entangled photon pairs.

The image resolution of 24×24 pixels was only limited by the sensor of our QMIC24x24tdc SPAD array camera. However, this sensor architecture is scalable to 96×96 pixels [123], enabling therefore quantum imaging with moderately high resolution, while maintaining $\sim$100% duty cycle. On the other hand, megapixel SPAD array cameras have now been demonstrated [155, 178], however with significantly lower duty cycles. In some applications it may nonetheless be interesting to trade duty cycle (and thus imaging speed) for a higher resolution.

Chapter 8

Conclusions

In this thesis, we developed a quantum imaging platform based on entangled photon pair emission through spontaneous parametric down conversion (SPDC), and coincidence imaging with single photon avalanche diode (SPAD) array cameras. We show advances in quantitative phase imaging enhanced through entanglement, demonstrating super-sensitivity as compared to equivalent classical measurements, in a practical wide-field imaging configuration. Through the progress presented in this thesis in the integration of novel software and hardware components, our quantum-enhanced optical imager was able to reach real-time acquisition speeds. This opened the door to additional applications enabled by SPDC entangled photon pairs, including real-time monitoring of entangled state fidelity, and real-time point spread function characterization of optical imaging systems.

The main achievements of this thesis are:

- The first experimental demonstration of a super-sensitive phase imager enabled by utilizing entanglement, operating in a wide-field configuration. This was achieved by exploiting hyper-entanglement, simultaneous N00N state entanglement in polarization and correlations in a massive pixel mode state space, enabling the retrieval of phase information with a large field-of-view (FoV) using a SPAD array camera.
- The evolution and optimization of our system towards real-time quantum imaging capability, as speed and practicality are two essential requirements for real use cases. First, we showed how the use of a visible-wavelength entangled photon source (VEPS) can enable high-speed quantum imaging, by operating at peak photon detection efficiency of mass-producible complementary metal oxide semiconductor (CMOS) SPAD array cameras. Second, we integrated into our system both a VEPS as well as a novel time-tagging SPAD array camera with near unity duty cycle. The resulting entanglement-enabled imager improved acquisition speed by at least four orders of magnitude compared to previous state-of-the-art quantum imaging demonstrations, with the ability to record $\sim$Hz frame rate entangled photon pair coincidence videos.

- Development of software methods to retrieve high signal-to-noise ratio (SNR) two-photon coincidence images, as well as videos consisting of many coincidence image frames, from raw data acquired by photon-counting and time-tagging SPAD array cameras. We also implemented holographic and direct phase retrieval methods in order to recover phase images from classical, and N00N state entanglement multi-photon interference.
- Demonstration of our quantum-enhanced imager's applicability to several realistic relevant imaging scenarios, including measuring nanometre-scale feature step heights in transparent material, biomedical protein microarrays, as well as birefringent phase samples.
- Demonstration of additional applications in the form of real-time entangled state fidelity monitoring, by imaging interference fringe contrast, and exploiting SPDC spatial correlations for real-time point spread function characterization of optical systems, which is important in adaptive optical imaging.
- The development of methods to calculate SNR in coincidence imaging, and sensitivity in phase imaging. This sensitivity, relating to measurement uncertainty, was quantified initially through analysing pixel-to-pixel noise in phase images, and later by dividing phase measurements into sub-acquisitions and looking at experimental variations independent of image spatial distribution. Sensitivity enhancements over equivalent classical measurements were found to agree with predictions according to theory described also in this thesis.

8.1 Outlook

The methods developed in this thesis represent a significant stepping stone towards obtaining real-world usefulness from quantum imaging. Nevertheless, further development will be necessary in order to reach this goal. Unconditional phase super-sensitivity still requires detection efficiencies higher than those achieved here (at least $\sim$70.7%), though we note that the latest SPAD array camera demonstrated in the literature are now approaching this critical threshold. Moreover, image resolutions of all experiments shown in this thesis were relatively low, limited by the sensors of our SPAD array cameras to the kilopixel range. However, the development of SPAD array cameras with large pixel numbers (even megapixel) represents an extremely active field of research, with novel high resolution sensors likely to become useful for coincidence imaging in the near future. We emphasize that all experimental techniques and computational methods from this thesis are immediately applicable in the case that a SPAD array camera with larger pixel number and higher photon detection efficiency becomes available That is, achieving the real quantum enhancement afforded by entangled two-photon states (e.g. in the case of phase sensitivity a factor of $\sqrt{2}$), is now a matter of "just" waiting for detector hardware advancements.

A broader question remains as to the usefulness of a $\sqrt{2}$ sensitivity enhancement in phase imaging, as made possible through the use of $N = 2$ N00N states. In the biomedical field there is still a lack of quantitative data regarding illumination thresholds for light-induced effects or even damage, for label-free quantitative phase imaging. As described in Sect. 5.5, "back of the envelope" calculations indicate that in some highly specific scenarios, light-induced changes become significant when probing living cell samples, at photon flux comparable to state-of-the-art entangled photon source (EPS) output levels. It is likely therefore that super-sensitive imaging with entangled photon pairs can become a tool in basic biology and biomedicine research, in niche applications at the cutting edge where extremely high sensitivity is required. Nonetheless, a far broader range of use cases will be enabled by a higher sensitivity enhancement of $\sqrt{N}$, if $N > 2$ N00N states (or indeed, other types of N-photon entangled states with large N) could be used for illumination. It is relatively straightforward to extend coincidence imaging protocols shown in this thesis to larger N00N states or other non-classical light states with $N > 2$ photons. However, despite several recent promising results, utilizing quantum dots, trapped atoms, and cavity based entangled photon sources, deterministically generating entangled states with many photons remains a largely open problem in experimental quantum optics, whose solution will doubtless have large impact in the field of quantum imaging.

On the other hand, a far more near-term impact could be provided by the real-time point spread function (PSF) characterization ability, as described in Sect.7.2. Relying exclusively on presently available technologies, there may be great potential in scattering analysis and adaptive optics applications where SPDC spatial correlations can be used. In terms of improving near-term usefulness, we also note that all coincidence "videos" presented in this thesis were calculated in post-processing. It would be promising to pursue the development of more efficient coincidence processing algorithms at runtime, or the use of accelerating hardware (e.g. graphics processing units), to reduce processing time required to obtain a coincidence image. This will enable true live quantum imaging of entangled photon pairs.

We note that the technologies presented in this thesis may have potential beyond quantum imaging, for example, in quantum communication and computation. One area to explore is the transmission and detection of space and momentum correlated entangled states through optical fibre for quantum cryptography using the developed entangled photon sources, SPAD arrays, and post-processing techniques. Another area is analogue (linear) quantum processing that could in principle be built using free space optical components.

Appendix A

Image similarity using zero mean normalized cross-correlation

For the work described in Chapter 5, we calculated the image similarity between the birefringent test sample applied to the SLM, and the phase images retrieved by classical and entanglement-enhanced interferometric measurements (as shown in Fig. 5.8, Sect. 5.4.3). The image similarity was quantified using the zero mean normalized cross-correlation (ZNCC), which is widely used in image template-matching [214]. The ZNCC parameter R_{ZNCC} varies between -1 and 1. The higher R_{ZNCC} is, the more similar two images I and J are, with

$$R_{\mathrm{ZNCC}} = \frac{\langle I(x,y) - \bar{I} | J(x,y) - \bar{J} \rangle}{\sqrt{\langle I(x,y) - \bar{I} | I(x,y) - \bar{I} \rangle \langle J(x,y) - \bar{J} | J(x,y) - \bar{J} \rangle}} . \tag{A.1}$$

For the ZNCC calculations, we downsampled the image of the Greek letter "ϕ" applied to the SLM (Fig. 5.6), such that it would have the same pixel resolution as the retrieved phase images measured with our SPAD array camera. We then calculated R_{ZNCC} between the downsampled SLM image (Fig. A.1A) and the retrieved phase image for the classical measurement (Fig. A.1B) and for the entanglement-enhance measurement (Fig. A.1C) respectively. Note that, as seen in Fig. A.1B and C, for the retrieved phase images we used only a central region of interest (ROI) of $\hat{\phi}_{\mathrm{Classical}}$ and $\hat{\phi}_{\mathrm{N00N}}$ (Fig. 5.8A and C), in order to avoid noisy edge effects. We obtained image similarity values R_{ZNCC} between the image applied to the SLM and the classically retrieved phase image of 0.823, and between the image applied to the SLM and the entanglement-enhanced retrieved phase image of 0.848. This demonstrates that the classical and entanglement-enhanced measurements retrieved the sample phase approximately as well as each other.

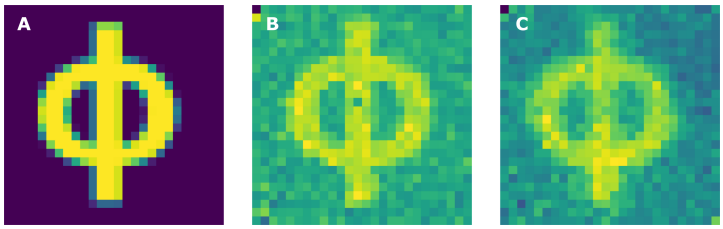

FIGURE A.1: **Images used for ZNCC calculation.** **(A)** Central ROI for downsampled image of test sample applied to SLM. **(B)** Central ROI for phase image retrieved by classical measurement. **(C)** Central ROI for phase image retrieved by entanglement-enhanced measurement.

Appendix B

Advantages of using a SPAD array camera for quantum imaging

Here we elaborate on the advantages of our SPAD array camera coincidence imaging approach, as compared to the pixel-to-pixel scanning approach demonstrated for example in Ref. [38] and [37]. For conciseness in the following, we denote method A to refer to the SPAD camera imaging protocol as demonstrated in this work, while method B refers to the scanning approach. Method B is implemented by focusing the illumination source to a small spot which determines the spatial resolution of the system. An image is then reconstructed pixel-by-pixel, either by scanning the sample against a stationary spot (using a motorized or piezoelectric scanner, as in Ref. [38] and [37]), or by scanning the illumination spot across a stationary sample (using galvo mirrors or a spatial light modulator). We note that single-pixel imaging is not well-suited for super-sensitive measurements, as optical efficiencies are intrinsically limited to 50% [215]. We restrict our comparison here to imaging with SPAD detectors (SPAD arrays and single SPADs, for methods A and B respectively), which at present show the highest technological maturity out of available single photon detection technologies.

For coincidence imaging to be useful in real-world applications, the following requirements must be satisfied: practicality and ease of use, sufficiently high image pixel number, low measurement duration, and high optical efficiency. We therefore compare methods A and B in light of these requirements.

B.1 Practical considerations

A significant practical advantage of method A is its lower cost when compared to method B. While method B requires multiple SPAD detector modules, a coincidence detection unit, as well as the scanning apparatus, in method A the SPAD array camera alone suffices for coincidence imaging.

In addition, pixel scanning in method B generally relies on mechanical movement (with the exception of spatial light modulator scanners), which can introduce noise into a measurement due to vibrations, as well as suffering from long-term reliability issues. For accurate image retrieval, pixel-scanning and light detection operations must also be synchronized in time, leading to non-trivial calibration procedures for the user (especially for fast scanning). Another important drawback of method B relates to non-static behaviours of the apparatus or the analyzed samples. If experiment fluctuations or sample dynamics occur on a timescale faster than the acquisition time, such temporal variations will translate to spatial variations in the acquired image as pixels are measured sequentially and not simultaneously. All of these issues can be avoided by method A.

B.2 Image resolution

The image resolution (the number of image pixels) was limited by the camera used in the present work. However, megapixel SPAD array cameras have already been demonstrated [178], which, while still suffering from comparatively slow readout, may in the future become suitable for practical high resolution quantum imaging. With regard to the short term, we note that Ref. [123] demonstrates a SPAD array optimized for coincidence imaging, scalable to 96×96 pixels. Therefore for method A, with present available technological advances, an image resolution of $\sim 10^4$ pixels can realistically be achieved.

On the other hand, there is no limit to the image resolution in method B, as one can scan over an arbitrarily high number of pixel steps. Therefore, method B is better suited for use cases requiring a very high image resolution. We also note that scalable and cost-effective fabrication of SPAD arrays is only possible in silicon, which limits method A to detecting photons with wavelengths $<1.1\,\mu$m, whereas for other wavelength ranges method B is at present the only feasible option.

B.3 Measurement duration

For obtaining a coincidence image with n_{pix} pixels and M photon-pair detections per pixel, the total acquisition time T is simply the time required to count $n_{pix}M$ photon pairs. For method A, this can be expressed as $T_A = n_{pix}M/r_A$, where r_A is the pair detection rate across the entire SPAD array camera. For method B, this can be expressed as $T_B = n_{pix}t_B$, where t_B is the time required to detect M photon pairs on one pixel. As mentioned in the previous section, with currently achievable technological advances, $\sim 10^4$ pixels is a realistic image resolution for method A. We therefore compare here the measurement durations for methods A and B, with $n_{pix} = 10^4$, and show that under realistic conditions $T_A < T_B$.

To begin, we note that in both methods currently achievable entangled photon generation rates are not a limiting factor in measurement speed. State-of-the-art photon pair sources achieve an estimated generated brightness of $\sim 10^7$

pairs/mW/s [93], corresponding to emission rates of $\sim 10^9$ pairs/s with commercially available lasers. Even at low PDEs, this yields a detectable photon pair flux higher than the maximum count rates of both SPAD array cameras and single SPAD detectors.

In method A, the factor r_A is determined by the achievable count rate of SPAD array cameras. While this was limited by the readout scheme of the general purpose camera used in the present work, new SPAD arrays dedicated to sparse event detection currently being developed are able to detect at much higher rates. For example, the SPAD array from Ref. [123], is able to read out two-photon coincidence detections in $<1\,\mu$s by employing row skipping. This enables a $>10^6$ pairs/s detection rate, and we obtain $T_A \approx n_{pix} M/10^6$ seconds.

In method B, the factor t_B is determined by two main considerations: (i) The saturation rate of available SPAD detectors: SPADs can count photons at a rate of up to $\sim 5 \times 10^5$ counts/s before distortions due to their deadtime become significant [216]. (ii) The time required to scan from one pixel to the next, which depends strongly on experimental details: setups which scan the sample against a stationary illumination spot are widely used due to their ease of use and comparatively low cost, but require tens to hundreds of milliseconds per scan step (e.g. the commercially available nano-positioning equipment from Physik Instrumente and Thorlabs). In contrast, scanning the spot over a stationary sample using resonant scanning galvo mirrors can be much faster, with negligible moving time per scan step (e.g. using the commercially available resonant scanner from Leica), however at the expense of significantly higher cost and experimental sophistication. Therefore we obtain, for the case of scanning the sample, $T_B \approx n_{pix}(\frac{M}{5\times 10^5} + 0.01)$ seconds (for an ideal situation of only 10 ms moving time), and for the case of scanning the illumination spot, $T_B \approx n_{pix} M/(5 \times 10^5)$ seconds.

For realistic desirable experimental parameters of $M = 1000$ and $n_{pix} = 10^4$, we therefore calculate acquisition times of $T_A \approx 10s$, and $T_B \approx 120s$ for the case of scanning the sample, and $T_B \approx 20s$ for the case of resonant scanning of the illumination spot. That is, with present achievable technological advances and at image resolutions up to $\sim 10^4$ pixels, we expect SPAD array cameras to perform quantum-enhanced imaging more rapidly than sample-scanning systems, principally because of two reasons: (i) They can count at higher rates than single-pixel SPADs because the photon flux is spread over a large number of pixels. Any single pixel in the array will thus count at rates far below saturation. (ii) In the case of scanning the sample in method B there is a constant overhead due to the time taken to scan from one pixel location to the next, which is avoided by method A. We also note that event-based readout SPAD array cameras are likely to yield even higher detection rates in the near future [39]. With optimized SPAD array camera readouts providing only the addresses of pixels which detected coincidences, we also do not expect a significant difference in processing time between the two methods.

B.4 Optical efficiency

For method A, the photon detection efficiency (PDE) of SPADs that can be fabricated in scalable, large image detector arrays peaks around 60% [179]. For method B the PDE of available single-pixel SPADs is slightly higher, peaking around 70% (e.g. the widely used Excelitas Single Photon Counting Modules). However, we note that to measure two-photon coincidences in all possible polarization bases (as was done in this work) a minimum of four SPAD detectors are required, in the layout shown in Fig. B.1A. When the two photons have polarizations perpendicular to each other, this setup can in principle detect all two-photon coincidences because the polarizing beam splitter (PBS) deterministically separates the photon pair. In contrast, when the two photons have the same polarization, only 50% of coincidences can be detected, as the beam splitters (BS) after the PBS only probabilistically separate the photon pair. That is, with 50% probability the situation shown in Fig. B.1B occurs, where one photon goes to each of the two SPADs and a coincidence is recorded. However, with 25% probability each, the scenarios depicted by Fig. B.1C and D occur, where both photons go together to only one of the SPADs and therefore no coincidence is detected. This issue can of course be mitigated by adding more BSs and SPADs to the setup from Fig. B.1A, to reduce the probability of two photons going to the same SPAD, but, requiring a larger number of detectors and optics, and a coincidence detection unit between many channels, this remedy carries a significant penalty in both cost and experimental complexity.

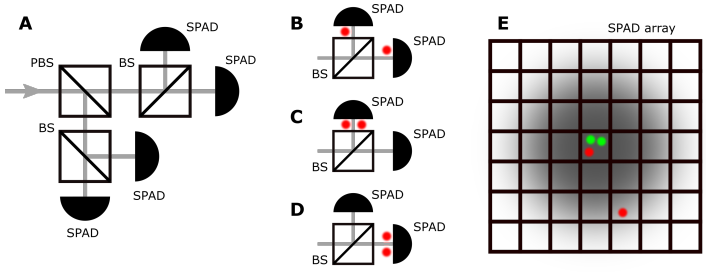

FIGURE B.1: **Coincidence detection of polarized photon pairs.** **(A)** Setup to detect two-photon coincidences using method B. PBS - polarizing beam splitter, BS - (non-polarizing) beam splitter. **(B)** Coincidence detected by BS and two single SPADs. **(C)** and **(D)** Coincidence not detected by BS and two single SPADs. **(E)** Coincidence detection using method A.

In method A on the other hand, the optical imaging system can always be designed such that the photon pair's spatial correlation width is larger than the SPAD array pixel pitch. This scenario is shown in Fig. B.1E, where the round gray shading represents the two-photon spatial correlation distribution. The probability for both photons to land on the same SPAD pixel (as depicted by the pair of green dots) is then low compared to the probability for the photons to be detected by different SPAD pixels (as depicted by the pair of red dots). Method A can

therefore inherently avoid the above coincidence efficiency issue faced by method B, without additional cost or experimental effort.

B.5 Quantum spatial correlations as a resource

Lastly, a unique advantage of a wide-field scan free approach such as ours relates to the accessibility of photon spatial correlations as an additional physical resources. The scanning setups shown in Ref. [38] and [37] did not have access to the spatial correlations of the 2-photon state, which necessitated strong focusing into the sample to achieve good spatial resolution. On the other hand, when weakly focusing into the sample, the 2-photon correlation width can stay small – enabling simultaneously high resolution and large field-of-view in our system combining free-space quantum illumination and SPAD array detection. This point is also crucial to obtain for instance images with resolution beyond the diffraction limit [24], which can in principle be accessed by method A regardless of the focusing conditions, as one can characterize the spatial correlations with the SPAD camera. With method B on the other hand, this would be impossible. We note also that in the weakly focused illumination regime of method A, the peak power density on a sample is lower than for the strongly focused illumination condition of method B, which may be significant for photosensitive samples that display a nonlinear response to light.

Bibliography

1. Mertz, J. *Introduction to optical microscopy* (Cambridge University Press, 2019).
2. Clarke, A., Eberhardt, C. & Eberhardt, C. N. *Microscopy techniques for materials science* (Woodhead Publishing, 2002).
3. Smith, W. J. *Modern optical engineering: the design of optical systems* (McGraw-Hill Education, 2008).
4. Goodman, J. W. *Statistical optics* Wiley classics library ed (Wiley, New York, 2000).
5. Zernike, F. Phase contrast, a new method for the microscopic observation of transparent objects. *Physica* **9,** 686–698 (1942).
6. Gabor, D. A New Microscopic Principle. *Nature* **161,** 777–778 (1948).
7. *Optical shop testing* 3rd ed. (ed Malacara, D.) (Wiley, Hoboken, N.J, 2007).
8. Park, Y., Depeursinge, C. & Popescu, G. Quantitative phase imaging in biomedicine. en. *Nature Photonics* **12,** 578–589 (2018).
9. Inoué, S. *Video microscopy* (Springer Science & Business Media, 2013).
10. Dowling, J. P. Quantum optical metrology – the lowdown on high-N00N states. *Contemporary Physics* **49,** 125–143 (2008).
11. Taylor, M. A. & Bowen, W. P. Quantum metrology and its application in biology. *Physics Reports* **615,** 1–59 (2016).
12. Gu, M. *Principles of three dimensional imaging in confocal microscopes* (World Scientific, 1996).
13. Booth, M. J. Adaptive optical microscopy: the ongoing quest for a perfect image. en. *Light: Science & Applications* **3,** e165–e165 (2014).
14. Klar, T. A., Jakobs, S., Dyba, M., Egner, A. & Hell, S. W. Fluorescence microscopy with diffraction resolution barrier broken by stimulated emission. *Proceedings of the National Academy of Sciences* **97,** 8206–8210 (2000).
15. Betzig, E. *et al.* Imaging intracellular fluorescent proteins at nanometer resolution. *science* **313,** 1642–1645 (2006).
16. Gilaberte Basset, M. *et al.* Perspectives for applications of quantum imaging. *Laser & Photonics Reviews* **13,** 1900097 (2019).
17. Moreau, P.-A., Toninelli, E., Gregory, T. & Padgett, M. J. Imaging with quantum states of light. *Nature Reviews Physics* **1,** 367–380 (2019).
18. Pirandola, S., Bardhan, B. R., Gehring, T., Weedbrook, C. & Lloyd, S. Advances in photonic quantum sensing. *Nature Photonics* **12,** 724–733 (2018).

19. Nagata, T., Okamoto, R., O'Brien, J. L., Sasaki, K. & Takeuchi, S. Beating the Standard Quantum Limit with Four-Entangled Photons. *Science* **316,** 726–729 (2007).
20. Wolfgramm, F., Vitelli, C., Beduini, F. A., Godbout, N. & Mitchell, M. W. Entanglement-enhanced probing of a delicate material system. *Nature Photonics* **7,** 28–32 (2013).
21. Defienne, H., Reichert, M., Fleischer, J. W. & Faccio, D. Quantum image distillation. *Science Advances* **5,** eaax0307 (2019).
22. Gregory, T., Moreau, P.-A., Toninelli, E. & Padgett, M. J. Imaging through noise with quantum illumination. en. *Science Advances* **6,** eaay2652 (2020).
23. Defienne, H., Reichert, M. & Fleischer, J. W. Adaptive Quantum Optics with Spatially Entangled Photon Pairs. *Physical Review Letters* **121,** 233601 (2018).
24. Tsang, M. Quantum Imaging beyond the Diffraction Limit by Optical Centroid Measurements. *Physical Review Letters* **102,** 253601 (2009).
25. Toninelli, E. *et al.* Resolution-enhanced quantum imaging by centroid estimation of biphotons. *Optica* **6,** 347–353 (2019).
26. Lemos, G. B. *et al.* Quantum imaging with undetected photons. *Nature* **512,** 409–412 (2014).
27. Ndagano, B. *et al.* Quantum microscopy based on Hong–Ou–Mandel interference. en. *Nature Photonics,* 1–6 (2022).
28. Anwar, A., Perumangatt, C., Steinlechner, F., Jennewein, T. & Ling, A. Entangled photon-pair sources based on three-wave mixing in bulk crystals. *Review of Scientific Instruments* **92,** 041101 (2021).
29. Fox, M. *Quantum optics: an introduction* (OUP Oxford, 2006).
30. Defienne, H., Reichert, M. & Fleischer, J. W. General Model of Photon-Pair Detection with an Image Sensor. *Physical Review Letters* **120,** 203604 (2018).
31. Defienne, H., Ndagano, B., Lyons, A. & Faccio, D. Polarization entanglement-enabled quantum holography. *Nature Physics* **17,** 591–597 (2021).
32. Parniak, M. *et al.* Beating the Rayleigh Limit Using Two-Photon Interference. en. *Physical Review Letters* **121.** (Visited on 03/28/2019) (2018).
33. Dussault, D. & Hoess, P. *Noise performance comparison of ICCD with CCD and EMCCD cameras* in *Infrared Systems and Photoelectronic Technology* **5563** (SPIE, 2004), 195–204.
34. Cusini, I. *et al.* Historical Perspectives, State of art and Research Trends of Single Photon Avalanche Diodes and Their Applications (Part 1: Single Pixels). *Frontiers in Physics* **10** (2022).
35. You, L. Superconducting nanowire single-photon detectors for quantum information. *Nanophotonics* **9,** 2673–2692 (2020).
36. Bachor, H.-A. & Ralph, T. C. *A guide to experiments in quantum optics* 2nd, rev. and enl. ed. en (Wiley-VCH, Weinheim, 2004).
37. Ono, T., Okamoto, R. & Takeuchi, S. An entanglement-enhanced microscope. *Nature Communications* **4,** 1–7 (2013).

38. Israel, Y., Rosen, S. & Silberberg, Y. Supersensitive Polarization Microscopy Using NOON States of Light. *Physical Review Letters* **112,** 103604 (2014).
39. Madonini, F., Severini, F., Zappa, F. & Villa, F. Single Photon Avalanche Diode Arrays for Quantum Imaging and Microscopy. *Advanced Quantum Technologies* **4,** 2100005 (2021).
40. Ndagano, B. *et al.* Imaging and certifying high-dimensional entanglement with a single-photon avalanche diode camera. *npj Quantum Information* **6,** 1–8 (2020).
41. Zarghami, M. *et al.* A 32 32-Pixel CMOS Imager for Quantum Optics With Per-SPAD TDC, 19.48% Fill-Factor in a 44.64-m Pitch Reaching 1-MHz Observation Rate. en. *IEEE Journal of Solid-State Circuits* **55,** 2819–2830 (2020).
42. Cusini, I. *et al.* Historical Perspectives, State of Art and Research Trends of SPAD Arrays and Their Applications (Part II: SPAD Arrays). *Frontiers in Physics* **10,** 606 (2022).
43. Unternährer, M., Bessire, B., Gasparini, L., Perenzoni, M. & Stefanov, A. Super-resolution quantum imaging at the Heisenberg limit. *Optica* **5,** 1150–1154 (2018).
44. Schirber, M. Nobel Prize: Quantum Entanglement Unveiled. *Physics* **15,** 153 (2022).
45. Mandel, L. & Wolf, E. *Optical coherence and quantum optics* (Cambridge university press, 1995).
46. Nielsen, M. A. & Chuang, I. L. *Quantum computation and quantum information* 10th anniversary ed. en (Cambridge University Press, Cambridge ; New York, 2010).
47. Aaronson, S. Introduction to Quantum Information Science Lecture Notes. en, 259.
48. *Saturday Morning Breakfast Cereal - The Talk* (visited on 09/12/2022).
49. Wang, Y., Hu, Z., Sanders, B. C. & Kais, S. Qudits and High-Dimensional Quantum Computing. *Frontiers in Physics* **8.** (Visited on 02/15/2023) (2020).
50. Renou, M.-O. *et al.* Quantum theory based on real numbers can be experimentally falsified. en. *Nature* **600,** 625–629 (2021).
51. Li, Z.-D. *et al.* Testing Real Quantum Theory in an Optical Quantum Network. *Physical Review Letters* **128,** 040402 (2022).
52. Mitchell, M. W. *Quantum optics for the impatient* (2007).
53. Kok, P. & Lovett, B. W. *Introduction to Optical Quantum Information Processing* (Cambridge university press, 2010).
54. Ou, Z.-Y. J. *Quantum optics for experimentalists* en (World Scientific, New Jersey, 2017).
55. O'Brien, J. L., Pryde, G. J., White, A. G., Ralph, T. C. & Branning, D. Demonstration of an all-optical quantum controlled-NOT gate. en. *Nature* **426,** 264–267 (2003).

56. Walther, P. *et al.* Experimental one-way quantum computing. en. *Nature* **434,** 169–176 (2005).
57. Kok, P. *et al.* Linear optical quantum computing with photonic qubits. *Reviews of Modern Physics* **79,** 135–174 (2007).
58. Aspelmeyer, M. *et al.* Long-Distance Free-Space Distribution of Quantum Entanglement. *Science* **301,** 621–623 (2003).
59. Resch, K. J. *et al.* Distributing entanglement and single photons through an intra-city, free-space quantum channel. *Optics Express* **13,** 202–209 (2005).
60. Ren, J.-G. *et al.* Ground-to-satellite quantum teleportation. en. *Nature* **549,** 70–73 (2017).
61. Liao, S.-K. *et al.* Satellite-to-ground quantum key distribution. en. *Nature* **549,** 43–47 (2017).
62. Forbes, A. & Nape, I. Quantum mechanics with patterns of light: Progress in high dimensional and multidimensional entanglement with structured light. *AVS Quantum Science* **1,** 011701 (2019).
63. He, C., Shen, Y. & Forbes, A. Towards higher-dimensional structured light. en. *Light: Science & Applications* **11,** 205 (2022).
64. Xu, F., Ma, X., Zhang, Q., Lo, H.-K. & Pan, J.-W. Secure quantum key distribution with realistic devices. *Reviews of Modern Physics* **92,** 025002 (2020).
65. Torres, J. P., Banaszek, K. & Walmsley, I. A. en. in *Progress in Optics* (ed Wolf, E.) 227–331 (Elsevier, 2011). (Visited on 09/21/2022).
66. Boyd, R. W. *Nonlinear optics* (Academic press, 2020).
67. You, C., Nellikka, A. C., Leon, I. D. & Magaña-Loaiza, O. S. Multiparticle quantum plasmonics. en. *Nanophotonics* **9,** 1243–1269 (2020).
68. Procopio, L. M., Rosas-Ortiz, O. & Velázquez, V. Spatial correlation of photon pairs produced in spontaneous parametric down-conversion. *AIP Conference Proceedings* **1287,** 80–84 (2010).
69. Procopio, L. M., Rosas-Ortiz, O. & Velázquez, V. On the geometry of spatial biphoton correlation in spontaneous parametric down conversion: On the geometry of spatial biphoton correlation in spontaneous parametric down conversion. *Mathematical Methods in the Applied Sciences* **38,** 2053–2061 (2015).
70. Walborn, S., Monken, C., Pádua, S. & Souto Ribeiro, P. Spatial correlations in parametric down-conversion. *Physics Reports* **495,** 87–139 (2010).
71. Fejer, M. M., Magel, G., Jundt, D. H. & Byer, R. L. Quasi-phase-matched second harmonic generation: tuning and tolerances. *IEEE Journal of quantum electronics* **28,** 2631–2654 (1992).
72. Ortega, E. A. *et al. Spatial and spectral characterization of photon pairs at telecommunication-wavelength from type-0 spontaneous parametric down-conversion* en. 2022. (Visited on 10/03/2022).
73. Sansa Perna, A., Ortega, E., Gräfe, M. & Steinlechner, F. Visible-wavelength polarization-entangled photon source for quantum communication and imaging. *Applied Physics Letters* **120,** 074001 (2022).

74. Lubin, G., Oron, D., Rossman, U., Tenne, R. & Yallapragada, V. J. Photon Correlations in Spectroscopy and Microscopy. *ACS Photonics* **9,** 2891–2904 (2022).

75. Zhang, Z., Peng, T., Nie, X., Agarwal, G. S. & Scully, M. O. Entangled photons enabled time-frequency-resolved coherent Raman spectroscopy and applications to electronic coherences at femtosecond scale. en. *Light: Science & Applications* **11,** 274 (2022).

76. Asban, S. & Mukamel, S. Distinguishability and "which pathway" information in multidimensional interferometric spectroscopy with a single entangled photon-pair. *Science Advances* **7** (2021).

77. Nikogosyan, D. N. Beta barium borate (BBO). en. *Applied Physics A* **52,** 359–368 (1991).

78. Kato, K. & Takaoka, E. Sellmeier and thermo-optic dispersion formulas for KTP. EN. *Applied Optics* **41,** 5040–5044 (2002).

79. Osorio, C. I., Valencia, A. & Torres, J. P. Spatiotemporal correlations in entangled photons generated by spontaneous parametric down conversion. *New Journal of Physics* **10,** 113012 (2008).

80. Edgar, M. P. *et al.* Imaging high-dimensional spatial entanglement with a camera. *Nature Communications* **3,** 1–6 (2012).

81. Eckmann, B. *et al.* Characterization of space-momentum entangled photons with a time resolving CMOS SPAD array. *Optics Express* **28,** 31553–31571 (2020).

82. Tasca, D. S., Walborn, S. P., Souto Ribeiro, P. H., Toscano, F. & Pellat-Finet, P. Propagation of transverse intensity correlations of a two-photon state. *Physical Review A* **79,** 033801 (2009).

83. Chan, K. W., Torres, J. P. & Eberly, J. H. Transverse entanglement migration in Hilbert space. *Physical Review A* **75,** 050101 (2007).

84. Fickler, R. *et al.* Quantum Entanglement of High Angular Momenta. *Science* **338,** 640–643 (2012).

85. Krenn, M. *et al.* Generation and confirmation of a (100$\times$ 100)-dimensional entangled quantum system. *Proceedings of the National Academy of Sciences* **111,** 6243–6247 (2014).

86. Fickler, R. *et al.* Interface between path and orbital angular momentum entanglement for high-dimensional photonic quantum information. en. *Nature Communications* **5,** 4502 (2014).

87. Fickler, R., Krenn, M., Lapkiewicz, R., Ramelow, S. & Zeilinger, A. Real-Time Imaging of Quantum Entanglement. en. *Scientific Reports* **3,** 1914 (2013).

88. Kwiat, P. G. *et al.* New High-Intensity Source of Polarization-Entangled Photon Pairs. *Physical Review Letters* **75,** 4337–4341 (1995).

89. Kwiat, P. G., Waks, E., White, A. G., Appelbaum, I. & Eberhard, P. H. Ultrabright source of polarization-entangled photons. *Physical Review A* **60,** R773–R776 (1999).

90. Steinlechner, F. *et al.* A high-brightness source of polarization-entangled photons optimized for applications in free space. *Optics Express* **20,** 9640–9649 (2012).

91. Steinlechner, F. *et al.* Phase-stable source of polarization-entangled photons in a linear double-pass configuration. *Optics Express* **21,** 11943–11951 (2013).

92. Steinlechner, F. *et al.* Efficient heralding of polarization-entangled photons from type-0 and type-II spontaneous parametric downconversion in periodically poled $KTiOPO_4$. *JOSA B* **31,** 2068–2076 (2014).

93. Jabir, M. V. & Samanta, G. K. Robust, high brightness, degenerate entangled photon source at room temperature. *Scientific Reports* **7,** 12613 (2017).

94. Domenico, G. D. *et al.* Direct generation of high brightness path entangled N00N states using structured crystals and shaped pump beams. *Optics Express* **30,** 21535–21543 (2022).

95. Hong, C. K., Ou, Z. Y. & Mandel, L. Measurement of subpicosecond time intervals between two photons by interference. *Physical Review Letters* **59,** 2044–2046 (1987).

96. Ghosh, R. & Mandel, L. Observation of nonclassical effects in the interference of two photons. *Physical Review Letters* **59,** 1903–1905 (1987).

97. Hong, C. K. & Mandel, L. Experimental realization of a localized one-photon state. *Physical Review Letters* **56,** 58–60 (1986).

98. Zhong, H.-S. *et al.* Quantum computational advantage using photons. *Science* **370,** 1460–1463 (2020).

99. Hensen, B. *et al.* Loophole-free Bell inequality violation using electron spins separated by 1.3 kilometres. *Nature* **526,** 682–686 (2015).

100. Shalm, L. K. *et al.* Strong Loophole-Free Test of Local Realism. *Physical Review Letters* **115,** 250402 (2015).

101. Giustina, M. *et al.* Significant-loophole-free test of Bell's theorem with entangled photons. *Physical review letters* **115,** 250401 (2015).

102. Cuevas, A. *et al.* Long-distance distribution of genuine energy-time entanglement. *Nature Communications* **4,** 2871 (2013).

103. Schmitt-Manderbach, T. *et al.* Experimental Demonstration of Free-Space Decoy-State Quantum Key Distribution over 144 km. *Physical Review Letters* **98,** 010504 (2007).

104. Pan, J.-W. *et al.* Multiphoton entanglement and interferometry. *Reviews of Modern Physics* **84,** 777–838 (2012).

105. Giovannetti, V., Lloyd, S. & Maccone, L. Advances in quantum metrology. *Nature Photonics* **5,** 222–229 (2011).

106. Reddy, D. V. *et al.* Superconducting nanowire single-photon detectors with 98% system detection efficiency at 1550 nm. *Optica* **7,** 1649–1653 (2020).

107. Slussarenko, S. *et al.* Unconditional violation of the shot-noise limit in photonic quantum metrology. *Nature Photonics* **11,** 700–703 (2017).

108. Sun, F., Xu, Y., Wu, Z. & Zhang, J. A simple analytic modeling method for SPAD timing jitter prediction. *IEEE Journal of the Electron Devices Society* **7,** 261–267 (2019).

109. Ramelow, S. *et al.* Highly efficient heralding of entangled single photons. EN. *Optics Express* **21,** 6707–6717 (2013).

110. Dixon, P. B. *et al.* Heralding efficiency and correlated-mode coupling of near-IR fiber-coupled photon pairs. *Physical Review A* **90,** 043804 (2014).

111. Kang, Y., Lu, H., Lo, Y.-H., Bethune, D. & Risk, W. Dark count probability and quantum efficiency of avalanche photodiodes for single-photon detection. *Applied Physics Letters* **83,** 2955–2957 (2003).

112. Yamashita, T *et al.* Origin of intrinsic dark count in superconducting nanowire single-photon detectors. *Applied Physics Letters* **99,** 161105 (2011).

113. Marini, L., Camphausen, R., Eggleton, B. J. & Palomba, S. Deterministic filtering of breakdown flashing at telecom wavelengths. *Applied Physics Letters* **111,** 213501 (2017).

114. Shibata, H., Shimizu, K., Takesue, H. & Tokura, Y. Ultimate low system dark-count rate for superconducting nanowire single-photon detector. *Optics Letters* **40,** 3428–3431 (2015).

115. Bronzi, D. *et al.* 100 000 Frames/s 64 32 Single-Photon Detector Array for 2-D Imaging and 3-D Ranging. *IEEE Journal of Selected Topics in Quantum Electronics* **20,** 354–363 (2014).

116. Reichert, M., Defienne, H. & Fleischer, J. W. Optimizing the signal-to-noise ratio of biphoton distribution measurements. *Physical Review A* **98,** 013841 (2018).

117. Reichert, M., Defienne, H. & Fleischer, J. W. Massively Parallel Coincidence Counting of High-Dimensional Entangled States. *Scientific Reports* **8,** 7925 (2018).

118. Chrapkiewicz, R., Jachura, M., Banaszek, K. & Wasilewski, W. Hologram of a single photon. *Nature Photonics* **10,** 576–579 (2016).

119. Fossum, E. R., Ma, J., Masoodian, S., Anzagira, L. & Zizza, R. The Quanta Image Sensor: Every Photon Counts. *Sensors* **16,** 1260 (2016).

120. Diouf, M., Lin, Z., Krishna, K. & Jr, K. C. T. *Multiphoton imaging using a quantitative CMOS camera* in *Multiphoton Microscopy in the Biomedical Sciences XXII* **11965** (SPIE, 2022), 88–94.

121. Ma, J., Zhang, D., Robledo, D., Anzagira, L. & Masoodian, S. Ultra-high-resolution quanta image sensor with reliable photon-number-resolving and high dynamic range capabilities. *Scientific Reports* **12,** 13869 (2022).

122. Wolley, O., Gregory, T., Beer, S., Higuchi, T. & Padgett, M. Quantum imaging with a photon counting camera. en. *Scientific Reports* **12,** 8286 (2022).

123. Madonini, F., Severini, F., Incoronato, A., Conca, E. & Villa, F. *Design of a 24 24 SPAD imager for multi-photon coincidence-detection in super resolution microscopy* in *Quantum Optics and Photon Counting 2021* **11771** (International Society for Optics and Photonics, 2021), 117710B.

124. Villa, F. *et al.* CMOS Imager With 1024 SPADs and TDCs for Single-Photon Timing and 3-D Time-of-Flight. *IEEE Journal of Selected Topics in Quantum Electronics* **20,** 364–373 (2014).

125. Gasparini, L. *et al. A 3232-pixel time-resolved single-photon image sensor with 44.64m pitch and 19.48% fill-factor with on-chip row/frame skipping features reaching 800kHz observation rate for quantum physics applications* in *2018 IEEE International Solid - State Circuits Conference - (ISSCC)* (2018), 98–100.

126. Unternährer, M. *On Quantum Imaging with Time-Resolving Detector Arrays* en. PhD thesis (2018).

127. Rech, I. *et al.* Optical crosstalk in single photon avalanche diode arrays: a new complete model. EN. *Optics Express* **16,** 8381–8394 (2008).

128. Kurtsiefer, C., Zarda, P., Mayer, S. & Weinfurter, H. The breakdown flash of silicon avalanche photodiodes-back door for eavesdropper attacks? *Journal of Modern Optics* **48,** 2039–2047 (2001).

129. Shi, Y. *et al.* Breakdown flash at telecom wavelengths in InGaAs avalanche photodiodes. EN. *Optics Express* **25,** 30388–30394 (2017).

130. Calandri, N., Sanzaro, M., Motta, L., Savoia, C. & Tosi, A. Optical Crosstalk in InGaAs/InP SPAD Array: Analysis and Reduction With FIB-Etched Trenches. *IEEE Photonics Technology Letters* **28,** 1767–1770 (2016).

131. Ito, K. *et al. A Back Illuminated 10m SPAD Pixel Array Comprising Full Trench Isolation and Cu-Cu Bonding with Over 14% PDE at 940nm* in *2020 IEEE International Electron Devices Meeting (IEDM)* (2020), 16.6.1–16.6.4.

132. Jahromi, S. & Kostamovaara, J. Timing and probability of crosstalk in a dense CMOS SPAD array in pulsed TOF applications. EN. *Optics Express* **26,** 20622–20632 (2018).

133. Lubin, G. *et al.* Quantum correlation measurement with single photon avalanche diode arrays. en. *Optics Express* **27,** 32863–32882 (2019).

134. Ficorella, A. *et al. Crosstalk mapping in CMOS SPAD arrays* in *2016 46th European Solid-State Device Research Conference (ESSDERC)* (IEEE, Lausanne, Switzerland, 2016), 101–104. (Visited on 08/14/2020).

135. Schneeloch, J. *et al.* Introduction to the absolute brightness and number statistics in spontaneous parametric down-conversion. en. *Journal of Optics* **21,** 043501 (2019).

136. Lantz, E., Moreau, P.-A. & Devaux, F. Optimizing the signal-to-noise ratio in the measurement of photon pairs with detector arrays. *Physical Review A* **90,** 063811 (2014).

137. Avenhaus, M. *et al.* Photon Number Statistics of Multimode Parametric Down-Conversion. *Physical Review Letters* **101,** 053601 (2008).

138. Wang, H. *et al.* Towards optimal single-photon sources from polarized microcavities. en. *Nature Photonics,* 1–6 (2019).

139. Senellart, P., Solomon, G. & White, A. High-performance semiconductor quantum-dot single-photon sources. en. *Nature Nanotechnology* **12,** 1026–1039 (2017).

140. Aasi, a. J. *et al.* Advanced LIGO. en. *Classical and Quantum Gravity* **32,** 074001 (2015).

141. Griffiths, D. J. *Introduction to electrodynamics* (American Association of Physics Teachers, 2005).

142. Yamaguchi, I. & Zhang, T. Phase-shifting digital holography. EN. *Optics Letters* **22,** 1268–1270 (1997).

143. Terborg, R. A., Pello, J., Mannelli, I., Torres, J. P. & Pruneri, V. Ultrasensitive interferometric on-chip microscopy of transparent objects. *Science Advances* **2,** e1600077 (2016).

144. Camphausen, R. *et al.* A quantum-enhanced wide-field phase imager. *Science Advances* **7,** eabj2155 (2021).

145. Afek, I., Ambar, O. & Silberberg, Y. High-NOON States by Mixing Quantum and Classical Light. *Science* **328,** 879–881 (2010).

146. Braun, D. *et al.* Quantum-enhanced measurements without entanglement. *Reviews of Modern Physics* **90,** 035006 (2018).

147. Thomas-Peter, N. *et al.* Real-World Quantum Sensors: Evaluating Resources for Precision Measurement. en. *Physical Review Letters* **107,** 113603 (2011).

148. Lubart, R., Lavi, R., Friedmann, H. & Rochkind, S. Photochemistry and Photobiology of Light Absorption by Living Cells. en. *Photomedicine and Laser Surgery* **24,** 179–185 (2006).

149. Byrnes, K. R., Wu, X., Waynant, R. W., Ilev, I. K. & Anders, J. J. Low power laser irradiation alters gene expression of olfactory ensheathing cells in vitro. en. *Lasers in Surgery and Medicine* **37,** 161–171 (2005).

150. Casacio, C. A. *et al.* Quantum correlations overcome the photodamage limits of light microscopy. en. *arXiv:2004.00178 [physics, physics:quant-ph].* (Visited on 04/21/2021) (2020).

151. Casacio, C. A. *et al.* Quantum-enhanced nonlinear microscopy. *Nature* **594,** 201–206 (2021).

152. Da Silva, N. S. & Potrich, J. W. Effect of GaAlAs Laser Irradiation on Enzyme Activity. en. *Photomedicine and Laser Surgery* **28,** 431–434 (2010).

153. Okamoto, R. *et al.* Beating the standard quantum limit: phase super-sensitivity of N -photon interferometers. en. *New Journal of Physics* **10,** 073033 (2008).

154. Ku, H. H. Notes on the use of propagation of error formulas. *Journal of Research of the National Bureau of Standards* **70,** 263–273 (1966).

155. Morimoto, K. *et al. 3.2 Megapixel 3D-Stacked Charge Focusing SPAD for Low-Light Imaging and Depth Sensing* en. in *2021 IEEE International Electron Devices Meeting (IEDM)* (IEEE, San Francisco, CA, USA, 2021), 20.2.1–20.2.4. (Visited on 10/11/2022).

156. Shimada, S. *et al. A SPAD Depth Sensor Robust Against Ambient Light: The Importance of Pixel Scaling and Demonstration of a 2.5m Pixel with 21.8% PDE at 940nm* in *2022 International Electron Devices Meeting (IEDM)* (IEEE, San Francisco, CA, USA, 2022), 37.3.1–37.3.4. (Visited on 02/07/2023).

157. Giovannetti, V., Lloyd, S. & Maccone, L. Quantum-Enhanced Measurements: Beating the Standard Quantum Limit. *Science* **306,** 1330–1336 (2004).

158. Stephens, D. J. & Allan, V. J. Light Microscopy Techniques for Live Cell Imaging. en. *Science* **300,** 82–86 (2003).

159. Eckert, K. *et al.* Quantum non-demolition detection of strongly correlated systems. en. *Nature Physics* **4,** 50–54 (2008).

160. Mitchell, M. W., Lundeen, J. S. & Steinberg, A. M. Super-resolving phase measurements with a multiphoton entangled state. *Nature* **429,** 161–164 (2004).

161. Sawyer, L., Grubb, D. T. & Meyers, G. F. *Polymer microscopy* 3rd ed. (Springer, New York, 2008).

162. Terborg, R. A. *Lens-free interferometric microscope for transparent materials* en. PhD thesis (2018).

163. Dey, P. *et al.* Label-free Bacteria Quantification in Blood Plasma by a Bioprinted Microarray Based Interferometric Point-of-Care Device. *ACS Sensors* **4,** 52–60 (2019).

164. Yesilkoy, F. *et al.* Phase-sensitive plasmonic biosensor using a portable and large field-of-view interferometric microarray imager. *Light: Science & Applications* **7,** 17152 (2018).

165. Fabri-Faja, N. *et al.* Early sepsis diagnosis via protein and miRNA biomarkers using a novel point-of-care photonic biosensor. en. *Analytica Chimica Acta* **1077,** 232–242 (2019).

166. Haegele, S. *et al.* Large field-of-view holographic imager with ultra-high phase sensitivity using multi-angle illumination. en. *Optics and Lasers in Engineering* **161,** 107315 (2023).

167. *ShinePhi – Phase Imaging Technology* en-US. (Visited on 11/08/2022).

168. Zhang, C., Zhao, J. & Sun, Y. Influences of the thickness, misalignment, and dispersion of the Savart polariscope on the optical path difference and spectral resolution in the polarization interference imaging spectrometer. *Applied Optics* **50,** 3497–3504 (2011).

169. Allen, R. D., David, G. B. & Nomarski, G. The zeiss-Nomarski differential interference equipment for transmitted-light microscopy. *Zeitschrift Fur Wissenschaftliche Mikroskopie Und Mikroskopische Technik* **69,** 193–221 (1969).

170. Di Lorenzo Pires, H. & van Exter, M. P. Near-field correlations in the two-photon field. *Physical Review A* **80,** 053820 (2009).

171. Avendaño-Alejo, M. & Rosete-Aguilar, M. Optical path difference in a plane-parallel uniaxial plate. *JOSA A* **23,** 926–932 (2006).

172. Stears, R. L., Martinsky, T. & Schena, M. Trends in microarray analysis. *Nature medicine* **9,** 140–145 (2003).

173. Icha, J., Weber, M., Waters, J. C. & Norden, C. Phototoxicity in live fluorescence microscopy, and how to avoid it. en. *BioEssays* **39,** 1700003 (2017).

174. Hui, S. P., Nag, T. C. & Ghosh, S. Characterization of Proliferating Neural Progenitors after Spinal Cord Injury in Adult Zebrafish. en. *PLOS ONE* **10,** e0143595 (2015).

175. Rainò, G. *et al.* Superfluorescence from lead halide perovskite quantum dot superlattices. *Nature* **563,** 671–675 (2018).

176. Peniakov, G. *et al.* Towards supersensitive optical phase measurement using a deterministic source of entangled multiphoton states. *Physical Review B* **101,** 245406 (2020).

177. Maleki, Y. & Zheltikov, A. M. A high-N00N output of harmonically driven cavity QED. *Scientific Reports* **9,** 16780 (2019).

178. Morimoto, K. *et al.* Megapixel time-gated SPAD image sensor for 2D and 3D imaging applications. EN. *Optica* **7,** 346–354 (2020).

179. Sanzaro, M. *et al.* Single-Photon Avalanche Diodes in a 0.16 m BCD Technology With Sharp Timing Response and Red-Enhanced Sensitivity. en. *IEEE Journal of Selected Topics in Quantum Electronics* **24,** 1–9 (2018).

180. Zhao, Q.-Y. *et al.* Single-photon imager based on a superconducting nanowire delay line. en. *Nature Photonics* **11,** 247–251 (2017).

181. Wollman, E. E. *et al.* A kilopixel array of superconducting nanowire single-photon detectors. en. *arXiv:1908.10520 [physics].* (Visited on 08/29/2019) (2019).

182. Higgins, B. L., Berry, D. W., Bartlett, S. D., Wiseman, H. M. & Pryde, G. J. Entanglement-free Heisenberg-limited phase estimation. en. *Nature* **450,** 393–396 (2007).

183. Thekkadath, G. S. *et al.* Quantum-enhanced interferometry with large heralded photon-number states. *npj Quantum Information* **6,** 1–6 (2020).

184. Kacprowicz, M, Demkowicz-Dobrzański, R, Wasilewski, W, Banaszek, K & Walmsley, I. Experimental quantum-enhanced estimation of a lossy phase shift. *Nature Photonics* **4,** 357–360 (2010).

185. Lee, S.-W., Lee, S.-Y., Lee, S.-Y. & Kim, J. Optimal quantum phase estimation with generalized multi-component Schrödinger cat states. *JOSA B* **37,** 2423–2429 (2020).

186. Defienne, H. *et al.* Pixel super-resolution with spatially entangled photons. en. *Nature Communications* **13,** 3566 (2022).

187. Zhou, R., Edwards, C., Popescu, G. & Goddard, L. *Semiconductor defect metrology using laser-based quantitative phase imaging* in *Quantitative Phase Imaging* **9336** (SPIE, 2015), 146–151.

188. Hegazy, S. F. & Obayya, S. S. A. Tunable spatial-spectral phase compensation of type-I (ooe) hyperentangled photons. *JOSA B* **32,** 445–450 (2015).

189. *www.refractiveindex.info*

190. Ecker, S. *et al.* Strategies for achieving high key rates in satellite-based QKD. en. *npj Quantum Information* **7,** 1–7 (2021).

191. Riccardo, S., Conca, E., Sesta, V., Velten, A. & Tosi, A. Fast-Gated 16 16 SPAD Array With 16 on-Chip 6 ps Time-to-Digital Converters for Non-Line-of-Sight Imaging. *IEEE Sensors Journal* **22,** 16874–16885 (2022).

192. Gulinatti, A., Ceccarelli, F., Ceccarelli, F., Ghioni, M. & Rech, I. Custom silicon technology for SPAD-arrays with red-enhanced sensitivity and low timing jitter. EN. *Optics Express* **29,** 4559–4581 (2021).

193. Stammer, P. *et al.* High Photon Number Entangled States and Coherent State Superposition from the Extreme Ultraviolet to the Far Infrared. *Physical Review Letters* **128,** 123603 (2022).

194. Thomas, P., Ruscio, L., Morin, O. & Rempe, G. Efficient generation of entangled multiphoton graph states from a single atom. en. *Nature* **608,** 677–681 (2022).

195. Meyer-Scott, E. *et al.* Scalable Generation of Multiphoton Entangled States by Active Feed-Forward and Multiplexing. *Physical Review Letters* **129,** 150501 (2022).

196. Juffmann, T., Klopfer, B. B., Frankort, T. L. I., Haslinger, P. & Kasevich, M. A. Multi-pass microscopy. en. *Nature Communications* **7,** 12858 (2016).

197. Schermelleh, L. *et al.* Super-resolution microscopy demystified. *Nature cell biology* **21,** 72–84 (2019).

198. Tenne, R. *et al.* Super-resolution enhancement by quantum image scanning microscopy. en. *Nature Photonics* **13,** 116–122 (2019).

199. Sroda, A. *et al.* SOFISM: Super-resolution optical fluctuation image scanning microscopy. *Optica* **7,** 1308–1316 (2020).

200. Novotny, L. & Hecht, B. *Principles of nano-optics* (Cambridge university press, 2012).

201. Dong, C.-Y., Koenig, K. & So, P. T. Characterizing point spread functions of two-photon fluorescence microscopy in turbid medium. *Journal of biomedical optics* **8,** 450–459 (2003).

202. Rodríguez, C. *et al.* An adaptive optics module for deep tissue multiphoton imaging in vivo. *Nature methods* **18,** 1259–1264 (2021).

203. Cameron, P., Faccio, D. & Defienne, H. *Quantum-assisted sensorless adaptive optics for imaging* EN. in *Imaging and Applied Optics Congress 2022 (3D, AOA, COSI, ISA, pcAOP) (2022), paper OW3G.1* (Optica Publishing Group, 2022), OW3G.1. (Visited on 10/17/2022).

204. Morrison, C. L. *et al.* Frequency-bin entanglement from domain-engineered down-conversion. *arXiv:2201.07259 [quant-ph].* (Visited on 02/16/2022) (2022).

205. Pepe, F. V., Di Lena, F., Garuccio, A., Scarcelli, G. & D'Angelo, M. Correlation plenoptic imaging with entangled photons. *Technologies* **4,** 17 (2016).

206. Abbattista, C. *et al.* Towards Quantum 3D Imaging Devices. en. *Applied Sciences* **11,** 6414 (2021).

207. Polino, E., Valeri, M., Spagnolo, N. & Sciarrino, F. Photonic quantum metrology. *AVS Quantum Science* **2,** 024703 (2020).

208. Ecker, S., Pseiner, J., Piris, J. & Bohmann, M. *Advances in entanglement-based QKD for space applications* en. 2022. (Visited on 10/06/2022).

209. Liu, W.-Z. *et al.* Toward a Photonic Demonstration of Device-Independent Quantum Key Distribution. *Physical Review Letters* **129,** 050502 (2022).

210. Rozema, L. A. *et al.* Scalable Spatial Superresolution Using Entangled Photons. *Physical Review Letters* **112,** 223602 (2014).

211. Shin, H., Chan, K. W. C., Chang, H. J. & Boyd, R. W. Quantum Spatial Superresolution by Optical Centroid Measurements. *Physical Review Letters* **107,** 083603 (2011).

212. Zhu, D. *et al.* A scalable multi-photon coincidence detector based on superconducting nanowires. en. *Nature Nanotechnology* **13,** 596–601 (2018).

213. Kong, L.-D. *et al.* Readout-efficient superconducting nanowire single-photon imager with orthogonal time–amplitude multiplexing by hotspot quantization. en. *Nature Photonics.* (Visited on 10/28/2022) (2022).

214. Di Stefano, L., Mattoccia, S. & Tombari, F. ZNCC-based template matching using bounded partial correlation. *Pattern recognition letters* **26,** 2129–2134 (2005).

215. Edgar, M. P., Gibson, G. M. & Padgett, M. J. Principles and prospects for single-pixel imaging. *Nature Photonics* **13,** 13–20 (2019).

216. Arlt, J. *et al.* A study of pile-up in integrated time-correlated single photon counting systems. *Review of Scientific Instruments* **84,** 103105 (2013).